Bangor University

DOCTOR OF PHILOSOPHY

Studies on the Processing and Stabilisation of Chromophores

Furnell, Leo

Award date:
2016

Awarding institution:
Bangor University

[Link to publication](#)

Studies on the Processing and Stabilisation of Chromophores

A thesis submitted for the degree of
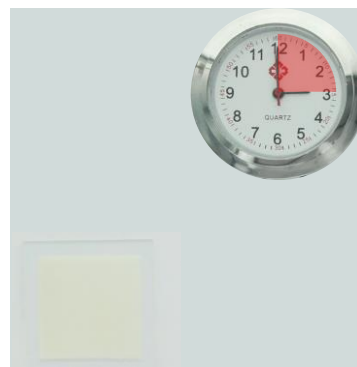
Doctor of Philosophy

SQ1 film prior to exposure   **SQ1 film post exposure**

SQ1 degradation under artificial light exposure

Prifysgol Bangor • Bangor University

© September 2016

by
Leo Furnell

"We live in a world bathed in 5,000 times more energy than we consume as a species in the year, in the form of solar energy. It's just not in usable form yet"

Peter Diamandis

Declaration and Consent

Details of the Work

I hereby agree to deposit the following item in the digital repository maintained by Bangor University and/or in any other repository authorized for use by Bangor University.

Author Name: Mr Leo Furnell

Title: Studies on the Processing and Stabilisation of Chromophores

Supervisor/Department: Dr Peter Holliman/School of Chemistry

Funding body (if any): EPSRC/Tata Case

Qualification/Degree obtained: Doctor of Philosophy in Chemistry

This item is a product of my own research endeavours and is covered by the agreement below in which the item is referred to as "the Work". It is identical in content to that deposited in the Library, subject to point 4 below.

Non-exclusive Rights

Rights granted to the digital repository through this agreement are entirely non-exclusive. I am free to publish the Work in its present version or future versions elsewhere.

I agree that Bangor University may electronically store, copy or translate the Work to any approved medium or format for the purpose of future preservation and accessibility. Bangor University is not under any obligation to reproduce or display the Work in the same formats or resolutions in which it was originally deposited.

Bangor University Digital Repository

I understand that work deposited in the digital repository will be accessible to a wide variety of people and institutions, including automated agents and search engines via the World Wide Web.

I understand that once the Work is deposited, the item and its metadata may be incorporated into public access catalogues or services, national databases of electronic theses and dissertations such as the British Library's EThOS or any service provided by the National Library of Wales.

I understand that the Work may be made available via the National Library of Wales Online Electronic Theses Service under the declared terms and conditions of use (http://www.llgc.org.uk/index.php?id=4676). I agree that as part of this service the National Library of Wales may electronically store, copy or convert the Work to any approved medium or format for the purpose of future preservation and accessibility. The National Library of Wales is not under any obligation to reproduce or display the Work in the same formats or resolutions in which it was originally deposited.

Statement 1:

This work has not previously been accepted in substance for any degree and is not being concurrently submitted in candidature for any degree unless as agreed by the University for approved dual awards.

Signed ………………………………………….. (candidate)
Date ………………………………………………..

Statement 2:

This thesis is the result of my own investigations, except where otherwise stated. Where correction services have been used, the extent and nature of the correction is clearly marked in a footnote(s).
All other sources are acknowledged by footnotes and/or a bibliography.

Signed …………………………………………. (candidate)
Date ………………………………………….

Statement 3:

I hereby give consent for my thesis, if accepted, to be available for photocopying, for inter-library loans and for electronic storage (subject to any constraints as defined in statement 4), after expiry of a bar on access.

Signed ………………………………………… (candidate)
Date …………………………………………

Statement 4:

Choose **<u>one</u>** of the following options

a) I agree to deposit an electronic copy of my thesis (the Work) in the Bangor University (BU) Institutional Digital Repository, the British Library ETHOS system, and/or in any other repository authorized for use by Bangor University and where necessary have gained the required permissions for the use of third party material.	
b) I agree to deposit an electronic copy of my thesis (the Work) in the Bangor University (BU) Institutional Digital Repository, the British Library ETHOS system, and/or in any other repository authorized for use by Bangor University when the approved **bar on access** has been lifted.	**YES**
c) I agree to submit my thesis (the Work) electronically via Bangor University's e-submission system, however I **opt-out** of the electronic deposit to the Bangor University (BU) Institutional Digital Repository, the British Library ETHOS system, and/or in any other repository authorized for use by Bangor University, due to lack of permissions for use of third party material.	

Options B should only be used if a bar on access has been approved by the University.

In addition to the above I also agree to the following:

1. That I am the author or have the authority of the author(s) to make this agreement and do hereby give Bangor University the right to make available the Work in the way described above.

2. That the electronic copy of the Work deposited in the digital repository and covered by this agreement, is identical in content to the paper copy of the Work deposited in the Bangor University Library, subject to point 4 below.

3. That I have exercised reasonable care to ensure that the Work is original and, to the best of my knowledge, does not breach any laws – including those relating to defamation, libel and copyright.

4. That I have, in instances where the intellectual property of other authors or copyright holders is included in the Work, and where appropriate, gained explicit permission for the inclusion of that material in the Work, and in the electronic form of the Work as accessed through the open access digital repository, *or* that I have identified and removed that material for which adequate and appropriate permission has not been obtained and which will be inaccessible via the digital repository.

5. That Bangor University does not hold any obligation to take legal action on behalf of the Depositor, or other rights holders, in the event of a breach of intellectual property rights, or any other right, in the material deposited.

6. That I will indemnify and keep indemnified Bangor University and the National Library of Wales from and against any loss, liability, claim or damage, including without limitation any related legal fees and court costs (on a full indemnity bases), related to any breach by myself of any term of this agreement.

Signature: ……………………………………………………

Date ………………………………………………………….

Table of Contents

Acknowledgements

Abbreviations

Abs	–	Absorbance
AO	–	Dyesol® 18NR Active Opaque Titania Paste
CDCA	–	Chenodeoxycholic acid
Cy	–	Cyanine dye
DSSC	–	Dye solar cell
ESI	–	Electrospray Ionization
FITS	–	Feed in tariffs
FPS	–	Frames per second
FTO	–	Fluoride-doped tin oxide
GW	–	Giga watts
HALS	–	Hindered amine light stabiliser
HFSQ	–	Half squaraine dye
HOMO	–	Highest occupied molecular orbital
HTM	–	Hole transport material
IPCE	–	Incident proton conversion efficiency
LUMO	–	Lowest unoccupied molecular orbital
Mesoporous	–	A material containing pores between 2 and 50 nm
Met	–	Meteorological
OPV	–	Organic photovoltaics
PSC	–	Perovskite solar cells
PV	–	Photovoltaics
RGB	–	Red, green and blue
RO	–	Renewables obligation
ssDSSC	–	Solid state dye solar cell
SQ	–	Squaraine
TBAH	–	Tetrabutylammonium hydroxide
TCO	–	Transparent conductive oxide
TEMP	–	2,2,6,6-Tetramethylpiperidine
TiO_2	–	Titanium dioxide
TPA	–	Triphenylamine
UPTS	–	Universal photovoltaic testing system
UV/Vis	–	Ultra violet visible spectroscopy

Abstract

This project focused on a range of sensitisers used in dye sensitised solar cells (DSSC) and tested their suitability in two main areas. The first was the stability of the dye which is essential for the long term success of DSSC devices. The second was to study dye sorption onto mesoporous TiO_2 films for the construction of DSSC devices.

First the stability of D35, N719, Cyanine, D131, methylene blue and the squaraine 1 and 2 dyes in ethanolic solutions were investigated by exposing to natural light for 64 days. Images after 0 days, 21 days and 64 were processed using RGB analysis and showed significant variation between dye stability. N719 showed the highest stability and squaraine 1 showed the lowest. The stability of N719, squaraine 1 and squaraine 2 was then compared on mesoporous TiO_2 films exposed under an artificial light for 4 hours. The results were concordant with the previous data that N719 was the most stable but also showed a higher stability for squaraine 2 than squaraine 1. Finally DSSC devices of N719 and D35 were constructed and exposed to artificial light. The devices were monitored by solar simulation and image analysis. Results confirmed N719 was again the most stable and showed a link between the efficiency and the colour of the device.

A process to achieve fast dye sorption to TiO_2 films on 15 cm long DSSC devices was developed. The process was conducted by passing the dye through the DSSC device cavity using a peristaltic pump. This method was tested individually with N719, squaraine 2, D131, half squaraine, rhodamine B dyes and also used to co-sensitise half squaraine and SQ1. The time taken for complete sorption was measured using image analysis. Data show that time taken for complete dye uptake varied greatly, with the shortest sorption time of 2 minutes achieved using rhodamine B dye with full coverage after two minutes and a longest sorption time of 1 hour for SQ2. The co-sensitisation of half squaraine and squaraine 1 showed that the order of the dyes was significant, with a dyeing time of 40 minutes for half squaraine first and 50 minutes with SQ1 first.

Chapter 1 Introduction

1.1 Overview

Recent evidence has shown the dangers of climate change due to increasing levels of atmospheric CO_2[1] as shown in Figure 1.1. Burning fossil fuels results in a heightened concentration of atmospheric CO_2 leading to an increase in the greenhouse effect[2]
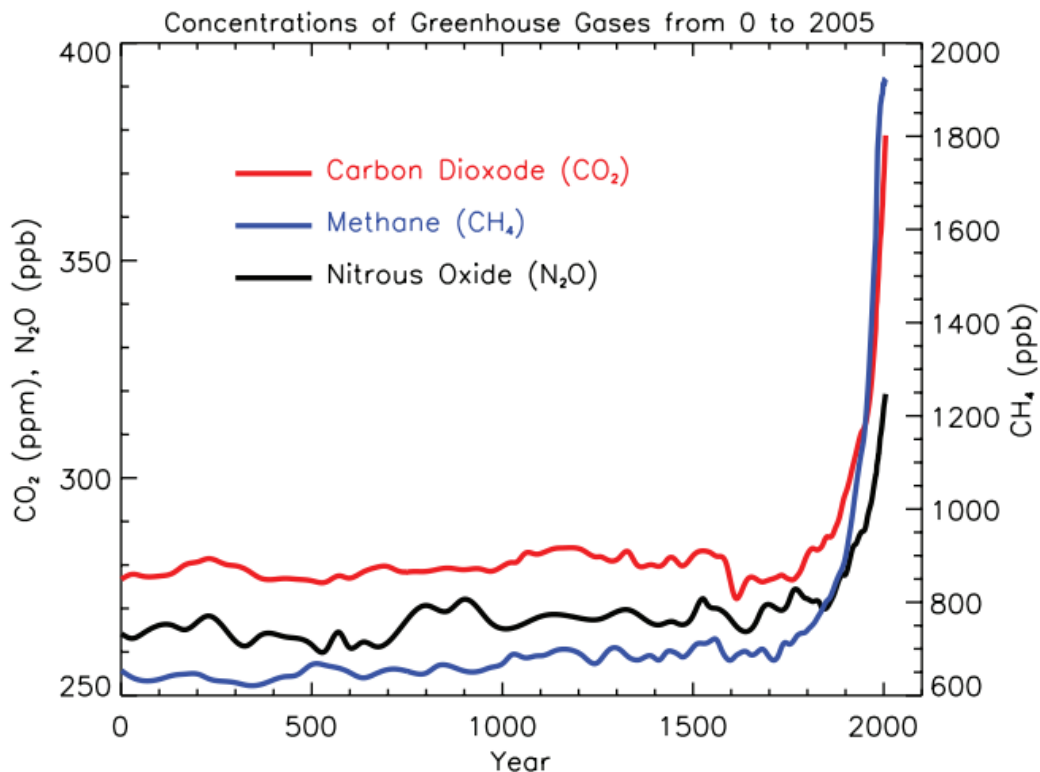
Figure 1.1 Concentration of greenhouse gasses from the year 0 to 2000. The substantial increase in greenhouse gasses present in the atmosphere occurs between 1750 and 2000 is attributed to human use of fossil fuels from the industrial revolution onwards. Graph from the contribution of working group I to the fourth assessment report of the Inter-governmental Panel on Climate Change (IPCC)[3].

The use of fossil fuels as an energy source has substantially increased due to much higher global energy demand[4] driven in part by population growth[5] but also by industrialisation[6].

In order to minimise the damage from fossil fuels and still meet global energy demand, renewable solar energy can be used as an alternative way to generate power with minimal CO_2 emissions[7].

1.2 Solar Cell Applications

Compared to fossil fuel power stations such as coal or gas, solar arrays have significant advantages[7]. Natural gas energy production produces between 300 and 900 g of CO_2/kWh[8] and coal produces between 600 and 1600 g of CO_2/kWh[8]. The units of kWh are defined as 1000W of power provided for 1 hour. The CO_2 emissions from the production and use of solar arrays are between 30 and 90 g of CO_2/kWh dependent on the type of PV used[8]. This is a significantly a lower (90%) carbon footprint[9] for solar energy than fossil fuel energy generation[10].

Producing the same gigawatt peak (GWp) of energy requires similar areas of land for both solar energy and fossil fuels[11]. However, solar arrays have the advantage that they can be constructed as part of a roof or wall, this is known as building integrated photovoltaics (BIPV)[12]. This is a more practical alternative as the space is widely available and land is not required exclusively for the photovoltaic system[13]. Placing solar cells on roofs allows energy to be supplied easily to the building they are attached to, cutting the cost of energy bills for the owner[14]. Additionally with smart grids excess energy can sold back to the national grid, generating an income[15].

If a homeowner wishes to purchase and install solar panels on their roof, there a range of factors they must consider. The first is the conversion efficiency of the solar panels. A higher conversion efficiency will provide more power to be used in the home or sold back to the grid. Using the conversion efficiency the watt per square meter can be calculated and used to determine the peak power that could be produced on a roof. Another significant factor is the cost of the solar panels and their installation. No matter how efficient the solar panels are, if the homeowner is unable to afford them they will not buy them. In addition the energy yield could be considered by homeowners hoping to reduce their environmental impact. The energy yield is the total energy produced in the lifetime of the solar panels minus the energy required for their production and processing. The cost per watt is another important factor which must be considered. This is the cost in pounds for each watt of energy produced. To provide a lower cost per watt solar technology can either be improved to produce a higher conversion efficiency or have a lower installation cost. Dye sensitised solar cells (DSSC) have the potential for a low cost per watt with improvements in efficiency[16].

In the last 4 years solar panels in the UK have become more widely installed for generating electricity in homes[17]. This is largely due to government feed in tariffs (FITs) which pay consumers for generating solar electricity. Additionally energy suppliers are required source a minimum percentage of renewable energy. This is known as renewable obligations and has led to a significant increase in capacity for grid power generation[18]. As a result of this growth of PV in the last 4 years, the UK now has over 10 GW peak of PV installed (shown in Figure 1.2). However, since the availability of FITs has reduced there has been less of a commercial incentive for the public to purchase solar panels and thus the demand in 2016 has slowed.
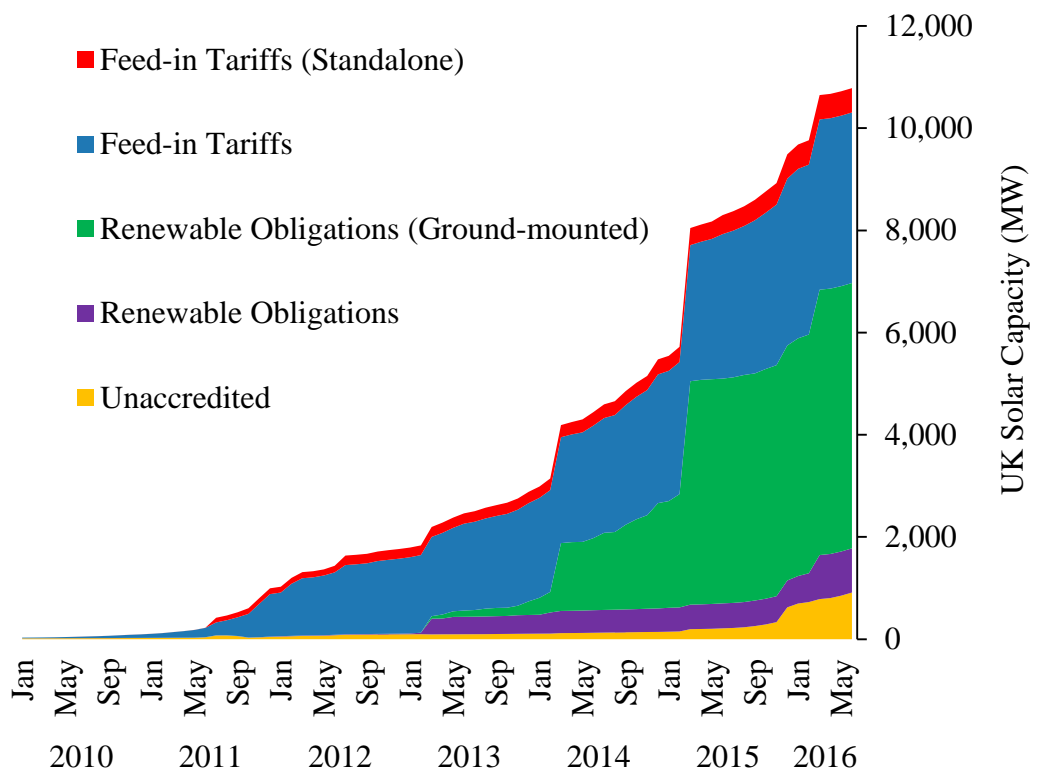
Figure 1.2 UK Solar photovoltaic installations in the last 4 years, data provided by the national statistics department[19]. A substantial increase in installations is shown between 2010 and 2015 with a slowdown in 2016 as FITs are reduced.

To offset the changing FITs there is an increased need to lower the cost of purchasing solar cells. To lower this cost, alternative photovoltaic technologies should be considered which have a lower production costs than silicon PV devices. The production cost is made up of the cost of materials, labour and processing required for fabrication of devices. One way to achieve this is scaled manufacturing which

probably requires continuous, roll-to-roll processing of the currently available PV technologies[20]. OPV, DSSC and PSC are all suitable for roll-to-roll processing.

The National Renewable Energy Laboratory (NREL) provides data on the record verified efficiencies. This data is for small scale solar devices and is grouped by the type of PV technology. This is shown below in Figure 1.3.
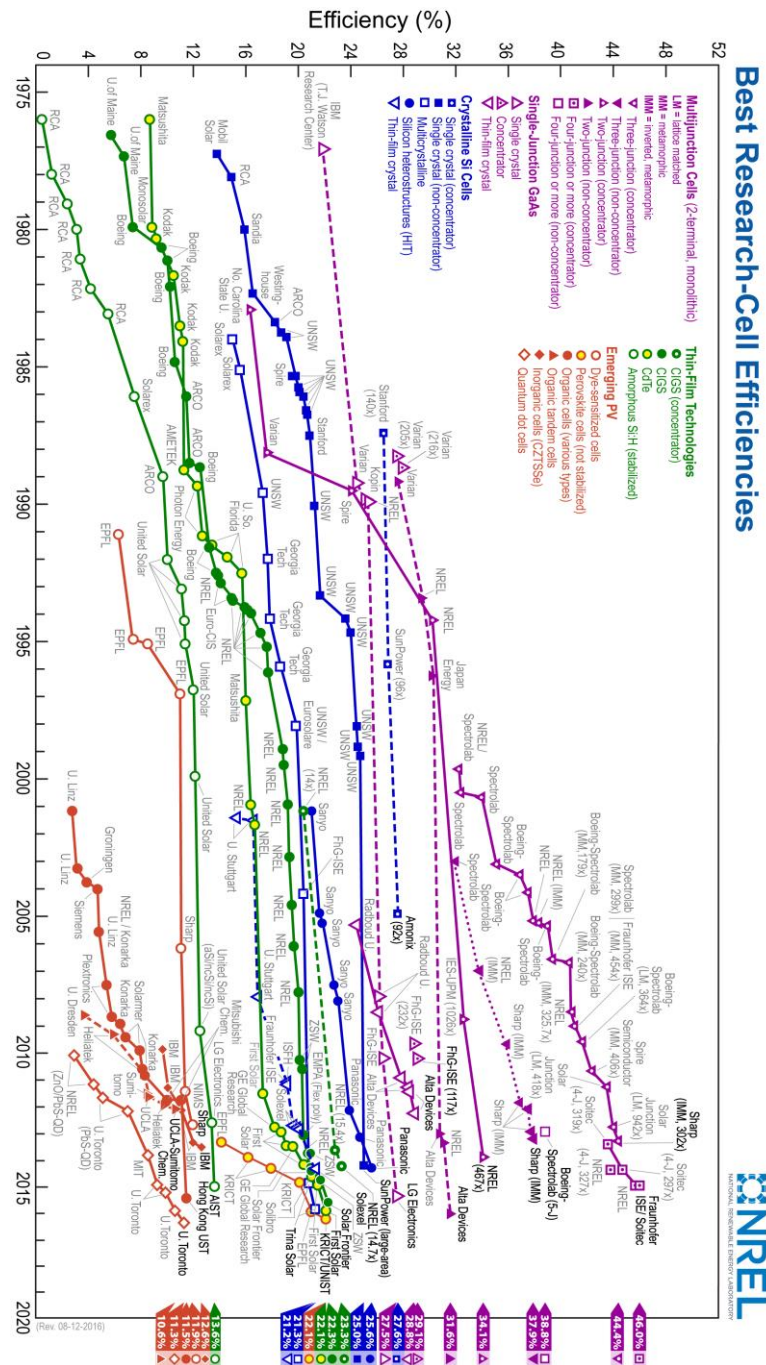

Figure 1.3 NREL data for the record solar cell efficiency for each type of photovoltaic technology[21].

Dye sensitised solar cells (DSSC) are a solar technology which have the advantage of a low energy payback time[22]. Energy payback is the time taken for the energy used in the production of the solar cell to be offset by energy generation. A low energy payback is a crucial criteria for the success of PV technologies. DSSC have been reported to have a shorter energy payback time than silicon cells[23]. Figure 1.4 shows a comparison of the energy payback time for multicrystalline, thin-film and DSSC devices.
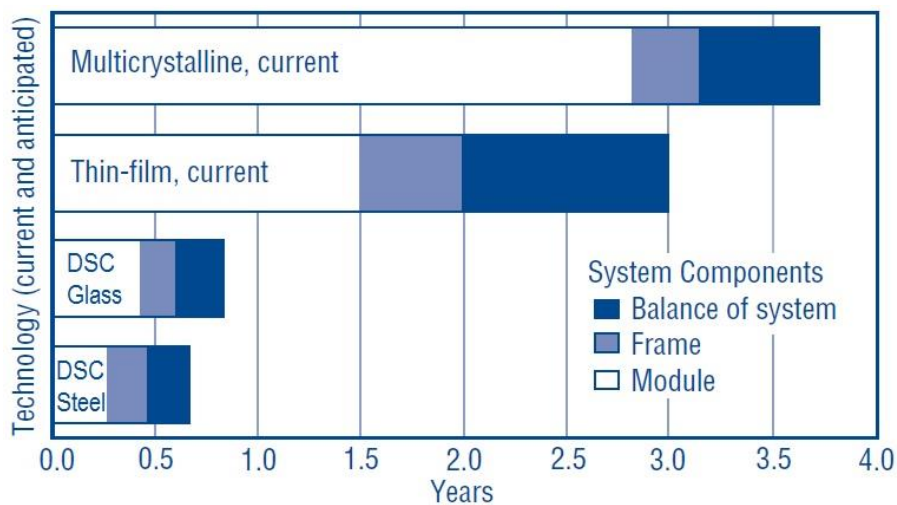
Figure 1.4 NREL data showing energy payback for multicrystalline, thin film PV technologies and DSSC on glass and steel. Current payback time is 3.7 years for multicrystalline devices, 3 years for thin film devices[24], 10 months for DSSC on glass and 7 months for DSSC on steel[23].

The efficiency of DSSC devices was increased significantly to 7% by O'Regan and Grätzel in 1991 by using Titanium dioxide (TiO_2).[25] Since then a considerable amount of research has been done on DSSC devices[26–30]. The DSSC devices have an advantage over silicon PV of operating more effectively at lower intensity light levels, whereas silicon solar cells are best suited to high intensity sunlight[31]. This means DSSC devices would be well suited for use in the UK all year round due to the high numbers of days with low light levels.

A significant factor in the cost of DSSC production is the dye used for sensitisation which is estimated to make up 15 to 22% of the overall cost[32]. Optimisation of the dye uptake and sensitisation process could reduce the quantity of dye used, lowering the overall cost of the cell. A reduction in the cost would allow DSSC devices to compete more easily against silicon photovoltaic devices and fossil fuels.

5

1.3 The Shockley-Queisser Limit

The optimum band gap for a solar cells will result in a theoretical maximum generation of current.[33] The band gap is the energy required for an electron to move from the HOMO to the LUMO. The higher the band gap, the greater the current generated from a single promotion of an electron. However at a higher band gap there are less photons which have enough energy to promote an electron. With a lower band gap, a far greater number of photons will have the required energy to promote an electron but at a lower current. Therefore there is a balance between a large and small band gap and an optimum can be found for maximum energy generation. The Shockley–Queisser limit shows how the band graph relates to device efficiency[34] and is shown in Figure 1.5.
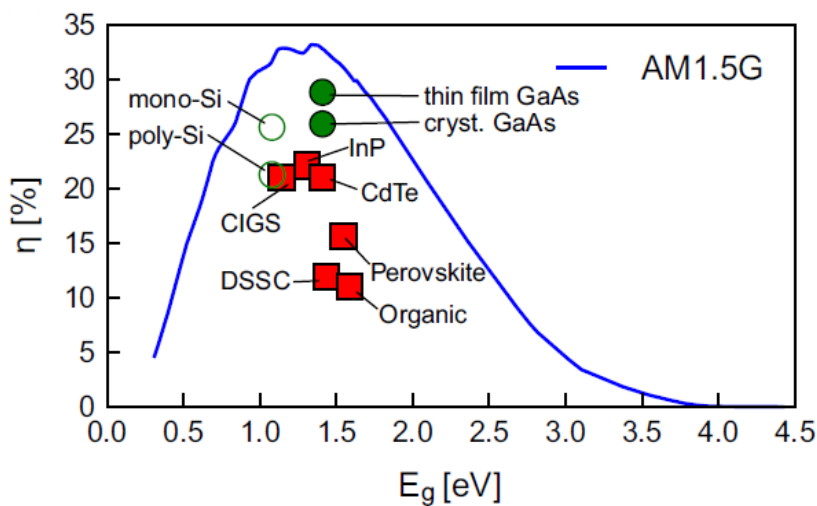
Figure 1.5 Shockley-Queisser limit for photonic electron excitation showing the maximum possible efficiency for a given energy gap. The current photovoltaic technologies have been marked to show the energy gap and current record efficiency. Figure taken from the literature[35].

The Shockley–Queisser limit is 33%[36] and corresponds to a band gap of 1.45 eV for AM1.5[37]. The semiconductors with the closest band gap to the limit are gallium arsenide with a band gap of 1.42 eV[38] and cadmium telluride with a band gap of 1.50 eV[39]. The band gap in silicon solar cells is 1.1 eV which means maximum possible efficiency is 30%[34] which is lower than the at Shockley–Queisser limit as the band gap is less favourable.

1.4 Dye Sensitised Solar Cells

Dye sensitised solar cells operate by using a dye to capture photons which are then converted into electricity.[40] First a photon excites an electron in the dye from the HOMO to the LUMO in a process known as electron promotion (K_1) resulting in the excitation of the dye (D) to (D*). The process takes place exclusively in the sensitising dye and takes a few nanoseconds.[41] Next the electron is injected from the dye into the conduction band of the mesoporous (containing pores 2 and 50 nm) TiO_2. Due to the dye being linked directly to the TiO_2 this process (K_2) is significantly faster than K_1 and K_3, taking only picoseconds.[42] The electron can then move through the TiO_2 and pass**es** through the conductive indium tin oxide (ITO) layer on the electrode to the load, powering an output. The electron then passes through the ITO layer on the counter electrode and diffuses through the electrolyte by redox of the iodide and triiodide. Next the iodine and triiodide in the electrolyte regenerate the dye (K_3). Due to the time taken for charge transfer this is the slowest process at 0.7 seconds.[42] Finally the electrolyte regains an electron from the counter electrode as shown in Figure 1.6.
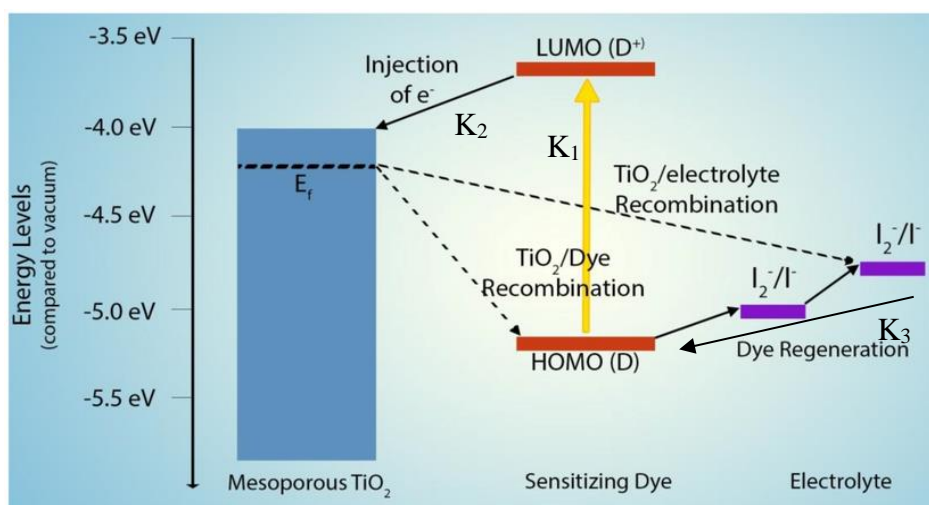
Figure 1.6 Energy levels of a DSSC device during operation. Image from literature[43].

DSSCs have the potential to be improved by development of a range of components such as the semiconductor[44], electrolyte[45] and dye[46].

1.5 Dye Solar Cell Device Components

Dye solar cell devices are typically made up of two electrodes joined together with a thermoplastic gasket to seal them together. The water vapour transmission rate of

surlyn thermoplastic used to seal the cells is 0.6 g/m²/day[47]. This transmission rate is high compared to that of the glass, but has a very small exposed area, $100\mu m^2$ for a $20\mu m$ gasket. The water vapour transmission is therefore 0.6pg/day which is negligible. The photoelectrode is comprised of semiconductor nanoparticles sintered onto mesoporous metal oxide film (usually TiO_2) which has been sensitised with a photoactive dye. The counter electrode is made up of platinum nanoparticles and acts as a catalyst to speed up electron transfer to the electrolyte. This increases the charge density which results in a higher current. In the cavity between the two electrodes electrolyte is placed to allow for charge transport between the two electrodes and regeneration of the dye. These components are shown in Figures 1.7 and 1.8.
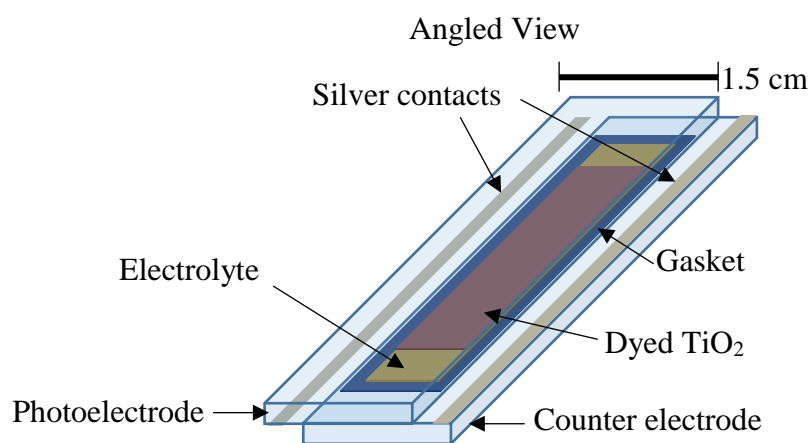
Figure 1.7 Schematic of cell architecture.
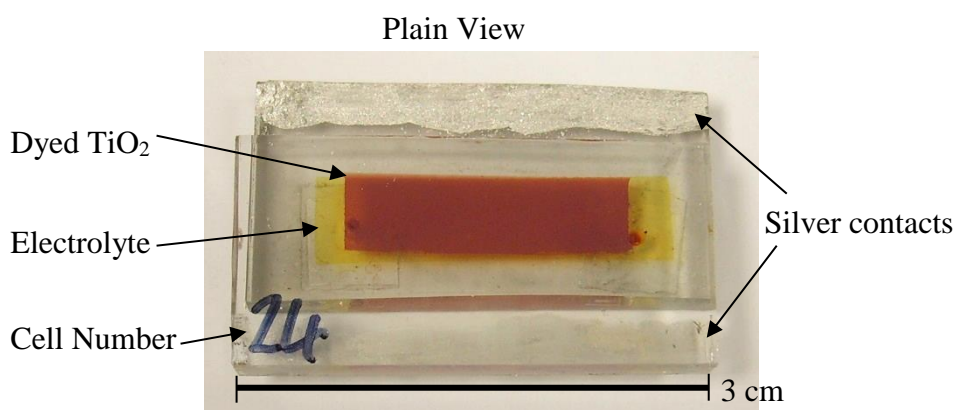
Figure 1.8 Image of a finished dye solar cell.

A typical procedure for electrode fabrication for DSSC is described below in Figure 1.9. Each part of this process is then discussed in further detail later on in this Chapter.

Photoelectrode

| Glass cleaning (15 min) | → | Doctor blading (10 min) | → | Sinter (30 min) | → | Dyeing (18 hours) |

Counter electrode

| Glass drilling (10 min) | → | Glass cleaning (15 min) | → | PT Deposition (5 min) | → | Sinter (30 min) |
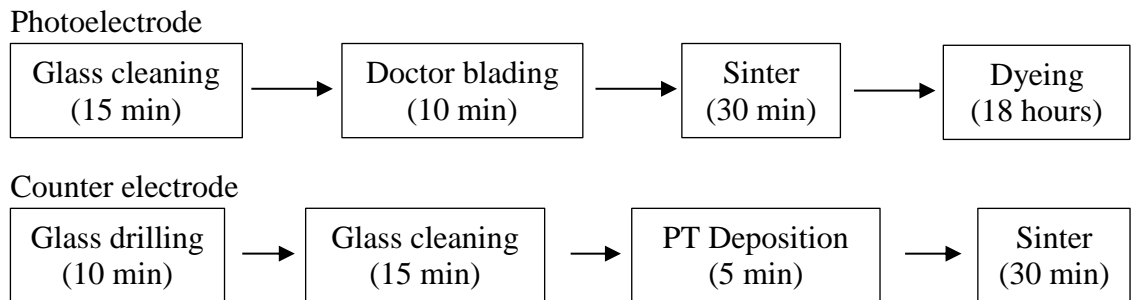
Figure 1.9 Block diagram of processing for fabrication of DSSC electrodes, taken from literature[48].

1.6 Semiconductors for Dye Sensitised Solar Cells

In semiconductors some of the electrons in the valence band have enough thermal energy to reach the conduction band, providing the temperature is above 0K. If the band gap is above 9 eV the material will act as an insulator where the required energy is too great for electrons to move between bands. If the energy levels overlap or the band gap is close to 0, the material will conduct electricity. Representations of the band structures are shown in Figure 1.10.
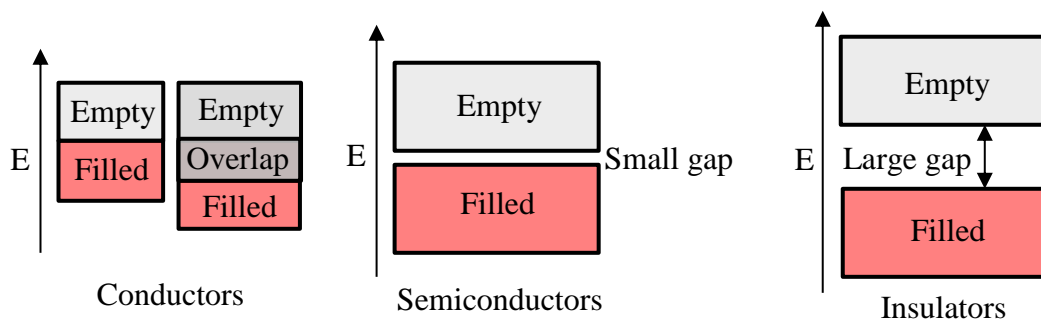
Figure 1.10 Band structure diagrams for metals, semiconductors and insulators. Note that metals can either have a single partially filled band or two overlapping bands. Diagram redrawn from literature[49].

The band gap of a material is calculated from experimental data. This is achieved by running UV-Vis spectroscopy on a powdered sample to determine the absorbance cut-off point. This is the lowest wavelength with an absorbance of zero. The wavelength can then be inserted into equation 1.1 to determine the band gap.

$$E = \frac{hC}{\lambda} \qquad \text{Equation } 1.1[50]$$

Equation 1.1 can be used to calculate an unknown band gap (E) by multiplying planks constant (h = 6.63 x 10^{-34} Js^{-1}) by the speed of light (C = 3 x 10^8 m/s) and then dividing the answer by the absorbance cut off wavelength (λ). TiO_2 used in the photoelectrode is a semiconductor with a wide band gap of 3.2 eV[51].

Titanium dioxide has a wide range of applications from use in cosmetic products such as sunscreen as a UV absorber[52] to a semiconductor in DSSC devices. The reason titanium dioxide is used in DSSC devices is because it has a band gap edge levels which can be adjusted by doping[53] to optimise electron injection for the dye and electrolyte used.

In DSSC devices TiO_2 films are used as a substrate for dye sorption[54]. There are three crystal forms of TiO_2 rutile[55], anatase[56] and brookite[57], these are shown in Figure 1.11
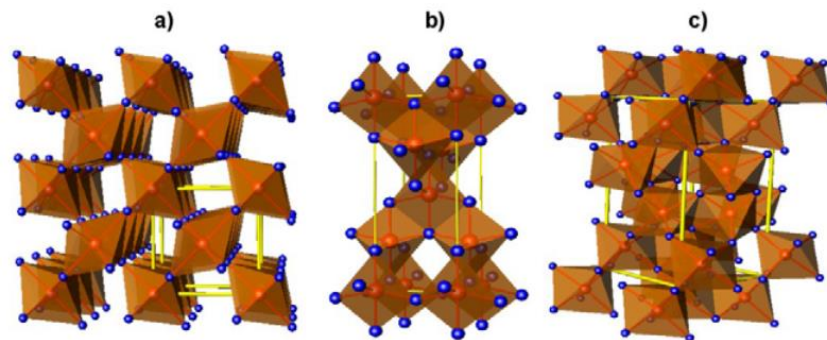
Figure 1.11 Image of the crystal structures of (a) rutile (b) anatase (c) brookite. Blue dots represent titanium, red dots represent oxygen and yellow lines indicate the unit cell[58].

The three forms of TiO_2 differ in their crystal structures with a tetragonal structure for anatase, a body centred tetragonal for rutile and an orthorhombic structure for brookite. The anatase form of TiO_2 has the widest band gap of 3.2 eV[59], brookite is slightly lower with a band gap of 3.13 eV[60] and rutile is the lowest with a band gap of 3.0 eV[61].

For a DSSC electrode, a paste made from anatase and rutile nanoparticles would be used with a binder, such as ethyl cellulose. To solidify the paste after deposition, the film would be heated to burn off the binder in a process known as sintering. After

sintering the film at 500 to 600°C most of the nanoparticles would be converted to anatase. At temperatures above 600°C, the nanoparticles would be completely transformed to rutile above [62]. The band gap for a TiO_2 film would therefore be 3.2 eV. Alternative semiconductors can be used such as ZnO, Mb_2O_3 and SnO_2, however to date the highest efficiencies has been reported with TiO_2[63].

Impurities can be purposely added to a semiconductor to alter the size of its band gap, this is known as doping. This can be used advantageously to optimise the band gap of a semiconductor to tailor it to the desired application. For example the band gap of rutile can be lowered from 3.0 eV to 2.4 eV by nitrogen doping using ammonia[64]. This has been reported to result in a stronger absorption in the visible light range which is beneficial for use in DSSC devices. Anatase can be doped with iodine to lower the band gap from 3.2 eV to 3.0 eV[65]. This also has the advantage of strengthening the absorption of visible light thus increasing the photocurrent.

Semiconductors can be further divided into two types. An n-type semiconductor has been doped with negatively charged ions giving a negative defect allowing the transport of electrons. TiO_2 is an n-type semiconductor[66] which is what allows it to conduct electricity via electron transport[67].

A p-type semiconductor contains positively charged defects allowing for hole transport. An example of a p-type semiconductor is nickel oxide (NiO). Devices made with NiO are much lower efficiency than TiO_2 with a current record efficiency of 2.42% achieved by Dini *et al.*[68]

1.7 Liquid Electrolytes

The liquid electrolytes in DSSC devices have two main functions. The first is to transport charge through the cell by redox reactions[69]. The second is to regenerate the dye. A range of electrolytes can be used but the most common one is iodine which has the following reaction for charge transport shown in Equation 1.2.

$$I_3^- + 2e^-(TiO_2) \rightarrow 3I^- \qquad \text{Equation 1.2[70]}$$
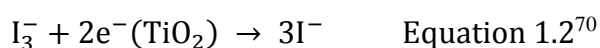
Equation 1.2 shows the electrons reduce the triiodide to iodide allowing for transport of electrons through the electrolyte. The reactions that occur inside a DSSC can be represented in the following equations from the literature[71].

$$D|TiO_2 + hv \xrightarrow{(i)} D^*|TiO_2 \xrightarrow{(ii)} D^+|TiO_2 + e^-_{cb}(TiO_2) \qquad \text{Equation 1.3}$$

$$D^+|TiO_2 + E \xrightarrow{(iii)} D|TiO_2 + E^+ \qquad \text{Equation 1.4}$$

$$D^+|TiO_2 + e^-_{cb}(TiO_2) \xrightarrow{(iv)} D|TiO_2 \qquad \text{Equation 1.5}$$
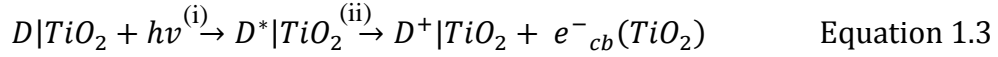
Key: $D|TiO_2$ = dye adsorbed on TiO_2

In Equation 1.3 the first step (i) shows the process of dye excitation by a photon. The second step in Equation 1.3 (ii) shows an electron is injected from the dye to the TiO_2. Equation 1.4 (iii) shows the reduction of the oxidised dye by the electrolyte (E^+). Equation 1.5 (iv) shows the back transfer reaction where the electron returns to the dye reducing it from D^+ to D[72].

Due to the kinetics of DSSC devices the forward process of current generation (Equation 1.3) is favourable. This is due to the high speed of dye injection from the excited state of the dye to the mesoporous TiO_2 compared to the slower back reactions of recombination of the dye and electrolyte (Equation 1.5)[73].

1.8 Standard Testing of Dye Sensitised Solar Cells

To quantify performance, DSSC devices can be tested on a solar simulator. A solar simulator is an artificial light source which is used as a more consistent substitute for the sun when testing solar cells. An ABET solar simulator can be used, which consists of a 120Wm^{-2} (1 sun) Xe arc lamp and a Keithley 2400 source meter for device measurements. This solar simulator is calibrated with a 4 cm^2 NREL certified silicon solar cell.

Devices are placed under the light source and connected to the Keithley with crocodile clips, one clip is attached to each electrode (as shown in Figure 1.12). The Keithley is then set to apply a bias voltage across the cell from 0 to 1V and measures the current output from the cell. From these data an IV curve is plotted and the cell efficiency, current, voltage and fill factor are determined.
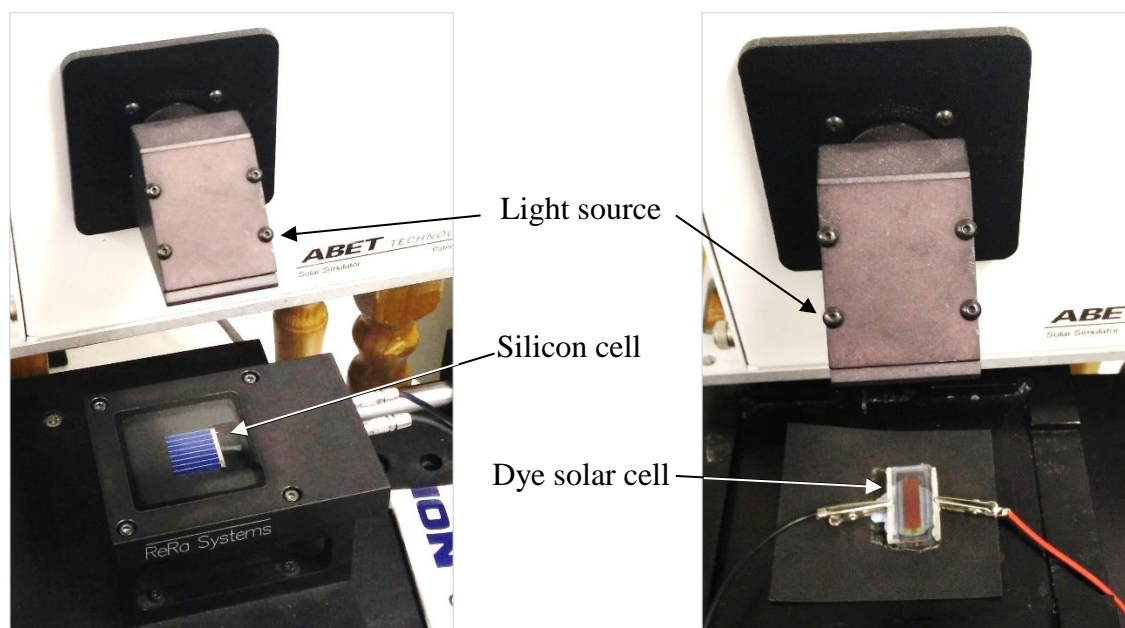
Figure 1.12 (Left) ABET solar simulator with a 4 cm^2 silicon cell for calibration. (Right) A 2 cm^2 dye solar cell connected to the solar simulator for analysis.

1.9 Light Soaking

DSSC devices have application indoors[74] in electonics[75] and externally in building integrated power generation[76]. It is therefore important to determine stability under both natural and artificial light. There are substantial differences between artificial light and natural sunlight[77] which should be considered. The intensity of sunlight fluctuates significantly between the time of day[78] and different seasons[79]. This is due to the angle of the sunlight hitting the earth[80] which is highest in the summer[81] and at midday[82]. When the angle of the light rays is high, rays are less spread out over an area of ground, resulting in a higher intensity. In winter the rays of sunlight are at a lower angle, meaning they are dispersed over a larger area, decreasing intensity and the power output of a solar cell.

For artificial light soaking a standard irradiance is used for testing. This is AM1.5 which represents the equivalent irradiance of the sun at 12 noon at an angle of 90°. AM1.5 is the standard spectra used to model sunlight falling on solar cells and therefore suitable for light soaking (shown in Figure 1.13).
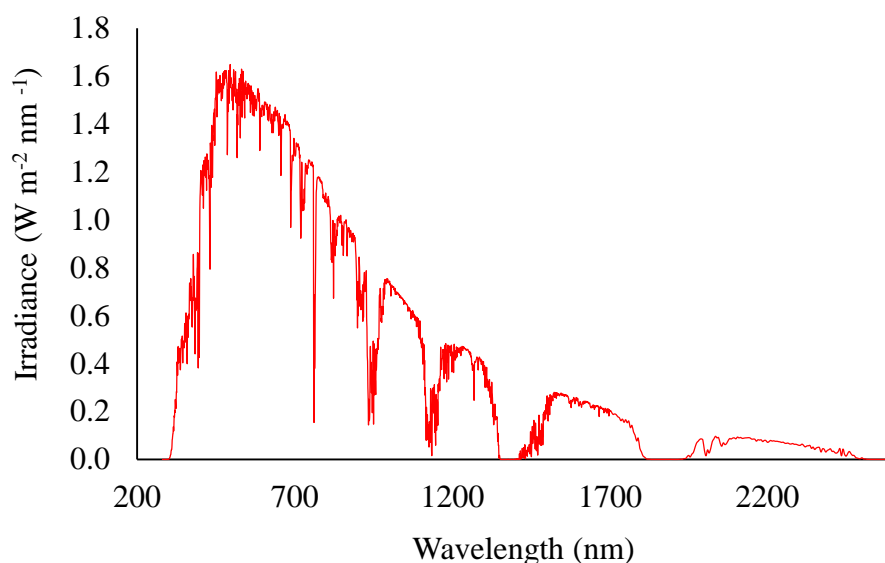
Figure 1.13 AM1.5 Global spectra provides the standard model for testing solar cells, NREL data[83].

The intensity of sunlight would however be less intense than AM1.5 for the great majority of exposure time[84]. This is due to the changes between seasons and the relative position of the sun in the sky throughout the day[85]. The number of hour's daylight should also be considered as degradation testing would expose samples to 24 hours artificial light each day. A 24 hour exposure to AM1.5 therefore represents much higher intensity exposure than a day's outdoor exposure.

1.10 Aims of Project

The aims of this thesis have been divided into two. The first was the development of a process to monitor the stability of the dyes. Any photovoltaic technology must have a lifetime which exceeds payback time. With poor stability, DSSC devices would never be commercially viable as there would be no long term benefit.

The second area was the uptake of dyes onto mesoporous TiO_2. Understanding this is an important requirement for the optimisation of the fast dye process as the end point could be determined, allowing the minimum quantity of dye to be used.

To begin with a method was developed to perform consistent and accurate image analysis on images captured by digital photography, it was as follows:

14

1) The errors of this process were determined and minimised to ensure reliable data could be generated.

2) The image analysis technique was then be applied to monitor degradation of DSSC devices and compare the relative stability of a range different dyes.

3) The image analysis process was then adapted to quantify the dye uptake process onto mesoporous TiO_2 films. The analysis was able to determine the end point of the fast dye process where complete dye coverage on the mesoporous TiO_2 films had been achieved.

4) The fast dye process was scaled up to allow larger DSSC devices to be fabricated on a short timescale. It was also necessary to adapt the fast dye process to allow the switching of dye solutions during processing. This allowed co-sensitisation with multiple dyes on a single device.

Chapter 2 Literature Review

2.1 Hole Transport Materials

An alternative to liquid electrolytes are hole transport materials (HTMs). HTMs work by transporting a vacancy in the electrons, known as an electron hole. A commonly used HTM is spiro-OMeTAD.[86] Devices have been made with spiro-OMeTAD where efficiencies of 5% were achieved by Wang *et al.*[87] however this is significantly lower than the record of 13% for DSSC achieved by Mathew *et al.*[88] Compared to I^-/I^3 redox electrolytes HTMs have the advantage of being less corrosive to the device and much less likely to leak than in liquid electrolytes[32].

Another HTM is AS44, which was used by Leijtens *et al* in 2012 to achieve efficiencies as high as 2.9%, they claimed could rival spiro-OMeTAD[89]. However this seems unlikely unless significant increases in efficiency are made with AS44 to allow similar efficiencies with both HTMs. A comparison of arylamine based HTMs has been made by Hsu *et al.*[90]

In order to work effectively the HTM must fill the TiO_2 pores to provide charge transport throughout the ssDSSC devices. There are two main methods of applying HTMs to a film, the most common is a process called spin coating and the other method is doctor blading. Spin coating is a process where a coating is applied by depositing a film and then spinning rapidly to remove excess solution, this is shown in Figure 2.1.
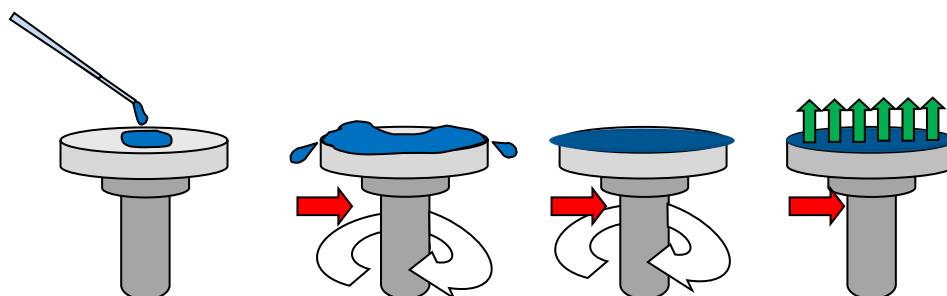
Figure 2.1 The spin coating process takes place in four steps. First the coating is deposited on the sample. Secondly the sample holder is spun to remove any excess coating. Next the sample is rotated at high speeds to fully distribute the coating. Finally the solvent from the coating is left to evaporate, leaving an even layer of coating on the sample. Adapted from literature[91].

Spin coating has been used by Cai *et al.* to construct ssDSSC devices with the highest efficiencies[14] as stated previously. This shows the process can be used to fabricate high quality devices on TiO_2 with a HTM. Ding *et al.* suggested that doctor blading could replace spin coating as a method for depositing hole transport materials[92]. They were able to achieve consistent efficiencies around 3% from cells constructed with both methods. The process for doctor blading is detailed in Figure 2.2.
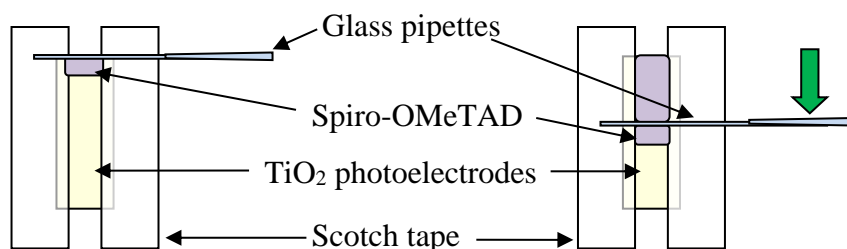
Figure 2.2 The process of doctor blading to fill pores in TiO_2 with the HTM Spiro-OMeTAD.

However these efficiencies were only half that achieved by Cai *et al*[93]. This would suggest that spin coating process fills more pores in the TiO_2 with HTM molecules than doctor blading, due to the increased efficiency of cells produced.
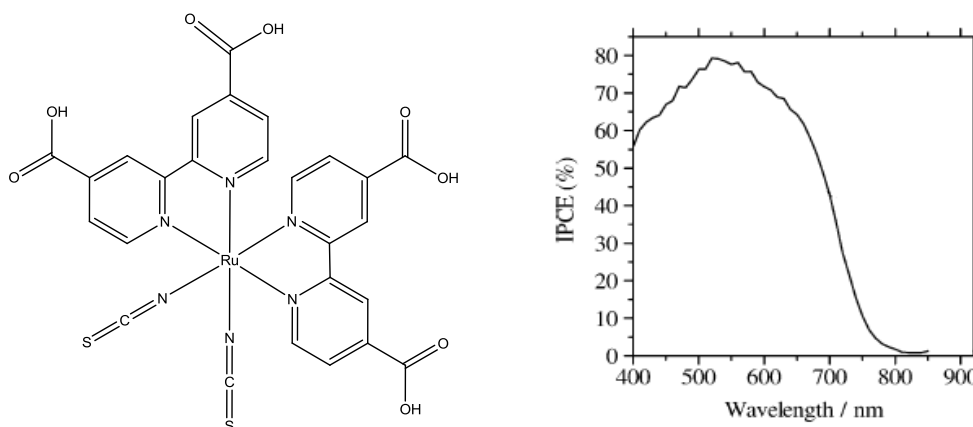

2.2 Sensitisers

There are a vast number of dyes available to use for DSSC devices.[27,42,94–97] However this thesis will focus mainly on N719, SQ1 and SQ2. Z907 and N719 are ruthenium based dyes. Both N719 and Z907 are expensive due high to purification costs of ruthenium[98]. The cost of 1 g of dye costs £124 for N719 and £100 for Z907[99].

There are two main processes used to dye the TiO_2. The first is passive dyeing, where the photoelectrode is submerged inside a dye bath and left for several hours to absorb the dye. The second is fast dyeing, where a pump is used to transfer the dye through a sealed cell for several minutes. Higher efficiencies have achieved using the fast dyeing[100].

To improve the cell performance a range of additives can be used. These additives have different functions and operate in different ways. One additive is chenodeoxycholic acid (CDCA) which is a co-sorbent[101]. CDCA binds onto the titania

and acts as a spacer between the dye[102]. This reduces dye aggregation, where multiple dye molecules join onto one site of the TiO_2, reducing the light which can reach the dye on the surface of the TiO_2 thus reducing efficiency. There is a considerable volume of literature available on the dyes suitable for DSSC devices. This section will look at the dyes mentioned previously in greater detail.

N3 is a ruthenium based dye with the following structure and incident photon to current conversion efficiency (IPCE) shown in Figure 2.3.

Figure 2.3 (Left) Structure of the ruthenium based N3 dye. (Right) IPCE of N3 dye[103] showing a wide peak with highest efficiency between 450 and 650 nm. Note there is negligible IPCE below 400nm.

N3 was first used to sensitise TiO_2 in DSSC devices to give an efficiency of 8.5% in 1993 by Nazeeruddin *et al.*[104] N3 dye excitation promotes an electron from the HOMO to the LUMO in the donor group, this is then injected into the TiO_2. Since then Nazeeruddin *et al.* have improved the efficiency of N3 based cells to 11.2%.[105]

This value is however still lower than the current record for DSSC device efficiency of 14.7%[63]. This record was achieved in 2015 by Kakiage *et al.* with the co-sensitisation of two dyes: ADEKA-1 and LEG4 the structures are shown in Figures 2.4 and 2.5.
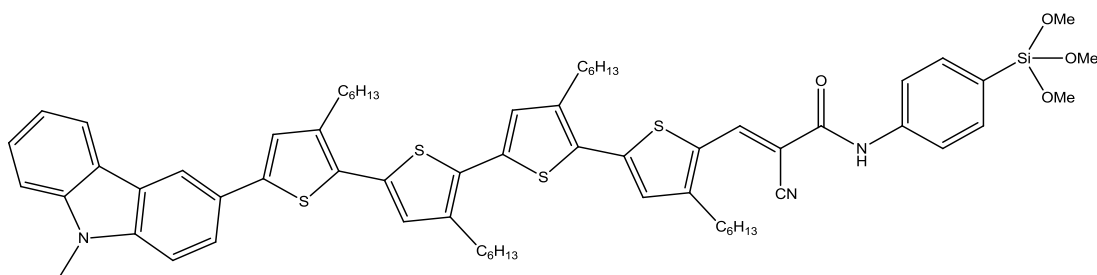
Figure 2.4 Structure of the with an alkoxysilyl- anchor dye ADEKA-1[106] used in combination with LEG4 to achieve record efficiency of 14.7%[63].

Figure 2.5 Structure of the carboxy-anchor organic dye LEG4[107].

N719 dye also a ruthenium based dye and is almost identical to N3 except for the addition of the TBA group which results in a lower percentage IPCE, the structure and IPCE are shown in Figure 2.6.
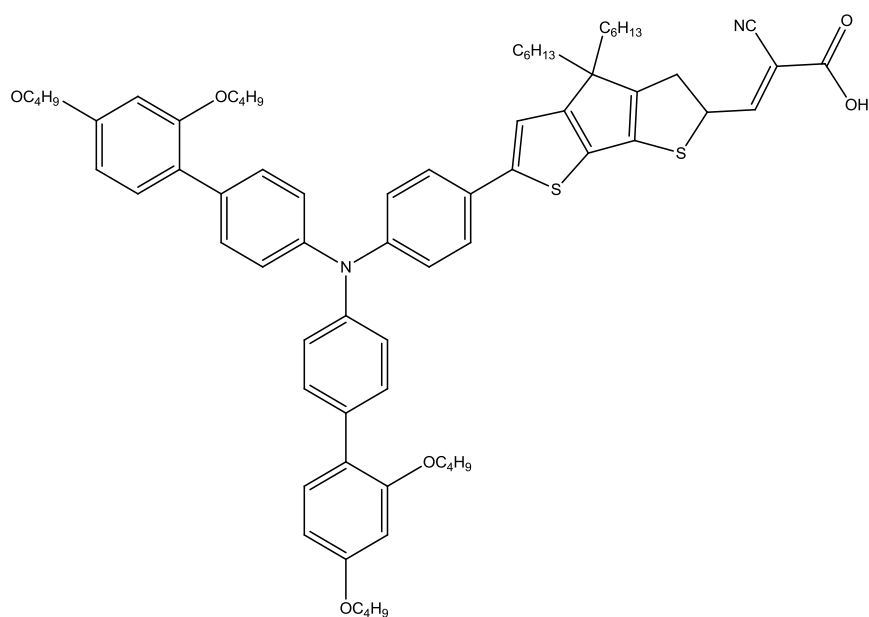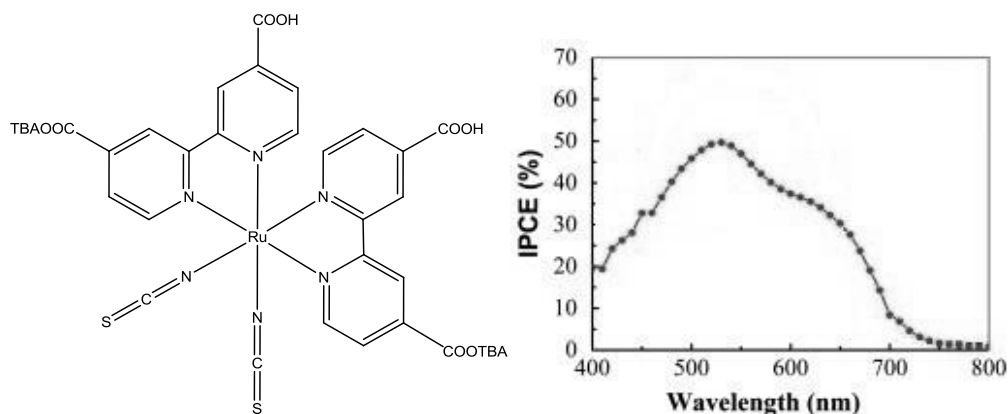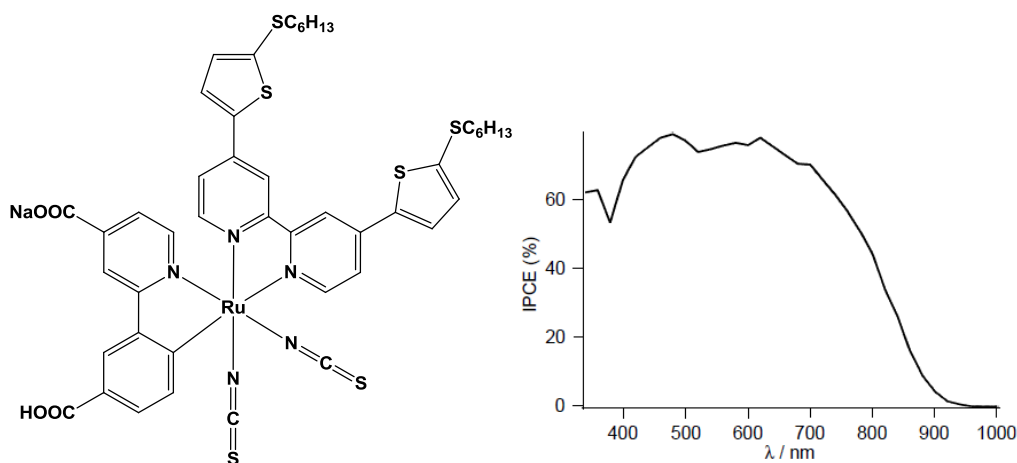
Figure 2.6 (Left) Structure of the ruthenium based N719 dye. (Right) IPCE of N719[108] showing highest efficiency between 500 and 550 nm.

Black dye is an unsymmetrical trithiocyanato ruthenium based dye, the structure and IPCE are shown in Figure 2.7.

Figure 2.7 (Left) Structure of the ruthenium based black dye and its IPCE[109]. (Right) This shows a wide range of high efficiency in the visible range and decreases as the wavelength moves towards infrared (above 750 nm).

Black dye was first used to sensitise TiO_2 cells in 1997 by Nazeeruddin *et al.*[110] The wide range of absorption observed on the IPCE showed cells made with black dye could convert most of the visible light range as well as infrared (IR), this showed it was highly suitable for sensitisation of DSSC devices.

Another ruthenium based dye is Z907 which is symmetrical and has a similar structure N719. This is shown in Figure 2.8.

Figure 2.8 (Left) Structure of the ruthenium based Z907 dye. (Right) IPCE of Z907[111] dye showing highest absorbance between 475 and 575 nm.

Another dye commonly used is the unsymmetrical indoline based organic dye D149, the structure and IPCE are shown in Figure 2.9.
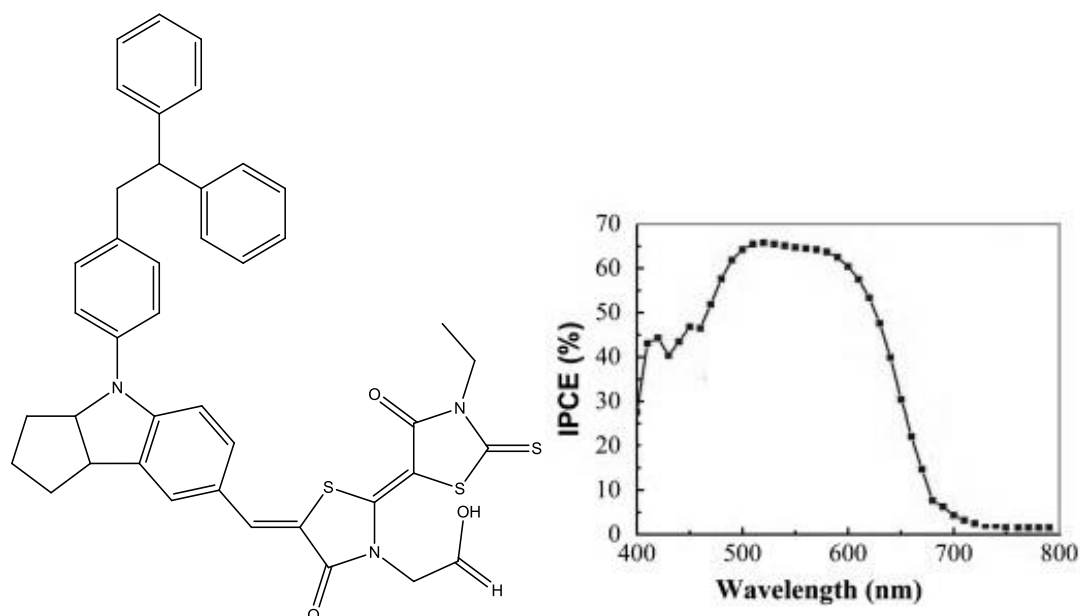
Figure 2.9 (Left) Structure of the organic dye D149. (Right) IPCE of D149[18] showing highest efficiency between 500 and 600 nm.
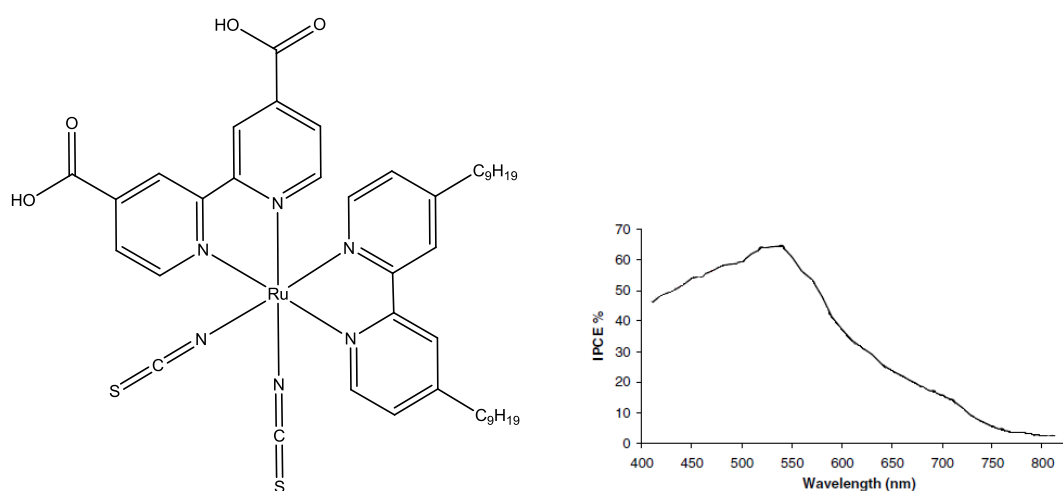
D149 has been used to achieve efficiencies as high as 5.6%[112] which was achieved by Hideki *et al* with a ZnO film.

SQ1 a low cost organic dye derived from squaric acid. The structure and IPCE are shown in Figure 2.10.
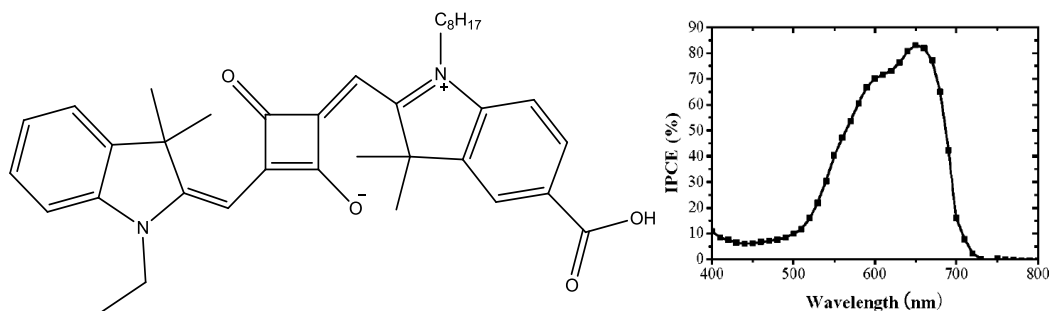
Figure 2.10 (Left) Structure of the organic based SQ1 dye. (Right) IPCE of SQ1 dye[113] showing highest efficiency between 450 and 500 nm.

SQ2 is an organic dye almost identical to SQ1. The structure and IPCE are shown in Figure 2.11.
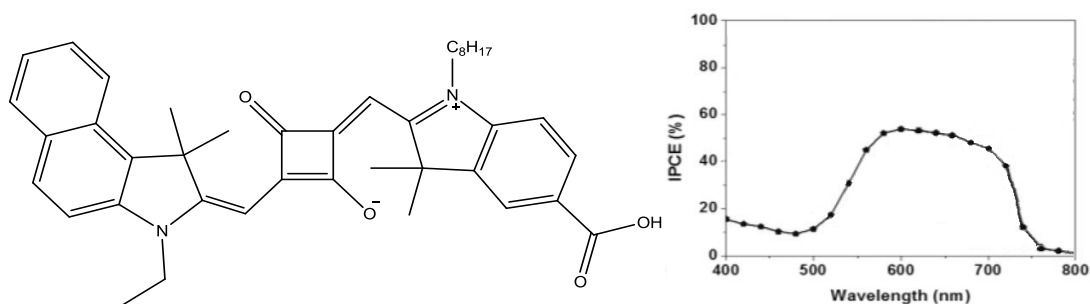
Figure 2.11 (Left) Diagram of the structure of the organic SQ2 dye. (Right) IPCE for Squaraine 2 dye[114] showing highest conversion between 450 and 500 nm.

2.3 Sensitisation Methods

In addition to the great number of dyes for DSSC devices, there are a wide range of processes used for sensitisation. These methods differ in processing time and efficiency of cells produced. Hinsch *et al.* used a method to dye a set of five cells in parallel by using a masterplate[115].

The masterplate held the cells in place and a filling unit passed dye through the fill holes in the cells. The cells constructed this way achieved a maximum efficiency of 5.4% with N3 dye, the masterplate is shown in Figure 2.12.
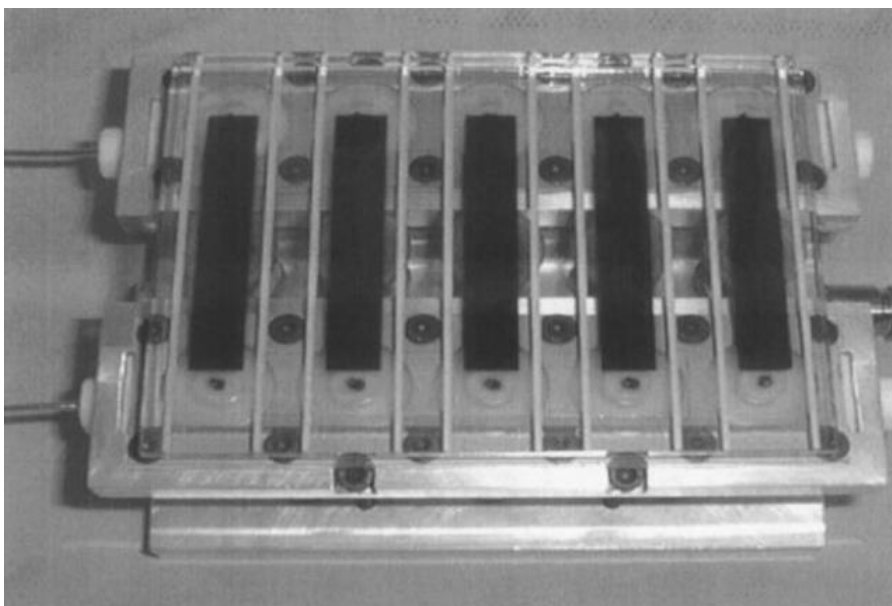
Figure 2.12 The masterplate (75 x 100 mm) used by Hinsch *et al.* to sensitise multiple small scale devices simultaneously, each with an active area of 4 cm^2. Devices were sensitised by pumping dye solution through the fill holes,

Another method for swift dye uptake was used by Grätzel *et al.*[105] In this method, the TiO$_2$ film was treated with TiCl$_4$ to boost efficiency and then sintered at 520°C. The electrode was then left to cool to 50°C before being added to N719 or N3 dye. Cells were then constructed using the swift dyed photoelectrodes. This process produced cells with a maximum efficiency of 9.2% for N719 and 7.7% for N3 dye.

2.31 Passive Dyeing

Passive dye uptake is the process of sensitising a film such as mesoporous TiO$_2$ by submerging in a dye solution. The time required for sensitisation is usually between 18 and 24 hours to ensure full coverage. The progress of passive dye uptake has been investigated by Watson *et al.*[116] and showed dye uptake could be successfully monitored with digital imaging and diffuse reflectance UV- Vis spectrophotometry.

One disadvantage of passive dyeing is the time taken for sensitisation. This is not a significant problem for small scale devices as electrodes can be left overnight for sensitisation. This may however be more of a problem in industry with a production line. If passive dyeing was used the passive dye time would most likely present a bottle neck, limiting the speed at which cells can be produced.

Another disadvantage of passive dyeing is the scalability of devices. For testing purposes small scale cells with an active are of 2 cm^2 are sufficient which can be easily submerged in dye solutions. For larger devices this presents a problem as 1 m by 1 m cell would need a significant dye solution for sensitisation. For larger devices, other options must be investigated.

2.32 Fast Dyeing

The method used by Holliman *et al.*[100] is the fastest dyeing process reported to date. This method differs from the masterplate method in that dye is injected directly into the cell cavity. In this method the cell is sealed in a vessel and dye is run through fill holes for several minutes using a syringe or a pump, as shown in Figure 2.13. This method was used to produce cells with N719 at 6.0% efficiency and 3.7% with SQ1[100].
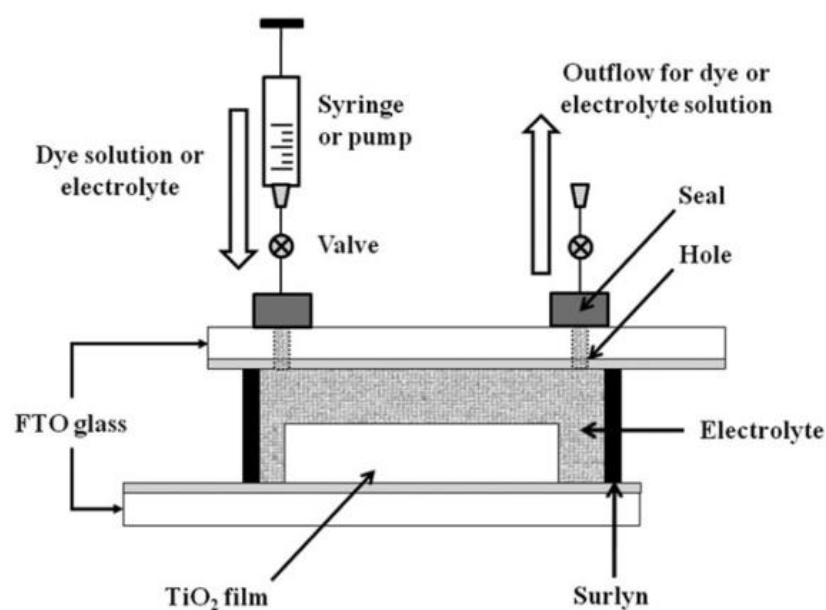
Figure 2.13 Literature diagram of the fast dyeing process used by Holliman *et al.*[100]

2.33 Co-sensitisation

Co-sensitisation is the sorption of more than one dye to a TiO$_2$ film. This can have several advantages. One advantage is that an inexpensive dye can be used with a more costly dye, reducing the quantity of expensive dye used in the sensitisation process. This could for example be the combination of N719 and the less expensive SQ1, as shown in Figure 2.14.
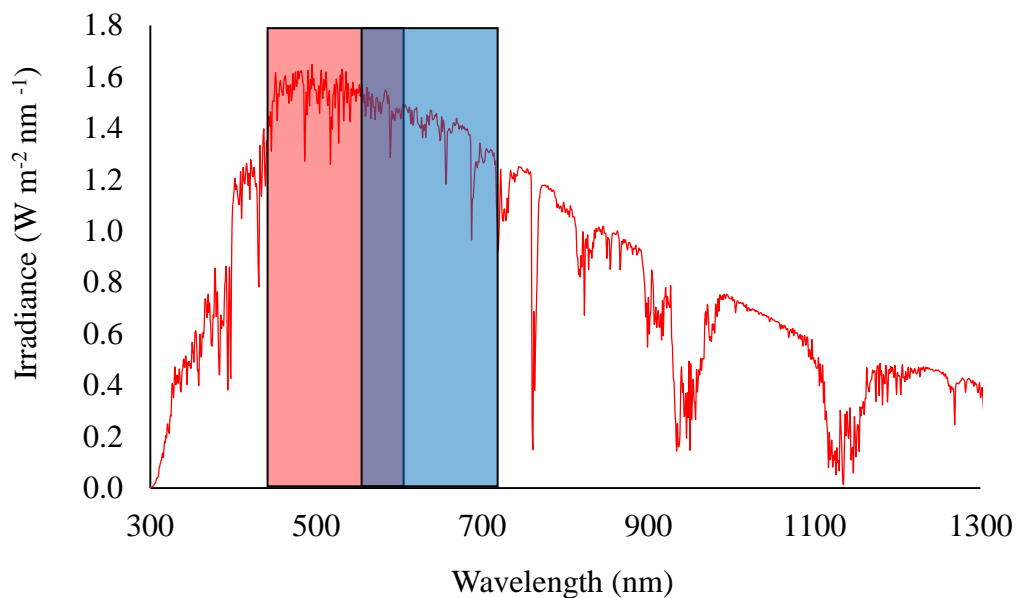
Figure 2.14 Solar **s**pectrum of sunlight AM1.5[83] with the strongest absorption wavelength of D149 indicated in red and the wavelength of SQ1 highlighted in blue. Note the overlap between the two dyes highlighted in purple.

The other advantage of co-sensitisation is that more of the visible spectrum of light can be absorbed by combining dyes which have a λ_{max} at different wavelengths.

Co-sensitisation was used to by Holliman *et al.* to dye with a mixture of N719 and SQ1 followed by SQ1 only[100]. This gave an increased efficiency of 7.9% showing co-sensitisation was successful as a higher efficiency was achieved than the dyes by themselves. The paper also stated that fast dyed cells had a higher efficiency than cells passively dyed for 18 hours.

2.4 Solid State Solar Cells

A major disadvantage of current DSSC devices are the long term effects of the liquid electrolyte[117]. The electrolytes used in DSSC devices are corrosive and can rupture the cell in very high or very low temperatures, causing leaks[118]. An alternative to this is to use a hole transport material (HTM) to carry the electrons from the counter electrode back to the dye. Cells that use this method are called solid state dye sensitised solar cells (ssDSSC).

The current record efficiency for DSSC devices with liquid electrolytes is 14.7%[119] which was achieved by Kakiage *et al.* using ADEKA-1 and LEG4 dyes. However ssDSSC devices have achieved significantly lower than this value with a record efficiency of 10.2% achieved by Chung *et al.*[120]

2.5 Perovskite Solar Cells

A very recent advance in solar cell technology is the development of perovskite solar cells. Perovskite solar cells work by using a perovskite instead of a dye to capture light. Early perovskite cells gave efficiencies of 3.5% in 2008 by Kojima *et al.*[124] This was quickly improved over the following years to 20.1% in 2014[125] and more recently in 2016 a further increase was achieved with an efficiency of 21.1% by Saliba *et al.*[126]

Perovskite cells are inexpensive to produce as well as being highly efficient which may give them an advantage over the more traditional silicon solar cells[127]. Due to significant investment in perovskite cells it is highly likely that the efficiency of perovskite cells will be further increased. Perovskite devices are shown in Figure 2.15.
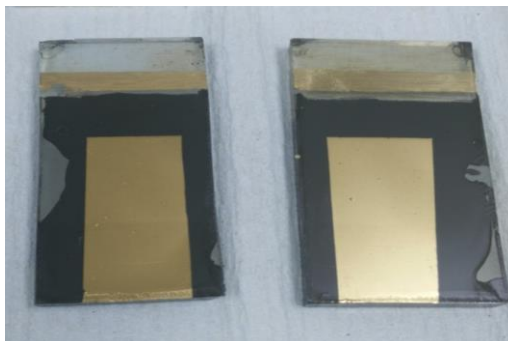
Figure 2.15 Lead iodide perovskite solar cells with a 4 cm^2 active area.

A major hurdle for perovskite cells is the sensitivity of cells to moisture[128]. Due to their low stability the practical applications of perovskite cells are currently limited due to the short lifetime of the devices. However, once more stable perovskites have been established or current perovskites have been successfully stabilised then perovskite devices will be suitable for industrial applications.

The other potential disadvantage to perovskite cells is the toxicity of the lead compounds. If an installed cell was damaged then there would be the danger that lead in the organo halide compound $CH_3NH_3PbI_3$ could contaminate the surrounding area which may include a water source. If this contamination was to occur significantly poisoning of marine life or even humans could occur.

As a non-toxic alternative, tin has been investigated to replace lead in perovskite cells by Noel *et al.* giving an efficiency of 6%[129]. Although the efficiency is currently much lower with further development it could be possible to get similar efficiencies to standard perovskite cells.

2.6 Gallium Arsenide Solar Cells

The semiconductor gallium arsenide has been investigated for use in solar devices due to the potential for a high conversion efficiency caused by the proximity of the 1.4 eV[130] band gap to the ideal value of 1.34 eV[37].

Early gallium arsenide devices constructed by Konagai *et al.* in 1978 showed efficiencies as high as 13.5%.[131] Further progress lead to the development of a device by Bauhuis *et al.* in 2008 with an efficiency of 26.1%[132]. This record was improved further to by LG electronics 27.5% in 2015[133].

In 2013 gallium arsenide devices were constructed by Krogstrup *et al.* with efficiencies as high as 40%[134]. This which is beyond the Shockley-Queisser limit. The efficiency exceeding the Shockley-Queisser limit was possible due to using nano wires to concentrate incident light.

Compared to silicon devices, gallium arsenide devices have the advantage of high flexibility as well as comparable device efficiency. A gallium arsenide device is shown in Figure 2.16.

Figure 2.16 Image of a gallium arsenide cell, demonstrating the flexibility of the device without damage. Image taken from literature[135].

2.7 DSSC Device Stability

There has been a huge amount of literature published on dyes for DSSC devices in the last 20 years with only a small fraction of the published work focused on dye stability[136]. In this context, the literature has reported on many individual dyes[137] instead of direct comparison between multiple dyes. This makes direct comparisons between dye stability difficult as the conditions and setup vary significantly.

The literature which has been published shows wide ranges in device stability, even with the same dye. N719 device testing is an example of this, when tested by Sommeling *et al.* DSSC devices were at open circuit and exposed to both light and heat for 1500 hours.[138] The poorest stability was reported to be from exposure to 1 sun at 85°C which caused the electrolyte to bleach and loss of I_2. N719 was also studied by Xue *et al.* and determined that a 20% drop in efficiency was observed after 1074 hours light exposure.[139] The failure mechanism in this study was determined to be from N719 dye degradation. The stability of N719 DSSC devices has also been tested by Guistini *et al.* using thermal cycling.[140] Grätzel *et al.* improved N719 stability by replacing the NCS^- ligand on the dye, this also resulted in an increased efficiency of 10.1%[141].

Interest on organic DSSC dyes has increased and studies have been made on triphenylamine-based (TPA)[142], half-squaraine[143,144] and indoline[145] dyes. Little work has been published on organic dye lifetime. However an exception to this is TPA dye which was determined to be stable for 1000 hours under light soaking by Holliman *et al*. with I_3^-/I^- redox couples.[146] In addition to this Joly *et al.* reported a stability of 2200

hours for a TPA dye with an I_3^-/I^- in an ionic liquid electrolyte while light soaking at 65°C.[147]

The degradation of D131 has been investigated by Tanaka *et al.* who concluded that the degradation mechanism was based on the decarboxylation of the cyanoacrylic acid which was accelerated by amine and electrolyte.[117] D35 dye lifetime has been studied with a Co(II/III) redox couple and tests the effect of additives on the dye stability during light soaking[148]

There has been some interest in the stability of squaraine based dyes SQ1[149] and SQ2[150] which are near-infrared dyes. Squaraine dyes have been co-sensitised with N719.[100,146] Despite high efficiencies of co-sensitised devices there are only a small number of studies on their stability. Lan *et al.* tested the stability of a porphyrin dye co-sensitised with a spiral dye for 1000 hours of light soaking.[151] Devices co-sensitised with N719 and TPA dyes showed a stability of 500 hours when light soaked by Wu *et al.*[152]

Panchromatic TPA modified squaraines have been tested by Ko *et al.* and showed a stability of 1000 hours.[153] Double linker squaraines with liquid electrolyte have been tested by Han *et al.* these were stable for 1000 hours.[154] The degradation of squaraine dye under visible light has been studied by Wu *et al.* and concluded that TiO_2 breaks down the dye by acting as a photocatalyst.[155] It is widely known that TiO_2 has a photocatalytic effect when exposed to light[156] this has been successfully utilised in water purification.[157] The stability of methylene blue and rhodamine B dyes have also been studied with to TiO_2 by Barkschat *et al.*[158]

Chapter 3 Experimental

3.1 Dye Sensitised Solar Cell Fabrication

To produce TiO_2 photo electrodes, unless otherwise stated TEC 15 (NSG Pilkington) fluoride tin oxide coated conductive glass of 15 $\Omega\square$ was cut to 3.1 cm by 1.5 cm using a glass cutter. The electrode was then cleaned with isopropanol and dried under nitrogen. Two strips of Scotch tape™ (3M Ltd) were then placed on each of longest sides of the glass, leaving a 1 cm wide gap in-between as shown in Figure 3.1. A single thin film of titanium dioxide paste (Dyesol® 18R-AO) was then deposited on the conductive side of the glass using doctor blading and the sections of tape were removed.
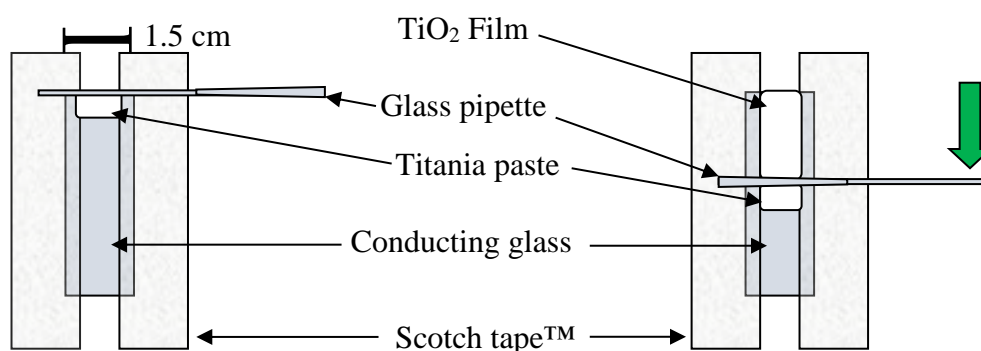
**Figure 3.1** Diagram showing the process of doctor blading where a TiO_2 film is deposited onto glass to function as the photoelectrode.

The electrode was then heated in a Carbolite™ ashing furnace under atmospheric conditions with a heating gradient of 10°C/min up to 500°C where the temperature was held for 30 min Figure 3.2.
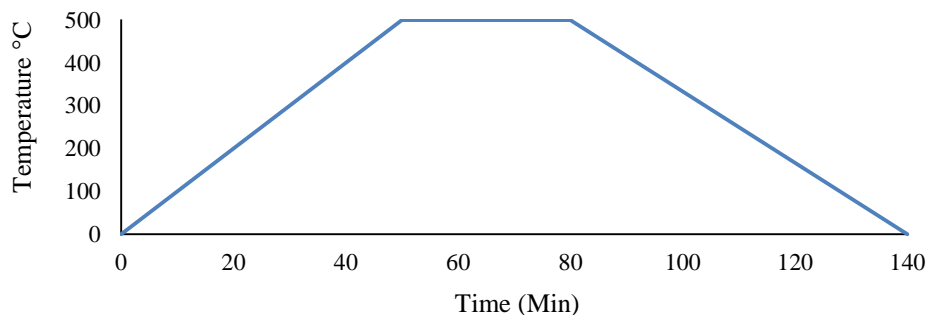
Figure 3.2 Heating profile of the sintering furnace used for TiO_2 photo-electrodes.

The edges of the dyed TiO$_2$ electrode were scraped with a microscope slide to remove outer sections of titanium dioxide, leaving a square 2 cm by 0.5 cm off centre of the glass as shown in Figure 3.3.

Photo electrode (TEC 15 Glass)

Counter electrode (TEC 8 Glass)
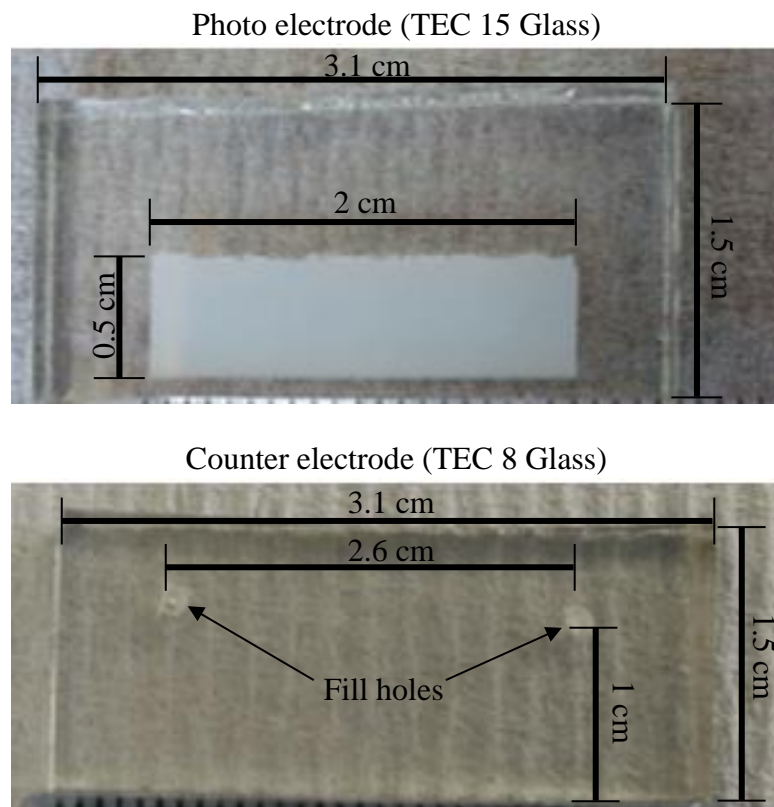
Figure 3.3 (Top) Photoelectrode showing the white section of titanium dioxide 2 x 0.5 cm, excess has been removed leaving an active area of 1 cm^2. (Bottom) counter electrode before platinisation showing fill holes drilled 2.6 cm apart, 0.3 cm from the longest side and 0.4 cm from the shorter sides.

For passive dyeing, sintered TiO$_2$ films were sensitised using a 0.5 mM ethanolic solution of dye, for example a solution of Dyesol di-tetrabutylammoniumcis-bis(isothiocyanato)bis(2,2'-bipyridyl-4,4'-dicarboxylato)ruthenium(II) (N719) and 10 mM chenodeoxycholic acid. These were left to sensitise in a dye bath for 18 hours. The electrode was then removed from the solution, rinsed with ethanol and dried under nitrogen.

Figure 3.3 shows counter electrodes which were constructed from NSG TEC 8 fluoride doped tin oxide conductive glass 8 Ω□ and cut to 3.1 cm by 1.5 cm with a glass cutter. Tec 8 glass is used for the counter electrodes as there is a lower sheet resistance. This lower resistance is achieved by using a thicker layer of fluoride doped tin oxide which

results in a lower transparency. A lower transparency is not a problem for the counter electrode but would not be suitable for the photo electrode due to the decrease in light transmission into the cell. The electrode was cleaned using the same method as stated for the TiO$_2$ electrode. Two holes were then drilled into the counter electrode. They were off centre 0.5 cm from the longest edge of the glass and 2.6 cm apart, as shown in Figure 3.3. A layer of platinum catalyst was added to the glass by depositing 100 µl of platinum paste (Dyesol PT1) using a micropipette. The layer was then spread using a capillary tube to ensure an even layer covered the glass. The electrodes were then heated under atmospheric conditions in a tube furnace at 10°C/min up to 400°C (Figure 3.4) where the temperature was held for 30 min and then left to cool to room temperature overnight in air.
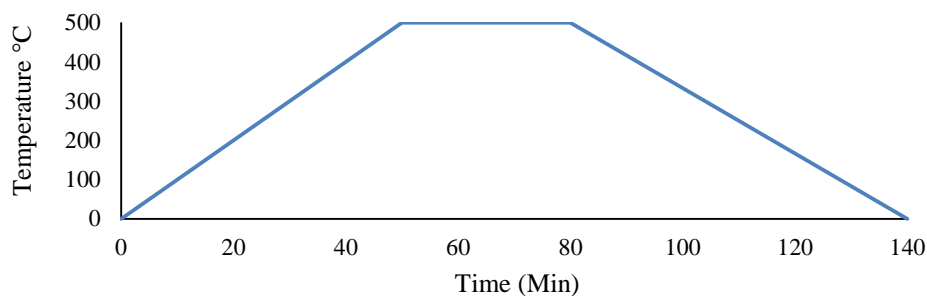

Figure 3.4 Heating profile of the furnace used to sinter counter electrodes after platinum deposition.

The two electrodes were then sealed together with a 25µm Surlyn™ thermoplastic gasket (DuPont) which was heated in a heat press at 120°C for 30 seconds. N719 and D35 electrolytes were prepared in CH$_3$CN containing I$_2$ (0.05 M) and guanadinium thiocyanate (0.05M). For N719, 1-methyl-3-propylimidazolium iodide (0.8 mM) and benzimidazole (0.3 mM) were added. For D35, tBu4NI (0.6M), LiI (0.1M) and 4-tBu pyridine (0.5 M) were added[159]. The cell was then injected with 20 µL of the appropriate electrolyte using a micropipette. Two 4 mm squares of 25 µm Surlyn™ were cut with scissors. Two similarly sized glass squares of were cut from a microscope cover slide. The Surlyn™ squares were then placed over the cell fill holes and the glass was then placed on top. The cell was sealed by pressing the sandwiched electrodes and coverslips together at 120°C for 10 seconds. Finally a silver paste (Agar fast drying suspension) was deposited with a paintbrush onto the edge of the conductive side of each electrode. The silver paste was left to dry on the surface, leaving a line of silver metal, this reduces the resistance and provides a good contact.

3.2 Lifetime Testing of Dyes

3.21 Degradation of Dyes under Natural Light
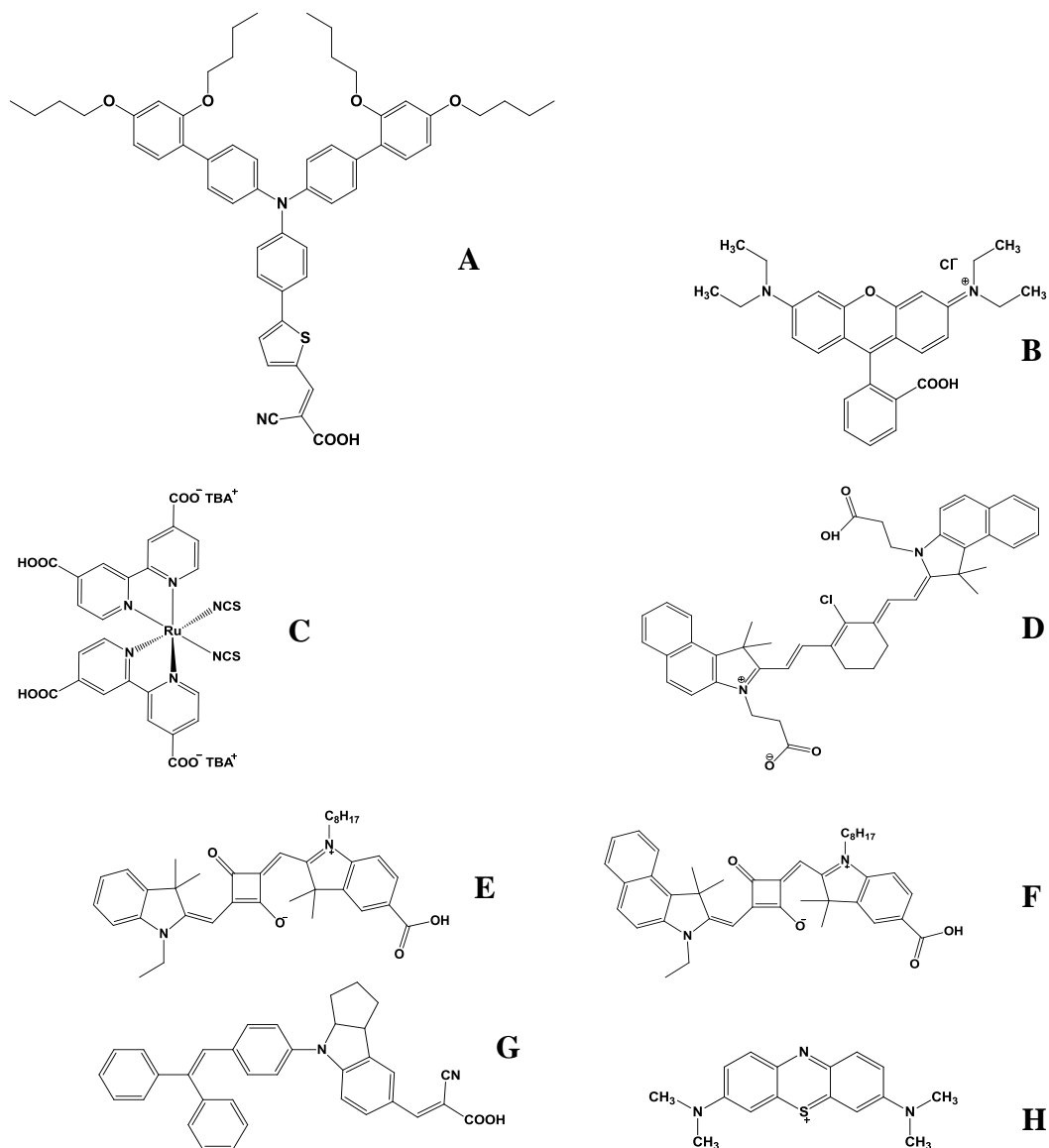
Scheme 1. Structures of (**A**) D35 - (E)-3-(5-(4-(bis(2',4'-dibutoxy-[1,1'-biphenyl]-4-yl)amino)phenyl) thiophen-2-yl)-2-cyanoacrylic acid[160] (**B**) Rhodamine B - [9-(2-carboxyphenyl)-6-diethylamino-3-xanthenylidene]-diethylammonium chloride[161] (**C**) N719 - Cis-bis(isothiocyanato)-bis(2,2'-bipyridyl-4,4'dicarboxylato)-Ru(II)[162] (**D**) Cyanine-3-(2-((E)-2-((E)-3-((Z)-2-(3-(2-carboxyethyl)-1,1-dimethyl-1,3-dihydro-2H-benzo[e]indol-2-ylidene)ethylidene)-2-chlorocyclohex-1-en-1-yl)vinyl)-1,1-dimethyl-1H-benzo[e]indol-3-ium-3-yl)propanoate[163] (**E**) SQ1 - (E)-4-((5-carboxy-3,3-dimethyl-1-octyl-3H-indolium-2-yl)methylene)-2-((E)-(1-ethyl-3,3-dimethylindolin-2-ylidene)methyl)-3-oxocyclobut-1-enolate[164] (**F**) SQ2 - (E)-4-((5-carboxy-3,3-dimethyl-1-octyl-3H-indolium-2-yl)methylene)-2-((E)-(3-ethyl-1,1-dimethyl-1H-benzo[e]indol-2(3H)-ylidene)methyl)-3-oxocyclobut-1-enolate[165] (**G**) D131 - (E)-2-cyano-3-(4-(4-(2,2-diphenylvinyl)phenyl)-1,2,3,3a,4,8b-hexahydrocyclopenta[b]indol-7-yl)acrylic acid[166] (**H**) Methylene blue - 3,7-bis(Dimethylamino)-phenothiazin-5-ium chloride[167].

0.5 mM solutions of the all the dyes shown in scheme 1 (except rhodamine B) were prepared in ethanol. 20ml of each of solution was then added to a clear glass sample vial. The solutions were then left on a south-westerly facing windowsill for two months from 24/1/14 to 24/3/14. Images were taken when the experiment was first begun and then at 28 days and at 48 days using flash photography and a tripod to ensure consistency, this is shown in Figure 3.5.
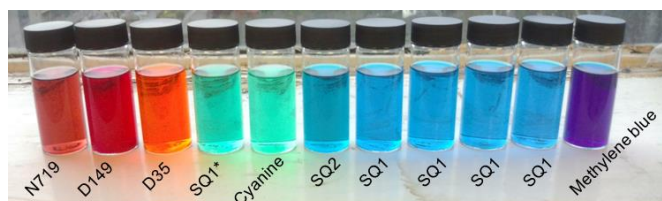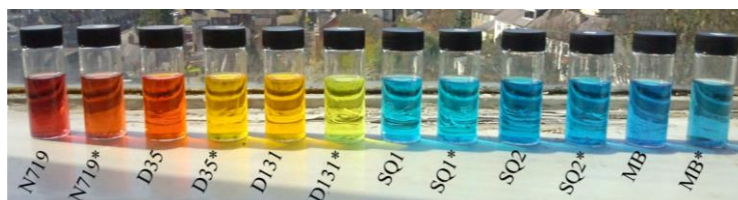

Figure 3.5 Setup for natural light degradation after 1 day, vials of dye were exposed on a south-westerly facing windowsill.

The absorbance of the solutions was measured using UV-Vis both before and after exposure.

3.22 Stabilisation of Dyes under Natural Light

A second degradation experiment was conducted with 0.5 mM solutions of N719, D35, D131, SQ1, SQ2 and MB (methylene blue) in ethanol. Two vials were used for each dye, one with additive and one without. The additive 2,2,6,6-tetramethylpiperidine (TEMP) was added in a concentration of 10 mM to the second bottle of each dye. For each dye, the first vial functioned as a control and no TEMP was added to this. The solutions were exposed to natural light on a south-westerly facing windowsill for 64 days from 09/01/14 to 9/6/14, this is shown in Figure 3.6.


Figure 3.6 Setup for natural light degradation with additives after 1 day of exposure. Dyes marked * have an additive of 10 mM TEMP.

As in the previous experiment, absorbance of the solutions was measured using UV-Vis spectroscopy both before and after exposure and image analysis was conducted. Errors were been calculated from the differences between the RGB values of the windowsill between photos, as these are due to variations in light levels

3.23 Analysis of Degradation under Artificial Light

To test dye solar cell (DSSC) device degradation, experiments were designed to be conducted using a Photosimile 200 lightbox, as shown in Figure 3.7.
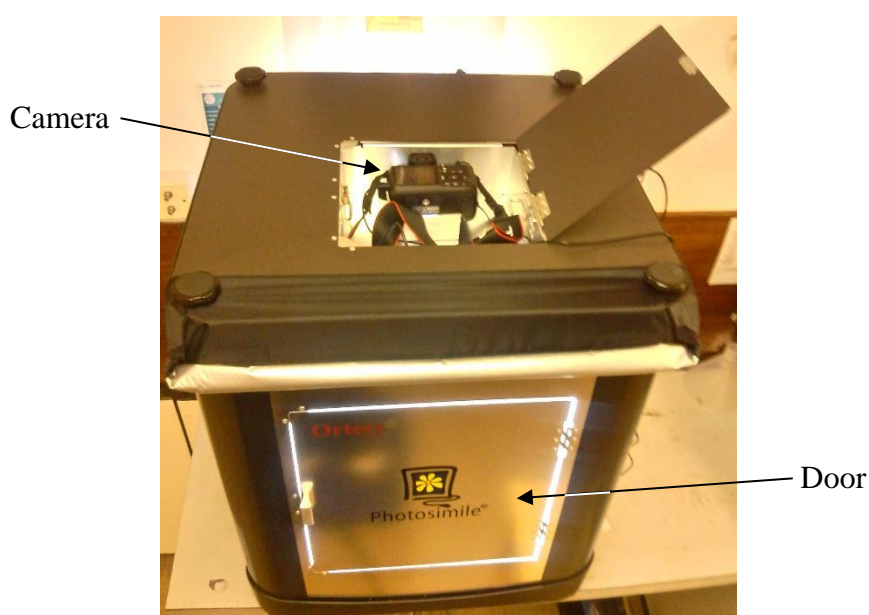

Figure 3.7 Angled view of the Photosimile 200 lightbox fitted with UV filtered halogen bulbs (400 W m^{-2}) with an EOS 1100D digital camera connected. Fans on the back of the lightbox helped to keep the lightbox temperature to a minimum with a temperature of 20°C which was constant after 1 hour.

To develop a method to compare degradation between different dyes, a series of control experiments were run. Initial experiments were conducted using control electrodes of mesoporous TiO_2 which had not been dyed. These control electrodes were constructed by depositing Dyesol® (AO) paste by doctor blading with a single layer of tape onto a 2.5 cm by 2.5 cm glass microscope slide. The film was sintered at 450°C for 30 minutes as described previously in Section 2.1. The control electrode was then placed in the lightbox. For initial experiments electrolyte was not used in the control electrode or the dyed electrodes so the dye stability alone could be measured. In order to record images, a Canon EOS 1100D was used on manual shooting mode

35

with an 18-55 VR Lens. The settings on the camera for white balance was kept constant to prevent flicker. The lens was focused manually and held in place with a lens band to prevent the lens moving, known as lens creep. The shutter speed was set to 0.3 seconds and the aperture was set to f16 to ensure consistent images. The camera was connected by USB cable to a computer and images were taken remotely every 5 seconds. The images were then analysed using a macro run on Sigma Scan which measured the colour of each electrode in the experiment in RGB format. The value of each electrode was then plotted against time.

3.24 Degradation of SQ1, SQ2 and N719 under Artificial Light

Following initial experiments in Section 2.23, an experiment was designed to measure the degradation rates of SQ1 (Solaronix), SQ2 (Solaronix) and N719 (Dyesol) sorbed onto mesoporous TiO_2 electrodes in a more controlled way using image analysis which was then compared with UV-Vis spectroscopy data. The setup is shown in Figure 3.8
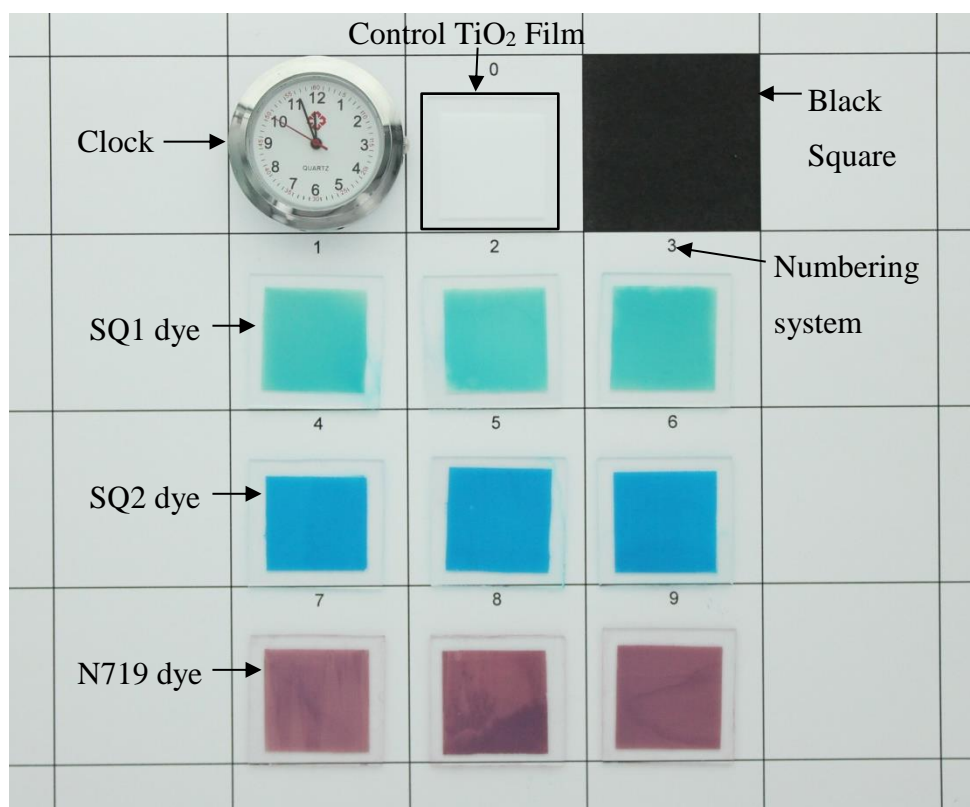
Figure 3.8 The final grid layout for the time-lapse images. The electrode at 0 is a control which has not been dyed, 1 to 3 are SQ1, 4 to 6 are SQ2 and 7 to 9 are N719. This image was taken at the start of exposure. Scale: squares are 4 cm x 4 cm

The electrodes were prepared by cutting a 2.5 cm by 7.5 cm microscope slide into three with a glass cutter to make a set of 2.5 cm by 2.5 cm squares. The glass was cleaned with acetone then sonicated for 15 minutes and dried under nitrogen. Active opaque paste (Dyesol) was then deposited by doctor blading, using a single layer of tape, to leave film of TiO_2 paste. They were then sintered at 450°C for 30 minutes in a furnace to remove solvent and organic polymer binder. After sintering, the electrodes were placed in dye baths of SQ1, SQ2 or N719 dyes all of which were at a concentration of 0.5 mM in ethanol. The electrodes were left to dye passively for 18 h then washed with ethanol and dried under nitrogen. The electrodes were then placed in the lightbox and light soaked under unfiltered halogen lights for 3 hours. Once exposure was complete, images were processed individually using macro analysis, as described in section 2.4.

3.25 Degradation of SQ1 at Low Light Levels

In the next experiment, mesoporous TiO_2 films 3 cm by 1.5 cm which had been sintered at 450°C for 30 min onto a cleaned TEC 15 glass substrate were dyed in 0.5 mM SQ1 for 18h. The electrode was then placed in a sealed container in air through which negligible light could enter. After 48 hours the electrode was removed and analysed by UV-Vis spectroscopy.

Following this a parallel experiment to monitor the dye degradation by UV-Vis spectroscopy was conducted. Electrodes were prepared as described in the previous paragraph. The electrode was then placed in a Lambda 35 UV-Vis Spectrometer. The spectrometer door was sealed so the only light exposure was from the machine itself. The scan range was set to 400 nm to 700 nm, with a slit width of 1 nm and a scan speed of 480 nm/min. The number of scans on the spectrometer was set to 60 and the interval between scans was set to 1 hour. This meant the spectrometer would run at hourly intervals for 60 hours, allowing the degradation to be monitored.

3.3 Image Analysis

To analyse images, a macro was used which contained the coordinates of the area being analysed. To find pixel coordinates for the macro, the first image was opened in Microsoft Paint.

The centre of the electrode was then marked and the cursor was moved 120 pixels up and 120 pixels left. The area to analyse was then drawn from this point and a box of 240 x 240 pixels was drawn around this area. The cursor was moved to each corner of the box and the coordinates displayed were noted down, as shown in Figure 3.9.
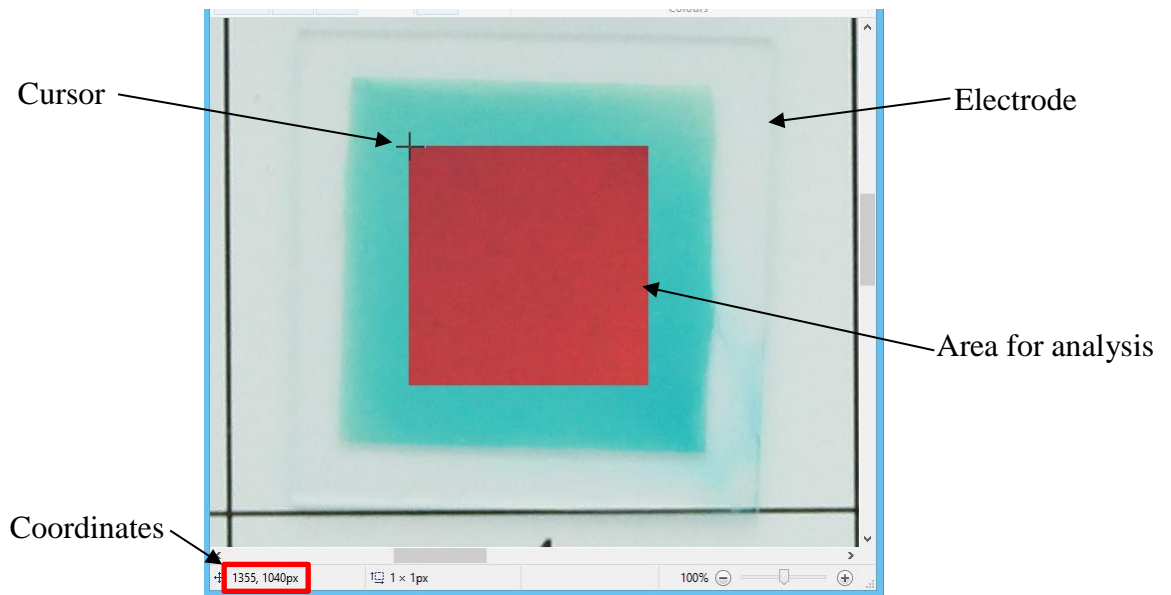
Figure 3.9 Paint image of dyed electrode with the area for analysis selected, coordinates for the top left corner are shown in the bottom right of the program.

After this the coordinates were checked visually for alignment by drawing them as a graph over the image, as shown in Figure 3.10.
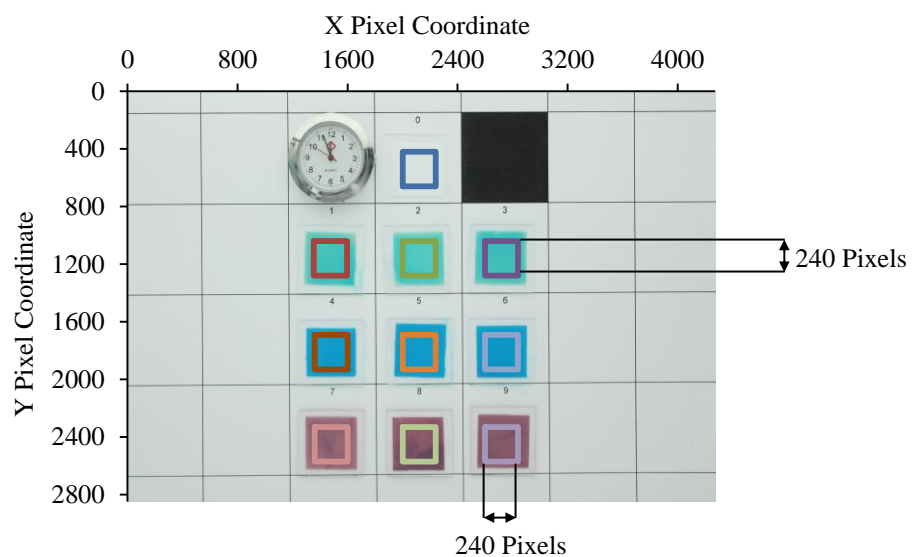

Figure 3.10 Pixel coordinates plotted over an image of the electrodes showing the area to be analysed.

38

The coordinates were then written into a macro for the degradation test. The macro was then opened in Sigma Scan 5 which analysed the images by selecting the each of the electrode as specified in the macro. Each of the areas were measured for colour intensity or red, green and blue (RGB) giving a value out of 255 for each colour.

3.4 Ultrafast Dyeing

3.41 Method Development

In the initial setup, a syringe was used to pump dye through the DSSC devices, as shown in Figure 3.11. First the cell was placed in a cell holder and needles were inserted into the cell. Bolts on the cell holder were then tightened to form a seal. The cell holder was then placed on a hotplate at 40°C and a 3 ml syringe was filled with dye. The syringe was then inserted into the cell and the dye was injected through the cell at a rate of approximately 3 ml/min or 0.05 ml/s.
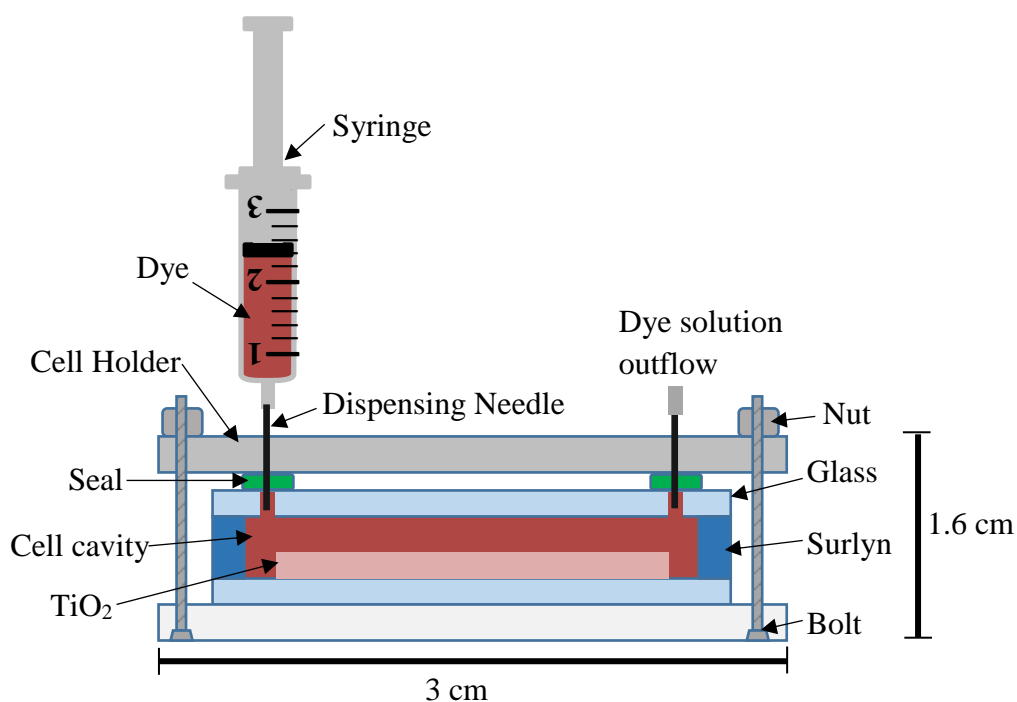
Figure 3.11 The setup for ultra-fast dyeing using a syringe. The dye is pumped from the syringe into the cell which is held sealed by the pressure from the nuts and bolts at each end of the device holder.

To control this process more accurately a pump was used as an alternative to the syringe, as shown in Figure 3.12. A peristaltic pump was chosen as this works by applying pressure to the outside of the tubing therefore preventing direct contact between the pump and the dye. This minimises the risk of contamination of the dye.
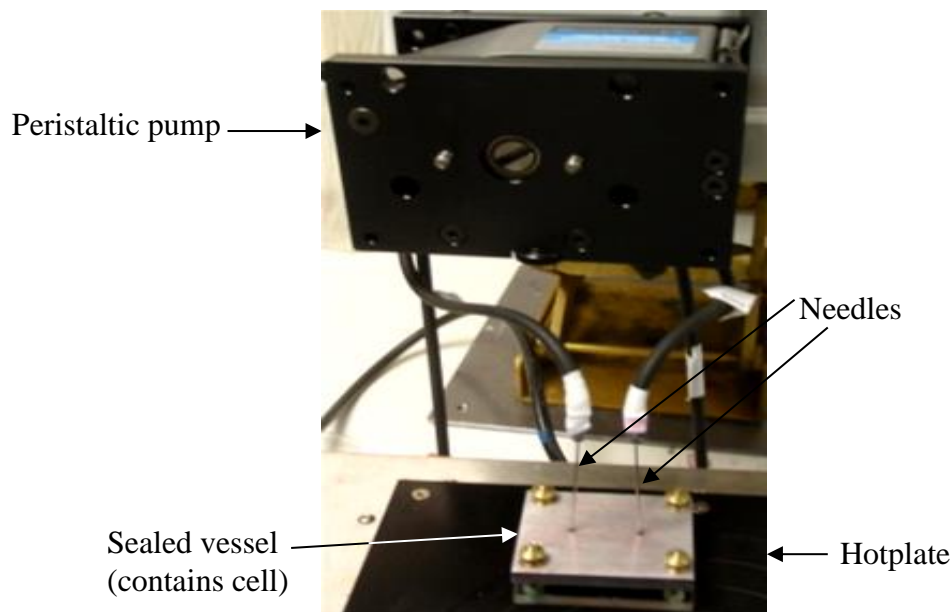
Figure 3.12 The initial setup for pump dyeing. The needles have been inserted into the cell which is inside the cell holder. The pump then pushes the dye through the cell sorbing onto the TiO_2.

The pump was preloaded with dye solution, then switched off and the two needles were inserted into the cell fill holes which were held in place with a cell holder. The cell holder (shown previously) was tightened to form a seal between the dispensing needles and the fill holes. The devices were placed on a hot plate at 40°C and dye was pumped through the cells for 5 minutes at the pump flow rate was set to 0.15 ml s^{-1}. 0.5 mM dye solutions of N719, SQ1 and SQ2 with 5 mM CDCA in ethanol were used. To determine the end point cells were run through with dye for 20 minutes and the images were analysed to determine how long it took for complete dye uptake. Cells were then filled with electrolyte and sealed.

Next a comparison was made between the dyeing rates of cells with different volumes. To do this, dye cells longer than 2.1 cm needed to be constructed so the cell holder was redesigned to accommodate. The cell holder was cut into two parts which could attach separately to each fill hole. Holes were then drilled into each part of the cell holder and screws were added. Significantly longer cells could be dyed using this setup, shown in Figure 3.13.
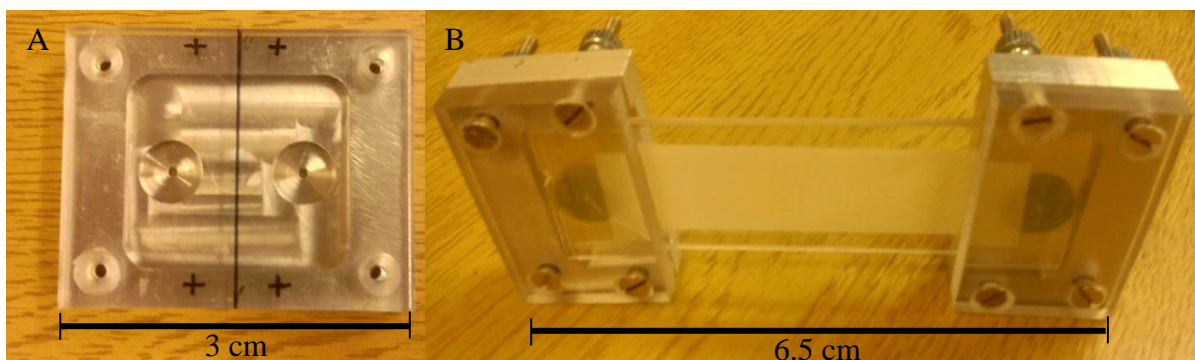
Figure 3.13 Left, original cell holder marked for the modifications. Right, new design of cell holder showing the two separate parts attached to a cell.

3.42 Dye Uptake Analysis

Longer devices 15 cm in length with 14 cm x 1 cm active area were constructed using the same glass making process but with larger dimensions. 15 cm by 2 cm TEC 15 glass was used for the electrodes. The cell was designed with an active area of 14 cm (1 cm by 14 cm TiO_2), shown in Figure 3.14.
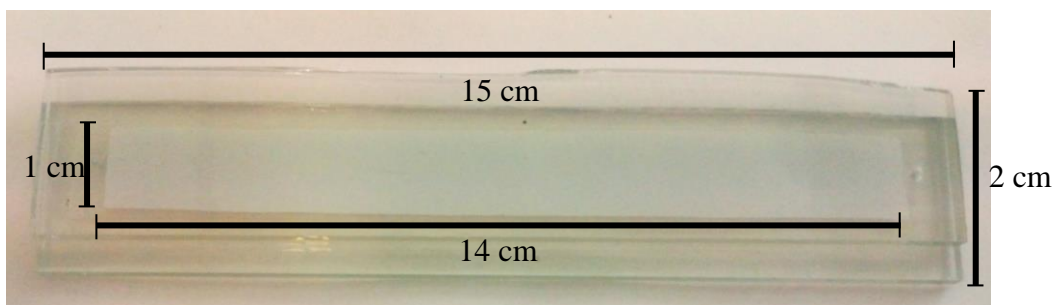

Figure 3.14 A large cell with a 14 cm^2 active area prior to pump dyeing.

The cell was then pump dyed and the dye uptake was recorded for image analysis with a Cannon EOS 1100D Camera.

Recordings were made at 25 frames per second (FPS) on the camera with a tripod for stabilisation (Figure 3.15) and overhead lighting was used to ensure consistency. The camera was manually focused to ensure a consistent focus throughout the recording. The frames from these recordings were extracted, enabling 25 images to be generated from each second of video. Each of these images were then run on a macro which analysed the RGB values. The macro analysed four separate areas of the cell, two at

41

the intake and two at the outtake as shown in Figure 3.16. These were the dye entry side, the dye exit side and a control on the glass below each of them.
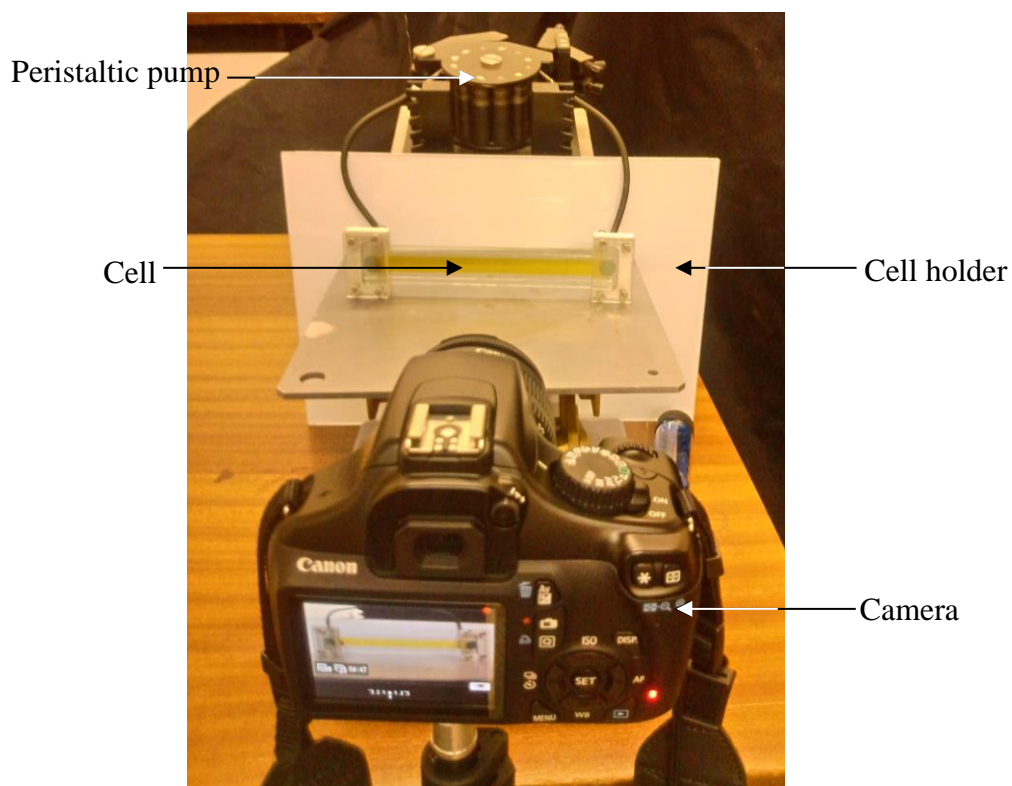
Figure 3.15 Setup for uptake analysis. Showing the pump connected to the cell by the cell holder with the camera recording the process.
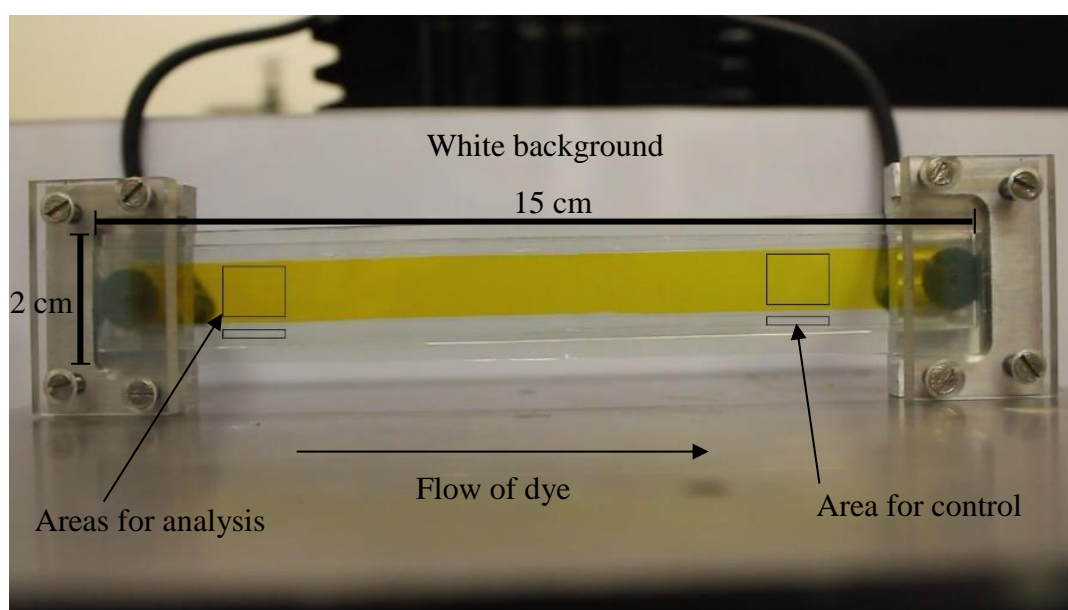

Figure 3.16 An image of extracted from a recording of the fast dye process for D131 dye. The areas inside the black boxes are analysed by the macro for RGB values. The areas for analysis are used to measure the dye uptake and the areas for control are used to monitor any changes in light levels.

## 3.5 Dye Sensitised Solar Cell Device Lifetime Testing

3.51 N719 and D35 Devices

A set of 36 DSSC devices were constructed under the same conditions as described previously. The cells were split into two sets, 18 were passively dyed with N719 and 18 were passively dyed with D35. Dye solutions were both 0.5 mM in ethanol. Each set of cells were then setup under different exposure conditions. The first row of cells were connected to a wire with crocodile clips which connected the counter and photoelectrodes together, shorting out the cell. The second row of cells did not have anything connected, meaning they were at open circuit. The third row had wires with a 10 Ω resistor in between them, simulating a load. The first five columns were covered by a UV-filter and the last two columns were left unfiltered as a control (Figure 3.17).
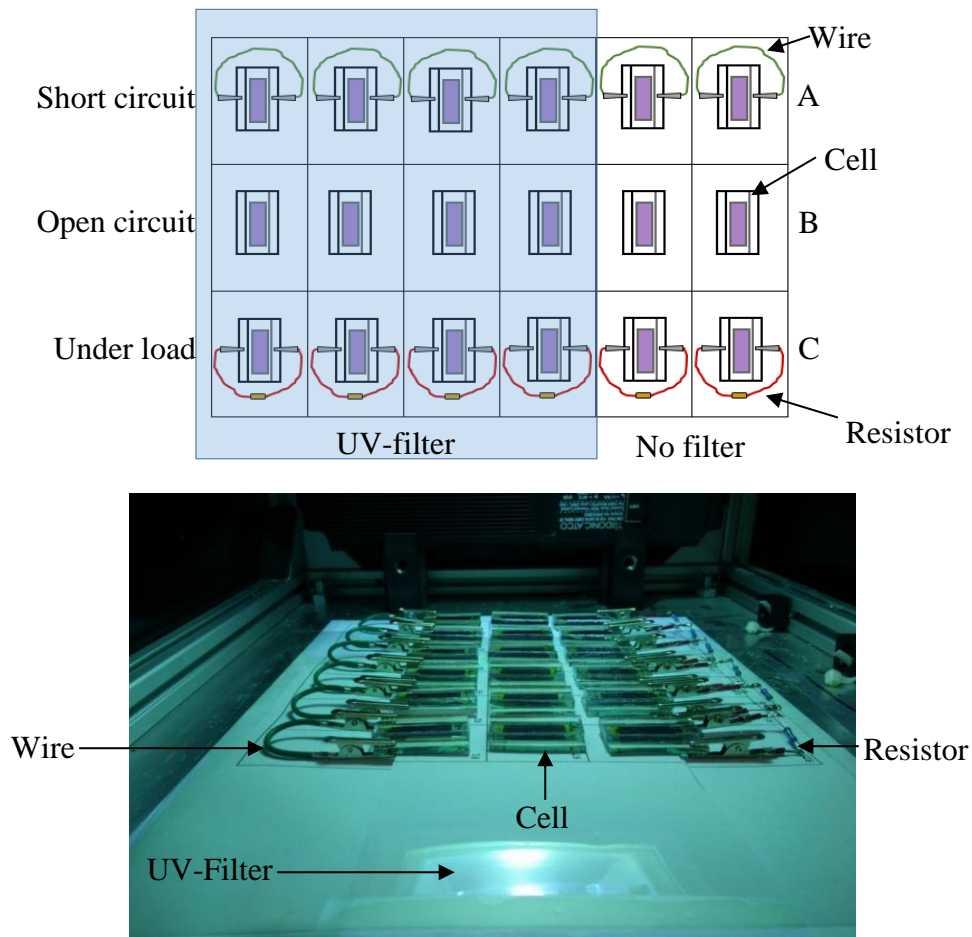

Figure 3.17 (Top) schematic of the DSSC device testing experiment (plan view) showing rows of replicate devices either with or without a UV filter. The top row is at short circuit with a wire between the 2 electrodes, the middle row is at open circuit with no connection between the 2 electrodes and the bottom row is under load with a resistor between the 2 electrodes. Bottom image shows the devices light soaking in the Dyesol UPTS.

The components connected to the DSSC devices are shown in Figure 3.18.
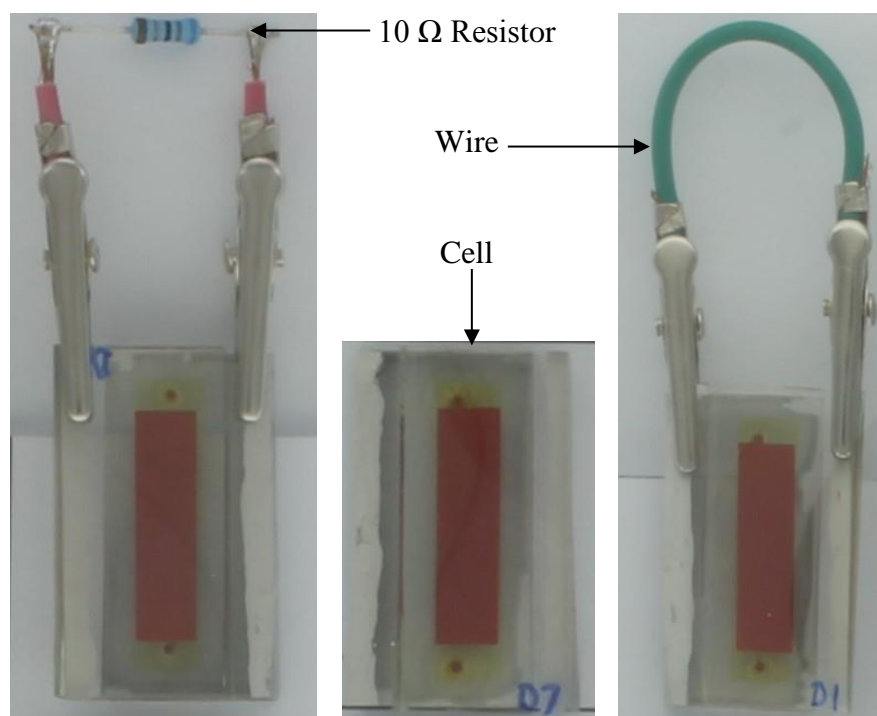
Figure 3.18 Close up of the cells used in the light soaking experiment prior to exposure. (Left) cell with a 10Ω resistor attached which functioned as a load. (Centre) cell with nothing attached, meaning the cell was at open circuit. (Right) cell with wire attached from one electrode to the other, short circuiting the cell.

The circuit conditions can be plotted on an IV curve, as shown in Figure 3.19.
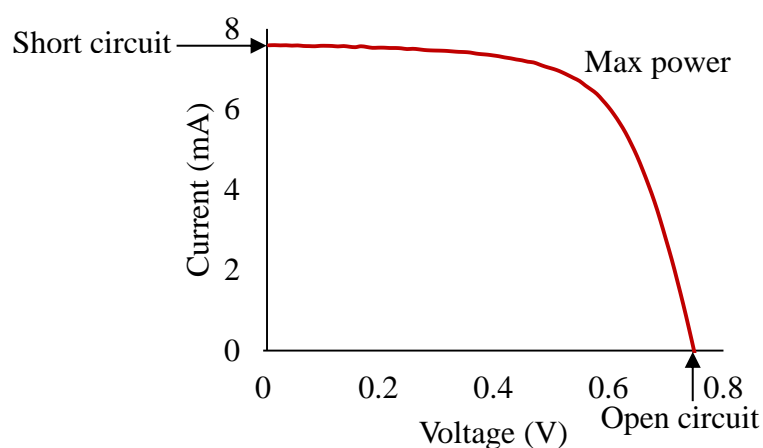
Figure 3.19 The differing circuit conditions used to compare the rates of degradation can be represented on an IV curve. When the voltage is 0 the cell is at short circuit, when the current is 0 the cell is at open circuit. Max power is the highest combined current and voltage and can be achieved by applying a load to the cell.

Prior to light soaking the devices were tested by solar simulation. The IV data for N719 is shown in Table 3.1.

Table 3.1 IV data for cells made with N719 dye prior to light soaking.

Device	FF	η/%	V_{oc}	I_{sc}/cm^2
Initial Measurements				
Short Circuit – UV filtered				
R1	0.50	4.4	0.78	11.28
R2	0.52	4.8	0.77	11.92
R3	0.54	4.5	0.78	10.62
R4	0.44	3.6	0.78	10.40
Short Circuit – non UV filtered				
R5	0.51	4.4	0.78	11.24
R6	0.55	4.5	0.77	10.71
Open Circuit – UV filtered				
R7	0.48	4.1	0.77	11.13
R8	0.52	4.7	0.78	11.60
R9	0.54	4.9	0.77	11.82
R10	0.58	5.2	0.79	11.44
Open Circuit – non UV filtered				
R11	0.58	5.1	0.79	11.23
R12	0.57	5.1	0.79	11.47
Under load – UV filtered				
R13	0.55	5.4	0.78	12.45
R14	0.60	4.8	0.75	10.75
R15	0.54	4.9	0.78	11.75
R16	0.56	5.2	0.78	12.04
Under load – non UV filtered				
R17	0.57	5.4	0.78	12.14
R18	0.60	5.4	0.78	11.51

Both sets of cells were light soaked inside a Dyesol Universal Photovoltaic Testing System (UPTS) under a 150 W halogen lamp at 0.4 sun. The cells were removed periodically and analysed by imaging and IV measurements. The imaging was taken by placing the cells in a lightbox and taking a digital photograph which was then analysed by a macro (Section 2.4). The IV curves were measured using a solar simulator. These measurements were taken on a regular basis until a cumulative exposure time of 2500 hours was reached for N719 and 660 hours for D35 when cells began to show significant signs of degradation.

The initial cell data for D35 devices is shown in Table 3.2.

Table 3.2. IV data for D35 devices prior to light soaking.

Device	FF	η/%	V_{oc}	I_{sc}/cm^2
D35 Devices - Initial Measurements				
Short Circuit – UV filtered				
D1	0.58	5.7	0.81	12.06
D2	0.64	5.5	0.79	10.90
D3	0.57	5.4	0.81	11.68
D4	0.58	5.2	0.79	11.50
Short Circuit – non UV filtered				
D5	0.54	4.5	0.81	10.38
D6	0.51	4.0	0.79	10.06
Open Circuit – UV filtered				
D7	0.58	5.7	0.81	12.11
D8	0.59	5.4	0.80	11.60
D9	0.58	5.4	0.81	11.32
D10	0.61	5.1	0.78	10.60
Open Circuit – non UV filtered				
D11	0.53	4.5	0.81	10.70
D12	0.43	3.8	0.82	10.80
Under load – UV filtered				
D13	0.61	5.7	0.81	11.47
D14	0.62	5.4	0.79	11.02
D15	0.59	5.3	0.81	11.10
D16	0.51	4.7	0.81	11.45
Under load – non UV filtered				
D17	0.50	4.2	0.79	10.73
D18	0.32	2.9	0.79	11.39

Chapter 4 Lifetime Testing of Dyes

4.1 Preliminary Analysis of Dye Stability in Solution

The purpose of this experiment was to determine if the degradation of dyes in solution could be monitored by imaging techniques. Thus, this initial experiment was conducted to compare rates of colour change between different dyes in solution when exposed to sunlight. The dyes solutions were exposed for 2 months from 24/1/14 to 24/3/14 on a south-westerly facing window to ensure there was adequate exposure to sunlight. Any colour change could indicate photobleaching of the dye. Initial dye solutions and their RGB values are shown in Figure 4.1.
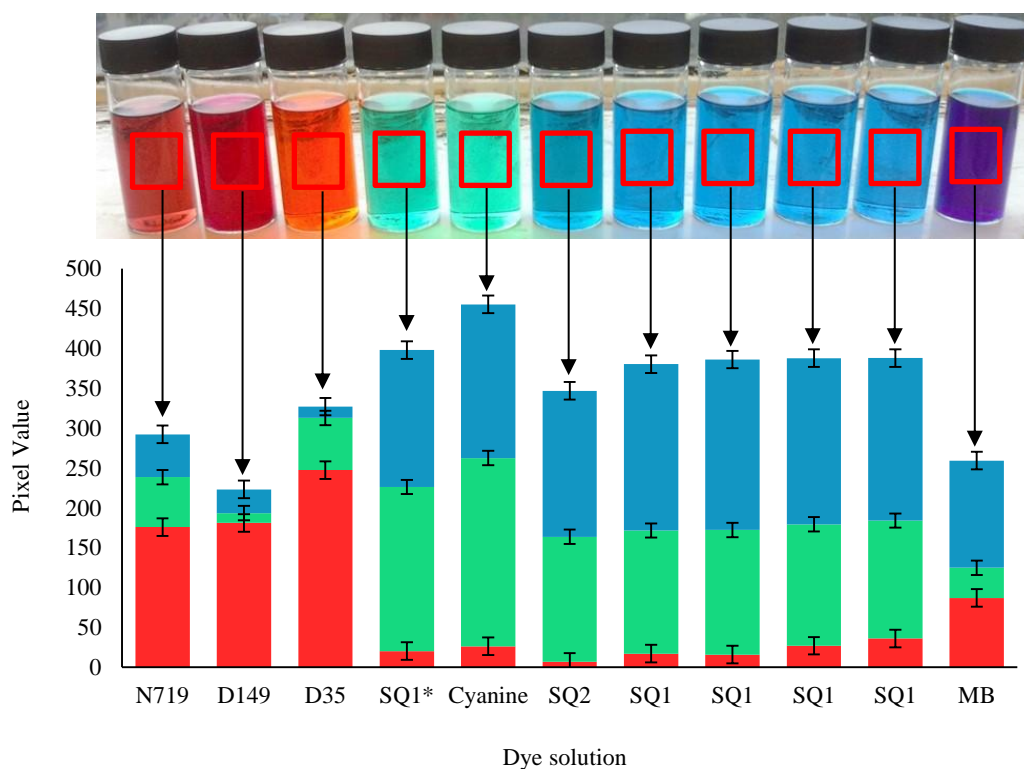
Figure 4.1 (Top) Dye solutions in ethanol at the start of the experiment (0 h exposure) (Bottom) Corresponding RGB values for each dye solution, the mix of red, blue and green are equivalent to the colour of the solution.

The image in Figure 4.1 was analysed by a macro which determined the RGB colours of each of the dye solutions to monitor for degradation. This preliminary experiment was designed to test the rate of degradation at high (0.5 mM) and low (0.05 mM) concentration for a selection of dyes. This was to determine if the photobleaching of the dyes would occur. From this the dyes could be selected for further degradation

analysis. It was important that the data was quantified in addition to the visual observations made. To do this an analysis of the digital images was conducted where the red green and blue (RGB) values were measured for each dye. If the RGB values changed then this could indicate degradation of the dye as this may be due to bleaching of the dye. Images of the dyes during exposure are shown in Figure 4.2.
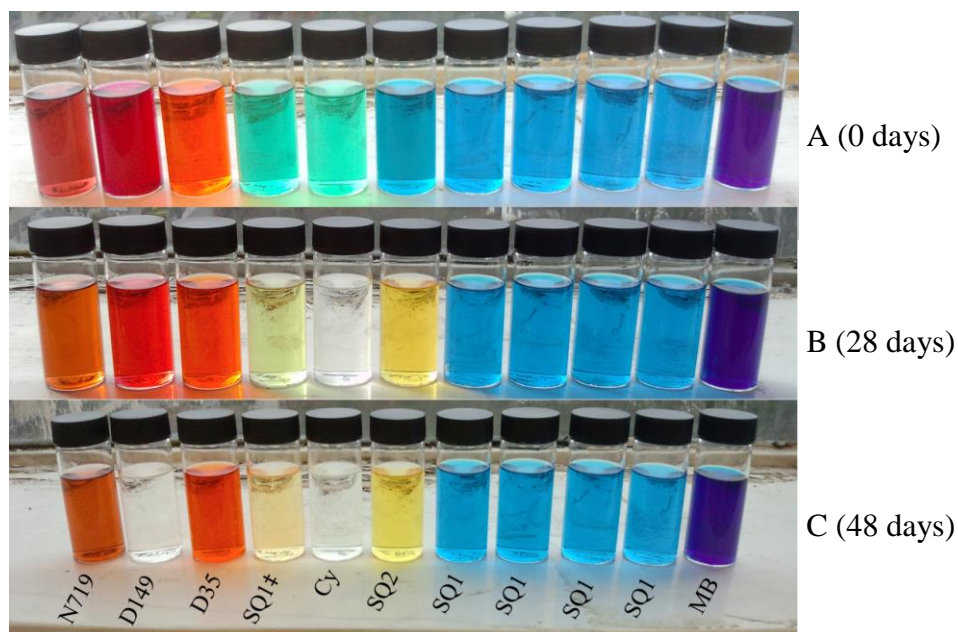
Figure 4.2 Ethanol dye solutions in glass sample vials. Note N719, D149, SQ1‡, Cy and SQ2 were all at a concentration of 0.05 mM the remainder of the dyes had a concentration of 0.5 mM. Note that the solution SQ1‡ was pre-exposed 2 weeks prior to the start of this experiment. The dyes marked Cy and MB represent cyanine and methylene blue dyes. Images show an exposure time of (Image A) 0 days, (Image B) 28 days, (Image C) 48 days.

Figure 4.2 shows the dyes at the lower concentration do degrade significantly over this timeframe, as indicated by the colour change. After 28 days SQ1‡, cyanine and SQ2 all show a very noticeable colour change indicating substantial degradation. After 48 days N719 showed a very slight colour change. The D149 had turned completely transparent indicating the dye had fully bleached (see structures in Section 2.31).

The irradiance of the light exposure during this time can be calculated. Solutions were exposed to a total of 185.5 sunlight hours according to Met Office records[168]. One sunlight hour corresponds to an irradiance of 120 W/m^2. Using this, the total exposure in sunlight hours can then be converted to irradiance. To do this the number of sunlight hours is multiplied by the irradiance of one sunlight hour.
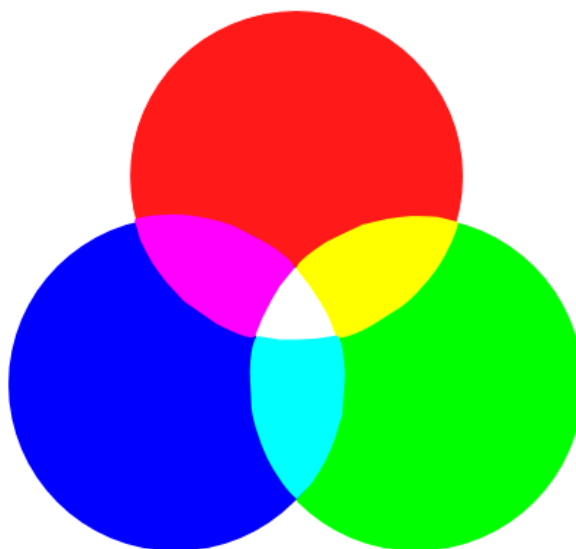
$$E_e = 185.5\text{h} \times 120 \text{ W/m}^2$$
$$E_e = 22260 \text{ Wh/m}^2$$

Dye solutions were thus exposed to a total of 22,260 Wh/m^2 during the experiment.

To interpret RGB data, it is important to understand how light combines to form colours. The combination of all three primary colours of light will form white[169]. Different combinations of lights are best represented in a Venn diagram as shown in Figure 4.3.

Figure 4.3 Venn diagram of primary colours of light, showing the combinations of all three colours make white light. Red and green make yellow, red and blue make magenta, green and blue make cyan. Figure redrawn from the literature.[170]

The combinations of red, green and blue form different colours when combined. These represent the colour of each solution and equal values of red green and blue would correspond to white. The way colour is perceived is based on which of the primary colours of light are absorbed or scattered, this is shown in Figure 4.4.
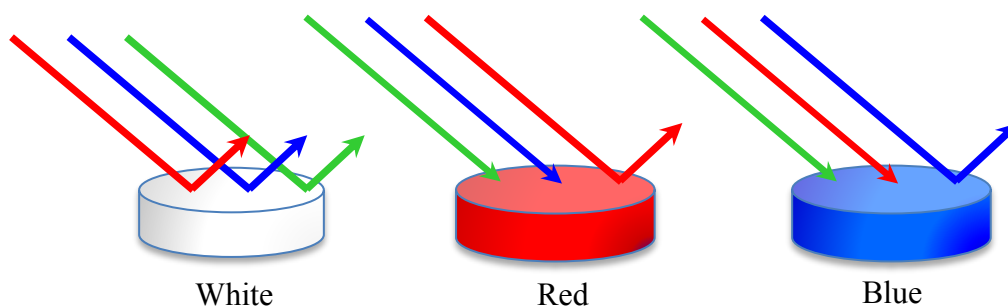
Figure 4.4 The colours of objects is determined by the light absorbed and scattered from them. A white solution will scatter all the primary colours, a red one will absorb green and blue light and scatter red light, a blue solution will absorb green and red light and scatter blue light.

Imaging analysis techniques have been used previously by Watson *et al* to monitor the colour of TiO_2 during passive sensitisation[116]. As in the previous study the images were analysed using a macro, however the macro in this experiment analysed the RGB values of the dye solutions.

The differences in the RGB values of the solutions could be compared to precisely judge any dye colour change. The area analysed was that in the centre of the dye solution to ensure consistency between samples (see Figure 4.1 at the start of this chapter). This was done to ensure that there were no distortions from the curved surface at the edge of the sample bottle.

Errors were calculated by analysing the colour of the windowsill between images. The colour of the windowsill should remain constant throughout the experiment and any variation in this colour would indicate changes in natural light intensity during the day.

The differences in colour of the windowsill between images was calculated to give the range. This range of RGB errors was 11 for red, 9 for green and 11 for blue. These values have been plotted as error bars in Figure 4.5.
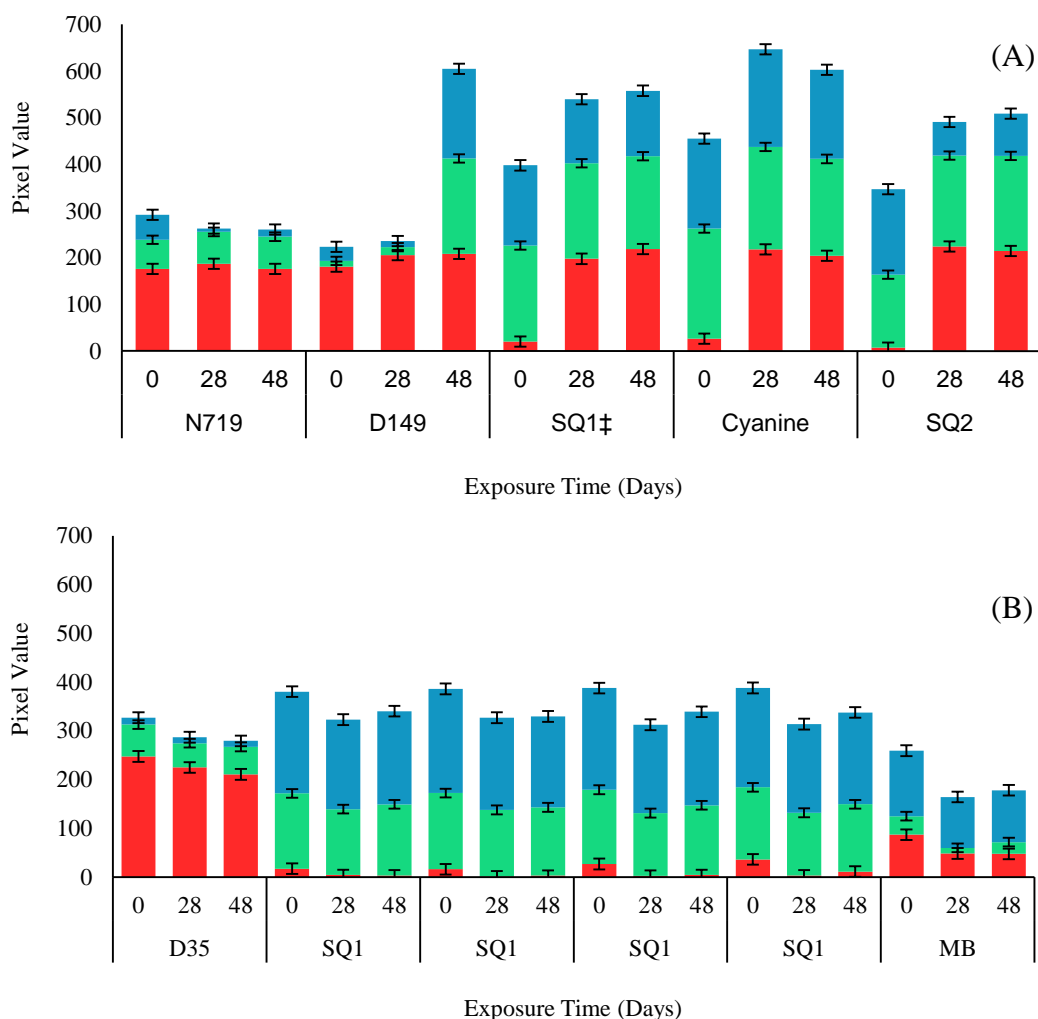
Figure 4.5 Red, green, blue (RGB) pixel values of dye for (A) solutions at low concentration (0.05 mM), (B) solutions at high concentration (0.5 mM). Note dye degradation is indicated by all three colours becoming equal; the absence of colour means the solution has turned transparent. This can be observed in D149 after 48 days, SQ1‡ and cyanine after 28 days. Note that SQ1‡ has received 2 weeks exposure prior to this experiment.

Figure 4.5 shows the effect of 0, 28 and 48 day light exposures on the RGB values of dye solutions. Part A shows solutions at low dye concentration (0.05 mM) and Part B shows high concentration (0.5 mM). N719 dye shows a small change in RGB values after 28 days, this indicates very little degradation has occurred. This is unsurprising as N719 is well known for its high stability[138]. D149 shows very little change in RGB values after 28 days and a substantial difference after 48 days. This indicates that the dye has remained stable for the first 28 days but broken down significantly by 48 days. SQ1* showed a change in RGB values after 28 days and then a further change after 48 days. This shows the dye has degraded after 28 days and further degrades after 48

51

days. The cyanine dye shows an increase in the red RGB value after 28 days and a decrease of all values after 48 days. This is indicative of significant degradation after 28 days and further degradation after 48 days as the colour fades. SQ2 showed a notable increase in the red RGB value after 28 days and comparable RGB values after 48 days. This implied that SQ2 had fully degraded after 28 days. D35 showed a very small decrease in the red RGB value after 28 days and a further slight decrease after 48 days. This indicated a slight degradation had occurred but that it was a very gradual process. Methylene blue showed a slight drop in RGB values after 28 days and then remained similar after 48 days. This suggests methylene blue is starting to degrade after 28 days but that it is a more gradual degradation.

To test the reproducibility of the data, four solutions of SQ1 were tested at concentration of 0.5 mM (see Figure 4.2). The four SQ1 solutions showed a small drop in all RGB values after 28 days which indicates the colour of the solution has faded very slightly suggesting minor degradation. The initial readings between the four solutions are very similar and any differences are within the error bars. There is some variation between the 28 day RGB values and the 48 day RGB values but these are also within the error bars, suggesting they are due to light level changes. This shows there is good repeatability between solutions as the RGB values should be the same for all of the SQ1 solutions when error is taken into account. This suggest that exposing the solutions on the windowsill and the image analysis is a valid method for degradation monitoring. If there were significant differences in the level of light exposure the same dye would have degraded at different rates. From this initial experiment, it is clear that dye solutions at a concentration of 0.5 mM are too high for short term degradation testing. Instead concentrations of 0.05 mM should be used to allow degradation of the dye to be more apparent. The dyes should also be spaced out further to reduce the issue of shadows being cast from one dye solution onto another. Once all this is considered, a key issue remains which is dye lifetime. The next step would be to study extending the lifetime of the dyes.

The mechanism of SQ1 degradation has been investigated previously and suggested that it degrades as a result of free radicals.[171] Thus, in order to reduce the rate of dye degradation an additive could be used which scavenges radicals. If these free radical could be captured then degradation could be reduced. To do this a hindered amine light

stabiliser (HALS) could be used. As HALS are not consumed in the process of collecting radicals are able to regenerate[172] meaning they could be used for long term stabilisation in a device[173].

4.11 Studies of Tetramethylpiperidine in Dye Solution

A second degradation experiment was conducted to analyse the effect of 2,2,6,6-tetramethylpiperidine (TEMP) on the rate of dye degradation. TEMP has been used previously to successfully inhibit photo-oxidation in polymers such as polypropylene[174]. TEMP works by scavenging oxygen radicals as shown in Figure 4.6.
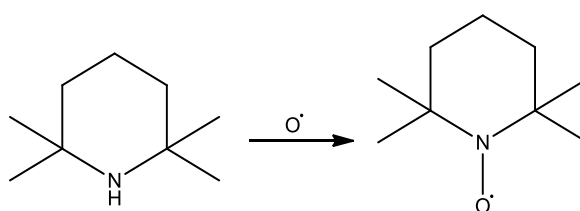
Figure 4.6 Oxygen radical scavenging of 2,2,6,6-Tetramethylpiperidine (TEMP) to form the non-reactive 2,2,6,6-Tetramethyl-1-piperidinyloxy (TEMPO). Redrawn from literature[175].

This set of dyes were exposed at the same location between 09/01/14 to 9/6/14. As stated previously in section 2.22, any colour change in the dye was considered an indication of degradation. The images taken are shown in Figure 4.7.

Figure 4.7 Dye solutions of 0.5 mM exposed to sunlight for (Image A) 0 days, (Image B) 21 days, (Image C) 64 days. Dyes marked with an * have an additive of 10 mM TEMP.

53

Figure 4.7 shows there was a significant difference in the rate of degradation of dyes with TEMP added than those without. Visual inspection shows that after 21 days exposure there was substantial fading of D131 and a lesser change in D131*, thus suggesting that the TEMP has been effective in reducing degradation of D131. Figure 4.7 also shows that SQ1 has also faded after 21 days and the additive has also slowed the degradation in SQ1*. The same effect could be observed for SQ2 as without the additive the dye faded significantly faster. Interestingly the opposite effect was shown in methylene blue. The addition of TEMP appeared to accelerate the fading of the dye.

After 64 days many of the dyes had degraded further. N719 appeared to be the same colour which was to be expected as N719 is widely known for being a stable dye[176]. The addition of the TEMP appears to have blue shifted the colour of N719 from red to orange. This may have been due to interaction between the Temp and solvent. D35 dye appears to have bleached fully after 64 days as the colour has faded to a transparent solution, suggesting the cromophore of the dye has broken down.

The centre of each dye vial was analysed and the windowsill in the background of the image was also analysed to quantify error between measurements as shown in Figure 4.8. Using this method the errors were determined as 13 pixels for red and 11 for both green and blue. These have been plotted as error bars in Figure 4.10.
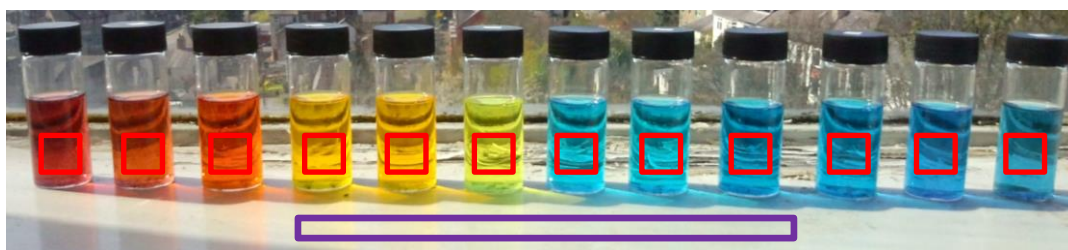
Figure 4.8 Dye solutions prior to exposure showing the areas analysed for each solution (red squares) and the control area (purple rectangle).

The addition of the TEMP instantly changed the colour of D35 suggesting a shift in absorbance of the dye. D35* was also highly stable showing no degradation after 64 days exposure. This observation was analysed by UV-Vis analysis shown in Figure 4.9. After 64 days D131, SQ1 and SQ2 all showed the same trend as they had at 21

days, the dye was fully degraded unless TEMP was added. Both methylene blue with and without TEMP had completely degraded by the end of this experiment.
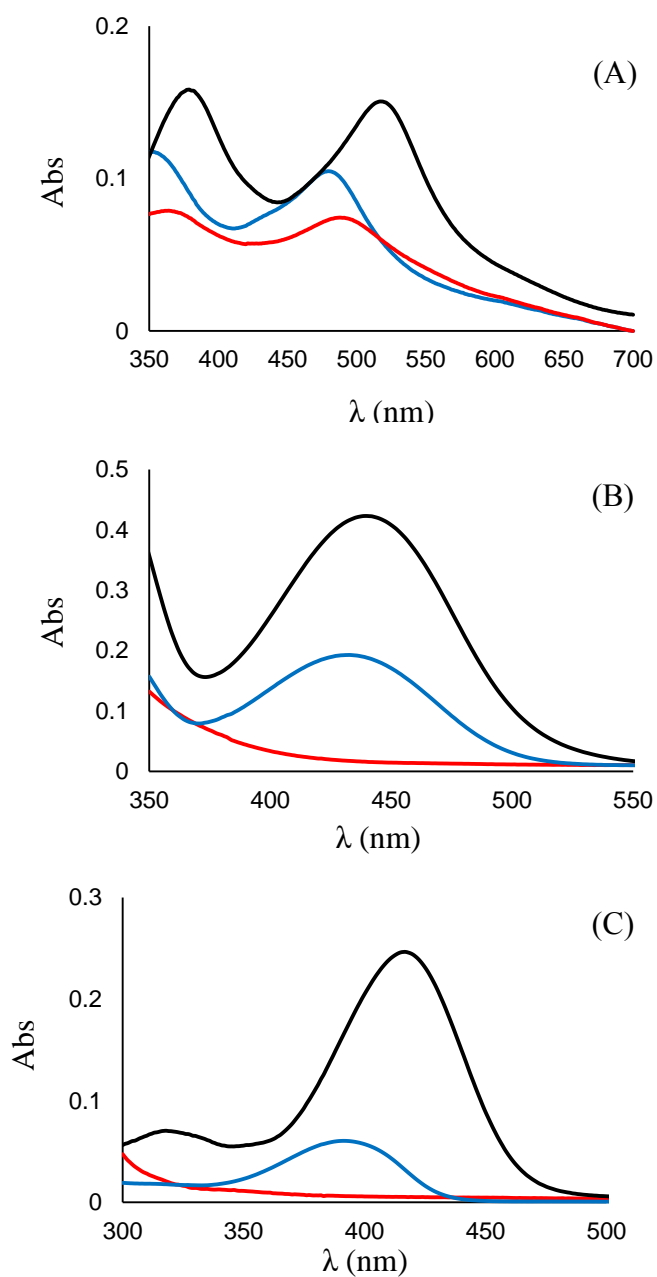
Figure 4.9 UV-Vis data of 0.05 mM ethanolic dye solutions of (A) N719, (B) D35 and (C) D131. Stock solutions of dye are shown in black, stock solutions after the addition of TEMP (blue) and after 2 months light exposure (red). Undiluted solutions were measured in a 1 mm cuvette.

Figure 4.9 shows the UV-Vis spectra of dye solutions before exposure, after the addition of TEMP and after exposure. This data show that the addition of TEMP makes an immediate difference in the absorbance of the dye. All of the dyes appear to show

a reduced absorbance after the TEMP addition and a blue shift to a varying degree. N719 shows a significant blue shift of 44 nm from 552 nm to 478 nm. This would explain the observed colour change from red to orange. D35 shows a shift of 8 nm from 442 nm to 434 nm. Therefore the colour change from orange to yellow is most likely due solvatochromism where colour is altered due to a change in solvent polarity. D131 shows a blue shift of 21 nm from 418 nm to 397 nm. This is in line with the colour change from yellow to light green. These trends from UV-Vis analysis are concordant with the RGB data analysis shown in Figure 4.10.
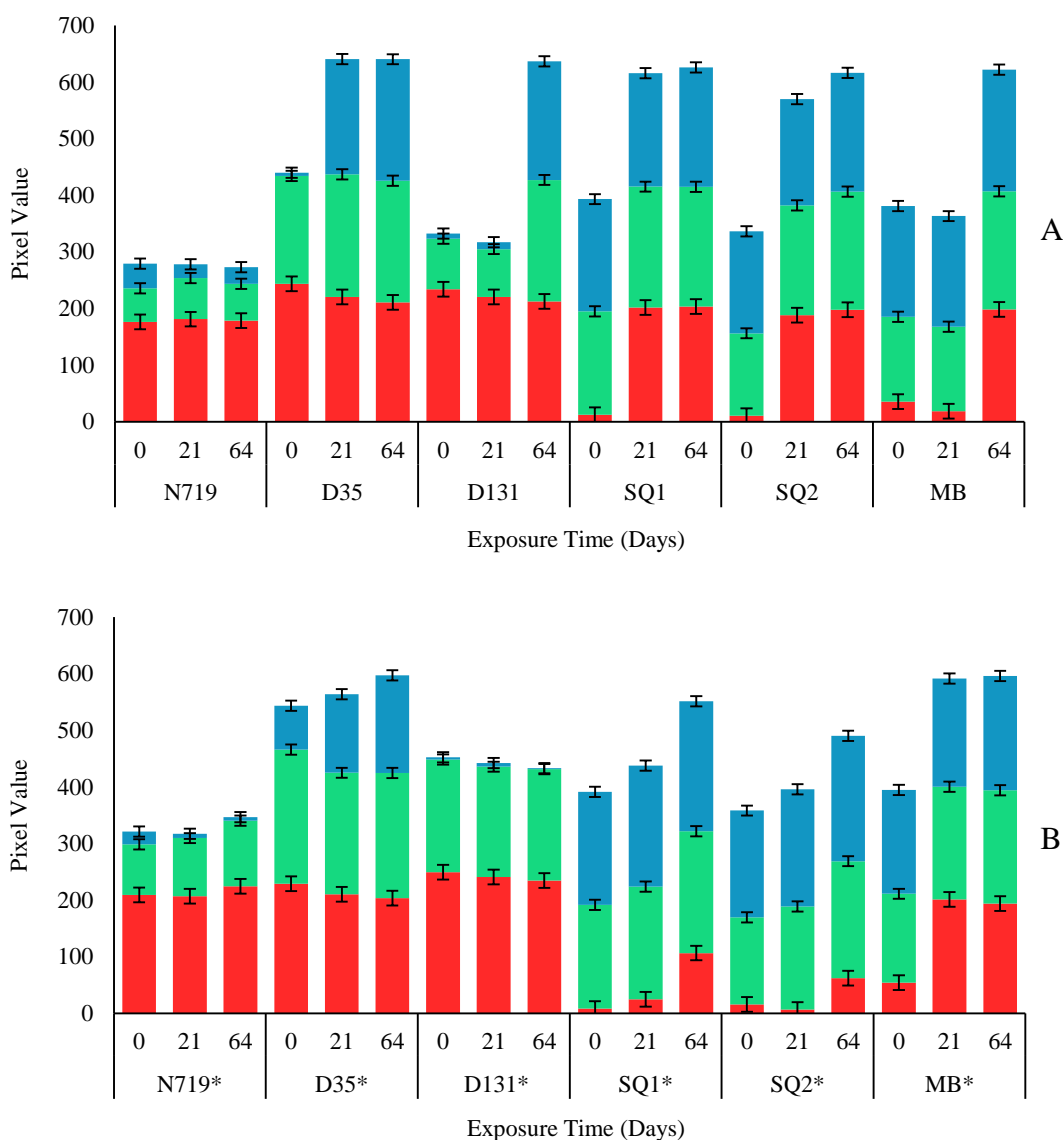
Figure 4.10 Red, green, blue (RGB) pixel values of dye with error bars for (A) solutions without TEMP, (B) solutions with the addition of 10 mM TEMP. Note dye degradation is indicated by all three colours becoming equal; the absence of colour means the white of the background is observed.

Observing the solutions initially, before the addition of the TEMP, N719 appears to have changed very little suggesting it has remained stable. D35 shows a slight degradation after 21 days but a very significant degradation after 64 days. D131 degrades very significantly after just 21 days, this is also the case with SQ1 and SQ2. Methylene blue shows a slight change after 21 days but substantial degradation after 64 days.

The solutions with additive are a slightly different colour to begin with (as shown in Figures 4.8 and 4.9). This suggests that the TEMP may have coordinated with the acidic linker groups on the dye, causing a shift of the dye absorption. With the additive N719* shows very little change after 21 days but does show a slight change after 64 days indicating there has been some degradation. D35* shows very little change throughout the exposure indicating it is highly stable. D131* fades significantly after 21 days as indicated by the increase in blue. The dye then fades further after 64 days indicating a gradual degradation. SQ1* shows a slight increase in red colour after 21 days, showing it has faded slightly. This trend continues to 64 days showing further degradation. SQ2* shows a slight change after 21 days which becomes more significant after 64 days. Methylene blue* shows a very sudden change to equal red green and blue values the dye remains the same after 64 days indicating complete degradation.

By comparing the two graphs in Figure 4.10, the effectiveness of the TEMP in the dye can be concluded. The addition of the TEMP to N719 appears to have a negative effect on the dye, accelerating degradation. This could be caused the reaction of the acid linkers on the N719 structure with TEMP to form a salt by an acid base reaction. Positive results were achieved with D35 where the use of the additive gives a significant increase in stability. As discussed previously the colour of D35 changes from orange to yellow upon the addition of the TEMP which suggests it is binding to the dye. D131 also showed improvement with the additive showing a significant reduction in degradation although there was some fading of the dye. Both SQ1 and SQ2 degraded very quickly without the additive. The addition of TEMP to the squaraine dyes made a substantial difference, greatly reducing the degradation. Methylene blue degraded much faster with the additive. This may be due to the

electron scavenging abilities of TEMP targeting the chlorine in the methylene blue and destabilising the cationic dye.

The RGB data can be quantified to calculate concentration. To achieve this, UV-Vis data is used to calculate the dye concentration at the start and end of the experiment using the beer lambert law. The concentration of the solution can then be plotted against the RGB data. This has been demonstrated with D131 dye in Figure 4.11.
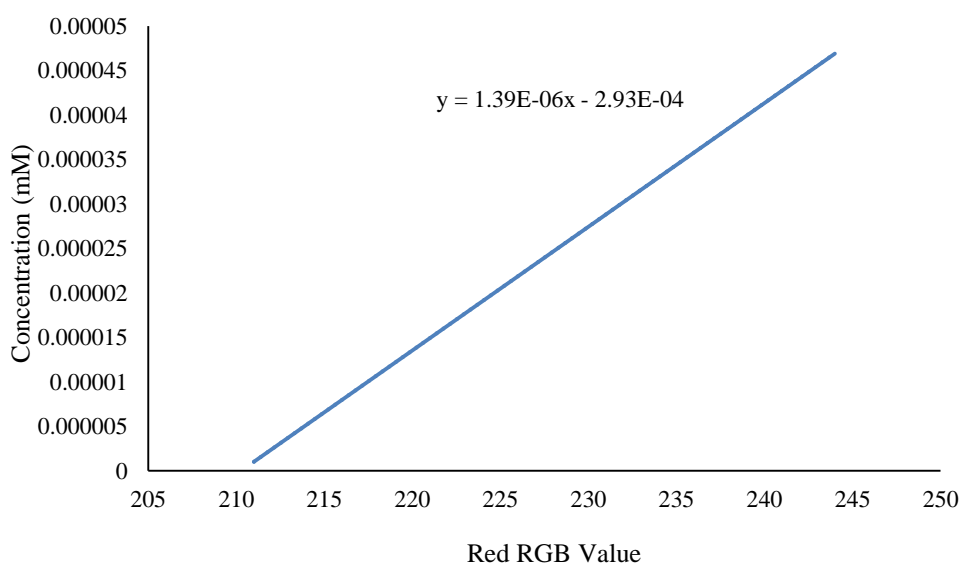
Figure 4.11 Graph of concentration vs Red RGB Value for D131 dye solution over 64 days exposure.

From the gradient of the graph shown in Figure 4.11 the following relationship can be determined:

$$\text{Concentration} = 1.39 \times 10^{-6} \times (\text{Red RGB value}) - 2.93 \times 10^{-4}$$

Using this formula an unknown concentration of dye can be calculated using only the RGB value. This can be demonstrated using the red RGB value of D131 dye at 21 days of 220.

$$\text{Concentration} = 1.39 \times 10^{-6} \times 220 - 2.93 \times 10^{-4} = 1.355 \times 10^{-5}\,\text{M} = 0.014\,\text{mM}$$

The rate constant for D131 can be determined by plotting the concentration against time. This is shown in Figure 4.12.

58
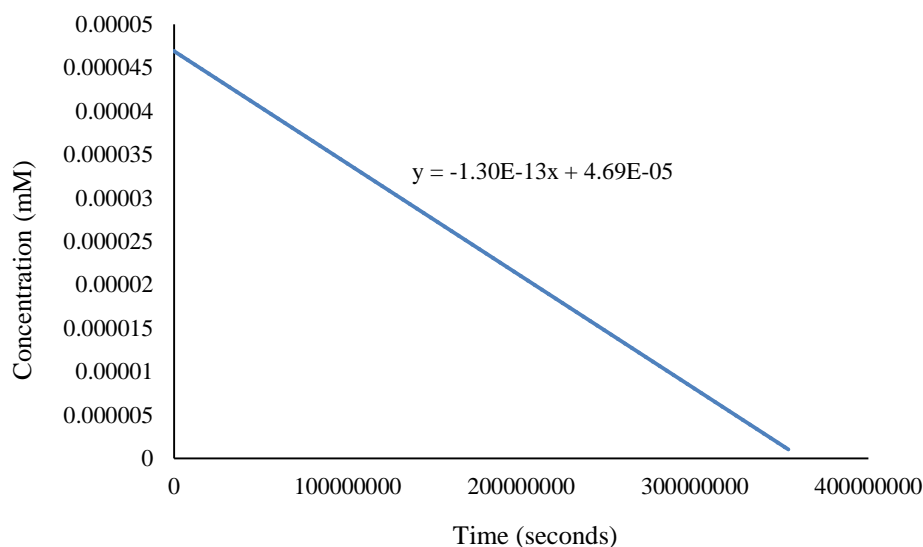
Figure 4.12 Graph of concentration against time for D131 dye solution under natural light exposure.

The graph in Figure 4.12 shows a linear gradient suggesting it is a first order reaction. The rate constant can be determined taking the inverse of the gradient in Figure 4.12. This gives a rate constant of 1.30×10^{-13} s^{-1}.

This process was repeated for N719 and D35 and the results are shown in Table 4.1.

Table 4.1 Summary of dye coefficients and rate constants.

Dye	RGB concentration coefficient	Rate constant
N719	3.87×10^{-07} x (red RGB value) - 2.90×10^{-05}	3.50×10^{-13} s^{-1}
D131	1.39×10^{-06} x (red RGB value) - 2.93×10^{-04}	1.30×10^{-13} s^{-1}
D35	3.31×10^{-05} x (red RGB value) - 7.27×10^{-03}	8.37×10^{-11} s^{-1}

Table 4.1 shows the RGB concentration coefficients and the rate constants for N719, D131 and D35. The RGB concentration coefficient allows calculation of the molar concentration of each dye in solution from the red RGB value. The red value has been used as these dyes have a red/orange colour. For other dyes such as SQ1 and SQ2 the blue RGB value would be more suitable as this matches their colour. The rate constants reveal that by far the fastest degradation occurs in D35 dye. The rate constant for D131 was two orders of magnitude higher showing significantly slower degradation. The rate constant for N719 was almost three times higher than D131 showing than N719 had the highest stability.

4.2 Investigation of SQ1 Stability under Low Light Levels

Initial observations showed that when left in a sealed and lightproof container a mesoporous TiO_2 film sensitised with SQ1 would degrade and eventually bleach without light exposure. To quantify this degradation an electrode was sensitised with SQ1 and then added to a UV-Vis spectrometer which was run hourly for 60 hours. The data is shown in Figure 4.13.
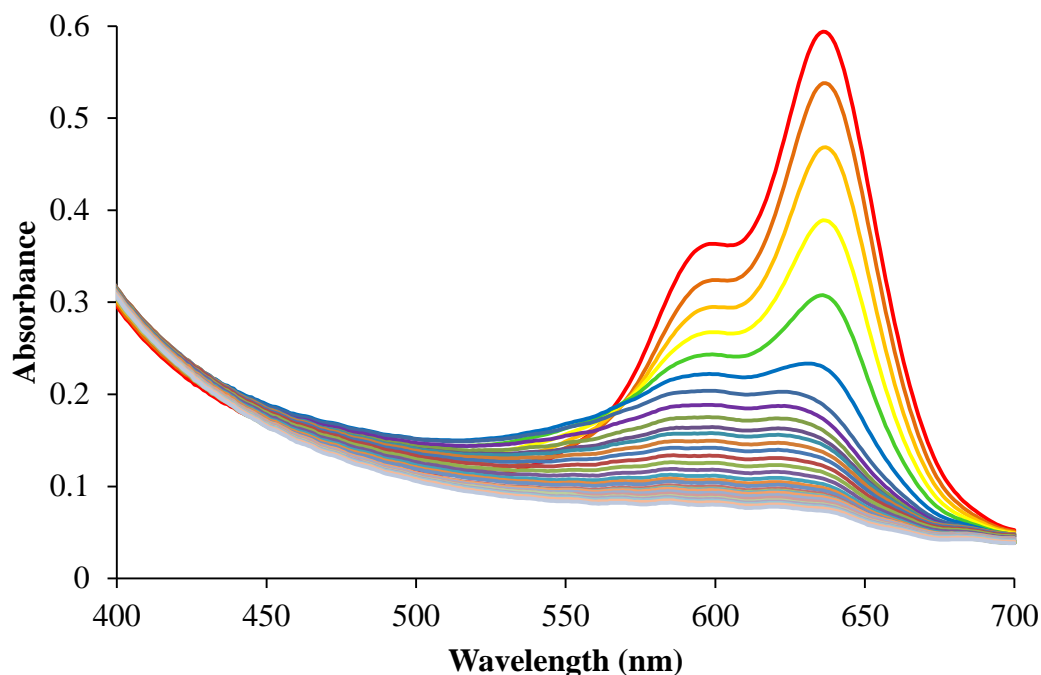
Figure 4.13 UV-Vis data showing the absorbance of SQ1 dyed mesoporous TiO_2 film over a period of 60 hours. The red line is at T = 0 hours and every line below is represents an additional 2 hours.

Figure 4.13 shows SQ1 degrades when sorbed onto a mesoporous TiO2 film despite the lack of light exposure. Data show a fast rate of degradation initially which slows after the first 6 hours. It is possible that the dye is being broken down by oxidation and breaks down fastest on the surface. This would explain the slower decrease in degradation as the outer layer is fully degraded and the inner layers are less exposed.

It is worth noting that due to the conditions of the experiment there would be a small amount of light exposure from the beam of the UV-Vis spectrometer. There would also be some exposure when the electrode was removed from solution and placed in

the UV-Vis. These small exposures could possibly be responsible for the degradation although it seems more likely that this degradation is catalysed by the TiO_2.

4.3 Studies of the Degradation of Dyes under Artificial Light

A decision was made to design time-lapse shooting with a macro using Jitbit Macro Recorder. The macro program was designed to control the computer to carry out a function such as taking images remotely. To make the macro the program, the "record" function was used and the capture button was clicked manually on the Photosimile software, once the image had been taken the save button was then clicked. The macro software then allowed the process to be played back, automatically taking the images. The whole process took 20 seconds allowing 180 images per hour. An example macro is shown in Figure 4.14.
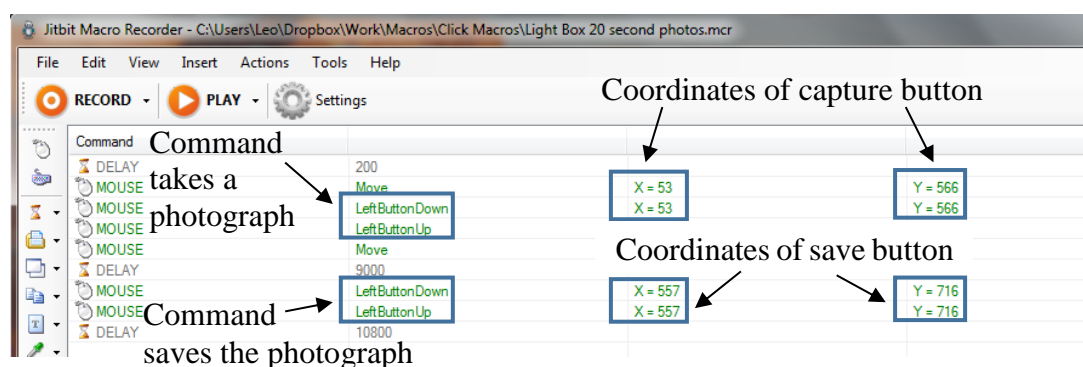
Figure 4.14 Macro for a 20 second time-lapse with the Photosimile Image Creator. The image would be taken and then saved using two clicks of the mouse. The macro could be set to repeat x number of times to determine the number of images taken, in addition the delay time between images could be altered if necessary.

This procedure enabled time-lapse photography to take place. The number of images or frames taken per second is known as the frames per second (fps). This setup was limited to a rate of *ca.* 1 image per 10 seconds (0.1 fps) by the speed at which data could be transferred from the camera to the computer.

Unfortunately the Photosimile software did not have an option to only save data on the camera. This meant the processing time could not be decreased with this piece of software as the transfer time slowed the process. Therefore a new piece of software was needed to enable a faster rate of data accumulation.

The software supplied with the Canon® camera included a program for taking images remotely. This was the Canon® EOS 1100D software, which had an inbuilt time-lapse function which allowed images to be automatically taken as quickly as 5 seconds apart. This allowed control of the camera from the computer to give twice the speed for time-lapse shooting, allowing for the collection of more data. This also removed the need for an image capture macro. The time-lapse settings are shown in Figure 4.15.
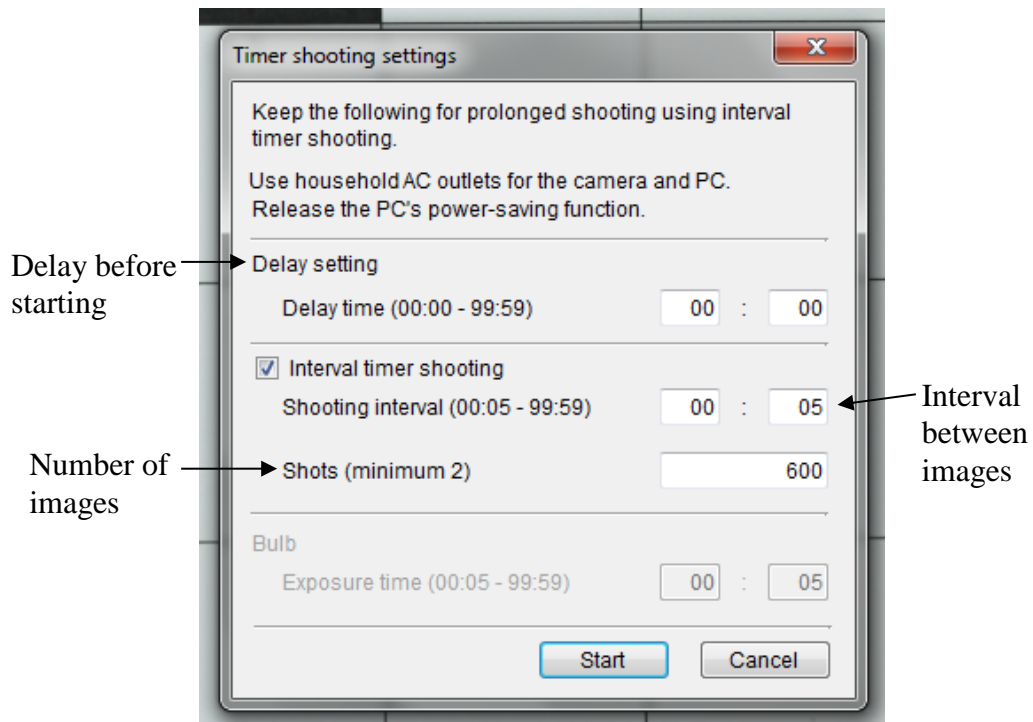
Figure 4.15 Canon® EOS 1100D software, showing the settings for time-lapse shooting.

However, the problem with this software was that 1 image per 5 seconds (0.2 fps) was still not quick enough to give adequate data to capture all changes. Additionally, there was still no option to save the files to the camera only. The reason why there was a 5 second delay was because the process was limited by the time taken of the files to be transferred from the camera to the computer.

A more suitable option was identified to be the program DSLR Remote Pro, since it had the ability to save images to the camera memory card. Additionally, the program had the option of time-lapse photography so a macro was not required for taking images at set intervals. The software did not have a minimum number of seconds

between images, so a one second time-lapse could be used. The settings are shown in Figure 4.16.
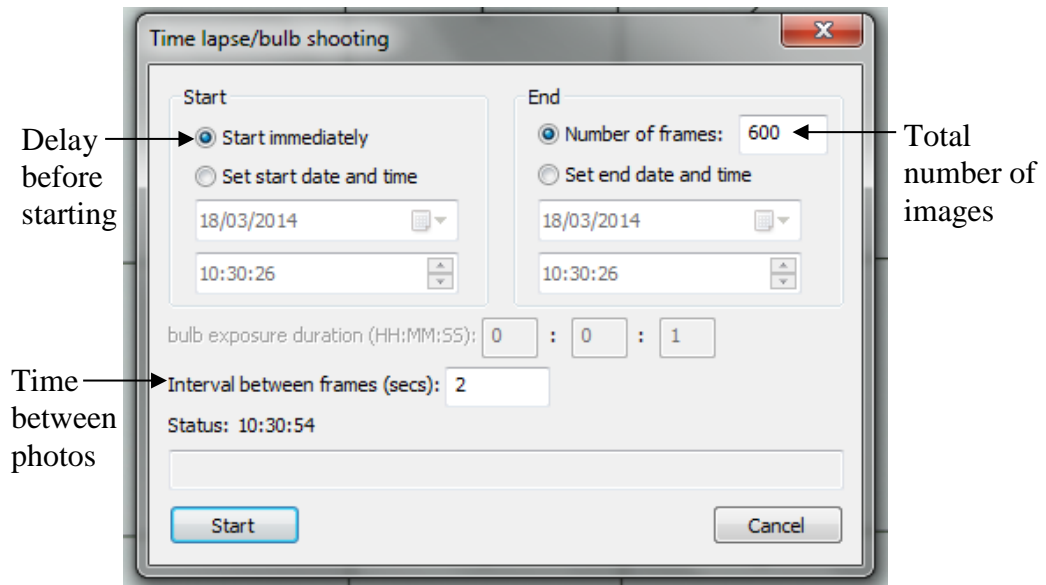
Figure 4.16 Screen capture of the DSLR Remote Pro program, showing the time-lapse settings for the camera. The total number of images or frames can be set as can the time between images, allowing for optimisation of the time-lapse.

Since the images were set to save to the camera memory card the fastest compatible memory card was chosen. Thus a class 10 memory card was chosen with a transfer speed of up to 45MB/s. This meant that the images could theoretically be saved in under a 10th of a second as the image size was under 4MB. This was faster than the 0.3 second shutter speed on the camera which was required to take an image. Therefore the speed of the images was no longer limited by the time it took the camera to save the file onto the memory card and a high speed time-lapse could be used.

Initial images of the electrodes were taken using a 1 second time-lapse with just the white background of the lightbox. Following this the decision was made to use an A4 sheet of paper with a 2.5 cm square grid to allow the electrodes to be positioned in the same place between experiments. This meant position of the cells would be constant between images. Numbers were also added to the squares in the grid to act as reference points for multiple samples. This initial setup is shown in Figure 4.17.

63
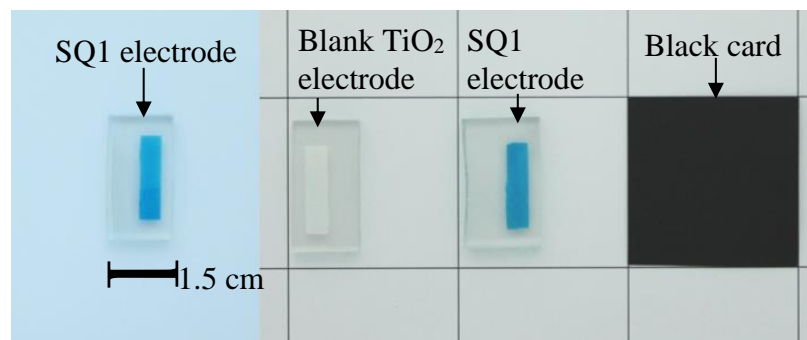
Figure 4.17 (Left) A photo-electrode dyed with SQ1 which has been placed on a blank background. (Right) Similar electrodes with a printed 4 x 4 cm grid background, a control electrode which has not been dyed and a square of black card to allow a better focus.

A black square of card was added to give the camera a clear focal point. The white and black paper also enabled maximum values to be checked as the darkest sample would have the lowest values with a RGB value of 000 for perfect black. The white paper would give the full scale deflection with the highest values with RGB values of 255, 255 and 255 for a perfect white colour. Additionally a small clock was added to show the time passing between each photograph and to check that the time-lapse images were being taken at the correct intervals. Once the images had been taken a method for analysis was developed.

4.4 Image Analysis

In order to quantify results from the dye degradation, an image analysis needed to be conducted. To conduct the analysis, Sigma Scan Pro 5 was used to analyse the active area on the electrodes and output the data as red, green and blue (RGB) values. Using Sigma Scan, the image could be opened and the electrode selected for analysis. The electrode was analysed by selecting trace mode, then drawing a square over the desired 240 by 240 pixel area. Jpg images have been used for the analysis as raw data was incompatible with Sigma Scan Pro 5. The settings used for the camera are detailed in Section 3.23.

To trial the analysis, the active area on each electrode on the grid then needed to be highlighted and marked for analysis. Carrying out this process manually for each image, was very time consuming due to the hundreds of images captured. To automate this process, a macro was developed to measure the same points in each image. The

use of a macro was possible because the grid was used to align electrodes in the lightbox so they were in exactly the same location between each image captured.

Two designs were considered for the macro. The first involved recording the macro in the Sigma Scan Pro software and then selecting each of the areas required for analysis. This macro could then be saved and run on multiple images. This first method would potentially have greater error as the selected areas would vary by approximately 5% between electrodes due to spatial errors from the manually drawn areas for analysis. Electrode selected with the initial method are shown in Figure 4.18.
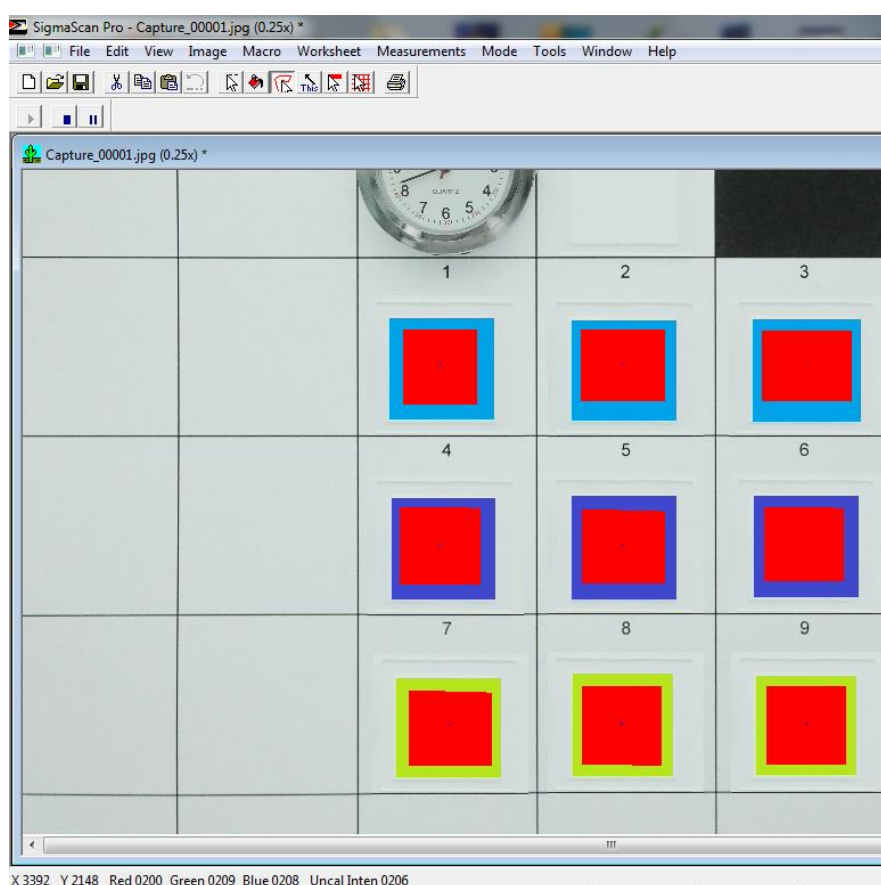
Figure 4.18 Macro recording in Sigma Scan Pro. The red areas have been selected for RGB analysis with trace mode, the macro was then saved. When the macro was played back the same areas were analysed across every image, allowing bulk image processing. Note electrode colours have been changed for the macro creation so the dyed areas stand out.

To improve this method, a decision was made to write the macro manually using pixel coordinates of the active area on the electrodes. Using this method gave greater control

as each of the electrodes could be measured with exactly the same number of pixels (240 x 240 pixels). With the camera positioned at the same height in the lightbox between photographs, the 240 pixels would correspond to a distance of 2 cm. This would give an area of 4 cm^2 which would also remain constant. The desired coordinates were determined using formulas in Microsoft Excel to calculate the coordinates from the top right corner of each electrode. This is shown in Figure 4.19.
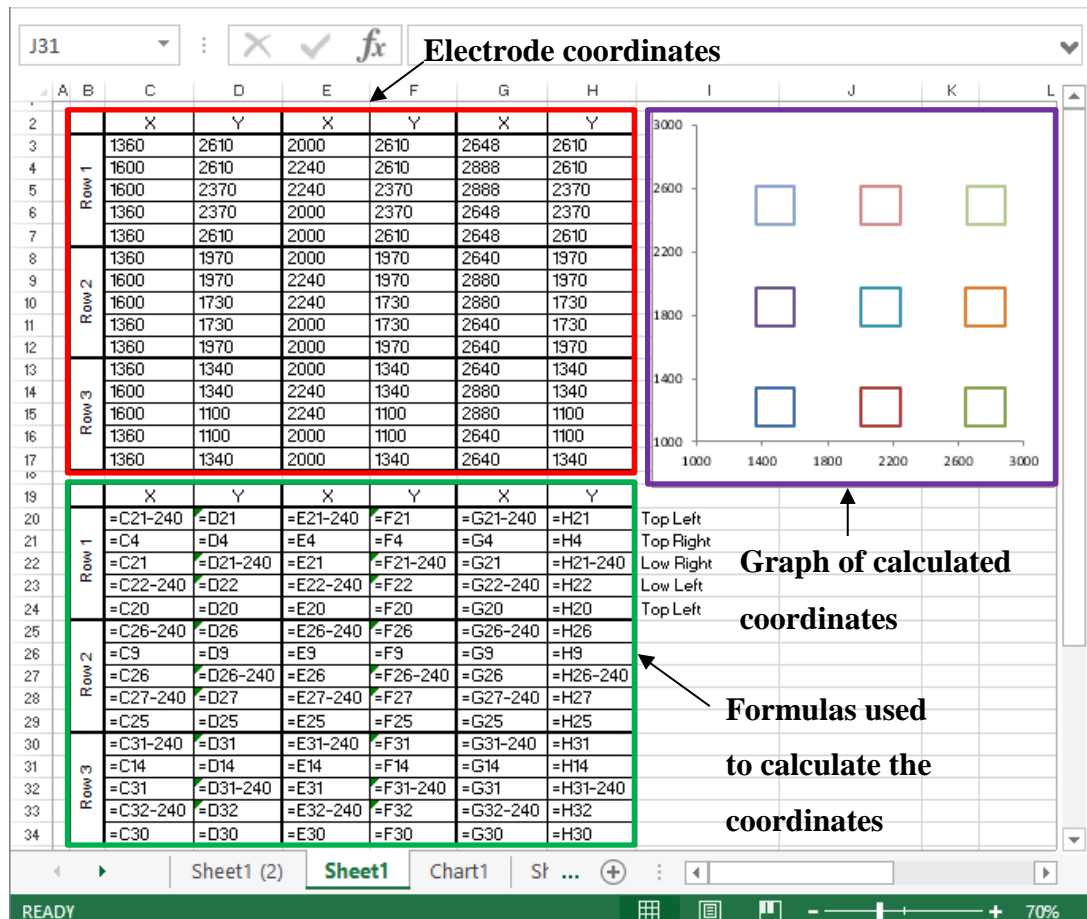
Figure 4.19 Screenshot of Microsoft Excel, showing the determination of the coordinates for the RGB analysis of the electrodes. The final coordinates for the macro (inside the red box) were calculated by the formulas (inside the green box). A graph of calculated coordinates was used to check consistency (inside the purple box).

The coordinates in Figure 4.19 were calculated from the top right coordinate which was found by moving the cursor to the right corner in Microsoft Paint which displayed the X and Y coordinates. The top left value was calculated from the top right X and Y coordinates. This was done by deducting 240 from the X value and using the same Y coordinate as the top right. The lower right was calculated by using the same X value

as the top right and deducting 240 from the Y coordinate. The lower left was calculated by deducting 240 from both the X and Y coordinates from the top right.

The calculated pixel values were then written into a macro, this is show in Figure 4.20.

Figure 4.20 Screenshot of the macro used for the RGB analysis of the electrodes. The coordinates used were calculated in Microsoft Excel and then written into the macro. The macro left clicked (shown in the blue box) at each corner of the electrode (shown in the red box) and then right clicked to finalise the area for analysis.

The macro selected each corner by left clicking at the pre-set coordinates. The macro then right clicked on the first corner to confirm the selected area. This macro was used for the RGB analysis of electrodes. The macro could be used between multiple

experiments as long as the electrodes were aligned correctly on the grid, resulting in the same coordinates for each electrode.

4.5 Light Soaking of Dyed Mesoporous TiO₂ Films

To gain a greater understanding of the stability of dyes in DSSC devices, the degradation of dye solutions on mesoporous TiO_2 films was tested. As a model of a DSSC device a single film of mesoporous TiO_2 was deposited on FTO using glass, Dyesol® active opaque paste was used. This film was then sensitised by passive dyeing in a 0.5 mM dye solution in ethanol.

As mentioned in section 3.23, control experiments were carried out at the start to measure the errors of the lightbox. In the initial control experiment the 50 Hz lamp was turned on at the start of the experiment and the camera shutter speed was 1/125 of a second which is 8 ms. A blank TiO_2 film was used as the control electrode. This was placed inside the lightbox and digital images were taken every 5 seconds. The pixel value of each colour was then plotted against time so any variation could be observed. This is shown in Figure 4.21.
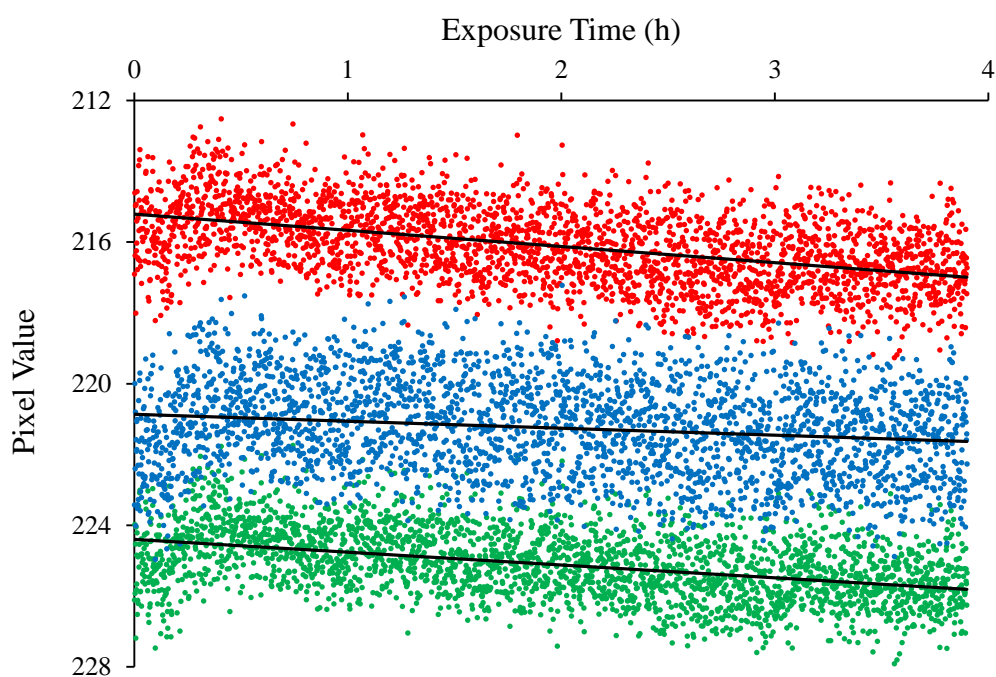
Figure 4.21 RGB values for a control electrode with a high shutter speed.

68

One possible cause of the error could be flicker of the light source and the warm up time of the lamp. Flicker was caused by the shutter speed on the camera being too fast. This caused a noticeable variation in the light intensity between images due to the high frequency changes in brightness from the lamp. The warm up time is the amount of time for the lamp to give a constant emission of light.

This first control experiment showed a wide variation in pixel value for each colour. The error was calculated as the range where the lowest value was deducted from the largest value. This gave a range of ± 7 pixels for red, ± 6 for green and ± 8 for blue. In Figure 4.21, the average error with this setup of ± 7 pixels was too high (2.7%) as subtle changes in colour could have be obscured by noise.

To test if it might be possible to reduce the noise from flicker, the shutter speed was decreased significantly to once every 0.25 seconds which was significantly higher than the frequency of the lamp, 50 Hz (0.02 seconds). The subsequent data (Figure 4.22) show that the issue of flicker was greatly reduced. At this stage, the lamp warm up time was still left at 0 hours.
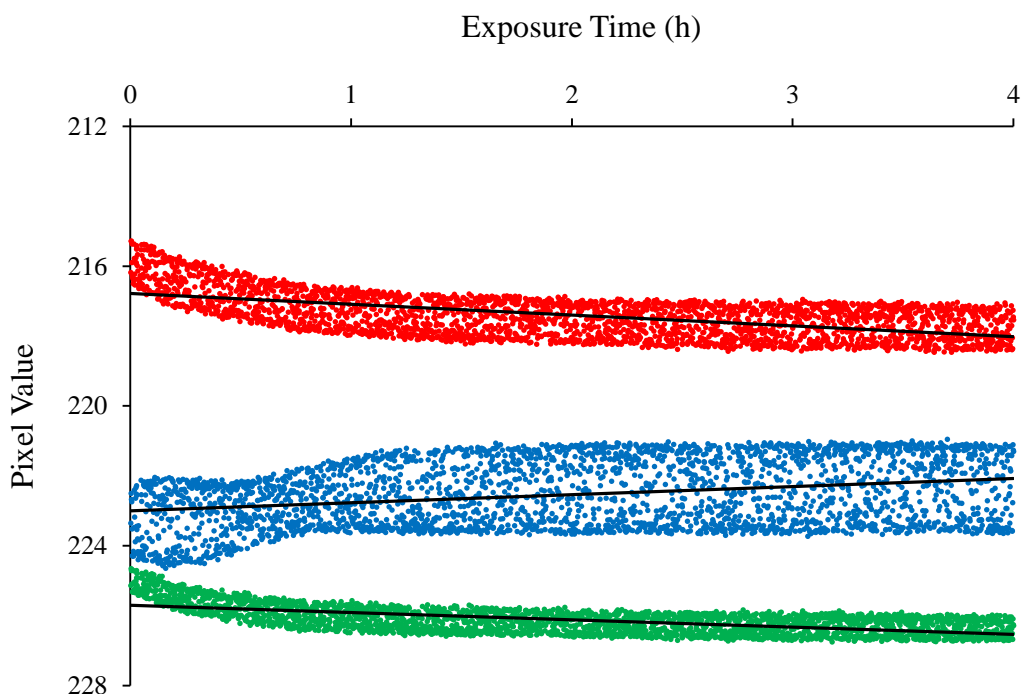

Figure 4.22 RGB values of a control electrode at a fast shutter speed with a warm up time of 0 h.

Figure 4.22 showed a greatly reduced noise level compared to Figure 4.21. The spread of the data was ±3 for red, ±2 for green and ±4 for blue which was a much lower average error of ±3 pixels (1.2%). The most notable part of the graph was in the first hour of the exposure time. The blue colour is decreasing while red and green increase indicating a slight change in colour. The data show that the pixel values appear to stabilise after 1 hour, suggesting the lamp had fully warmed up and provided a uniform light output. To test this effect, the lamp was left to warm up for one hour before running an experiment.

In the third experiment the effect of a slow shutter speed and the lamp warm up time were tested together to determine if there was a further improvement in the data, as shown in Figure 4.23.
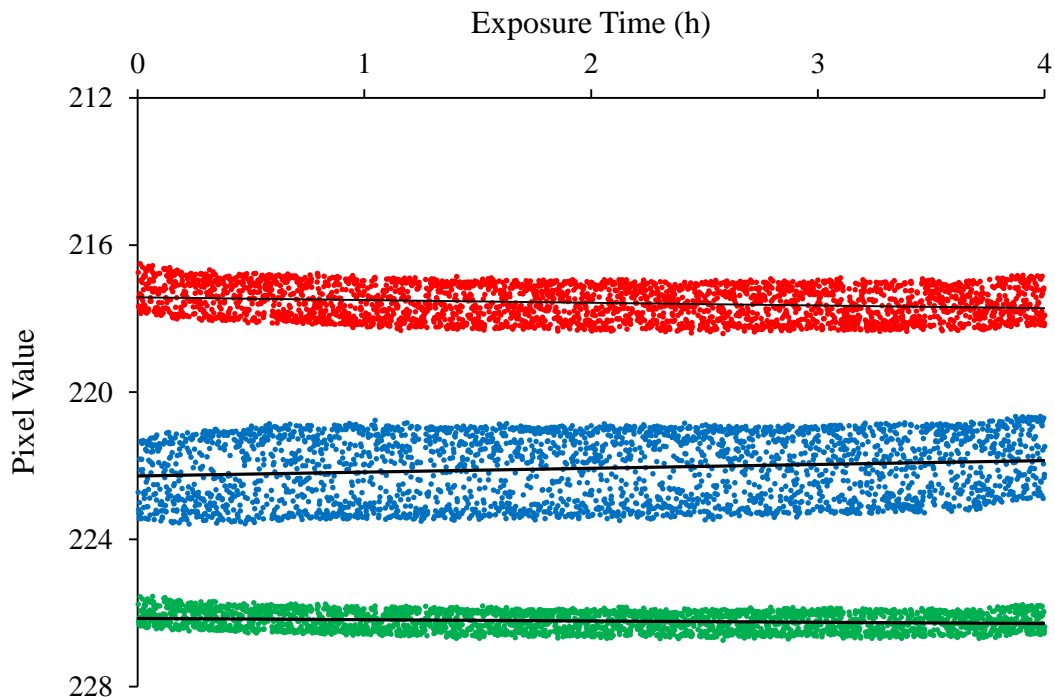
Figure 4.23 RGB values of a control electrode at a 0.25 s shutter speed with a warm up time of 1h.

Figure 4.23 showed a further decrease in the noise level. The range of the data was ±2 for red, ±1 for green and ±3 for blue. This gives an average error of ±2 pixels which is a significant improvement as the error levels are now less than 1% (2 in 255 pixels).

It is worth noting that the error on the blue pixel value always shows a higher variation (±3 pixels). Digital cameras contain a sensor which converts light into electric signals

which is then used to build a digital image[177]. Digital cameras which contain a CCD (charge coupled device) sensor usually have a lower spectral sensitivity to blue colour[178]. Thus there is a higher percentage error for the blue pixel values taken using a camera with a standard CCD sensor such as with the Canon EOS 1100D used in this thesis. The Quantum efficiency for a range of CCD sensors is shown in Figure 4.24.
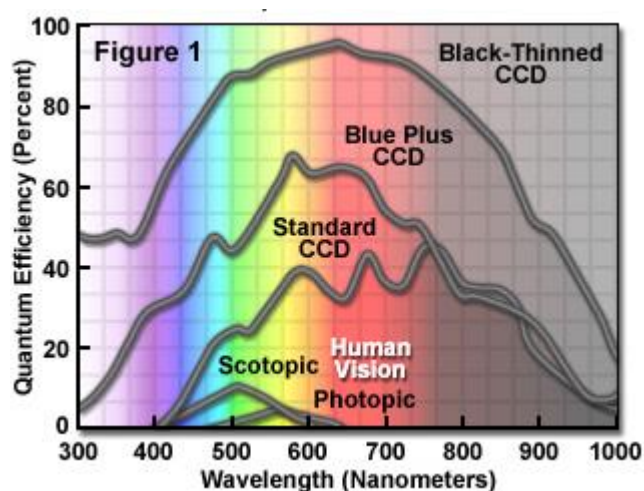
Figure 4.24 Spectral responses of different methods of colour detection, from the human eye to the CCD (charge coupled device) sensors used in cameras. Image from literature[179].

4.51 Lifetime Testing of SQ1, SQ2 and N719 on Mesoporous TiO$_2$

SQ1, SQ2 and N719 dyed TiO$_2$ electrodes were light soaked, as shown in Figure 4.25.
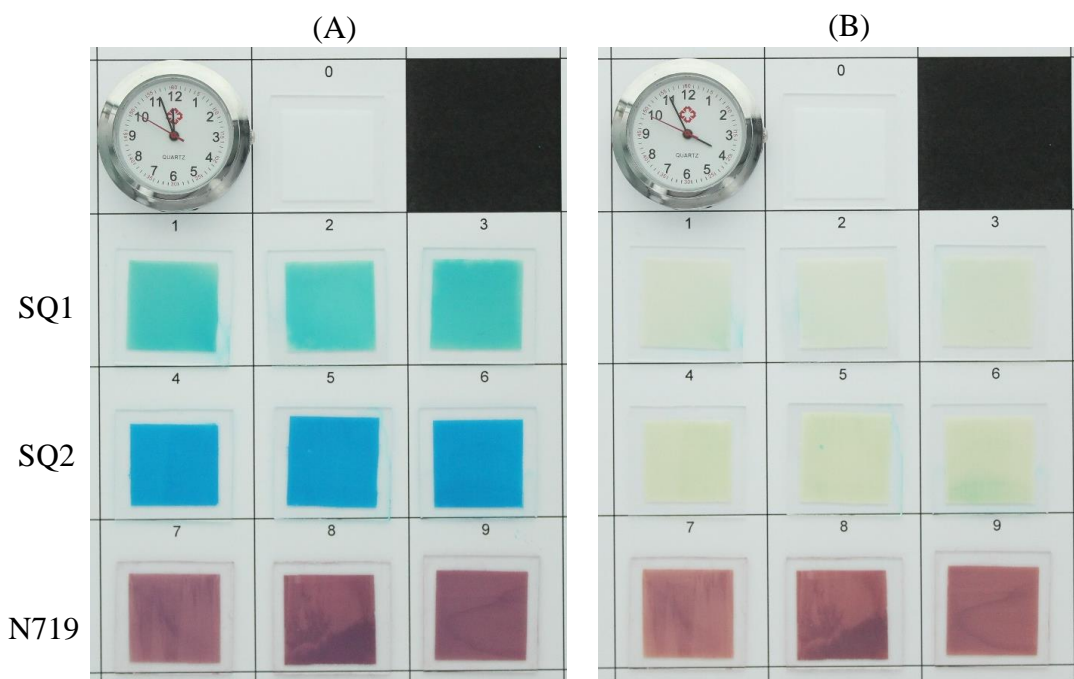
Figure 4.25 Images of (A) electrodes at before exposure and (B) electrodes after 4 hours of exposure.

	(A)			(B)		
	0			0		
SQ1	1	2	3	1	2	3
SQ2	4	5	6	4	5	6
N719	7	8	9	7	8	9
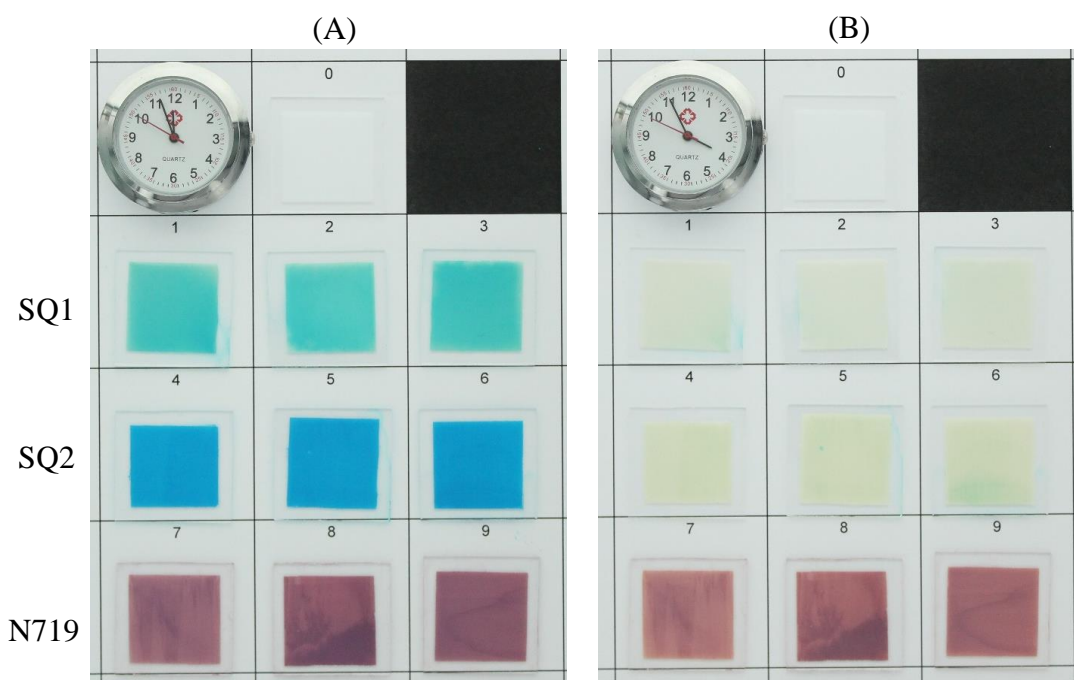
Figure 4.25 shows that the squaraine dyes (SQ1 and SQ2) were the least stable of those tested under natural light (section 3.12). In contrast N719 was one of the most stable dyes. The structures of SQ1 and SQ2 are almost identical (see Scheme 1) so it would be interesting to determine if they degrade at the same rate under a more controlled artificial light exposure. N719 was used as a control due to its well established high stability.[176,180,181] To directly compare the degradation rates of these dyes, they were exposed to artificial light concurrently to ensure equal light exposure. To do this, electrodes were constructed from 2.5 by 2.5 cm FTO glass with a mesoporous TiO_2 film (Dyesol® active opaque). Electrodes were passively dyed in 0.5 mM solutions of SQ1, SQ2 or N719 for 12 hours. The electrodes were then removed and placed on a grid labelled 0 to 9 with a control at 0. Grid numbers 1 to 3 were SQ1, 4 to 6 were SQ2 and 7 to 9 were N719. Images were taken every 5 seconds to monitor colour changes, whilst the electrodes were exposed to artificial light for 4 hours.

To quantify and compare the rates of degradation between the three dyes, the digital images were analysed with a macro. To determine the variation in light levels throughout the experiment a control electrode was added. This consisted of a non-dyed mesoporous TiO_2 film which was exposed at the same time as the other electrodes. This is shown in Figure 4.26.
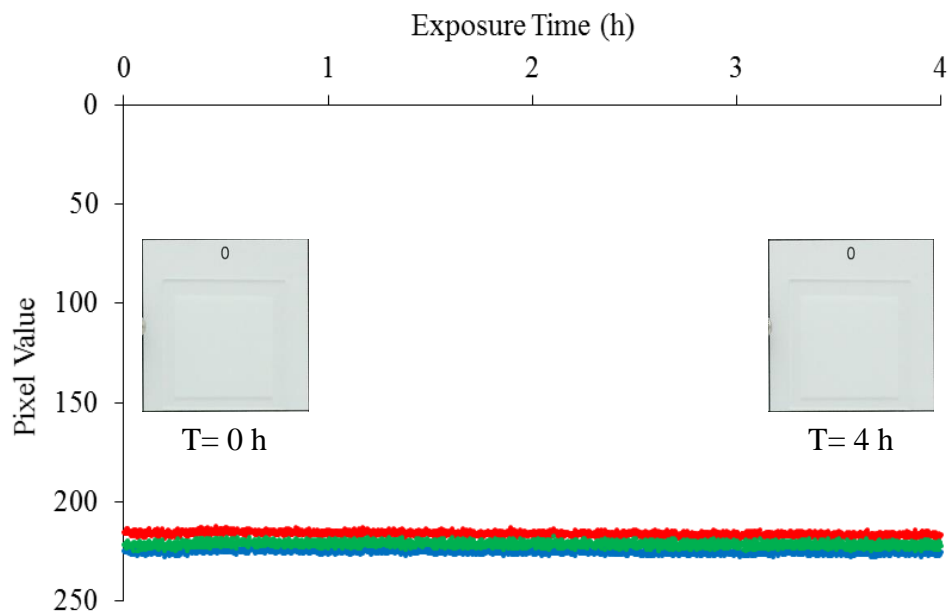
Figure 4.26 Control Electrode – RGB analysis of non-dyed mesoporous TiO$_2$ film used as the control for the experiment. The low spread of data indicates a low error. All three RGB values are roughly equal which corresponds to the white colour of the electrode as there is no change in gradient the electrode is highly stable.

Figure 4.26 shows the variation in the light levels between images of the electrode corresponds to an average error of ±2 pixels. The electrode appears to have remained stable during the experiment as indicated by the consistently flat gradient of all the 3 RGB values throughout. Next the N719 dyed electrode was analysed to determine if there was a colour change which indicated degradation. As shown in Figure 4.27.
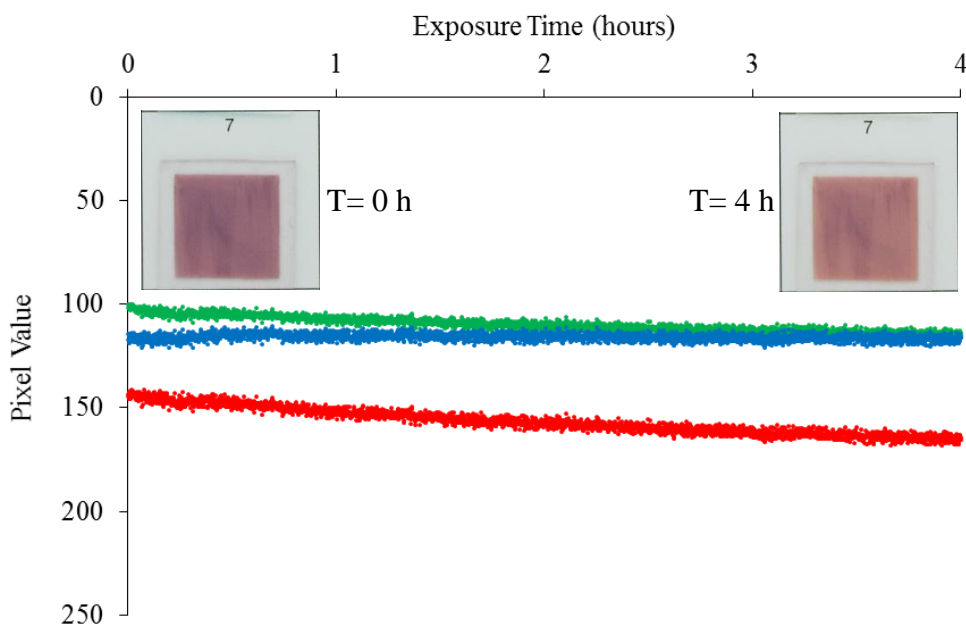
Figure 4.27 N719 electrode – RGB analysis of the N719 dyed mesoporous TiO$_2$ film used in the experiment. (Top left) electrode prior to exposure, (top right) electrode after 4 hours exposure.

As shown by Figure 4.27 there was a very slight fading of the colour of the electrode. This indicates that a small amount degradation did occur. Next the SQ1 electrode was analysed, this is shown in Figure 4.28.
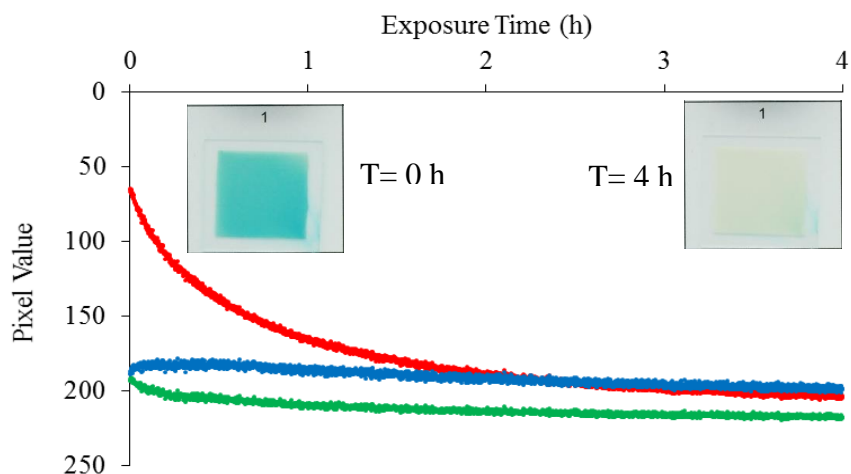
Figure 4.28 SQ1 electrode – RGB analysis of the SQ1 dyed mesoporous TiO_2 film used in the experiment. (Top left) SQ1 dyed electrode prior to exposure, (top right) the same SQ1 electrode after 4 hours exposure showing the colour loss of the dye.

As shown in Figure 4.28 there is a high rate of change of the red component from 0 to 2 hours and then the RGB pixel values become approximately equal at *ca.* 200, indicating bleaching of the electrode. This suggests a high rate of colour change initially after which the dye has photobleached. Thus SQ1 is highly unstable as it breaks down in under 2 hours. The data for the electrode made with the similar SQ2 dye is shown in Figure 4.29.
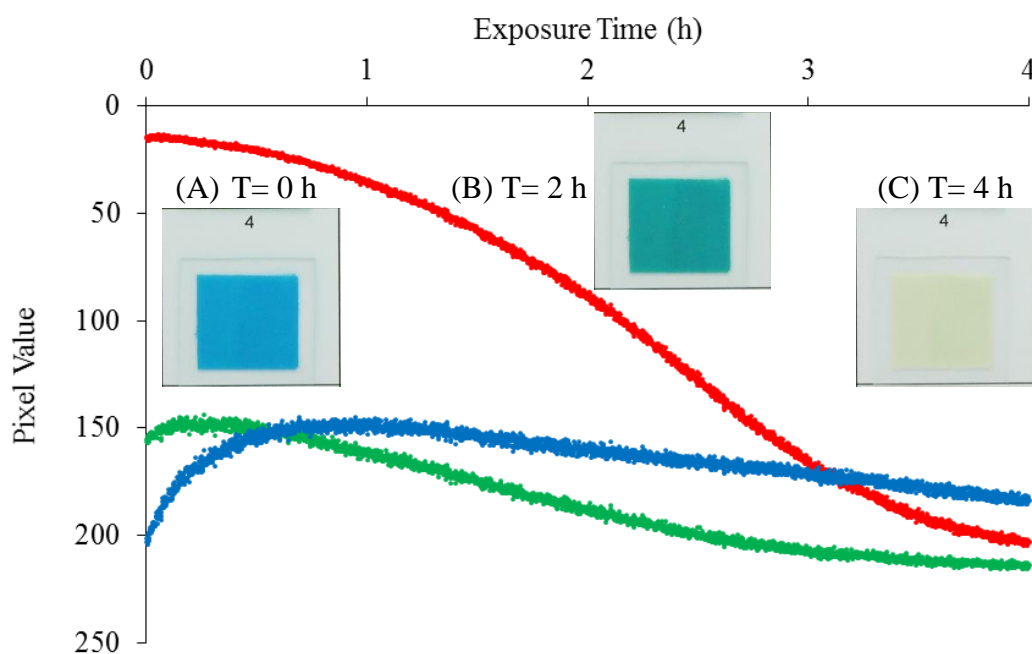
As shown in Figure 4.29 red component of the RGB values decreases more gradually in SQ2 than SQ1. SQ2 shows a lower gradient and appears have to more gradual photobleaching process. These electrodes successfully simulated dyed films and showed differences in stability. Tests were repeated three times showing consistency. To gain a better understanding of the stability of dyes DSSC devices were also made.

4.6 Dye Solar Cell Device Lifetime Testing

This experiment was designed to investigate the link between RGB analysis and DSSC device performance. To do this, 18 N719 DSSC devices were light soaked in a Dyesol UPTS for 2500 h and analysed on a solar simulator at regular intervals to determine if degradation had occurred. A comparison was made between the electrical loads on the devices to determine if this affected degradation. The effect of a UV filter on device stability was also investigated. Images were taken throughout the experiment to monitor colour changes. Images at 0 h and after 2500 hours are shown in Figure 4.30.
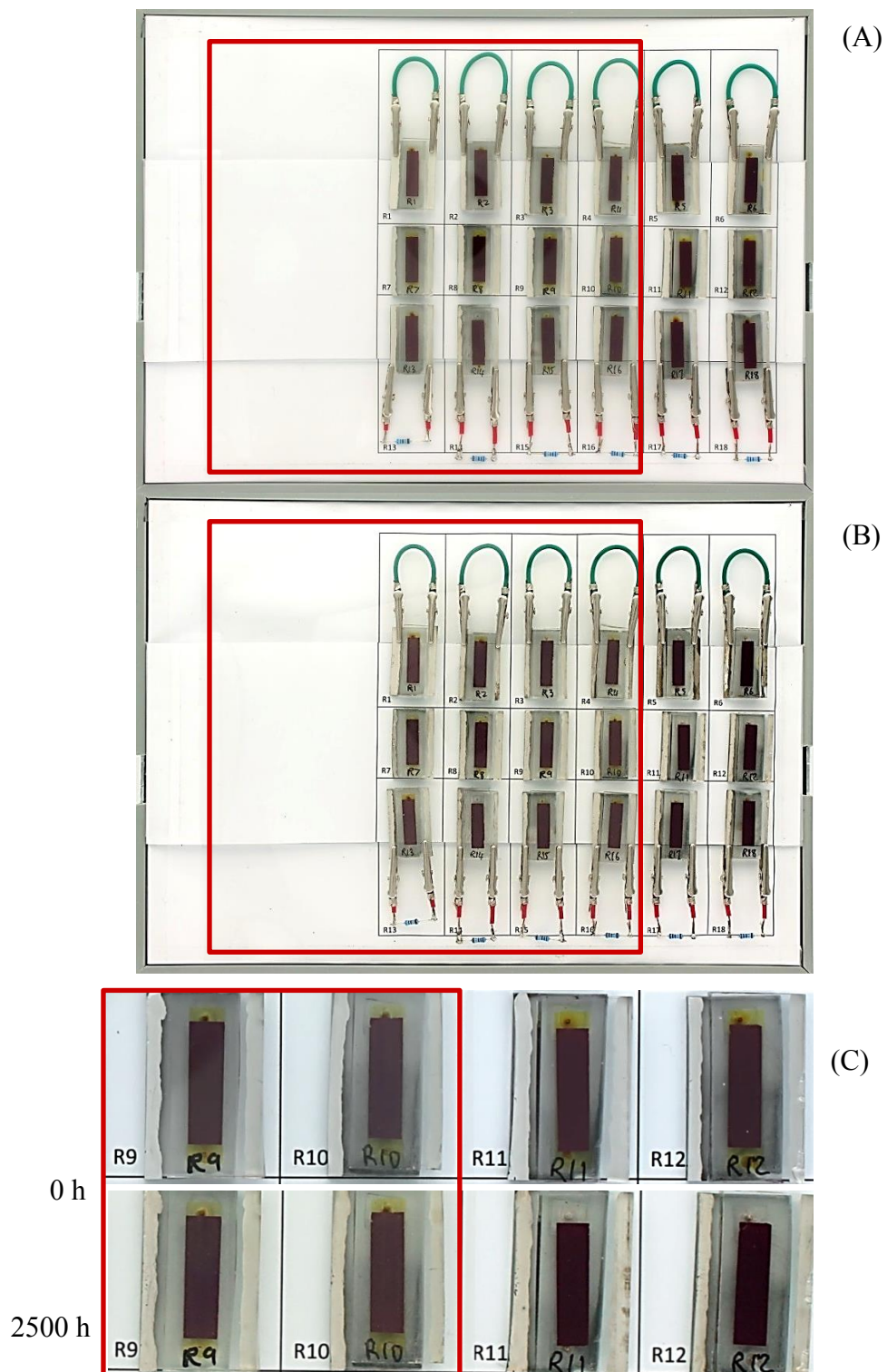
Figure 4.30 Images of N719 devices after (A) 0 h light exposure, (B) 2500 h light exposure and (C) close up of images of UV-filtered and unfiltered samples showing both the N719 dye (dark red) and the electrolyte (yellow or transparent). The UV filter is outlined by the red box.

Figure 4.30 A and B show the setup devices were tested under. The short circuit was achieved by connecting the two electrodes together (top row, green wires). Devices at open circuit were tested by leaving the cell unconnected (middle row). A load was simulated by connecting the two electrodes together with a 10 Ω resistor (bottom row,

red wires). The cells at each electrical configuration were also tested with and without a UV filter (highlighted by the red box).

Figure 4.30 C shows a close up of the cells with and without UV filtration. This shows the electrolyte has changed colour after 2500 hours of exposure without a UV filter. In contrast to this, the electrolyte did not change when filtered. This suggests that the electrolyte has degraded when exposed the UV light. To determine if degradation had occurred the devices were also tested on a solar simulator periodically during the experiment. The conversion efficiencies were plotted as averages for the groups of devices based on circuit conditions and UV filter, as shown in Figure 4.31.
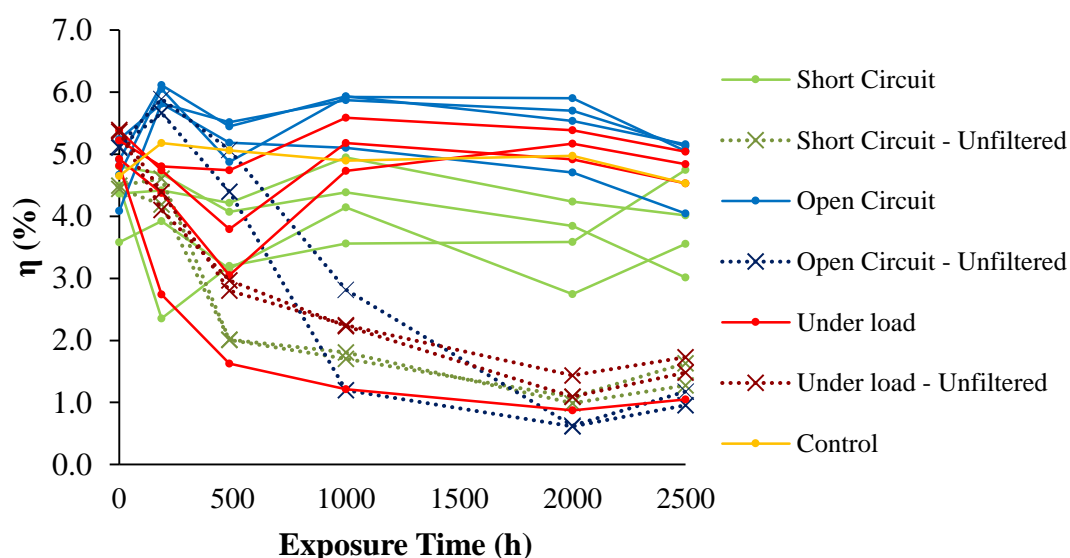
Figure 4.31 Efficiency (η) against time for N719 DSSC devices. Devices were exposed under a Dyesol® UPTS lamp (400Wm^{-2}) for 2500 hours. Dotted lines represent unfiltered cells, solid lines are unfiltered. The electrical configuration of devices was either under load (red lines), at open circuit (blue lines) or short circuit (green lines). The control cell (yellow line) was not exposed to any light.

Figure 4.31 showed the highest stability was at open circuit, with less than a 1% drop in efficiency after 2500 hours exposure. The presence of the UV filter was essential for reducing the degradation. Note the filter was removed before testing devices. RGB analysis was conducted on the electrolyte to determine if the drop in performance of unfiltered cells was due to the breakdown of electrolyte, as shown in Figure 4.32.
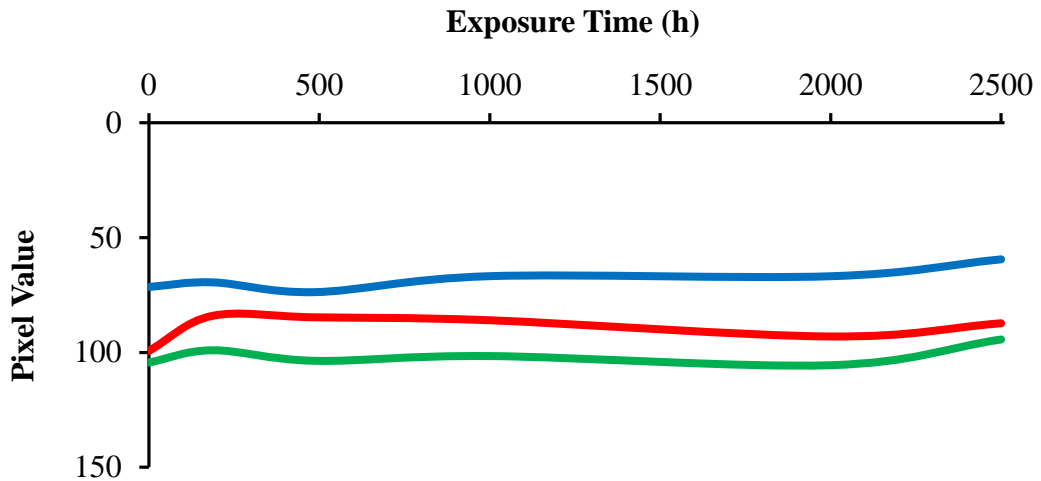
Figure 4.32 RGB values against time for electrolyte in N719 devices with UV filtration.

Figure 4.32 shows that with a UV filter the colour of the electrolyte shows a very slight variation in fading of colour as all of the RGB values have decreased by 2500 hours. This may indicate some degradation has occurred but could also be due to errors. RGB analysis was also conducted on the unfiltered devices and is shown in Figure 4.33.
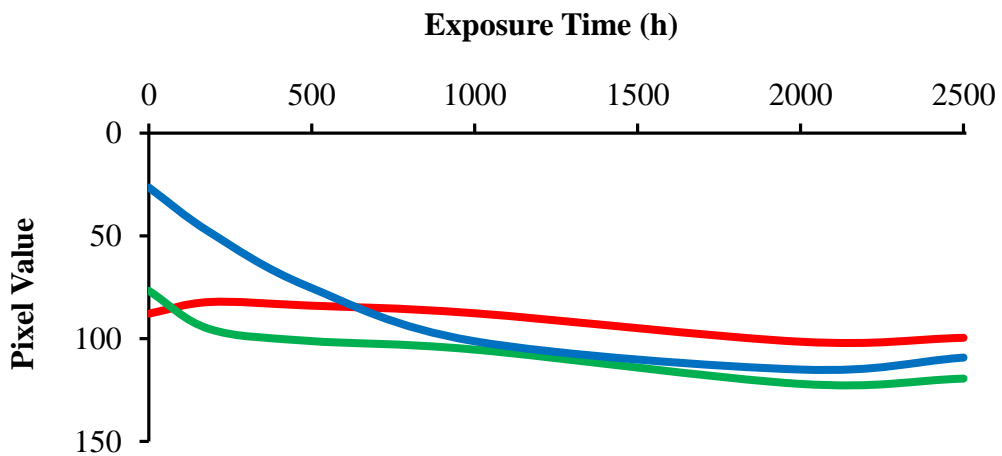

Figure 4.33 RGB values against time for electrolyte in N719 devices without a UV filter.

The differences between the initial RGB values in Figure 4.32 and Figure 4.33 are due to the presence of the UV filter which has resulted in higher initial RGB values in Figure 4.32. The blue RGB value was increased significantly due to the blue colour of the filter. Figure 4.33 shows an increase in the blue RGB value for the non-filtered devices at approximately 500 hours. This indicates bleaching of the electrolyte as all three RGB colours are roughly equal which means the electrolyte has become

transparent. This is concordant with the drop in efficiency for unfiltered devices at the same time in the experiment. This shows that RGB imaging can be successfully used to monitor DSSC devices for degradation. The analysis of the dye has shown very little change in RGB values during exposure suggesting it remained stable, conversely the electrolyte RGB values have increased significantly indicating degradation. This indicates that the drop in device efficiency is primarily due to electrolyte degradation.

To quantify the electrolyte degradation electrolyte was extracted from the DSSC devices after light soaking. UV-Vis was run on these electrolyte solutions (Figure 4.34) and calibration curves of lithium iodide and I_2 were drawn (Figure 4.35) to determine the molar extinction coefficients. The concentration of these unknown samples could be determined by multiplying the absorbance by the molar extinction coefficient.
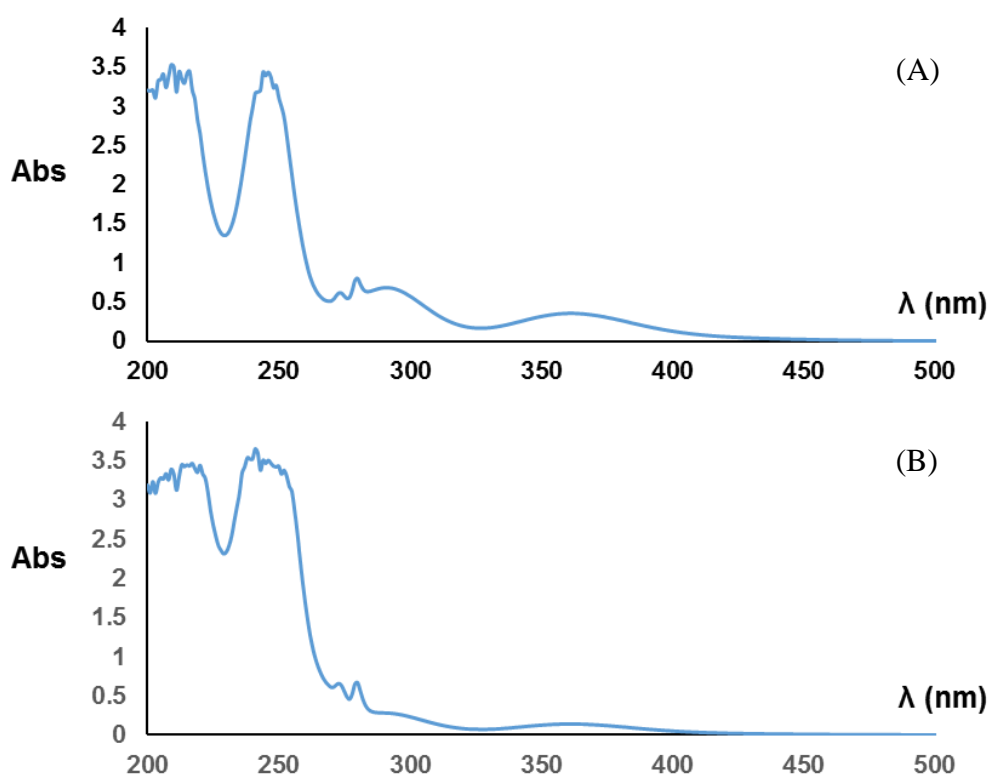
Figure 4.34 UV-Vis spectra of electrolyte extracted from devices after 2500 hours of light soaking (A) with UV filtration (B) without UV filtration. The change in peak shape at 250nm from (A) to (B) is a result of detector saturation due to a high intensity absorbance.
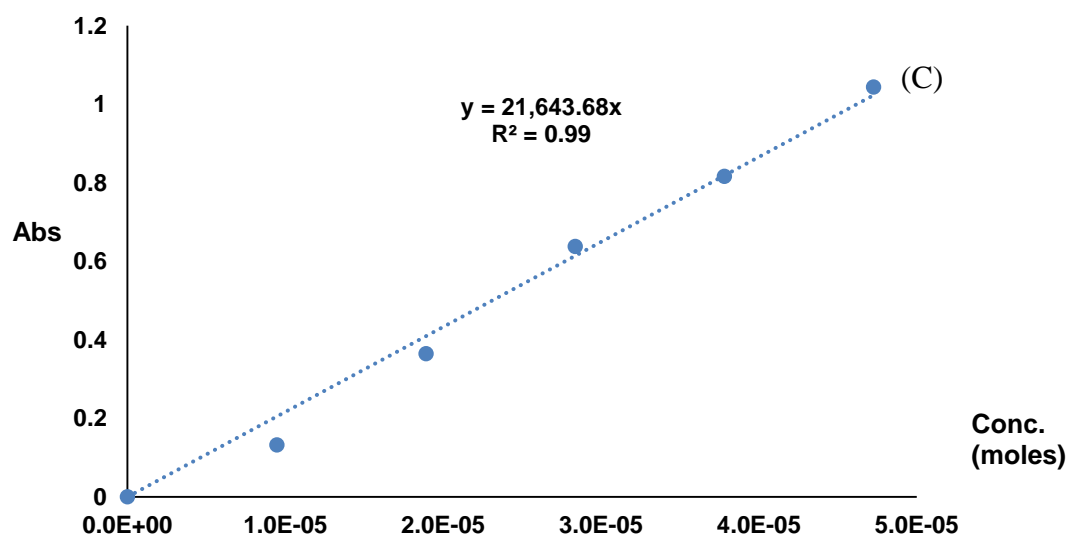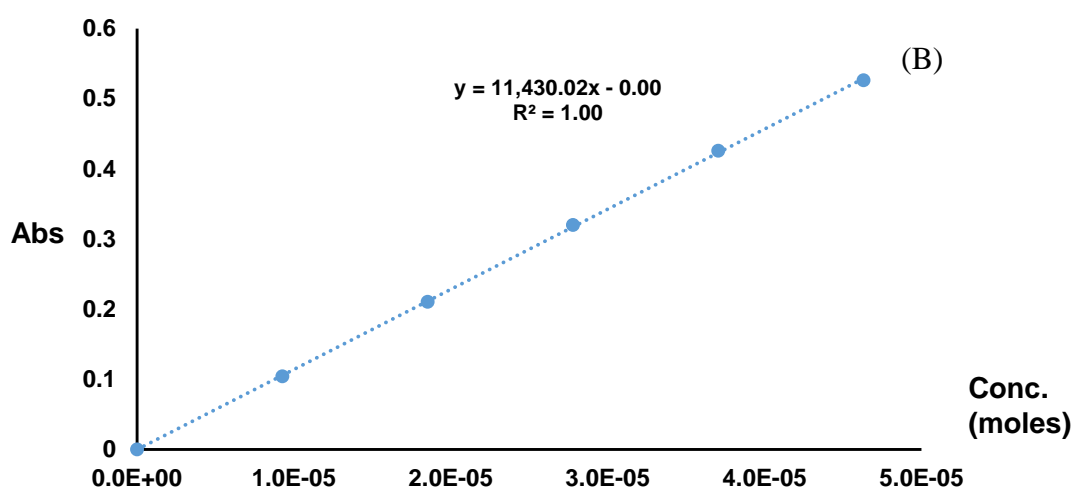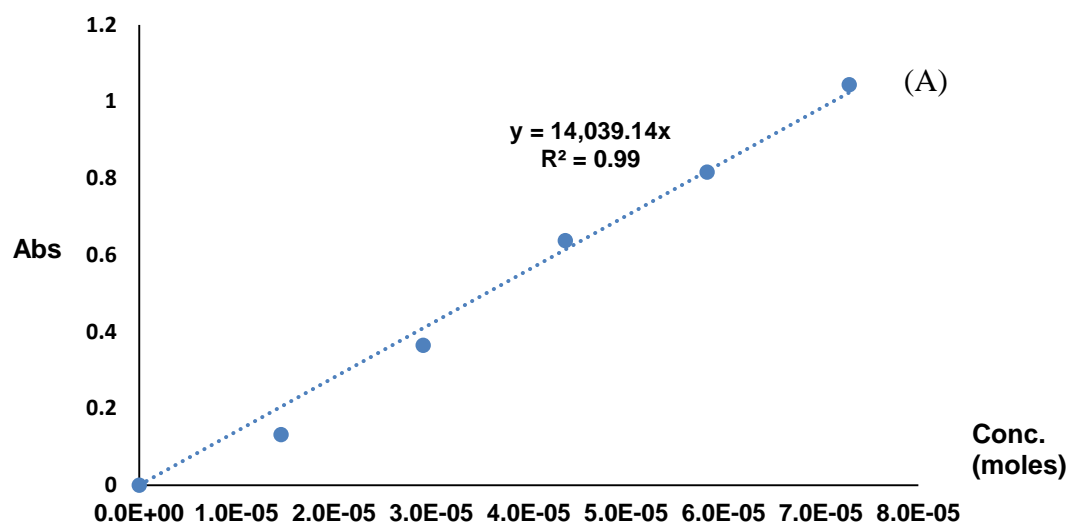
Figure 4.35 Calibration curves determined using UV-Vis spectroscopy showing (A) LiI at $\lambda_{max} = 245$ nm (B) I_2 at $\lambda_{max} = 363$ nm (C) a 1:1 mix of LiI and I_2 at $\lambda_{max} = 363$ nm.

To determine if the dye remained stable the RGB analysis was also run on the sensitised part of the cell (as shown in Figures 4.36 and 4.37).

Exposure Time (h)
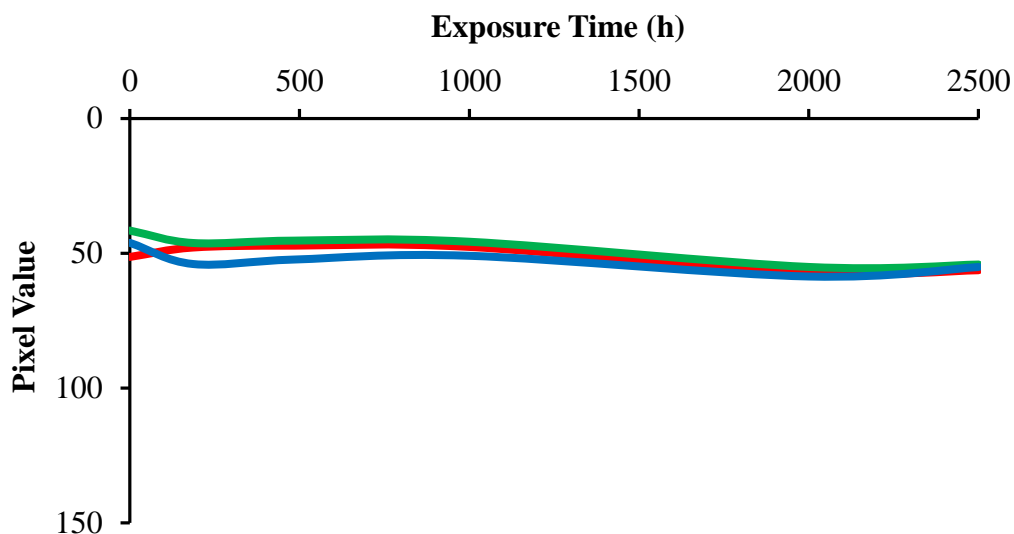
Figure 4.36 RGB values against time for N719 dye in devices with UV filtration.

Exposure Time (h)
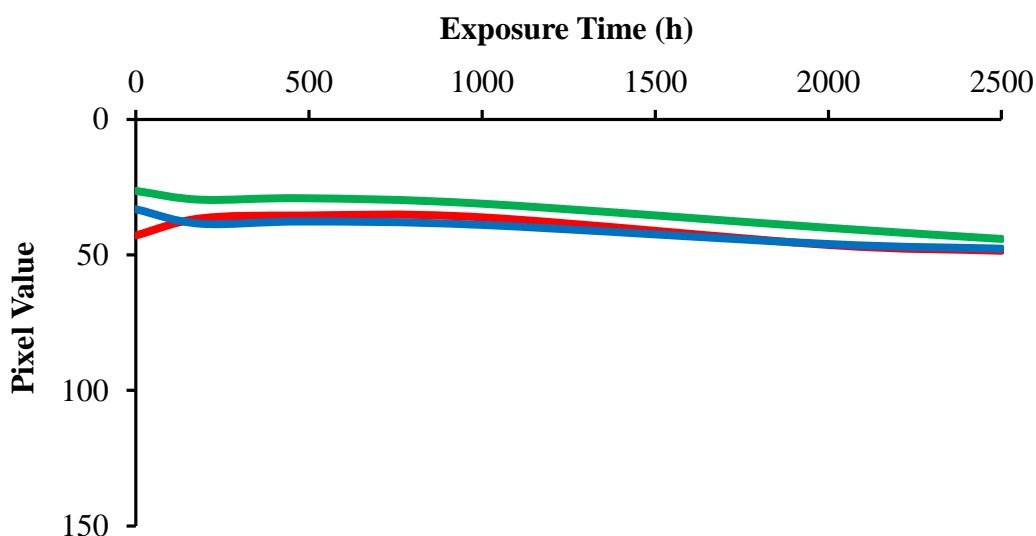
Figure 4.37 RGB values against time for N719 dye in devices without UV filtration.

Figures 4.36 and 4.37 showed the RGB analysis of the N719 dyes showed little change in colour over the experiment. Data suggests the dye has remained stable and not broken down during light soaking. To test the hypothesis, dyes were desorbed from the surface using tertbutylammonium hydroxide (TBAH) and analysed with mass spectrometry as shown in Figures 4.38 to 4.40.
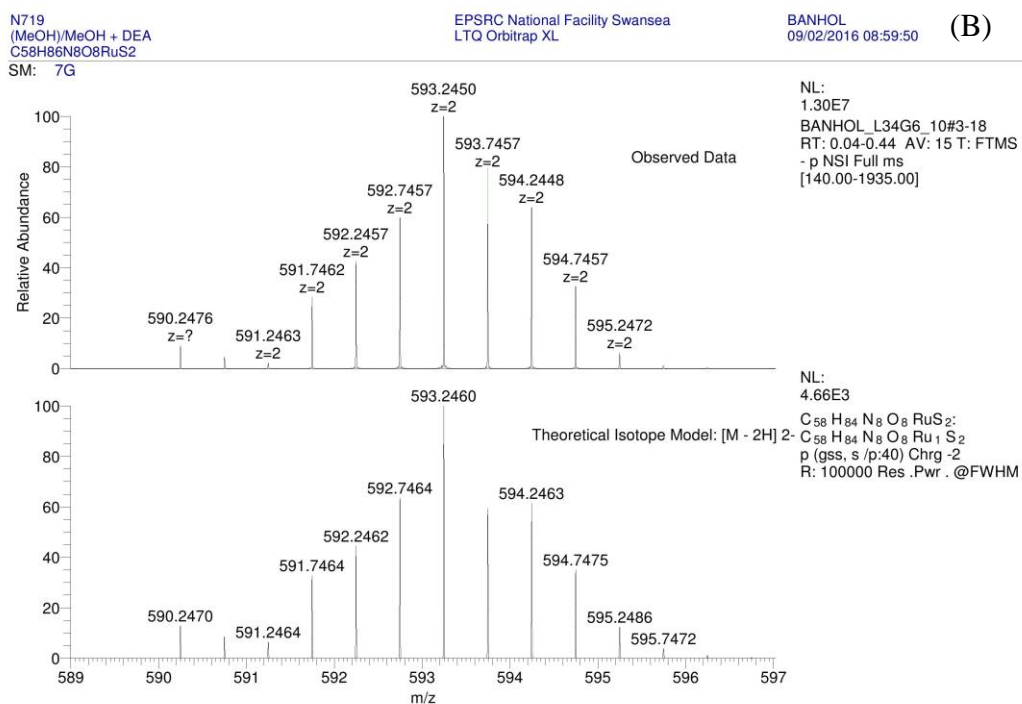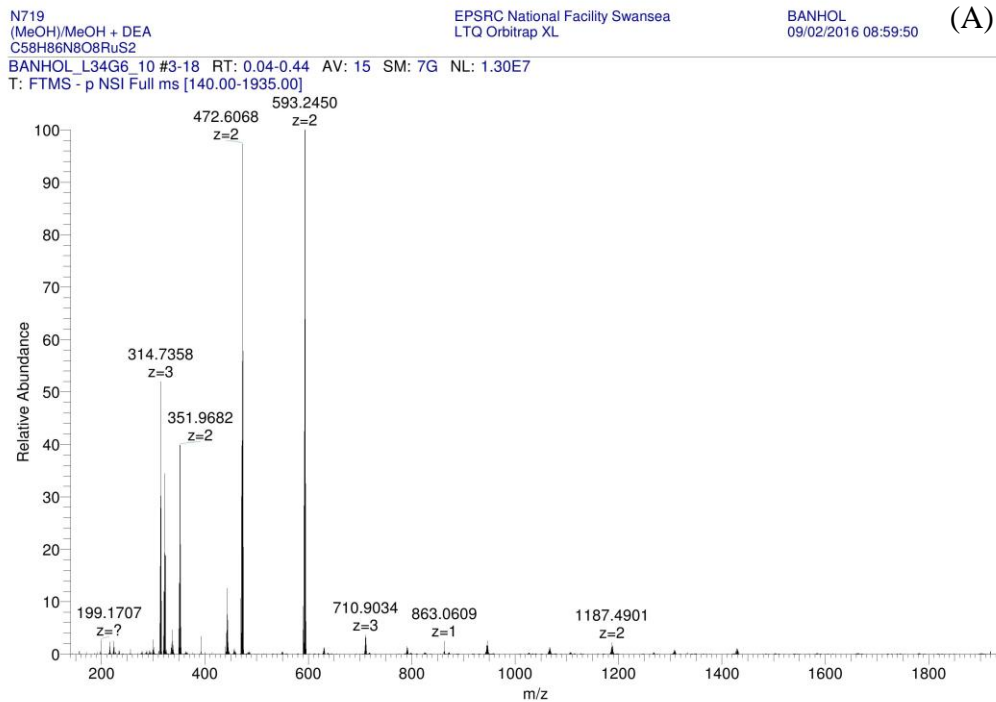
Figure 4.38 Negative Ion Electrospray Ionization (ESI) mass spectrometry data run on N719 stock crystals, this shows (A) mass range from 140 to 1935 m/z (B) isotope pattern and accurate mass showing a base peak of 593 which corresponds to half the molar mass of N719.
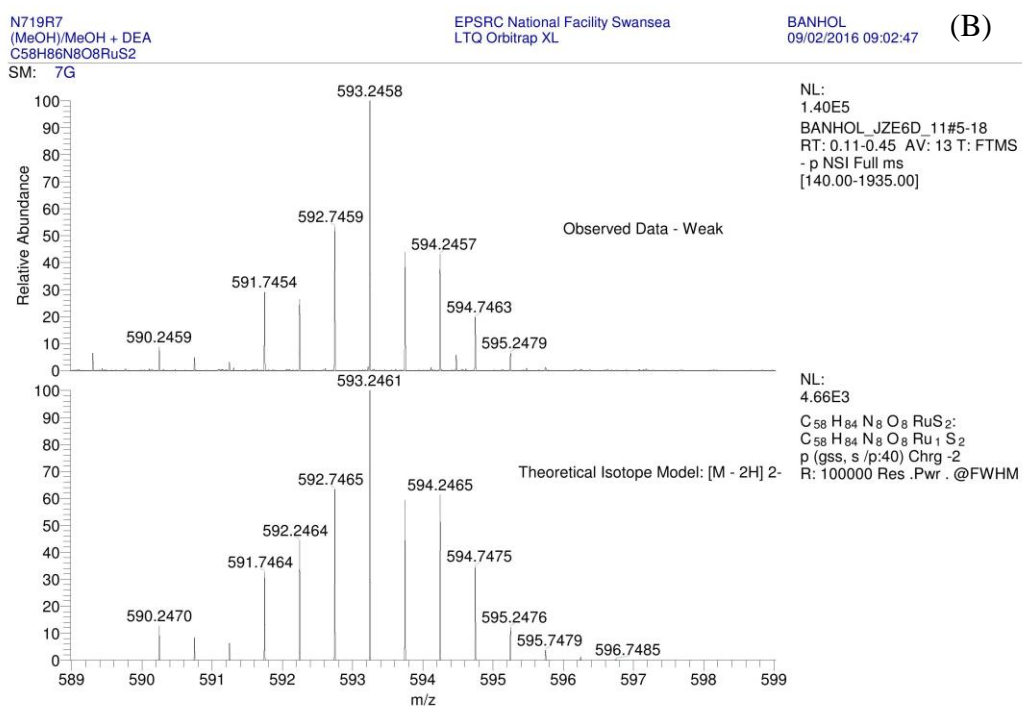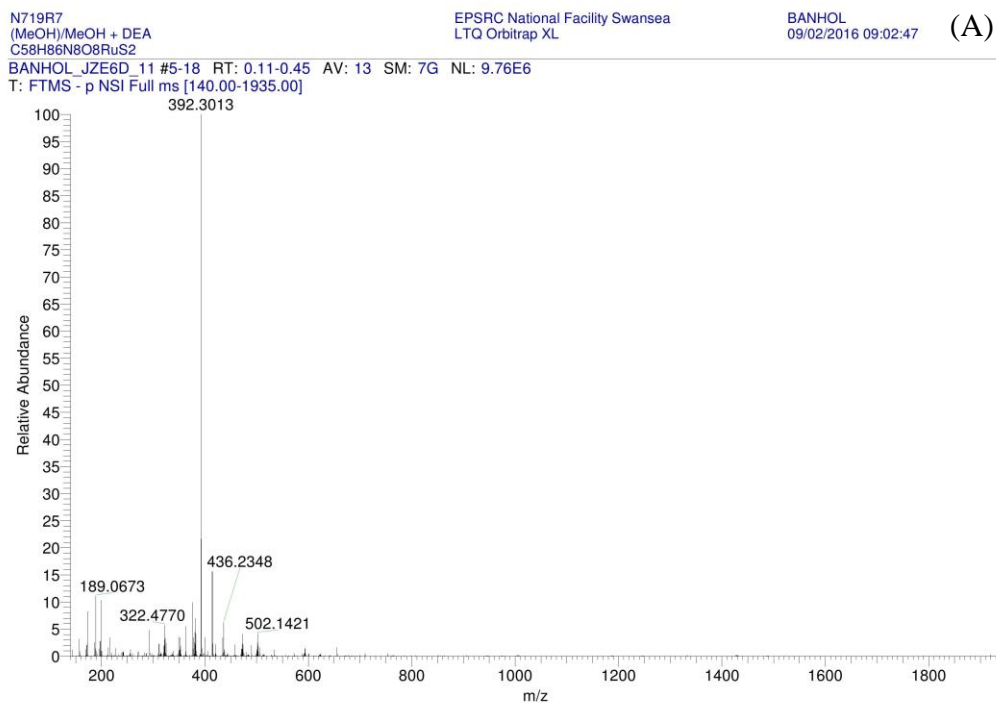
Figure 4.39 Negative Ion Electrospray Ionization (ESI) mass spectrometry data run on N719 crystals desorbed from photo electrodes after 2500 hours of light soaking with a UV filter. This shows (A) mass range from 140 to 1935 m/z (B) isotope pattern and accurate mass showing a base peak of 593 which corresponds to half the molar mass of N719.
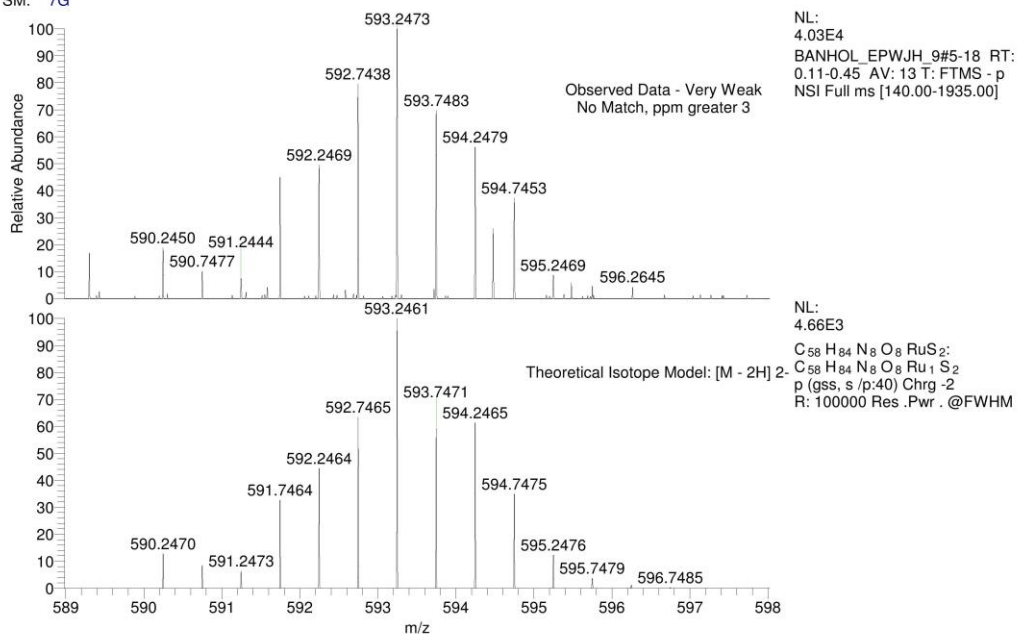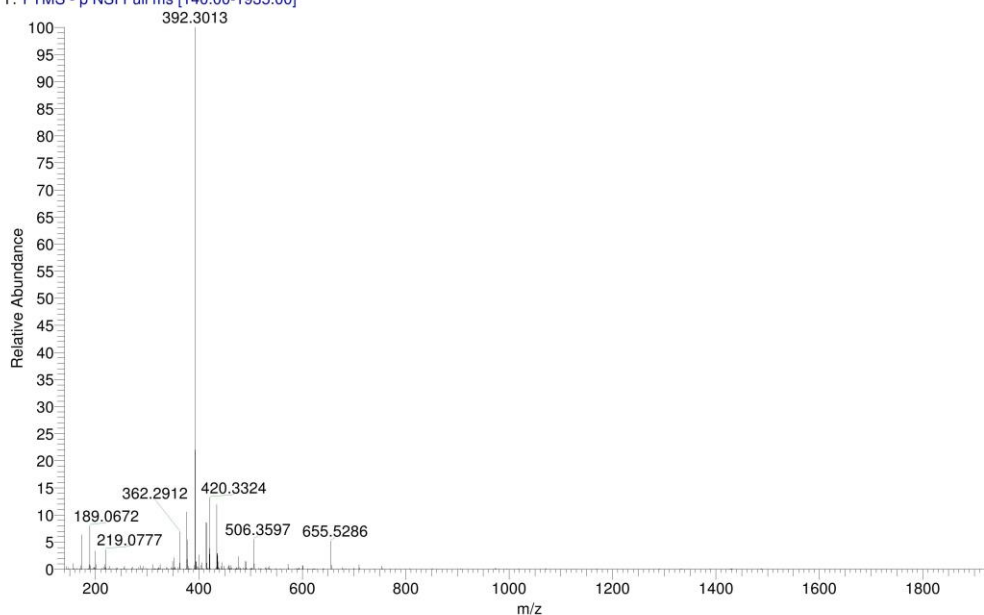
Figure 4.40 Negative Ion Electrospray Ionization (ESI) mass spectrometry data run on N719 crystals desorbed from photo electrodes after 2500 hours of light soaking without a UV filter. This shows (A) Mass range from 140 to 1935 m/z (B) Isotope pattern and accurate mass showing a base peak of 593 which corresponds to half the molar mass of N719.

The RGB analysis of N719 dye colour showed that the UV-filter made little difference due to the high stability of the dye. This was confirmed by the mass spectrometry of the stock and degraded samples which showed the same mass regardless of whether the UV-filter was used. However the UV filter significantly slowed the rate of electrolyte bleaching.

Electrolyte stability has been investigated previously by Carnie *et al.*[182] who determined that iodine based electrolytes are liable to failure when exposed to unfiltered light for an extended period. He also discovered that this degradation can be negated by applying a reverse bias across the cell which regenerated the I^{3-} ions.

The data for devices at open circuit in Figure 4.31 show an efficiency increase at 200 hours. This increase is not present in the devices which are at short circuit or under load. This is caused by the stabilisation of the cells which is normally observed during aging. It seems likely that the cells at short circuit and under load do not show this increase as it is overshadow by the efficiency drop from the degradation.

The limiting factor in the lifetime of a DSSC device is always determined by the first component to fail. UV-Vis analysis was run on the electrolytes of the devices after exposure. For the filtered N719 devices the I^{3-} concentration remained constant throughout the 2500 hours of the experiment. In contrast, the I^{3-} concentration in the unfiltered devices drops from 50 mM to 20.7 mM which is concordant with the RGB analysis.

These results confirm the literature claims that N719 is highly stable and suitable for long term light exposure in DSSC devices[176]. This also proves that RGB analysis is a suitable method for monitoring DSSC lifetimes. In addition the data show that open circuit is the most favourable setup for degradation testing.

The same experimental method was repeated to determine the stability of DSSC devices made with D35 dye. Images taken before and after exposure of the devices are shown in Figure 4.41.
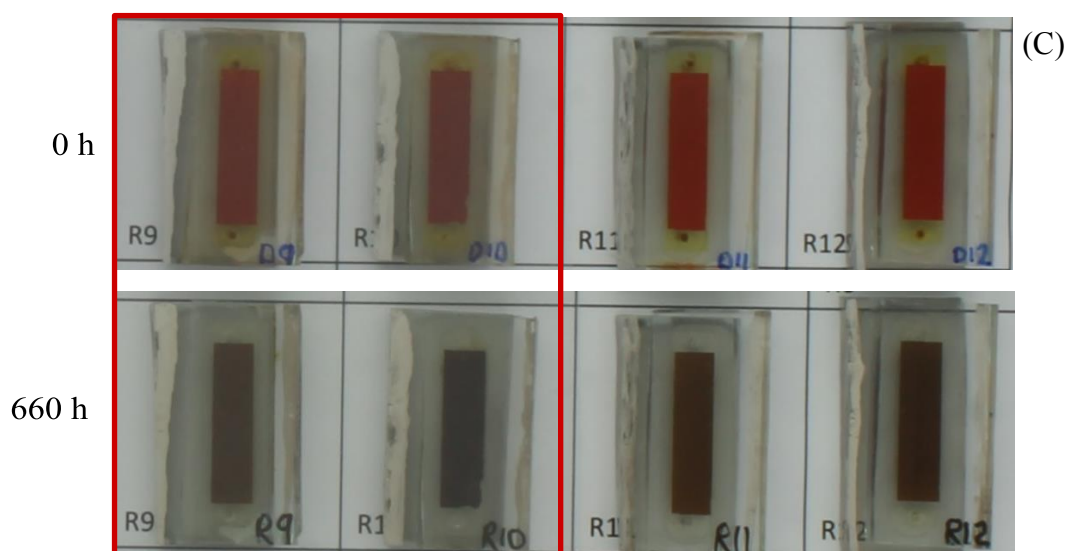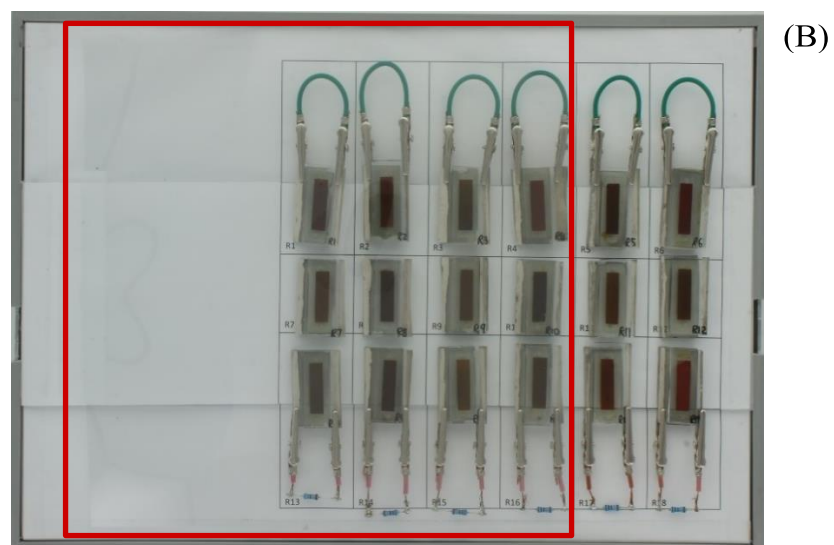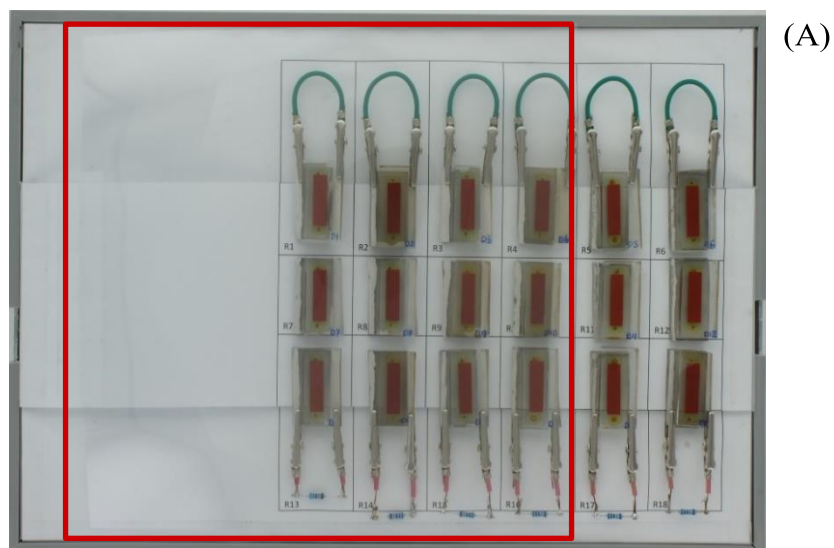
Figure 4.41 Images of D35 devices after (A) 0 h light exposure, (B) 660 h light exposure and (C) close up of images of UV-filtered and unfiltered samples showing both the D35 (red then black) and the electrolyte (yellow or transparent). The UV filter is outlined by the red box.

Figure 4.41 showed that the D35 devices darkened from red to black after the 660 hour exposure. This suggests that substantial degradation had occurred. To quantify the degradation cell efficiencies were monitored throughout the experiment, this is shown in Figure 4.42.
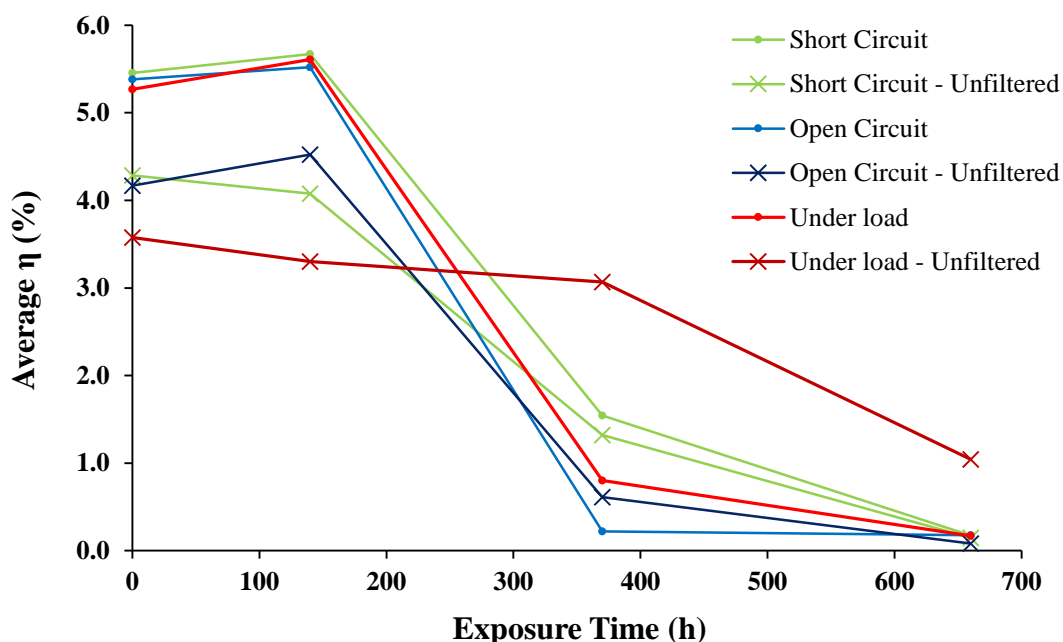
Figure 4.42 Average efficiency (η) against time for D35 DSSC devices exposed for 660 hours. Dotted lines represent unfiltered cells, solid lines were UV filtered. The electrical configuration of devices was either under load (red lines), at open circuit (blue lines) or short circuit (green lines).

Figure 4.42 shows a substantial drop in efficiency after just 370 hours. The efficiencies drop even further after 660 hours with all the cells except one under 1% efficiency. This data show that D35 devices are unstable and highly prone to degradation from light exposure.

RGB analysis was conducted on the electrolyte to determine if the drop in performance of unfiltered cells could be due to breakdown of the electrolyte. The RGB analysis of cells which had been filtered is shown in Figure 4.43.
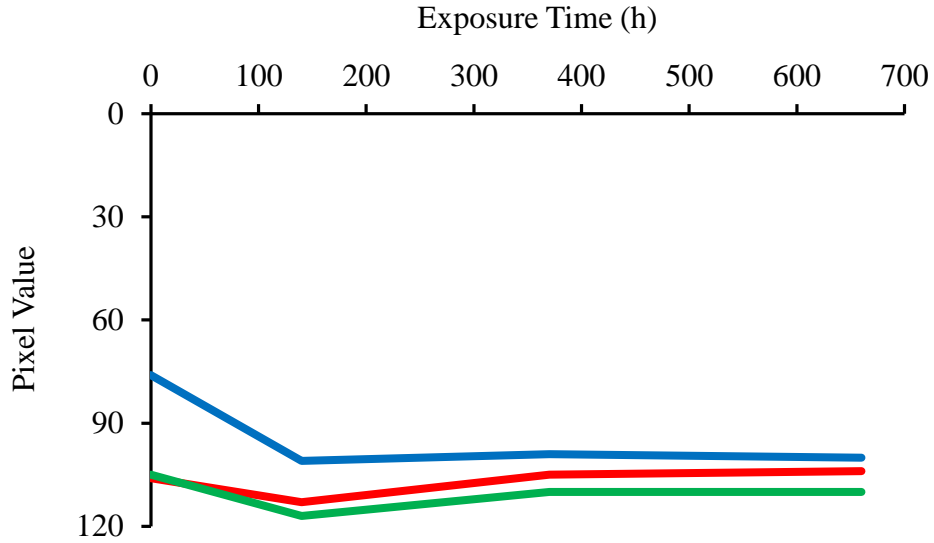
Figure 4.43 RGB values against time for electrolyte in D35 devices with UV filtration.

Figure 4.43 shows a clear loss of colour after 140 hours, indicating degradation has occurred. The RGB values become approximately equal for the remainder of the experiment suggesting that the dye has fully degraded. The devices without a UV filter were also analysed, this is shown in Figure 4.44.
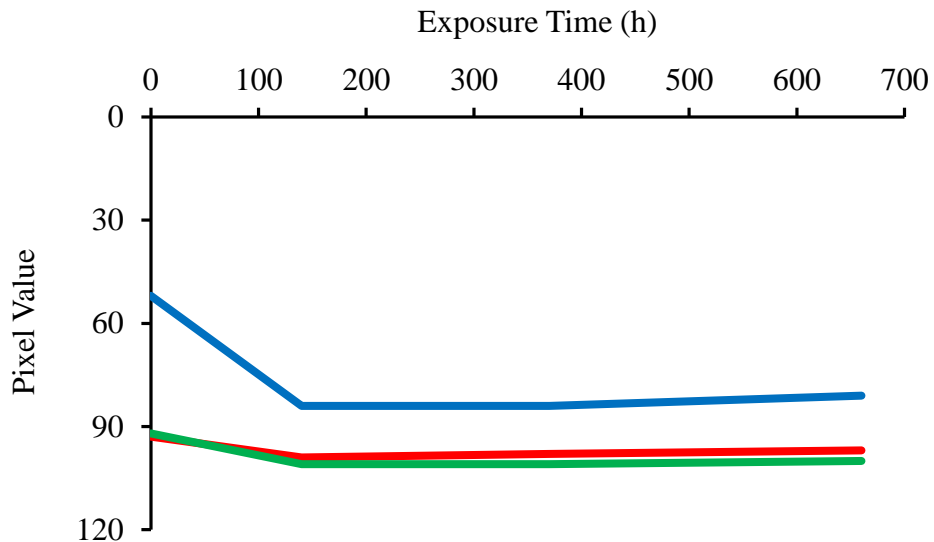

Figure 4.44 RGB values against time for electrolyte in D35 devices without a UV filter.

Figure 4.44 shows a conclusive loss of electrolyte colour after 140 hours. This shows that the electrolyte had degraded. There is negligible further colour change suggesting the electrolyte is fully degraded.

UV-Vis was used to determine the extent of the electrolyte degradation in the D35 DSSC devices, the data is shown in Figure 4.45.
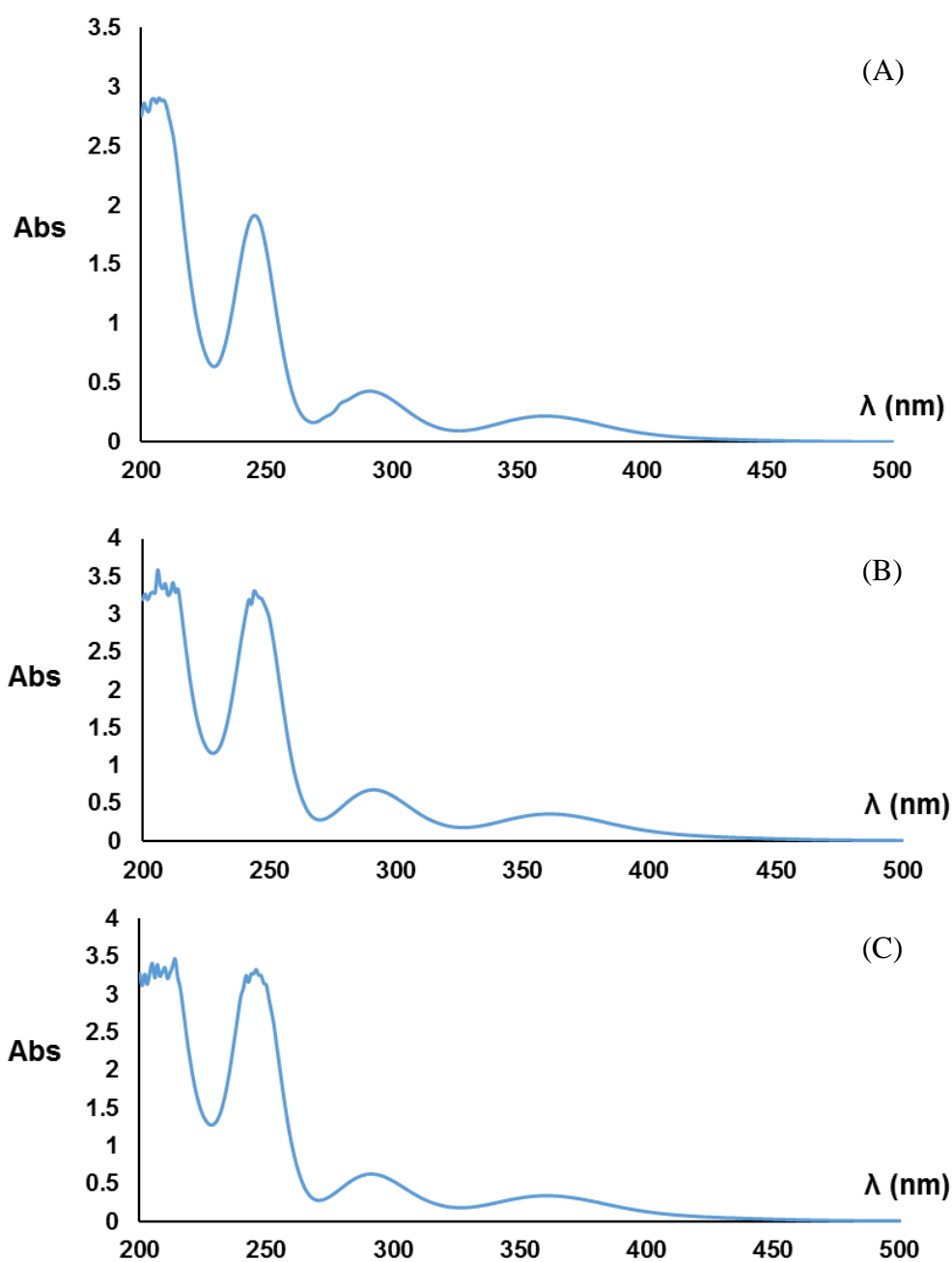
Figure 4.45 UV-Vis spectra of electrolyte (A) from the stock solution (B) extracted from devices after 660 hours of light soaking with UV filtration (C) extracted from devices after 660 hours of light soaking with without UV filtration.

Figure 4.45 shows that the electrolyte concentration did not decrease during exposure, indicating that the electrolyte remained stable.

The dye in the devices was also monitored for degradation with RGB analysis. The data for the devices with UV filtration is shown in Figure 4.46.
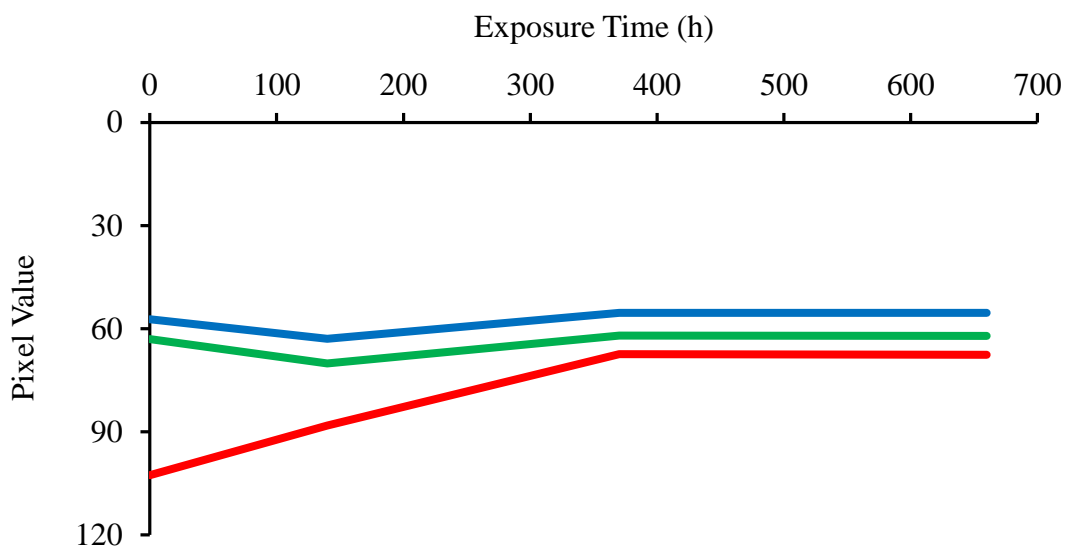
Figure 4.46 RGB values against time for dye in D35 devices with UV filtration.

Figure 4.46 shows a significant decrease in the red RGB values after 370 hours, indicating a loss of red colour from the dye. This indicates that the dye is degrading as D35 is a red dye so the cromophore must be breaking down. The unfiltered devices were also monitored by RGB analysis as shown in Figure 4.47.
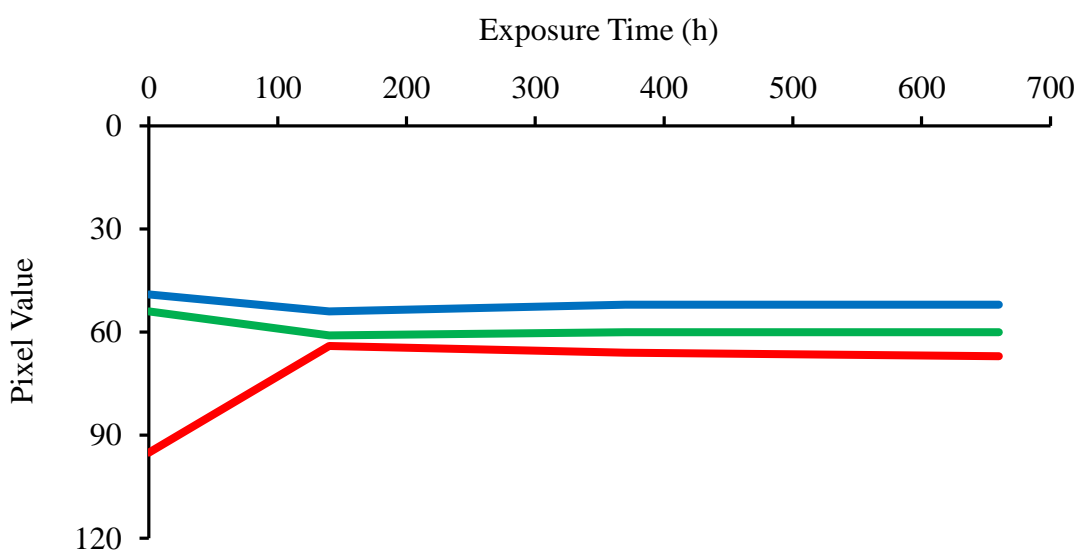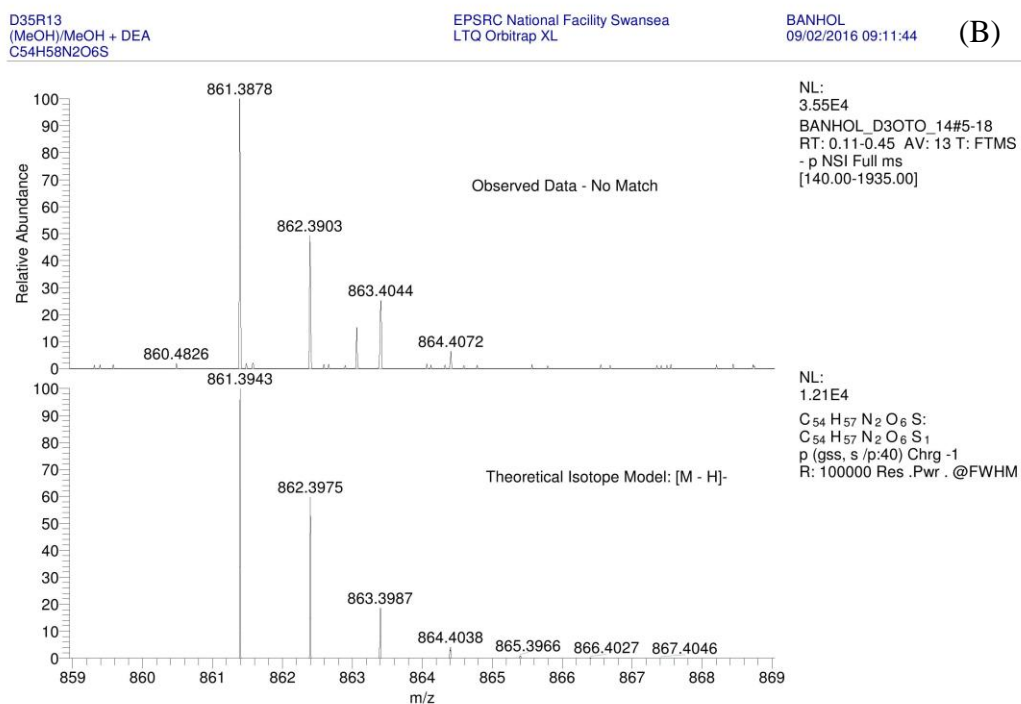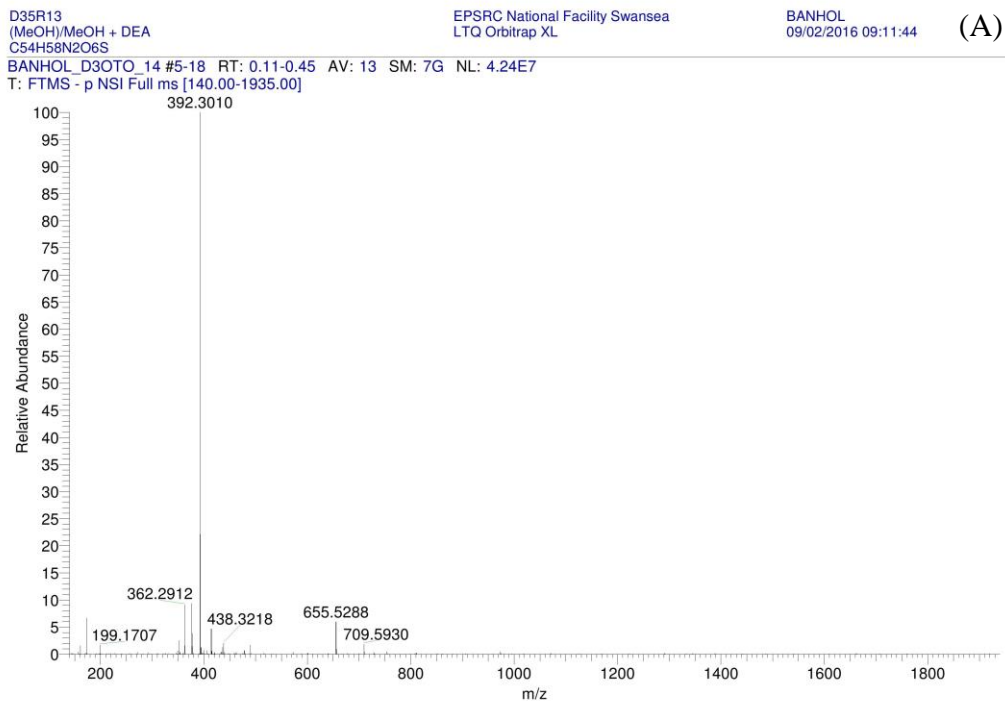
**Figure 4.47** RGB values against time for dye in unfiltered D35 devices.

Dyes were desorbed and analysed with mass spectrometry (Figures 4.48 to 4.50).
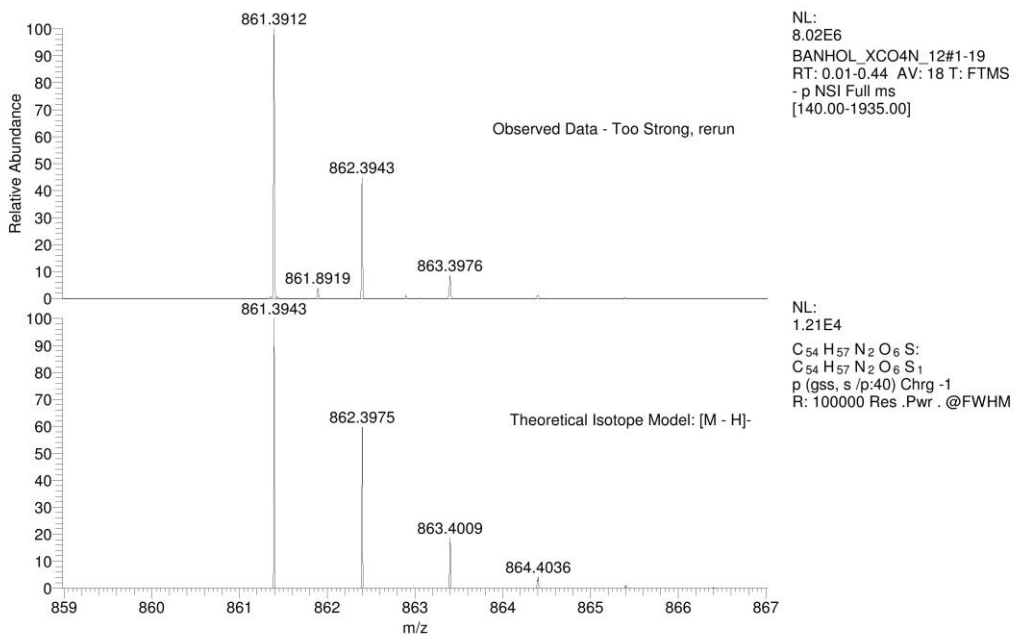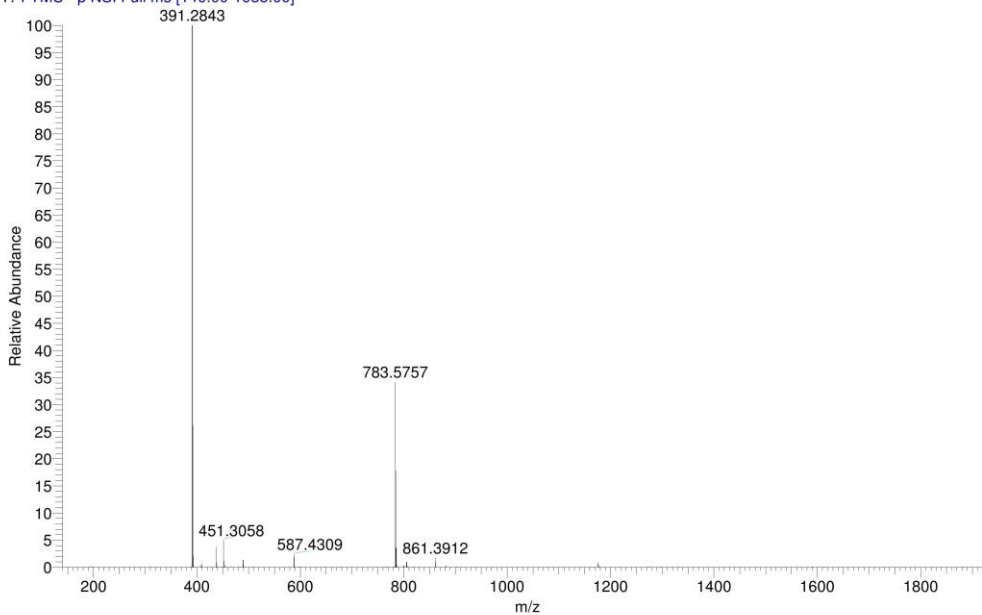
Figure 4.49 Negative Ion Electrospray Ionization (ESI) mass spectrometry data run on D35 crystals desorbed from photo electrodes after 2500 hours of light soaking with a UV filter. This shows (A) Mass range from 140 to 1935 m/z (B) Isotope pattern and accurate mass showing a base peak of 861 which corresponds to the molar mass of D35. In addition to this there are a several low intensity peaks which indicate degradation of the molecule has occurred.
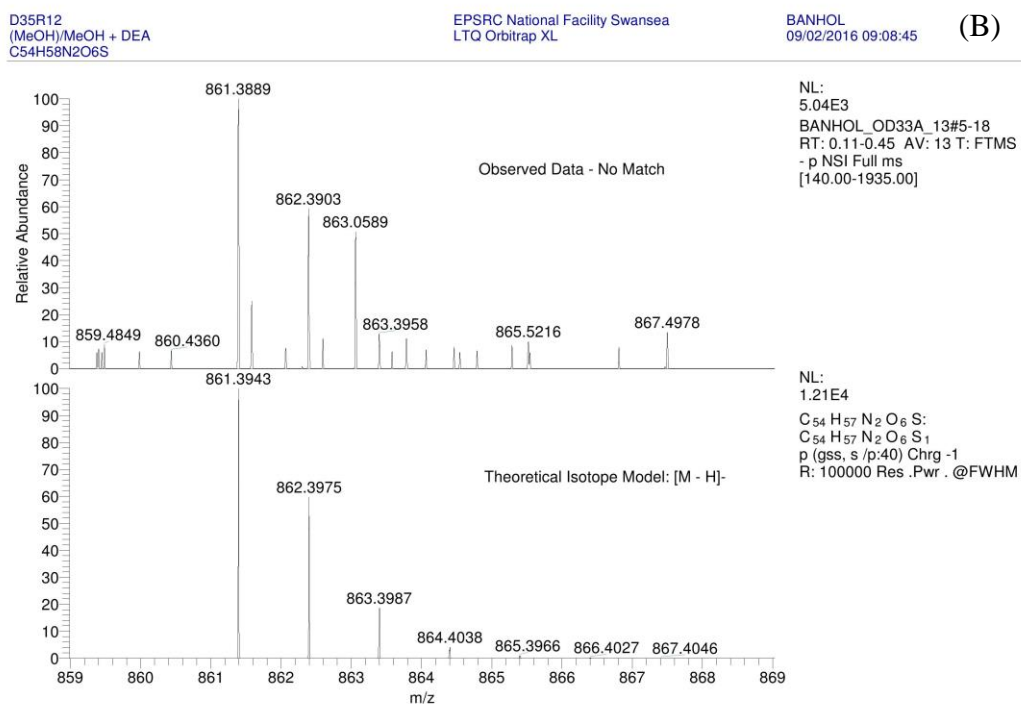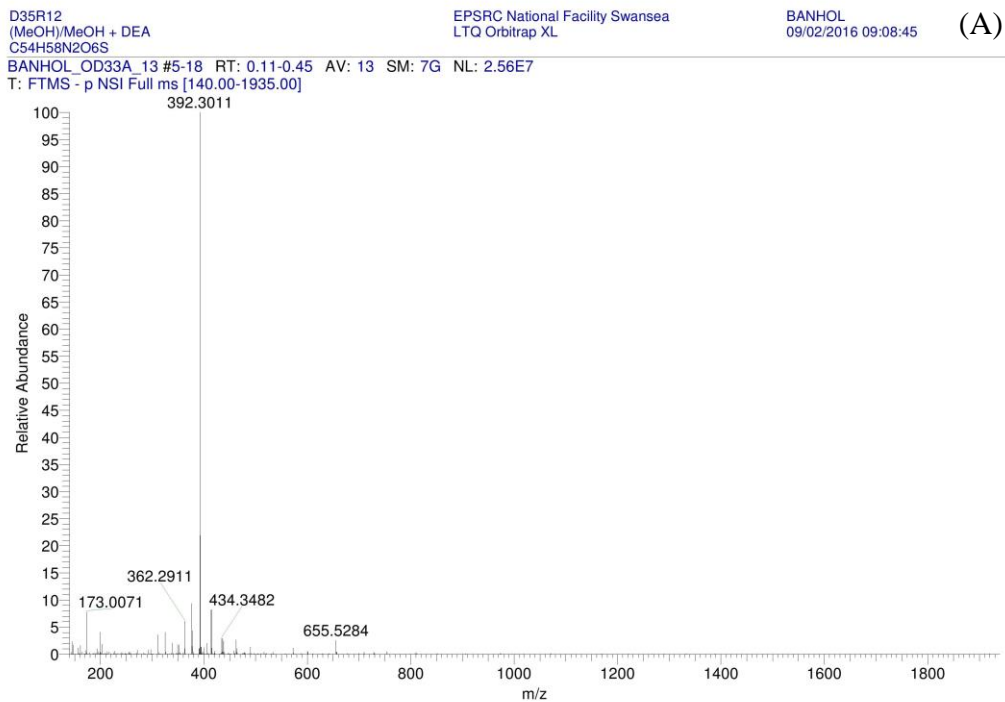
Figure 4.50 Negative Ion Electrospray Ionization (ESI) mass spectrometry data run on D35 crystals desorbed from photo electrodes after 2500 hours of light soaking without a UV filter. This shows (A) Mass range from 140 to 1935 m/z (B) Isotope pattern and accurate mass showing a base peak of 861 which corresponds to the molar mass of D35. In addition to this there are a large number of low intensity peaks which indicate degradation of the molecule has occurred.

Figure 4.47 shows a significant drop in the red RGB value after 140 hours indicating that D35 dye degrades significantly faster without UV filtration. To determine if the dye or the electrolyte was the failure mechanism for failure in the D35 cells the electrolyte was replaced and the cells were tested on a solar simulator. This data is shown in Figure 4.51.
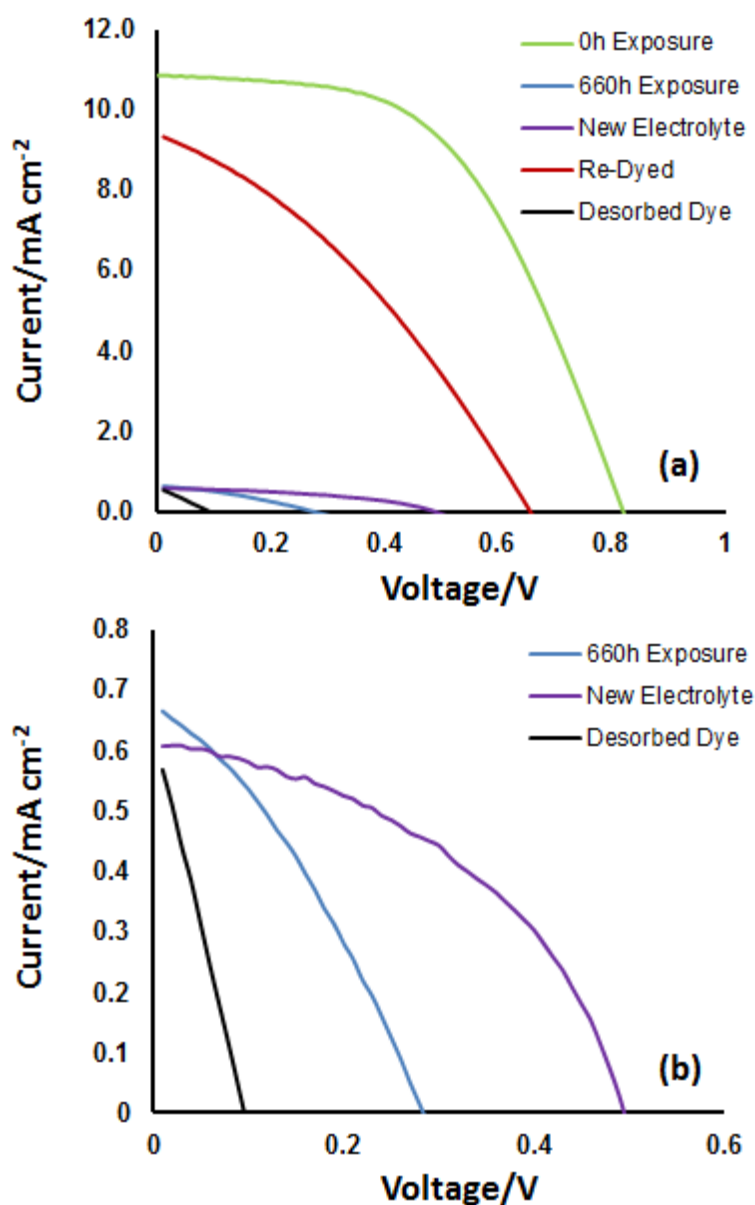
Figure 4.51 IV data of (a) the cell prior to exposure, post exposure, with fresh electrolyte, re-dyed and desorbed with TBAH (tetrabutylammonium hydroxide) (b) enlarged data of the cell post exposure, with new electrolyte and after dye desorption. The output of a current for the cell with the desorbed dye shows that there is still some residual dye on the cell but the effect of this is negligible compared to the IV curve of the original cell.

Figure 4.51 supports the theory that the dye has degraded significantly due to light exposure. Data show that replacing the electrolyte fails to restore the device to its original efficiency. In addition to this, desorption of the dye and re-dyeing of the device improves the efficiency. This suggests that the dye degradation was much more significant with regard to the drop device performance than the degradation of the electrolyte and therefore responsible for the failure of the devices.

The dye desorbed from the device after exposure was run on UV-Vis and compared to the original dye solution. This is shown in Figure 4.52.
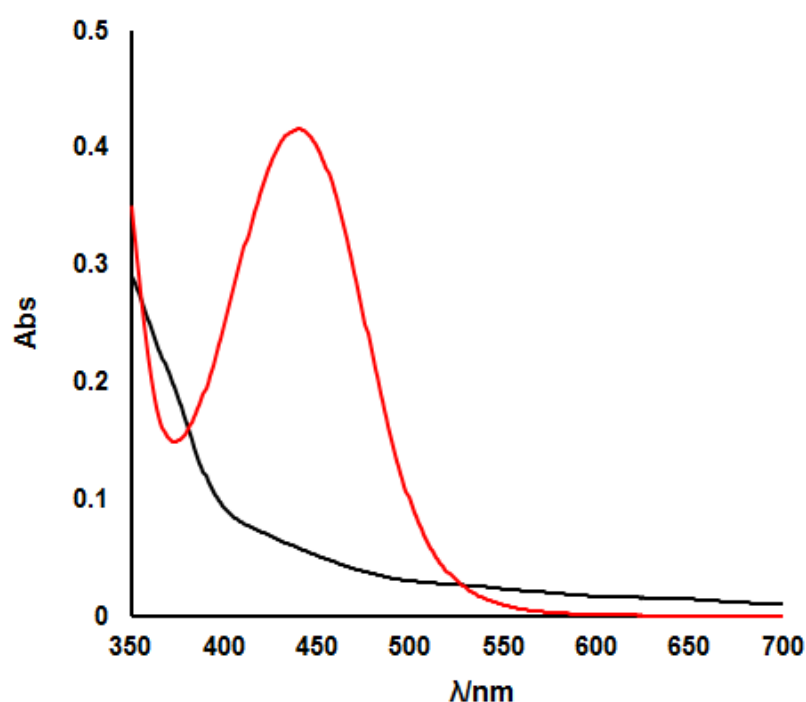
Figure 4.52 UV-vis of 0.5 mM D35 stock solution (red) and the desorbed dye from an unfiltered device exposure (black).

Figure 4.52 also supports the argument that the dye has degraded. This is indicated by the lack of a peak at 450 nm for the desorbed dye. This indicating degradation of the dye has occurred on the mesoporous TiO_2 film while inside the DSSC device.

4.7 Conclusions from Lifetime Testing of Dyes

Firstly the method to monitor the stability of dyes by image analysis has been demonstrated successfully. Dyes have been analysed while dissolved in solution and also while sorbed onto TiO_2. The stability tests in solution revealed N719 dye was the most stable without the use of additives.

The effect of dyes in solution with the addition of a radical scavenger had been investigated for the first time. After the addition of TEMP, the UV-Vis spectra of N719, D35 and D131 all showed a blue shift and a decreased intensity. This corresponded with the observed colour changes in all three dyes. The stability tests in solutions with the addition of TEMP showed highest stability in D35*. The addition of TEMP decreased the stability slightly in N719 and significantly in methylene blue. With the addition of TEMP to D35, D131, SQ1 and SQ2 an increased stability was achieved demonstrating the advantage of using TEMP with these dye solutions. This suggests free radicals are a driving force for dye degradation.

Additionally an image analysis method has been used to successfully monitor dyes sorbed onto TiO_2. Camera imaging has been optimised to obtain data witha high accuracy giving error to as low as ±1 pixels. On TiO_2 films SQ1 showed poor stability under artificial light with the film bleaching after 2 hours. In the same setup SQ2 showed a significantly higher stability with 3 hours before the film had bleached significantly. N719 showed excellent stability with only a slight fading after 4 hours light soaking.

Device data for N719 also showed good stability with negligible degradation after 2500 hours for cells at open circuit with UV filtration. The failure mechanism was determined to be the due to degradation electrolyte which was caused by UV exposure.

Conversely, D35 showed very poor stability with cells significantly degraded after 370 hours and fully degraded after only 660 hours. The analysis determined that the failure mechanism for D35 cells is degradation of the dye as opposed to the electrolyte in N719. This has shown that N719 dye has far greater stability than D35 in DSSC devices and would be more suitable for long term exposure.

Chapter 5 Ultrafast Dye Uptake

5.1 Introduction

In order to viably manufacture DSSC devices, processing times and costs must be kept to a minimum. A substantial cost of DSSC production is of the dye used to sensitise the device[32]. One way to reduce the overall cost of the dye is to use the minimum amount to sensitise the device. Using the optimum dye loading on devices also gives the advantage of an increased current. However too much dye on the surface can cause aggregation which reduces photocurrent.[183] In this situation, dye molecules attach to ones already sorbed onto the TiO_2, absorbing light but not injecting electrons into the TiO_2. A lack of dye on the surface also reduces the current produced by the cell as fewer dye molecules would be available for excitation and thus there would be less electron injection. To measure the loading of the dye on the cell a base (e.g. NaOH) can be used to remove dye from the surface of the electrode. This can be a useful way of measuring dye loading but requires disassembly of the device. Instead a way of measuring device dye loading in situ would be advantageous.

To do achieve in situ-testing, digital image analysis can be used to measure the colour intensity of the electrode. The intensity can then be measured during dye uptake and the process can be stopped once the optimum level has been reached. This chapter describes studies of RGB analysis where the digital red, green and blue values of pixels on images are each ranked out between 0 and 255 with 255 being the highest intensity. Once the device has been fully loaded, the colour of the cell should no longer change. The work will also consider if dye aggregation will result in a further colour change. This would be determined by whether saturation was reached with a monolayer where a single layer of dye covers the TiO_2, or if additional dye molecules stack on top of dye molecules already sorbed to the TiO_2.

A fast dye process needed to be developed to achieve low processing times. To develop a fast dye process, a peristaltic pump was chosen where the moving parts of the pump did not directly come into contact with the dye. The use of a peristaltic pump was to avoid contamination between different dyes and the corrosion of the pump components due to the acidity of the dye. A cell holder was then constructed using a transparent sheet of Perspex with an aluminium backing as shown in Figure 3.12. The Perspex cell

holder was used initially but was not ideal as the true colour of the dye appeared to be changed by the colour of the Perspex and the seals/aluminium behind. Hence the cell holder was modified by cutting it into two separate sections which left a large gap in the centre for observation, as shown in Figure 3.13. Thus allowing the cell to be analysed without its colour being influenced by the cell holder, allowing for a more accurate analysis. Another advantage of the new cell holder was to allow larger cells to be fast dyed. The development of the fast dye process is shown in Figure 5.1.
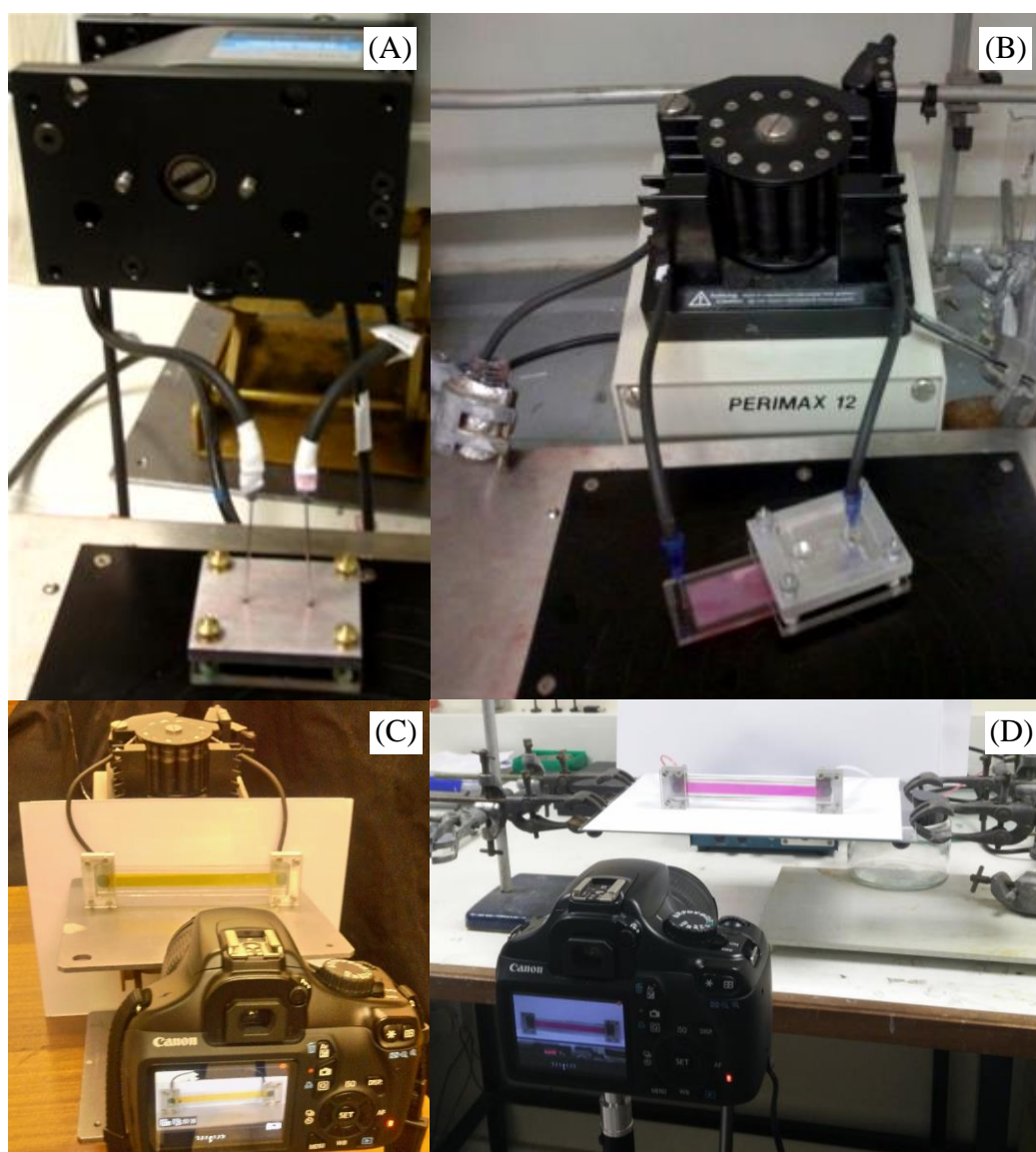
Figure 5.1 The development of the fast dye process. (A) The initial setup with the original cell holder where dye was repeatedly circulated through the cell, this had the disadvantage of decreasing dye concentration over time. (B) The second setup with the original cell holder which allowed dye to pass through the cell and out into waste, avoiding recirculation. (C) The first setup with the modified cell holder, allowing large devices to be fast dyed. (D) The final setup where a white card background was used with lighting to reduce errors, note that in this setup the dye was not recirculated.
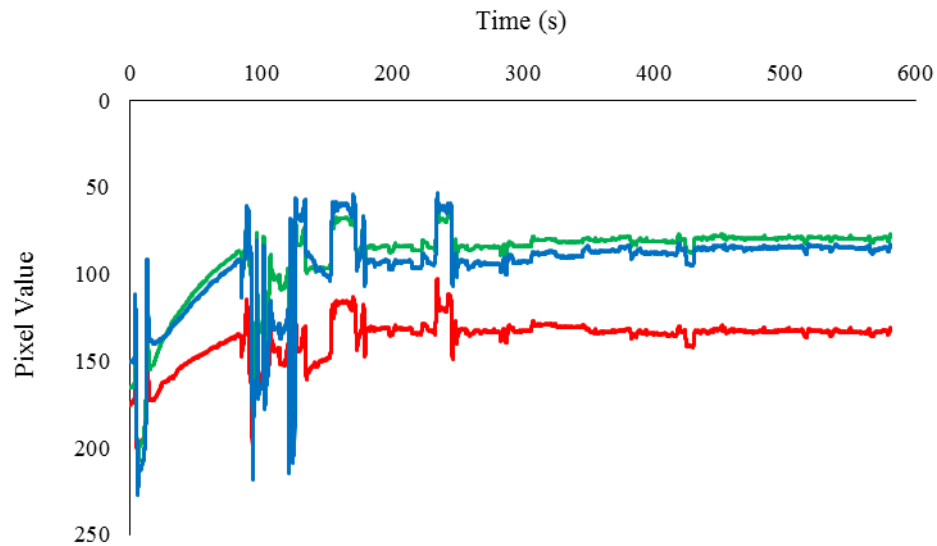
5.2 N719 Dye Analysis on Active Opaque Paste

N719 dye is widely considered an industry standard[184] for use in DSSC devices due to having high efficiency[185] and good stability[176]. It is therefore a likely option for industrial upscaling of dye sensitised solar cells and an ideal starting point for analysis. The Dyesol active opaque paste was used for the construction of this device. Image analysis to determine red, green and blue colour levels was conducted on the left and right side of the cell and an area below each one was also analysed to determine the variation in light levels (method as described in section 3.42). Images taken at the start and finish of the sensitisation process are shown in Figure 5.2.
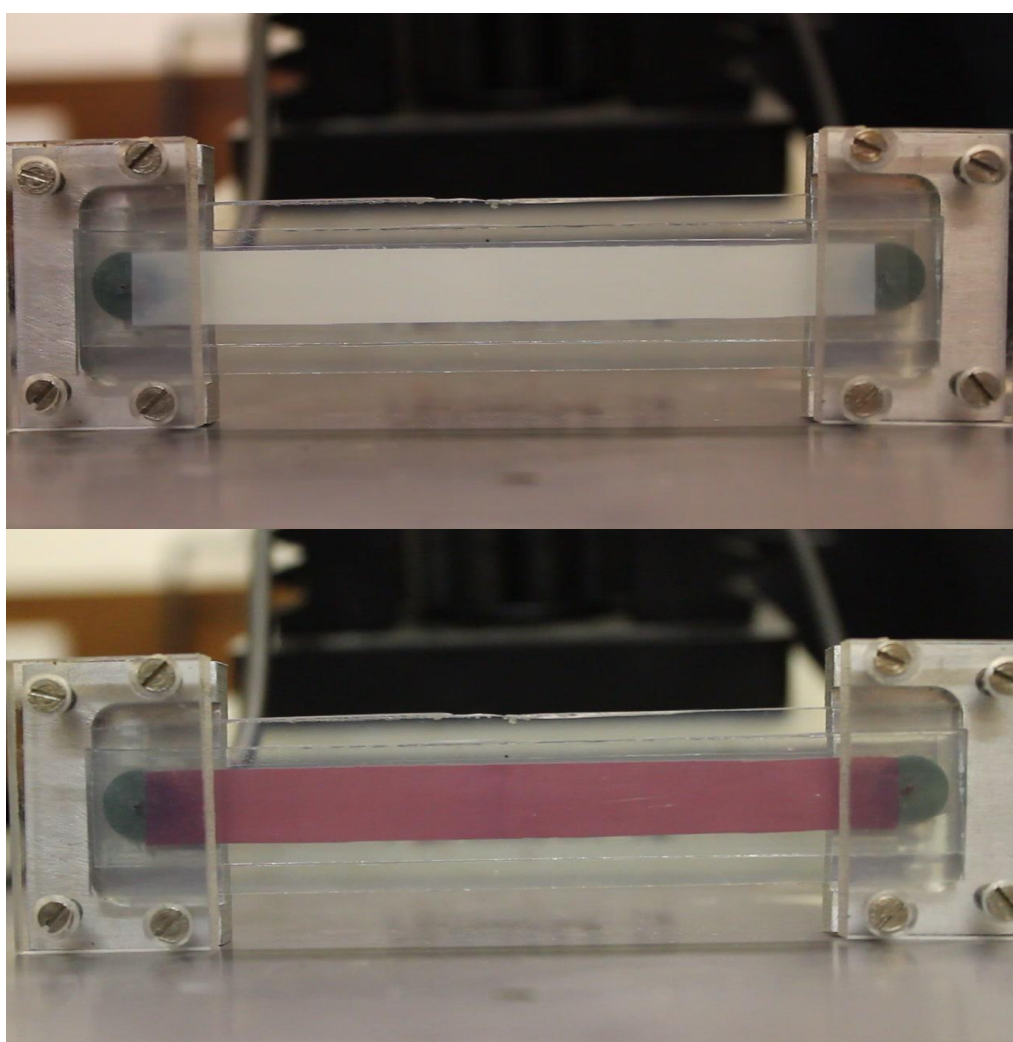

Figure 5.2 Images of the device before sensitisation (Top) and after pump dyeing with N719 (Bottom) on active opaque.

The images were analysed using a macro to determine RGB colour data. The data from the image analysis was then plotted on two separate graphs. The dye intake was on the left side and the outtake was on the right side. The data for the left and right side RGB analysis is shown in Figure 5.3 and Figure 5.4 respectively.
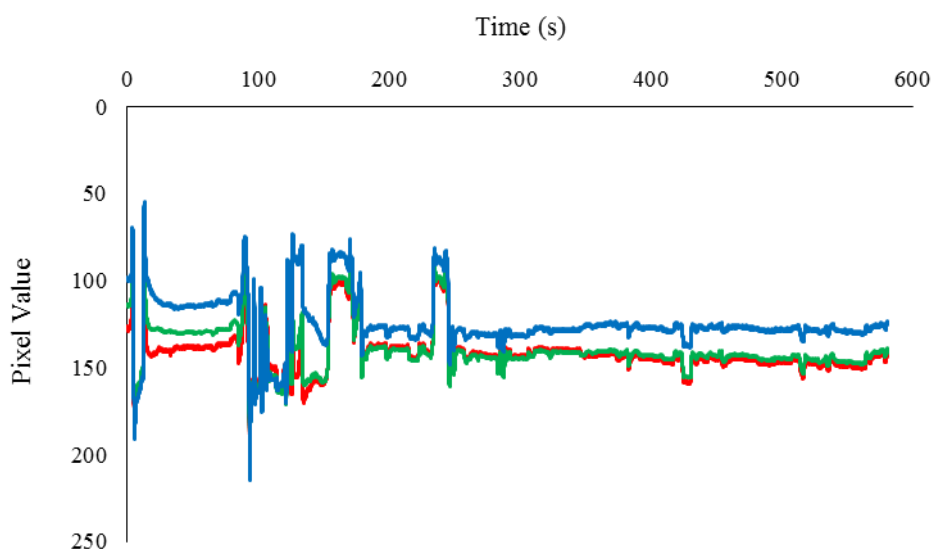

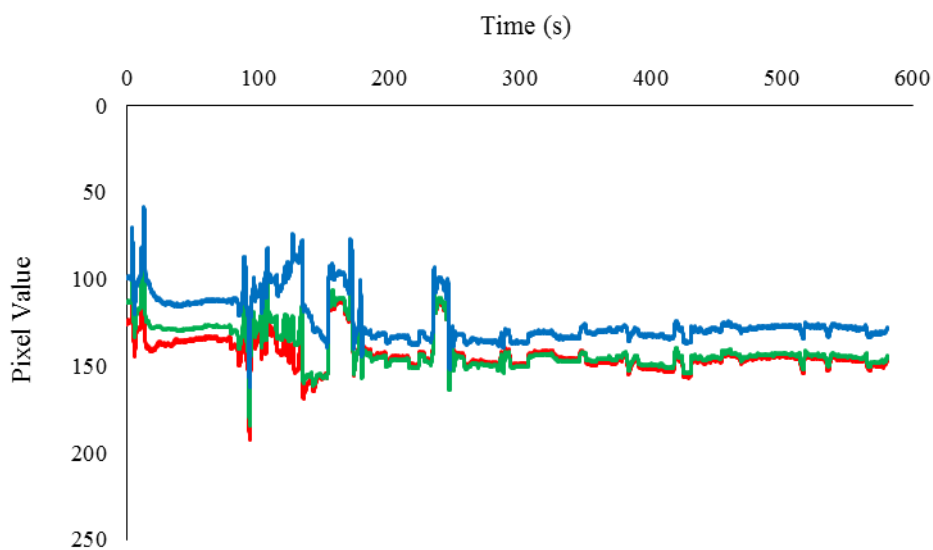**Figure 5.3** Left side RGB analysis for N719 dye uptake on active opaque paste.
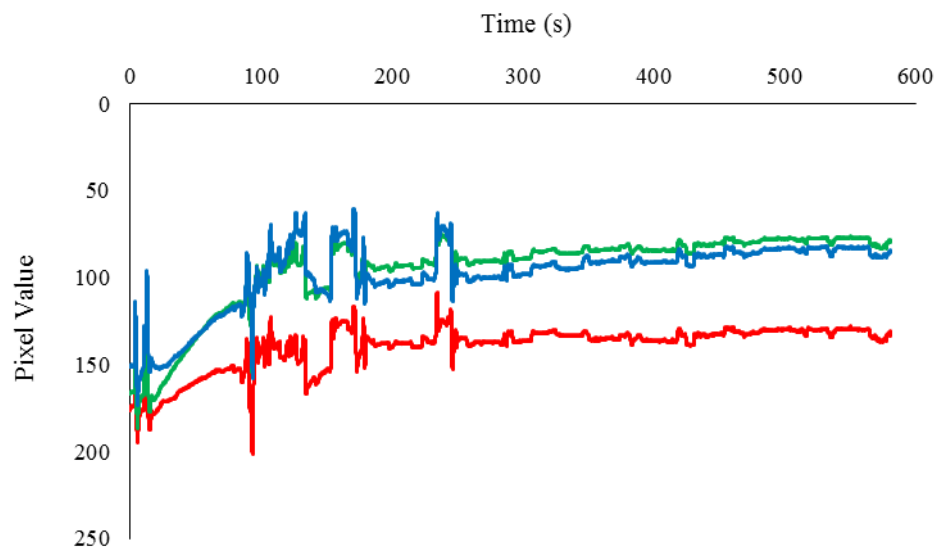
Figure 5.4 Right side RGB analysis for N719 dye uptake on active opaque paste.

The two graphs show gradual dye uptake in the first 200 seconds, before levelling out. However spikes in intensity are present which are caused by significant changes in light levels. The sudden changes in light levels are due to the door to the room being

opened and closed. To reduce this error a control was taken on each side of the cell on the glass below the TiO_2. The control should have remained constant throughout the experiment as only the TiO_2 had changed colour. Therefore any changes to the control were due to differences in light levels and can therefore be deducted from the uptake data. The data for the control analysis was then plotted, showing the changes in light levels at each side of the cell. The data for the left and right side RGB analysis is shown in Figure 5.5 and Figure 5.6 respectively.

Figure 5.5 Left side control image analysis for N719 dye uptake on Active Opaque paste.


Figure 5.6 Right side control image analysis for N719 dye uptake on Active Opaque paste.

These data show there is both positive and negative noise on the data. To remove the noise from the original data the deviation of the control data must be calculated and then subtracted. The mean deviation will be used instead of standard deviation as it is more appropriate when adjusting for measurements made in error[186], such as from a sudden spike in light levels. The mean deviation can be calculated using the following formula:

$$D_i = x_i - m(X)$$

Where D_i is the mean deviation, x_i = RGB value and $m(X)$ = average control value. The mean deviation of the control data was then calculated and plotted as shown in Figure 5.7 and Figure 5.8.
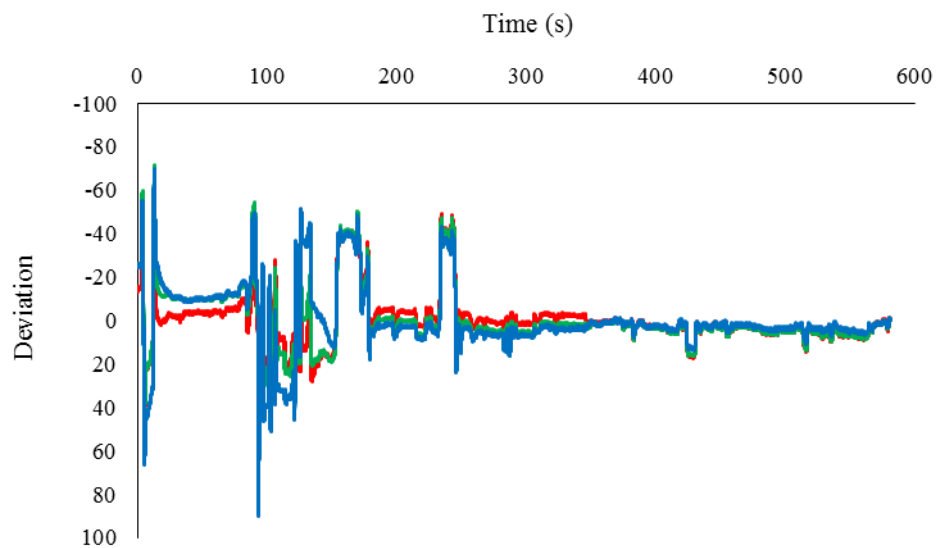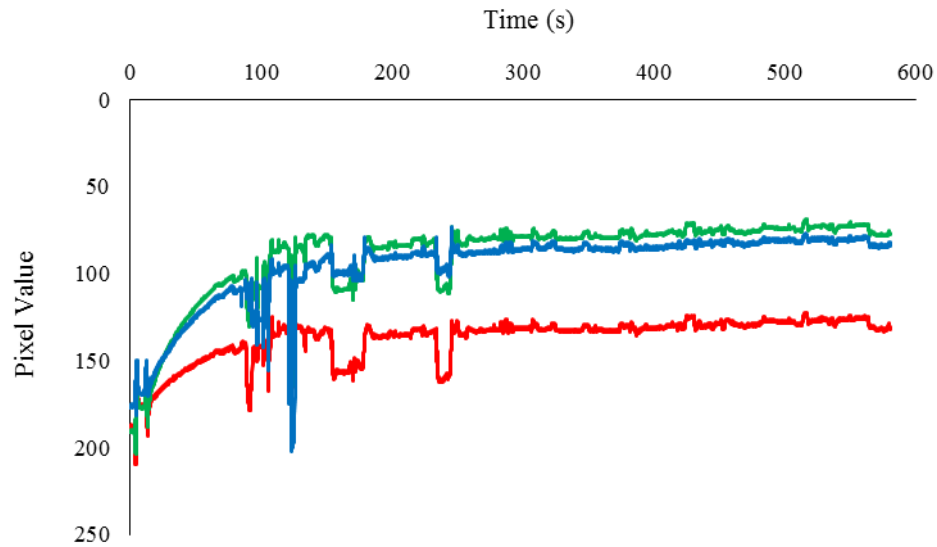

**Figure 5.7** Left side control mean deviation for N719 dye uptake on Dyesol Active Opaque paste.
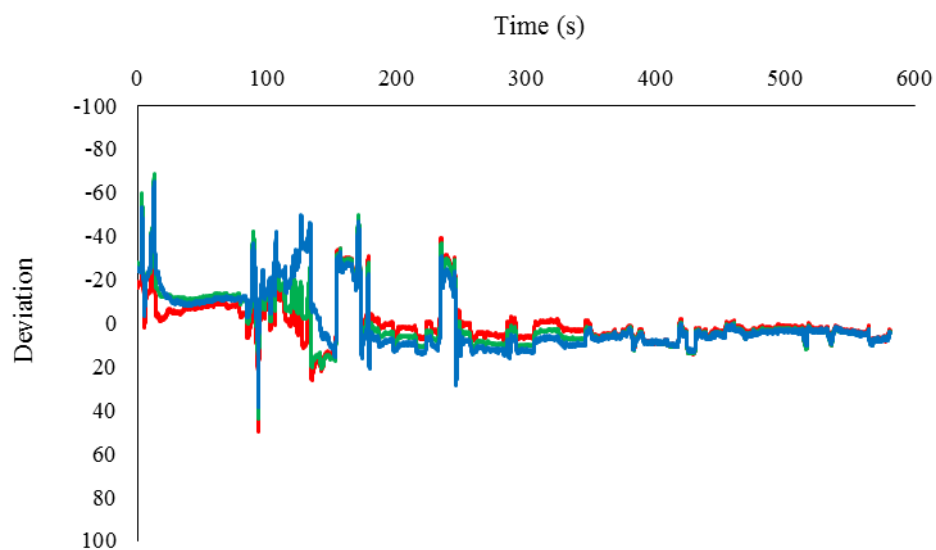
Figure 5.8 Right side control mean deviation for N719 dye uptake on Dyesol Active Opaque paste.

The mean deviation could then be subtracted from the original data value to reduce the noise from light level changes as shown in Figure 5.9 and Figure 5.10.

Figure 5.9 Left side image analysis of N719 with noise reduction.
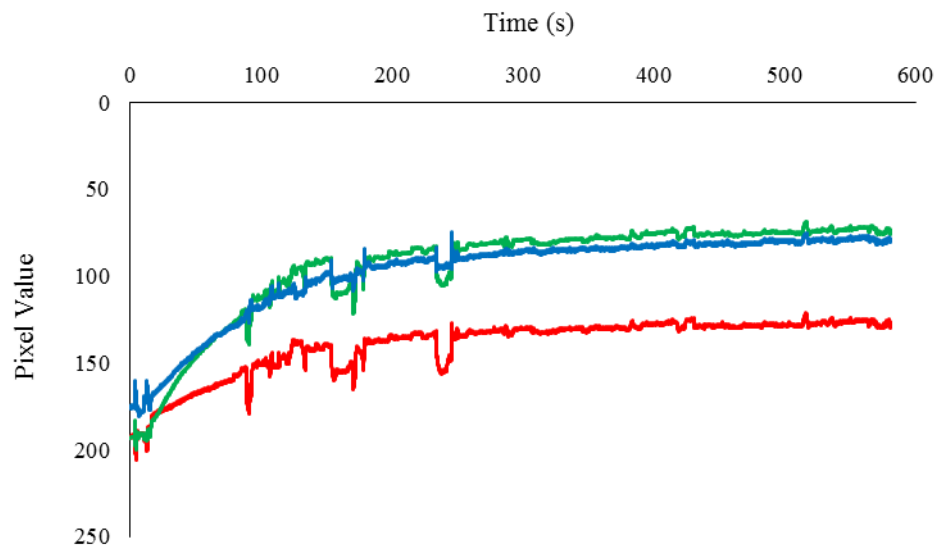

Figure 5.10 Right side image analysis of N719 with noise reduction.

The error reduction technique appears to have significantly reduced the noise compared to the original RGB data. Interestingly the right side of the image shows lower variation than the left one. This may be because the left side was closer to the door so was affected more by the sudden increase in light levels from the door being opened. Ideally a separate room could be set up for image analysis where recordings could be made in a controlled environment.
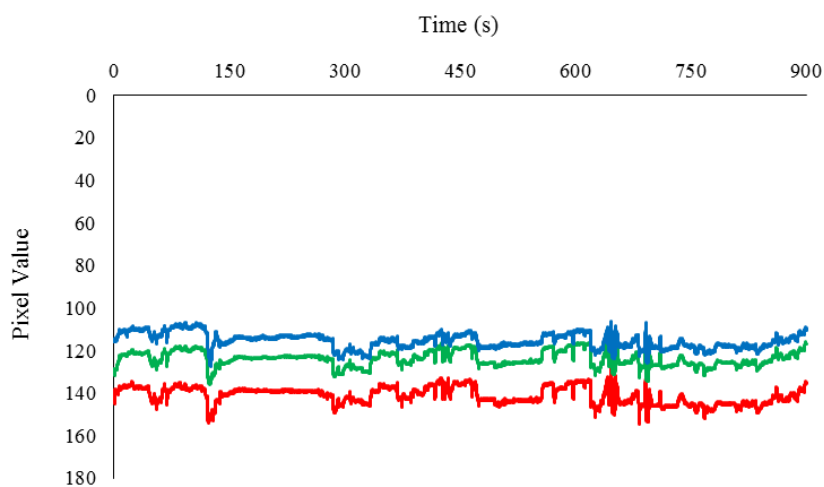
5.3 N719 Dye Analysis on 18NRT Paste

The dye uptake of N719 dye was also analysed with Dyesol 18NRT paste. This was so that a comparison could be made between the two pastes. The 18NRT is purposely designed to be transparent so the colour changes from dye uptake were more subtle compared to the active opaque paste. It is important that image analysis is also possible for a transparent type of paste, as they can be used for specialist DSSC devices, such as for transparent photovoltaic windows[187]. Images taken at the start and finish of the sensitisation process are shown in Figure 5.11.
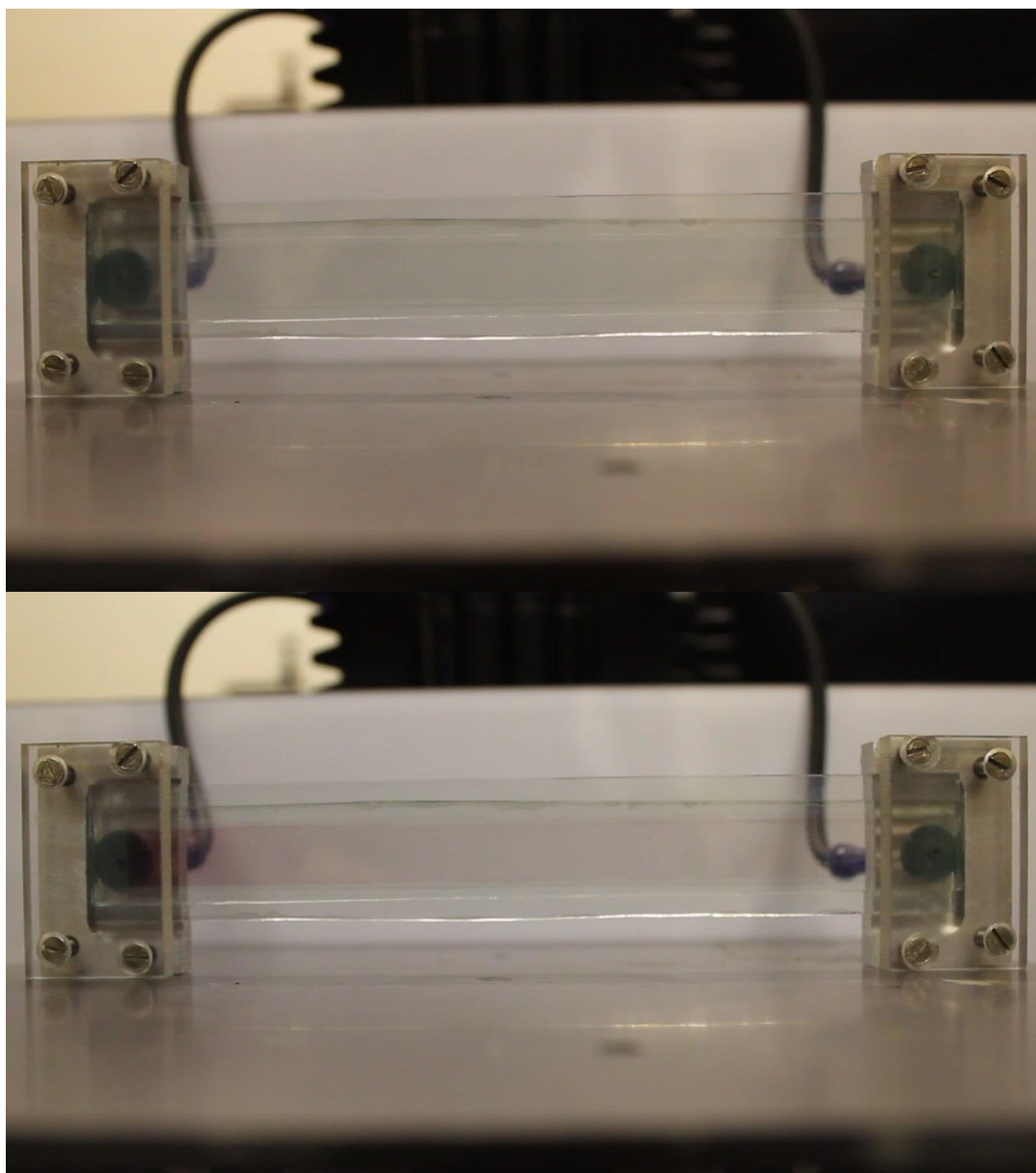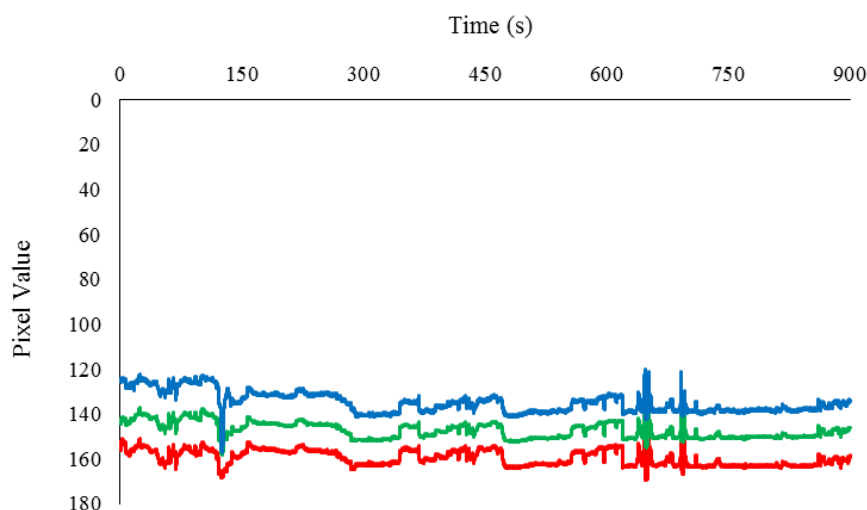

Figure 5.11 Images of the device before sensitisation (Top) and after pump dyeing with N719 (Bottom) on 18NRT paste.

The RGB analysis was then conducted on the images. The raw data is shown in Figure 5.12 and Figure 5.13.

Figure 5.12 Left side RGB analysis of N719 dye uptake on 18NRT Paste**.**

Figure 5.13 Right side RGB analysis of N719 dye uptake on 18NRT Paste.

Data show high variation in gradient for RGB values on both the left and right sides with a slight increase between 800 and 900 seconds. The error levels were lower in this experiment than the previous N719 experiment since the recording was made earlier when the room was less busy. However the error was still high compared to the low gradient so it is difficult to accurately determine whether the end point was reached on either the left or right side of the device. The low gradient was due to the more subtle change in colour from dye uptake of the transparent paste 18NRT.

The control deviation was then deducted from the original RGB values to reduce the error. Corrected data is shown in Figure 5.14 and Figure 5.15
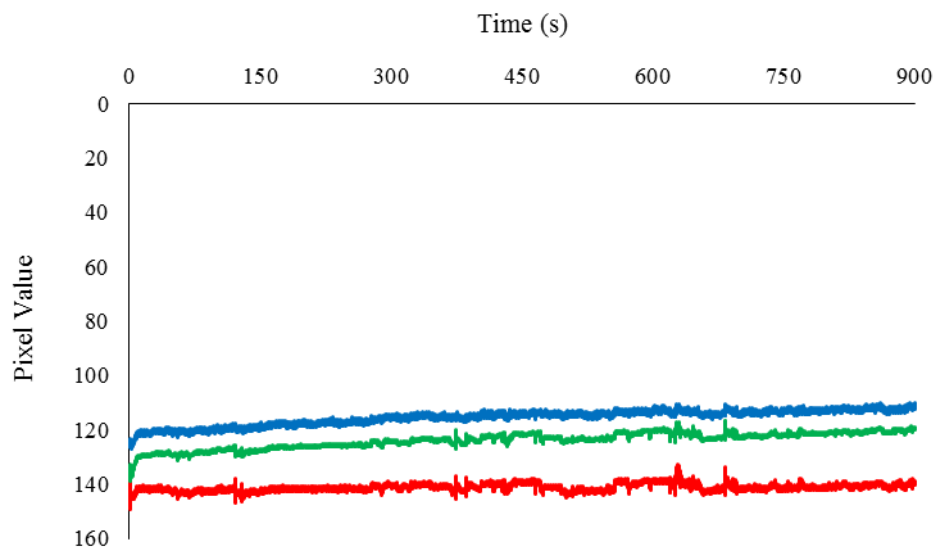
Figure 5.14 Left side RGB analysis of N719 with noise reduction on 18NRT.
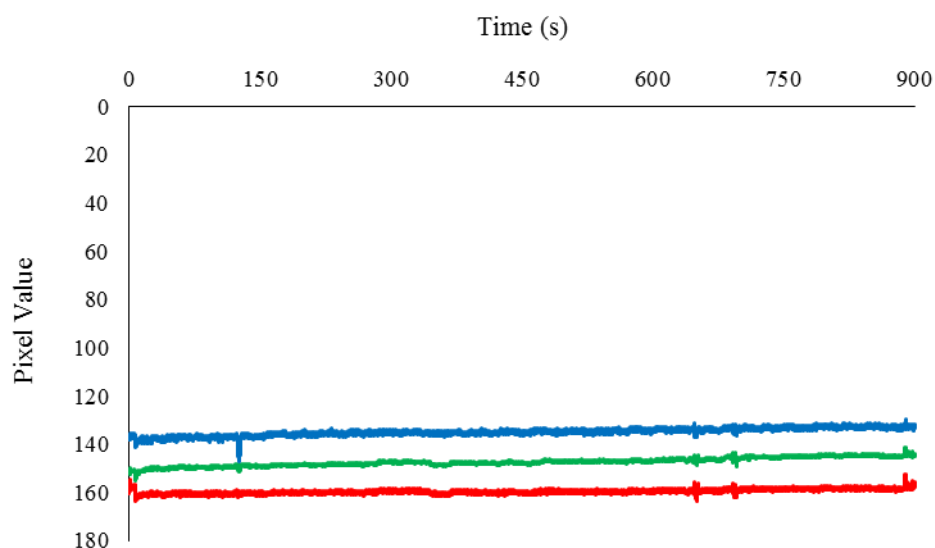
Figure 5.15 Right side RGB analysis of N719 with noise reduction on 18NRT.

The noise reduction appears to have worked very well with this experiment. The noise levels on the left hand side are very low but the noise on the right side is even lower. Due to this it is now possible to interpret the data. The left hand side shows a steep initial decrease in all colours. Both sides show a very gradual increase that continues throughout the experiment. This shows that the dye is sorbing to the TiO_2 surface but is not fully saturated. Therefore more time should be taken to dye 18NRT paste with

106

N719 under these conditions. The experiments with N719 on Dyesol Active Opaque paste and 18NRT paste have shown very significant differences. Even before the analysis was run, the intensity of the colour with Active Opaque was noticeably higher after sensitisation compared to the 18NRT paste. The 18NRT paste showed a barely noticeable colour change after sensitisation. This could be due to the lower porosity of the 18NRT paste compared to the Active Opaque due to the lower range in sizes of the nanoparticles present. 18NRT paste contains uniform anatase nanoparticles of *ca.* 20 nm[188] whereas Active Opaque paste contains a mix of small anatase particles *ca.* 20 nm and large anatase particles as big as 450 nm designed to scatter light[189]. The effect of a wider range of particle sizes is that there are more spaces (or pores) between anatase particles in the paste than if all the particles were 20 nm. This allows dye to infiltrate the TiO_2 via the pores and allows dye sorption to a larger surface area[190]. This would result in a stronger colour as the dye would cover more of the TiO_2 allowing for a greater dye loading[191]. A diagram of this is shown in Figure 5.16.

450 nm TiO_2 Particles   20 nm TiO_2 Particles
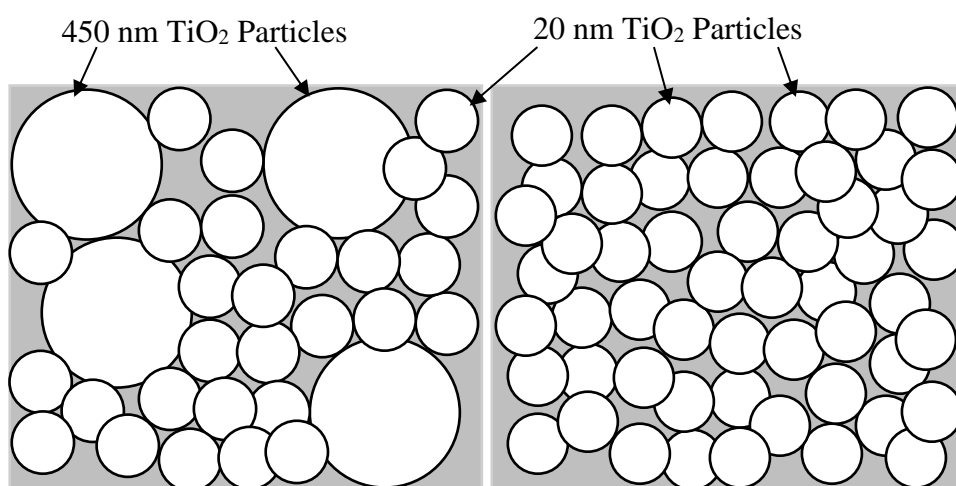
Figure 5.16 Left: anatase nanoparticles in Active Opaque paste showing a mixture of 20 nm particles and 450 nm particles. Right: anatase nanoparticles in 18NRT paste showing uniform 20 nm particles.

The other factor affecting the colour of the electrode is the refractive index of the paste. With a higher refractive index the TiO_2 will be less transparent, as is the case with Active Opaque paste. With a high refractive index the light is scattered more rather than passing straight through the film. 18NRT has a lower refractive index, making it higher transparency and thus more difficult to analyse with RGB analysis.

The two experiments have shown a direct comparison between Active Opaque and 18NRT paste with N719 dye. This has determined that the dye uptake on the 18NRT paste is much more difficult to monitor than the Active Opaque paste. It is therefore logical that other dyes would show similar results. Therefore for future testing with additional dyes, 18NRT paste should be used as a proof of concept. If dye uptake can be successfully monitored with 18NRT paste then dye uptake on Active Opaque paste should also provide acceptable results.
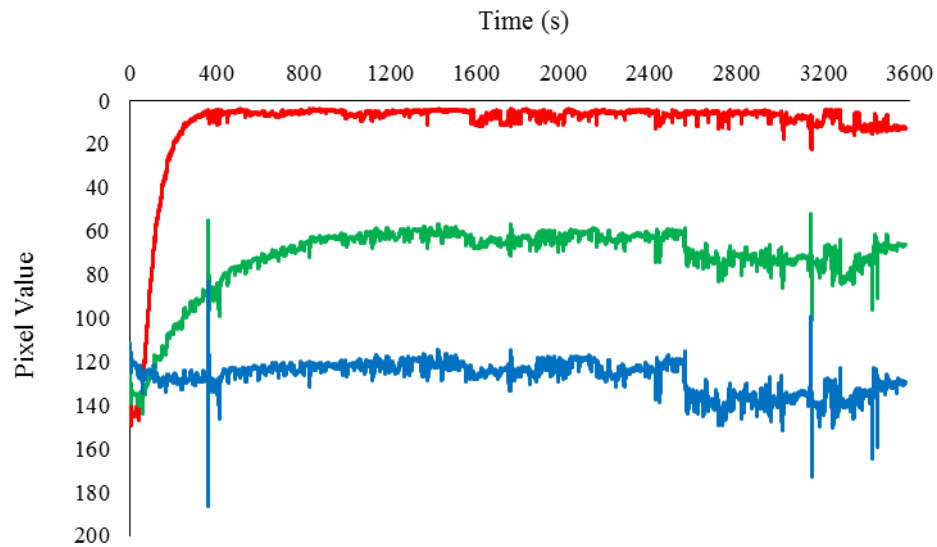
5.4 SQ2 Dye Analysis

As the more stable of the two squaraine dyes SQ1 and SQ2, SQ2 could be used as a cheaper alternative to N719 dye. Images taken at the before and after the sensitisation process are shown in Figure 5.17.
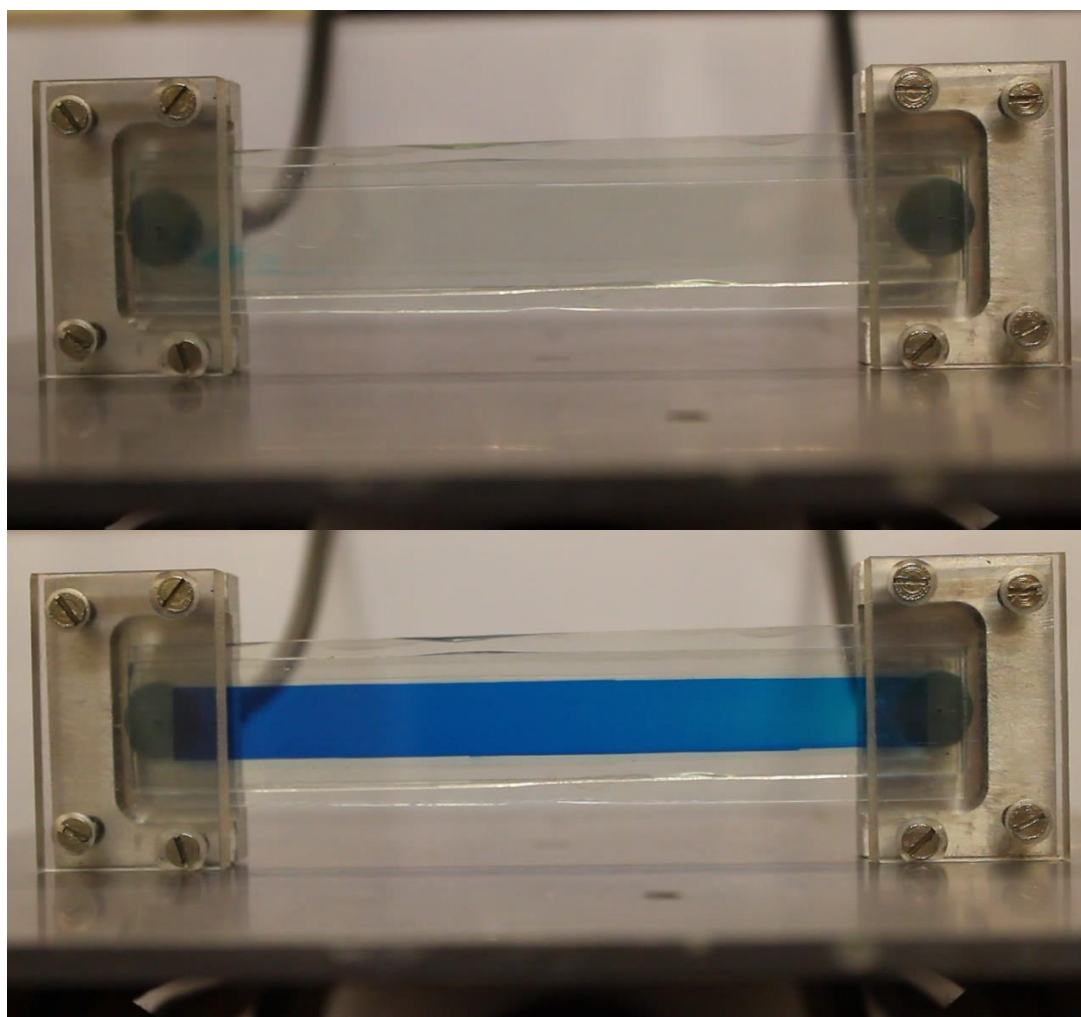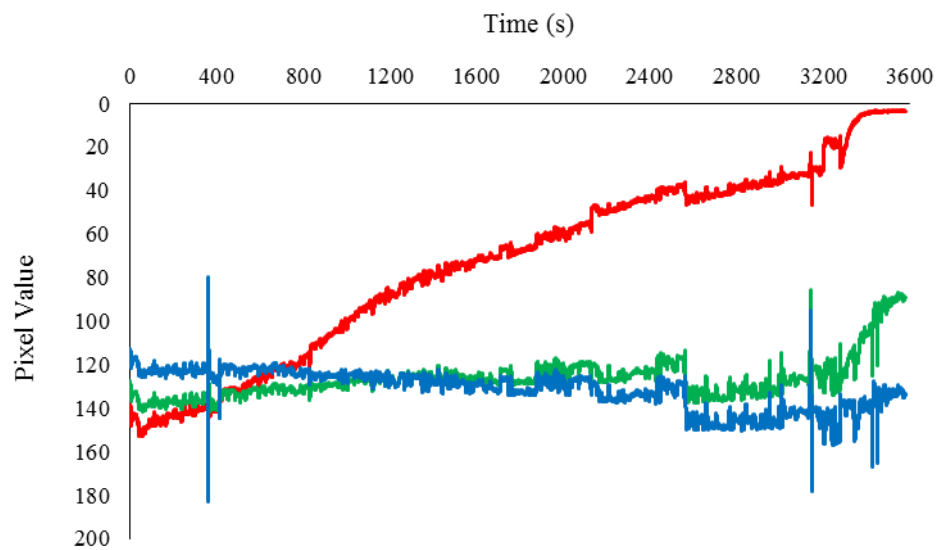

Figure 5.17 Images of the device before (Top) and after sensitisation with SQ2 (Bottom).

As with the N719 analysis the sorption of the SQ2 was monitored with RGB analysis. The raw data from the analysis is plotted below in Figure 5.18 and Figure 5.19.

Figure 5.18 Left side RGB analysis of SQ2 dye uptake on 18NRT Paste.

Figure 5.19 Right side RGB analysis of SQ2 dye uptake on 18NRT Paste.

The data showed a very fast dye uptake on the left hand side of the cell with complete dye uptake at roughly 400 seconds. The right side data shows a much slower dye uptake. This is unsurprising as the fresh dye enters the cell on the left so dye concentration is reduced when it reaches the right side. Due to this effect, the dye concentration can eventually become too low to sorb onto the surface.

The control deviation was then deducted from the original data, reducing the errors. The corrected data is shown in Figure 5.20 and Figure 5.21.
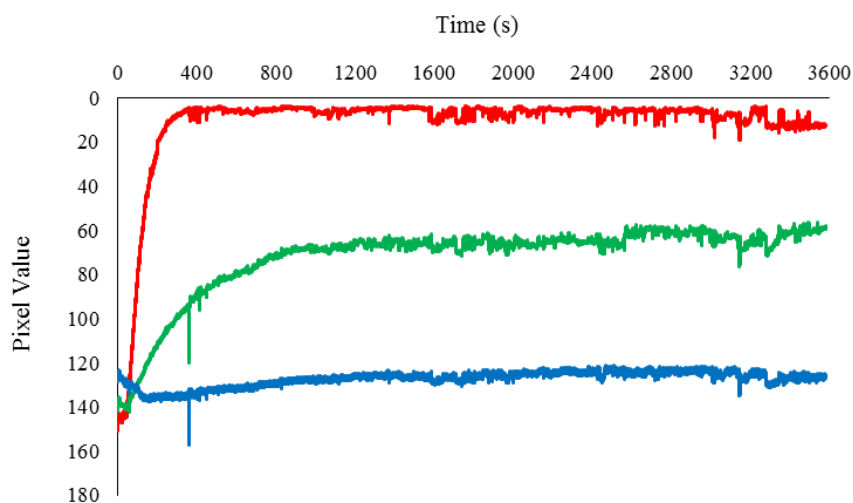
Figure 5.20 Left side RGB analysis of SQ2 with noise reduction.
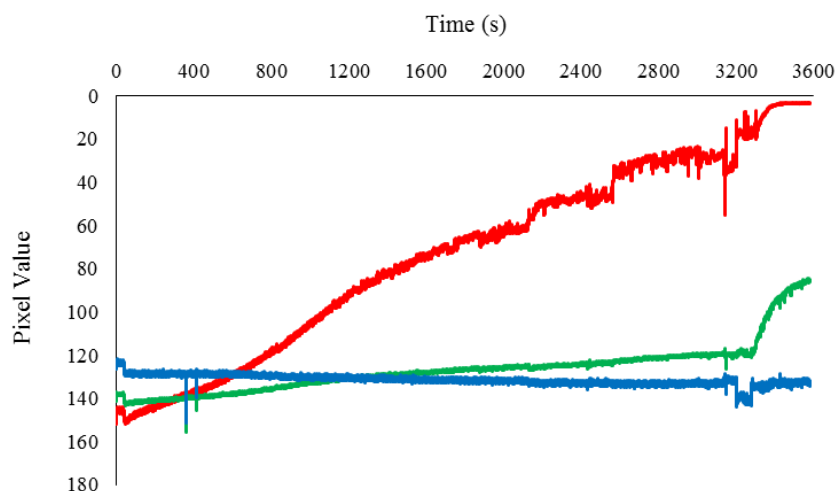
Figure 5.21 Right side RGB analysis of SQ2 with noise reduction.

The left side RGB data show a sharp increase between 0 and 400 seconds. This shows that the dye has sorbed onto the TiO_2 successfully and has reached saturation as the level remains constant for the remainder of the experiment. The right side RGB data show a more gradual dye uptake throughout the experiment and a final increase between 3200 and 2600 seconds. The reason for this slow uptake is the dye concentration has become too low to fully dye the device. Fresh dye was therefore added to the system at 3200 seconds which fully dyed the cell.

5.5 D131 Dye Analysis

D131 is another cheaper alternative to N719 so is a possible option for industrial production of solar cells. The RGB image analysis was conducted as stated previously with the dye intake on the left and the outtake on the right. Images were taken prior and post sensitisation, they are shown in Figure 5.22.
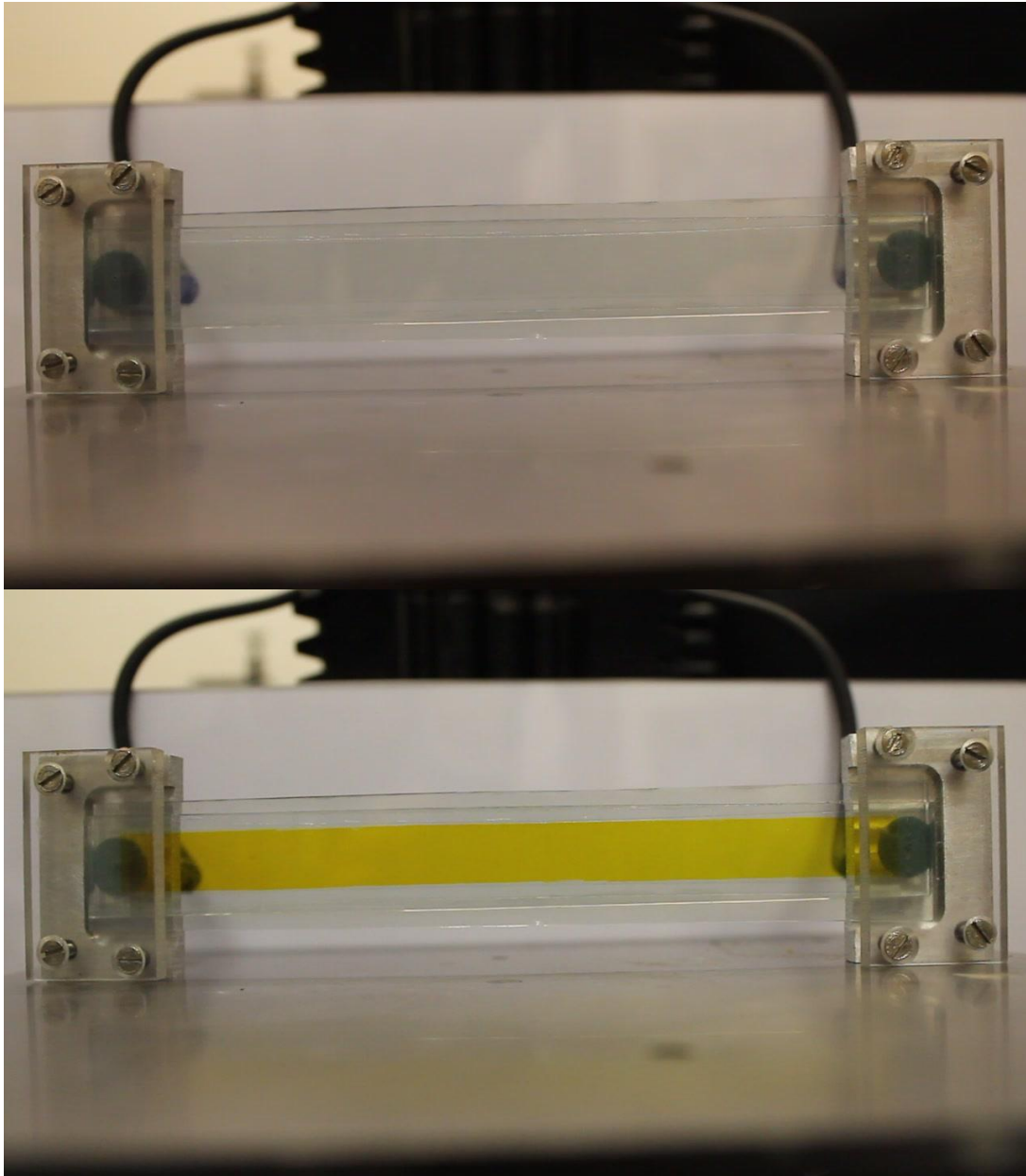
Figure 5.22 Images of the device before (Top) and after sensitisation with D131 (Bottom).

The images were then analysed, the raw data is shown in Figure 5.23 and Figure 5.24.

Figure 5.23 Left side RGB analysis of D131 dye uptake on 18NRT Paste.

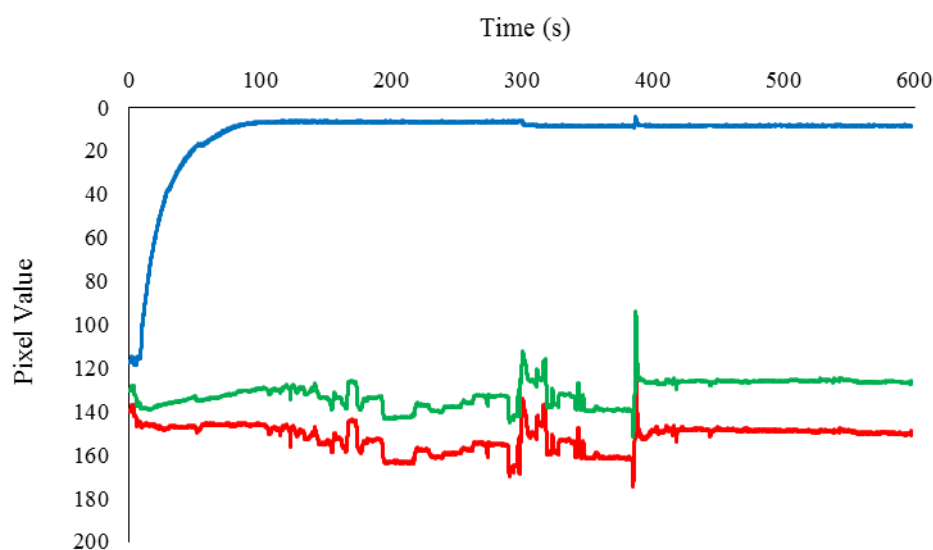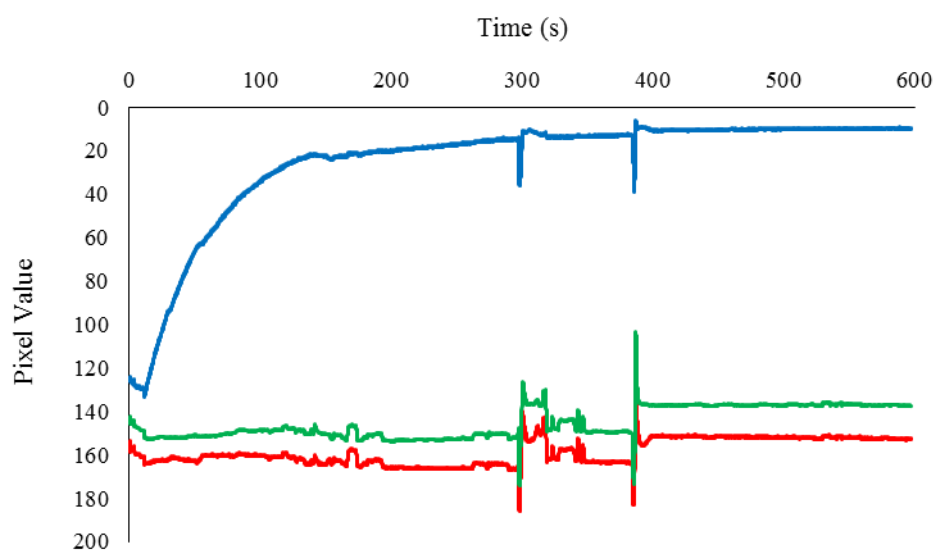
Figure 5.24 Right side RGB analysis of D131 dye uptake on 18NRT Paste.

The left side RGB data show a sharp decrease in the blue intensity in the first 100 seconds before levelling out. This indicates that the left side of the cell has fully dyed after this time. The right side RGB data show a shallower gradient for the first 150 seconds which then decreases between 150 and 400 seconds before levelling out. This indicates that the right side was also fully dyed but after *ca.* 400 seconds. The differences between the two sides are not surprising as once again the dye concentration will have been reduced by the time it reaches the right side of the device.

The control deviation was then subtracted from the original RGB values to give a reduction in the noise from changes in light levels. Corrected data is shown in Figure 5.25 and Figure 5.26.
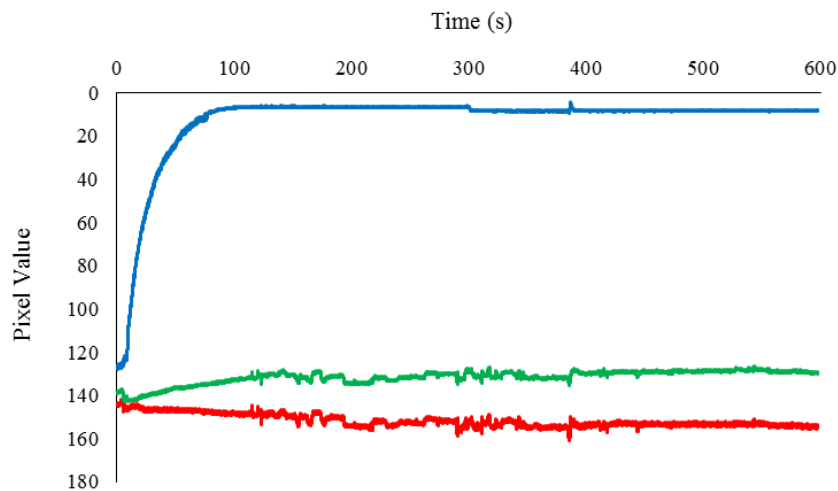
Figure 5.25 Left side RGB analysis of D131 with noise reduction.
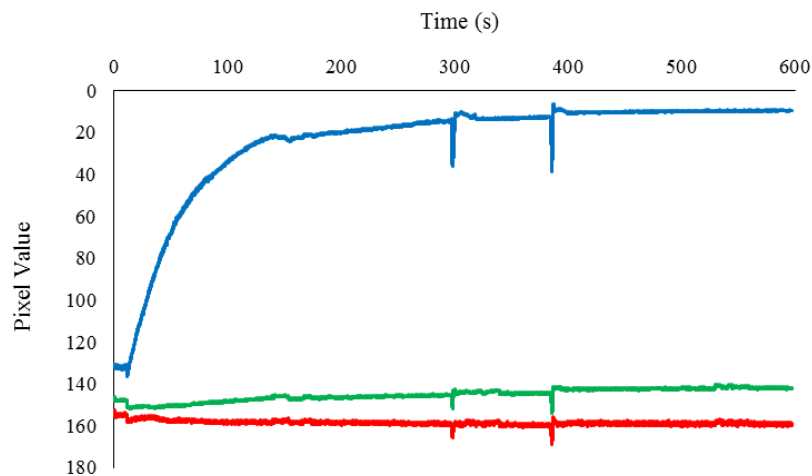
Figure 5.26 Right side RGB analysis of D131 with noise reduction.

The left side RGB data show very little noise and complete dye coverage at *ca*. 100 seconds. The right side RGB data show a couple of spikes in noise at 300 and 400 seconds. These spikes could not be removed from the blue pixel values using the noise reduction technique as they were so close to 0. When close to 0 changes in light levels have a much lower effect compared to the control value. This means if error reduction was used a negative value would be obtained.

5.6 Half Squaraine Dye Analysis

Half squaraine is a cheaper alternative to the full squaraine molecule which could be used to make devices with a low cost per watt. Therefore it is a real possibility that industrial sized devices could be manufactured with this dye. Images before and after sensitisation are shown in Figure 5.27.
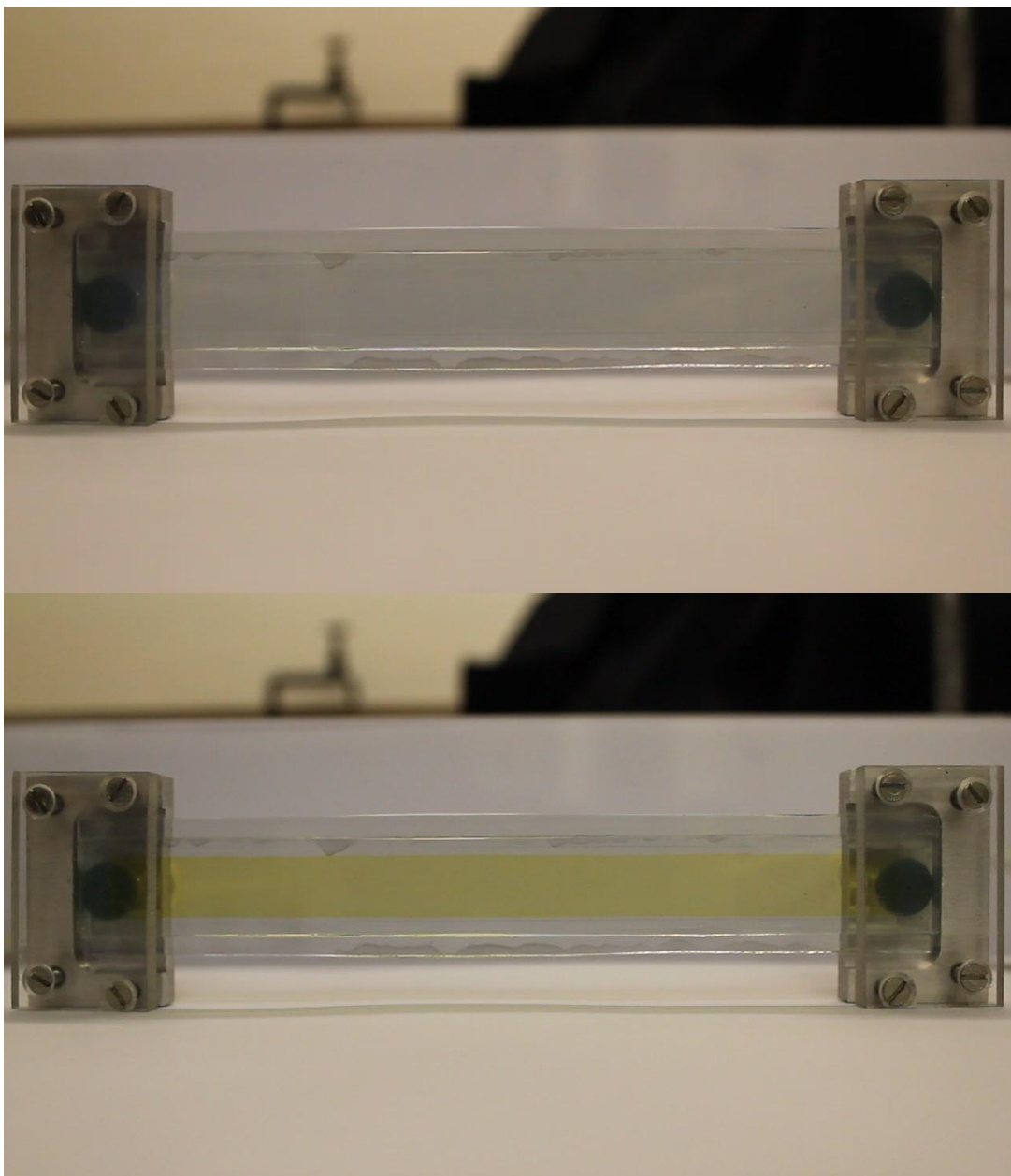
Figure 5.27 Images of the device before (Top) and after sensitisation with half squaraine (Bottom).

The images were then analysed to extract raw data, this is shown in Figure 5.28 and Figure 5.29.
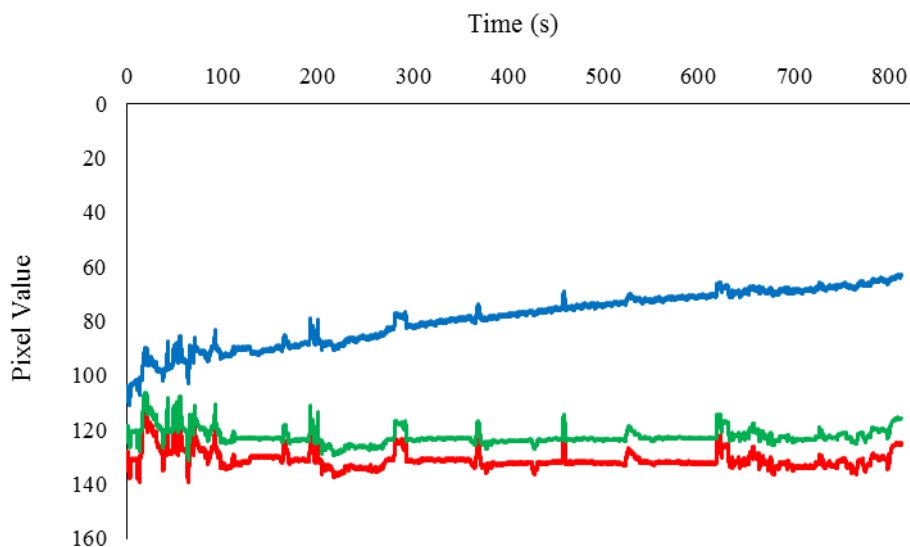
Figure 5.28 Left side RGB analysis of half squaraine dye uptake on 18NRT Paste.
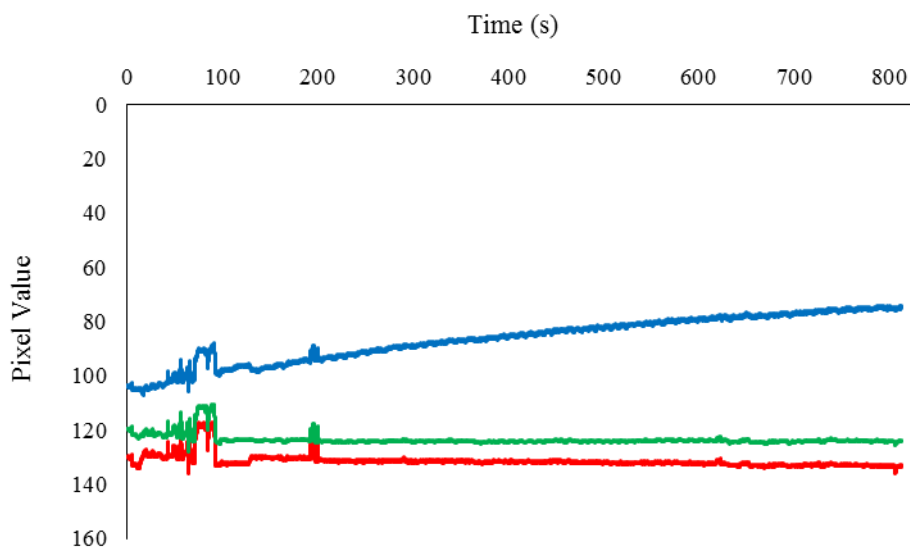
Figure 5.29 Right side RGB analysis of half squaraine dye uptake on 18NRT Paste.

The left side RGB data show a considerable quantity of noise throughout the experiment. The gradual decrease in the blue pixel value indicates the dye is sorbing onto the TiO_2 successfully, however due to noise it is difficult to determine the end point. The right side RGB data show much less noise than the left side. The right side also shows a steady decrease in the blue pixel value which gradually levels out towards the end of the experiment.

The control deviation was then deducted from the initial RGB values to give a reduced error. The corrected data is shown in Figure 5.30 and Figure 5.31.
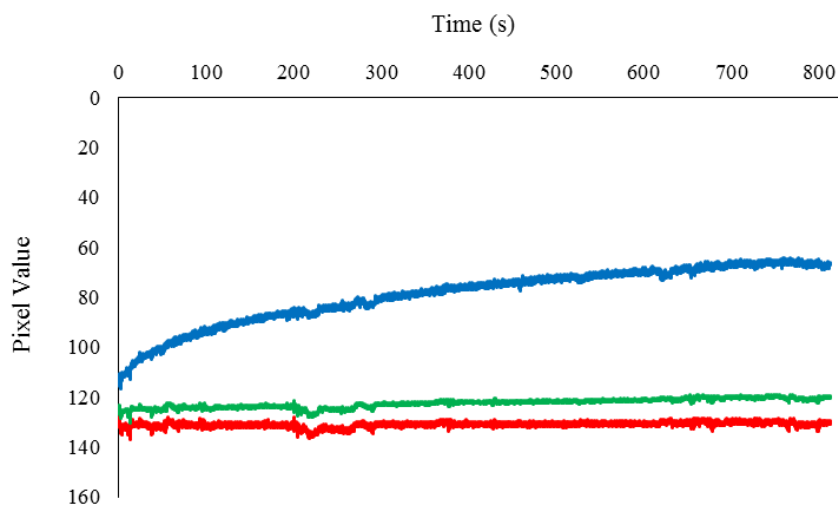
Figure 5.30 Left side RGB analysis of half squaraine with noise reduction.
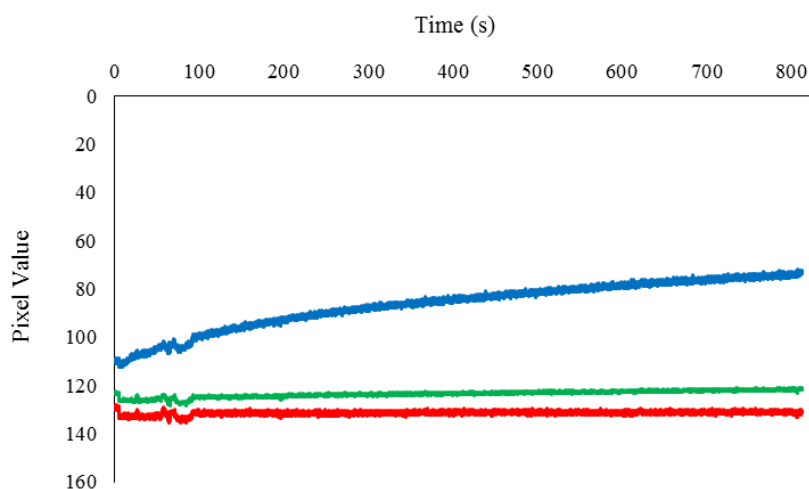
Figure 5.31 Right side RGB analysis of half squaraine with noise reduction.

Figure 5.30 shows an initially steep gradient in the blue pixel value indicating a fast colour change to begin with between 0 and 100 seconds. The blue value then continues to decrease gradually between 100 and 700 seconds as more dye sorbs to the surface of the cell. The blue value then levels out between 700 and 800 seconds indicating the device has almost reached saturation. Figure 5.31 shows a lower initial gradient. The blue pixel value then gradually increases but does not level out. This experiment was stopped when the surface appeared saturated, however RGB analysis shows this was not the case. More dyeing time would therefore be needed to fully saturate the surface.

116

5.7 Rhodamine B Dye Analysis

Rhodamine B is a fluorescent dye often used in biotechnology and as a biological stain[192]. The uptake of the dye to the TiO_2 surface was extremely fast, giving an intense colour after just a few minutes, this is shown in Figure 5.32.

Figure 5.32 Images of the device before (Top) and after sensitisation with Rhodamine B (Bottom).

The RGB values of the images were then analysed using Sigma Scan Pro and the data plotted, as shown in Figure 5.33 and Figure 5.34.
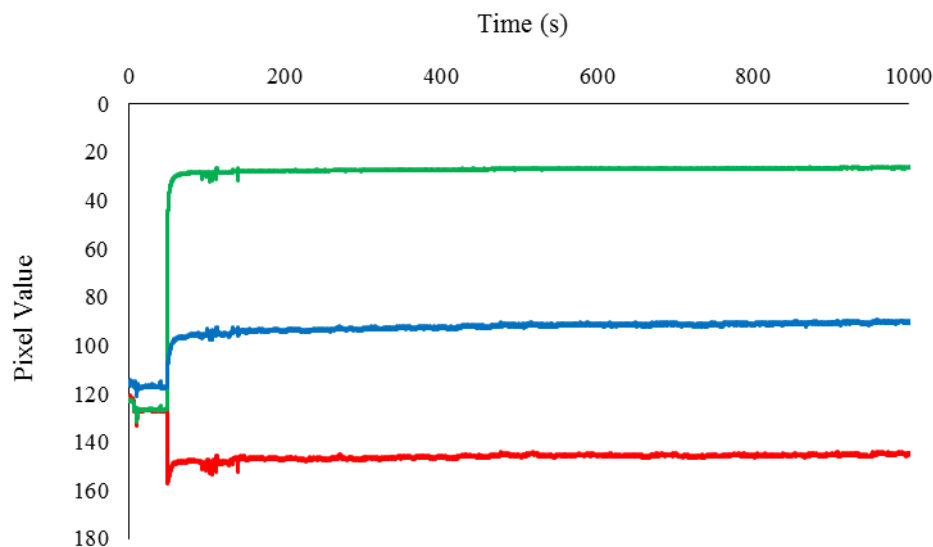
Figure 5.33 Left side RGB analysis of Rhodamine B dye uptake on 18NRT Paste.
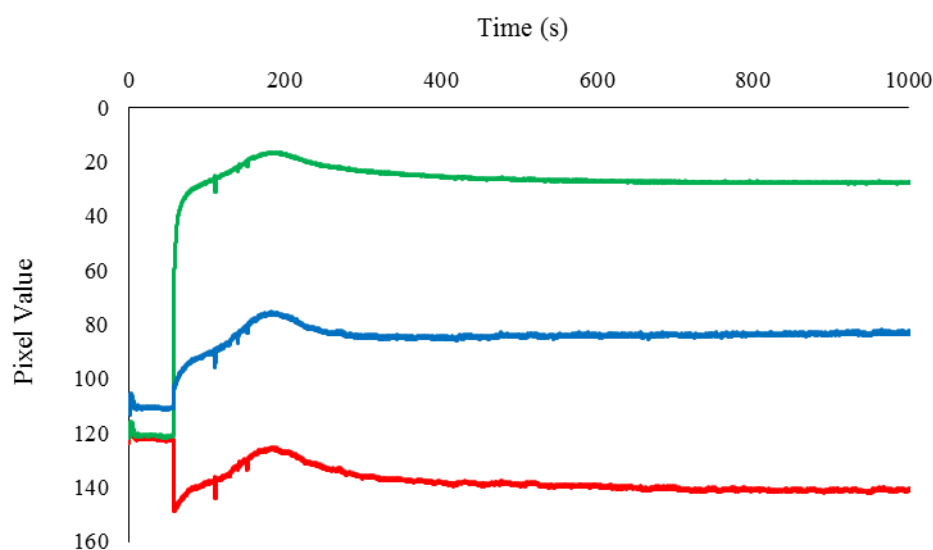
Figure 5.34 Right side RGB analysis of Rhodamine B dye uptake on 18NRT Paste.

The left side analysis shows an extremely fast colour change initially followed by a very gradual gradient. This suggests the dye uptake with Rhodamine B is almost instantaneous with 18NRT paste. The right side also shows a fast change in colour initially which then levels out. Surprisingly there is a peak in the RGB values which then decreases at *ca.* 200 seconds. This could be either due to an increase in light levels or some of the dye that was sorbed to the surface initially has been removed.

The control deviation was then deducted from the initial RGB values to give a noise reduction. Corrected data is shown in Figure 5.35 and Figure 5.36.

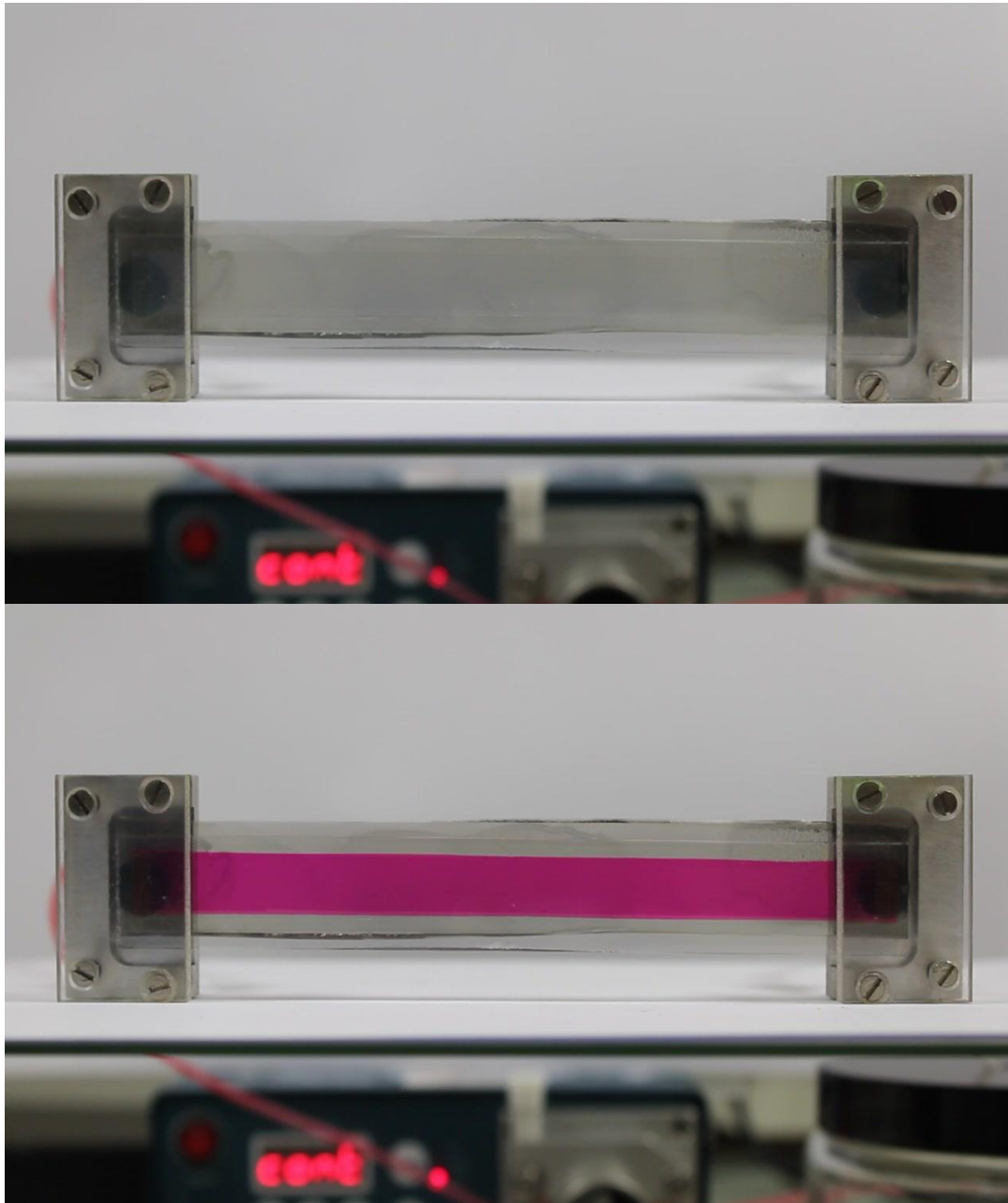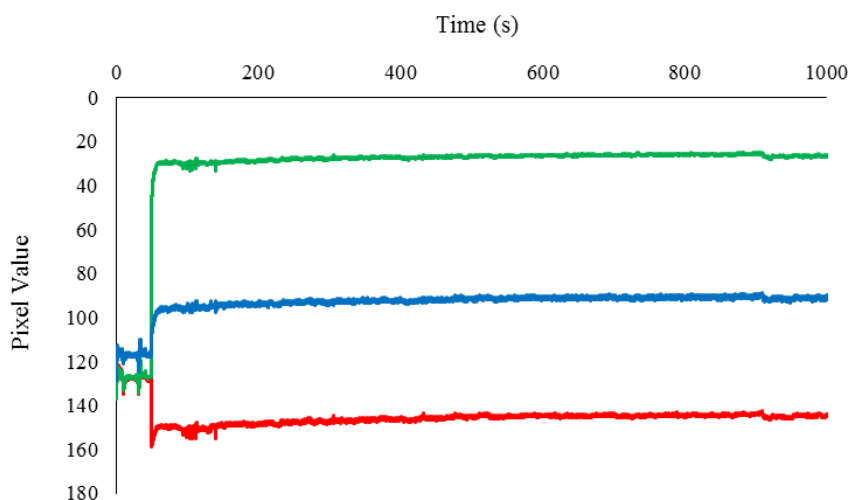**Figure 5.35** Left side RGB analysis of Rhodamine B with noise reduction.
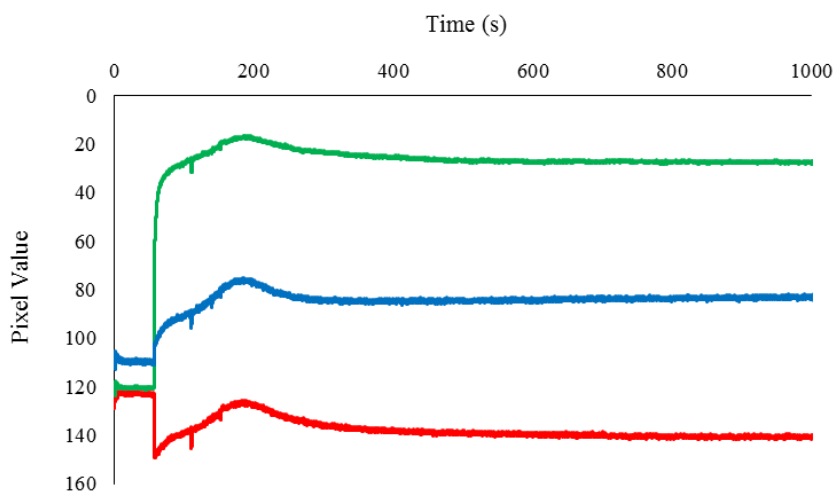
Figure 5.36 Right side RGB analysis of Rhodamine B with noise reduction.

The left hand side analysis shows a very slight change with the noise reduction. Even with the error reduction the right hand side analysis still showed a peak at *ca.* 200 seconds. This means the peak is not due to a change in light levels or shadowing as this would have been observed on the control data. Therefore this peak could be due to aggregation of the dye on the surface. This reaches a point where the linker group attached to the TiO_2 cannot support the dye attached to it. The linker group then breaks and the formerly attached dye is swept off the surface.

119

5.8 Dye Analysis of HFSQ followed by SQ1 Co-Sensitisation

The technique of co-sensitisation can be used to broaden the wavelengths of light available for adsorption by a device. This is achieved by combining two dyes that absorb at different wavelengths, allowing for a higher conversion of sunlight. The co-sensitisation can also have a stabilizing effect that would be advantageous when used with the less stable SQ1. Images taken prior to sensitisation, after sensitisation with HFSQ and after Co-sensitisation with SQ1 are shown in Figure 5.37.
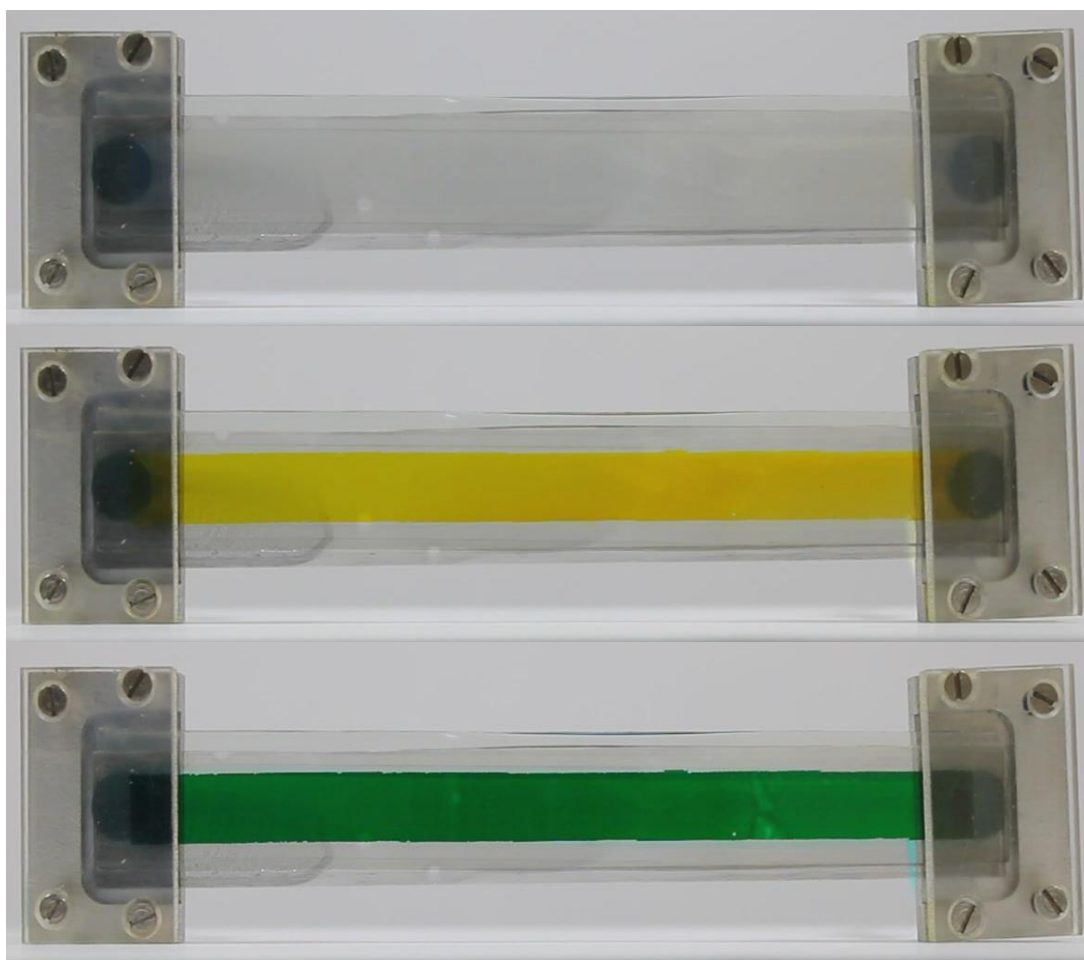
Figure 5.37 Images of the device before sensitisation (Top), after pump dyeing with half squaraine (Middle) and after pump dyeing with SQ1 (Bottom). Note that the green colour of the device is due to the combination of the yellow dye half squaraine and the blue dye SQ1.

The RGB values of the images were then analysed as stated previously and plotted. Initial data is shown in Figure 5.38 and Figure 5.39.
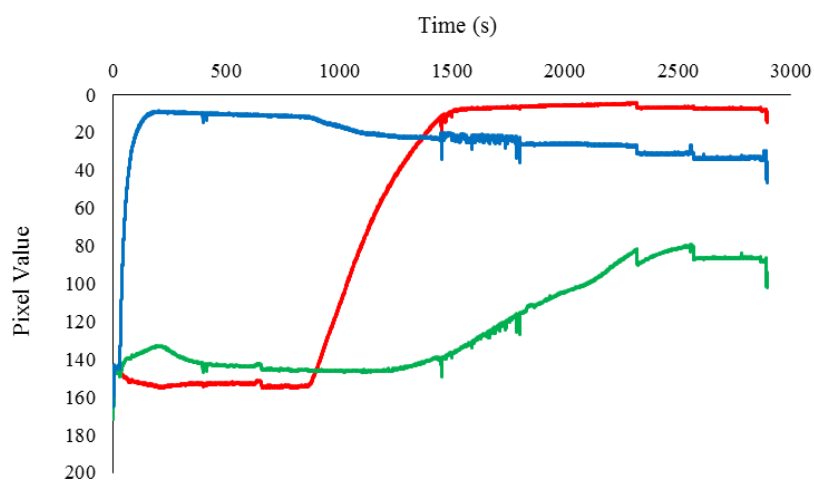
Figure 5.38 Left side RGB analysis of half squaraine then SQ1 dye uptake on 18NRT Paste.
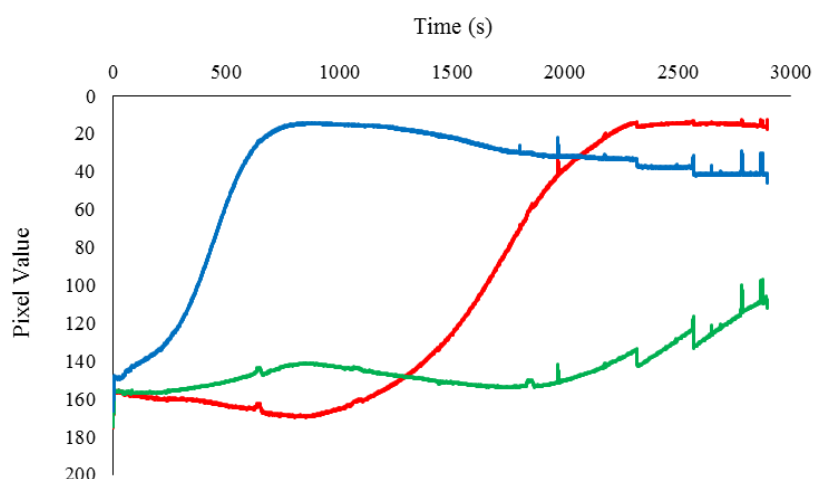
Figure 5.39 Right side RGB analysis of half squaraine then SQ1 dye uptake on 18NRT Paste.

The left side RGB analysis shows an initially high gradient in the first 100 seconds indicating a fast half squaraine dye uptake. The gradient then levels out as the surface becomes saturated with half squaraine. At *ca.* 800 seconds the SQ1 dye was pumped through the cell, this is shown by the significant drop in the red pixel value between 1000 and 1500 seconds. The gradients then level out after 2500 seconds. The right side shows the same pattern but with a much more gradual colour change for half squaraine due to the decreased dye concentration.

The control deviation was deducted from the RGB values to give a reduction in noise levels. Corrected data is shown in Figure 5.40 and Figure 5.41.

Figure 5.40 Left side RGB analysis of half squaraine then SQ1 with noise reduction.

Figure 5.41 Right side RGB analysis of half squaraine then SQ1 with noise reduction.

The data for both sides show a high speed dye uptake for half squaraine. The pixel values then level out before the SQ1 dye uptake begins. The dye uptake for SQ1 is much slower which could be due to the fact that the half squaraine has already been sorbed to the surface. This would leave less free sites for SQ1 to bind to so could explain the slower dye uptake. Alternatively this could be due to a lower binding energy for half squaraine than SQ1. Further experimentation is required to determine which of these theories is correct.

5.9 Dye Analysis of SQ1 followed by HFSQ Co-Sensitisation

This experiment was designed to determine if the order of the dyes used for co-sensitisation affects the overall sensitisation of the device and the speed of dye uptake. Therefore the same dyes were used from the previous experiment but SQ1 was pumped through the cell initially and then co-sensitised with half squaraine. The setup and the speed of the pump was also kept constant to allow for comparable results. Images at the start of the sensitisation process, after sensitisation of SQ1 and after co-sensitisation with HFSQ are shown in Figure 5.42.

Figure 5.42 Images of the device (Top) before sensitisation, (Middle) after pump dyeing with SQ1 and (Bottom) after pump dyeing with half squaraine. Note that the green colour of the device is due to the combination of the blue dye SQ1 and the yellow dye half squaraine.

The RGB values of the images were then analysed as stated previously and plotted. The initial data is shown in Figure 5.43 and Figure 5.44.
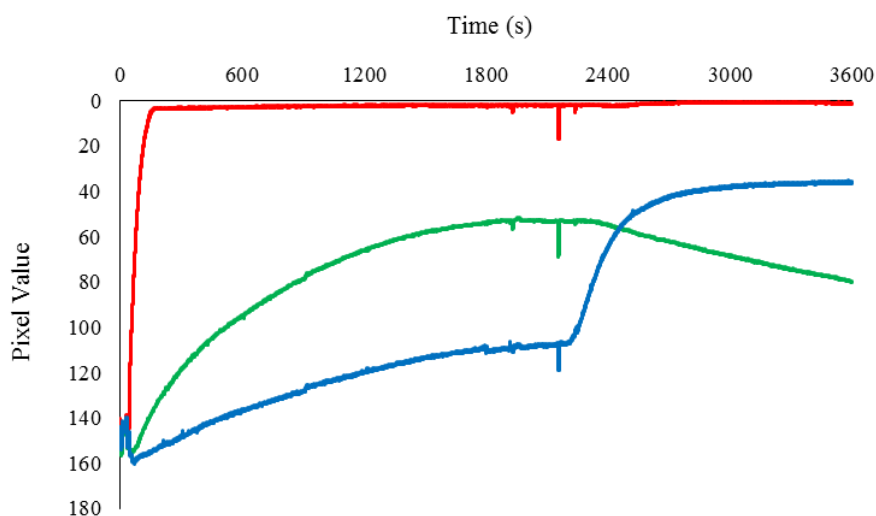
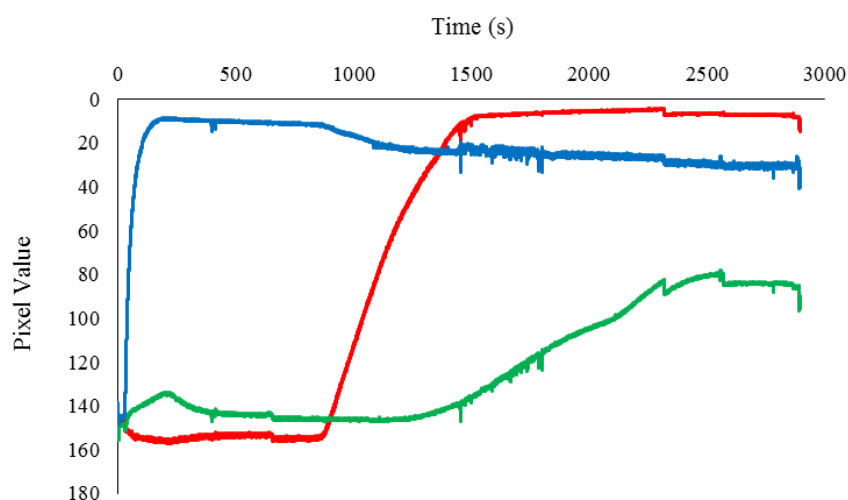**Figure 5.43** Left side RGB analysis of SQ1 then half squaraine dye uptake on 18NRT Paste.
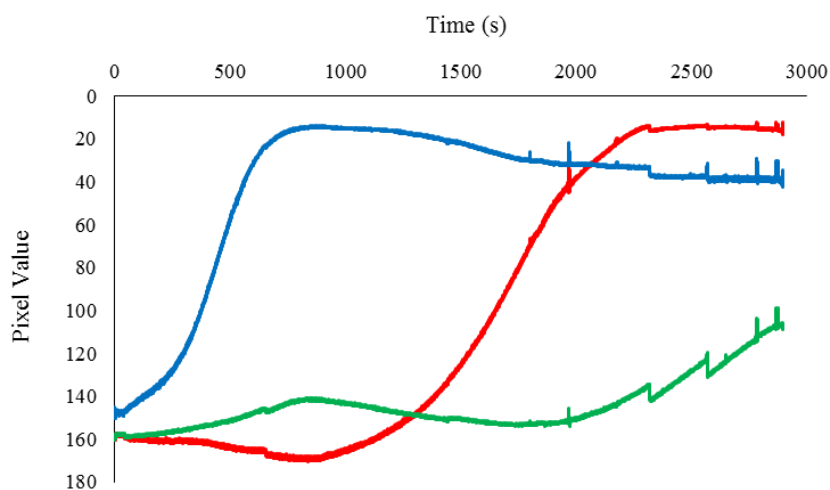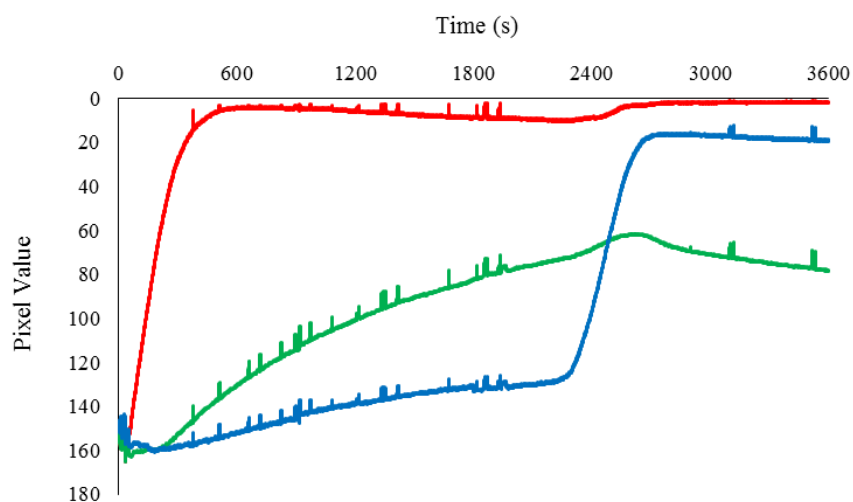

Figure 5.44 Right side RGB analysis of SQ1 then half squaraine dye uptake on 18NRT Paste.

The left side RGB data show a high initial gradient, indicating a fast dye uptake with SQ1. The RGB values then gradually level out, indicating complete dye uptake. At *ca.* 2200 seconds the half squaraine dye is pumped through the cell, indicated by a steep drop in the blue pixel value due to the yellow colour of the dye. The right side shows a lower initial gradient for the SQ1 dye uptake. The RGB values still have a positive gradient when the half squaraine was added. Therefore a longer time is needed before adding the half squaraine to ensure saturation.

The control deviation was deducted from the RGB values to give a reduction in noise levels. The corrected data is shown in Figure 5.45 and Figure 5.46.

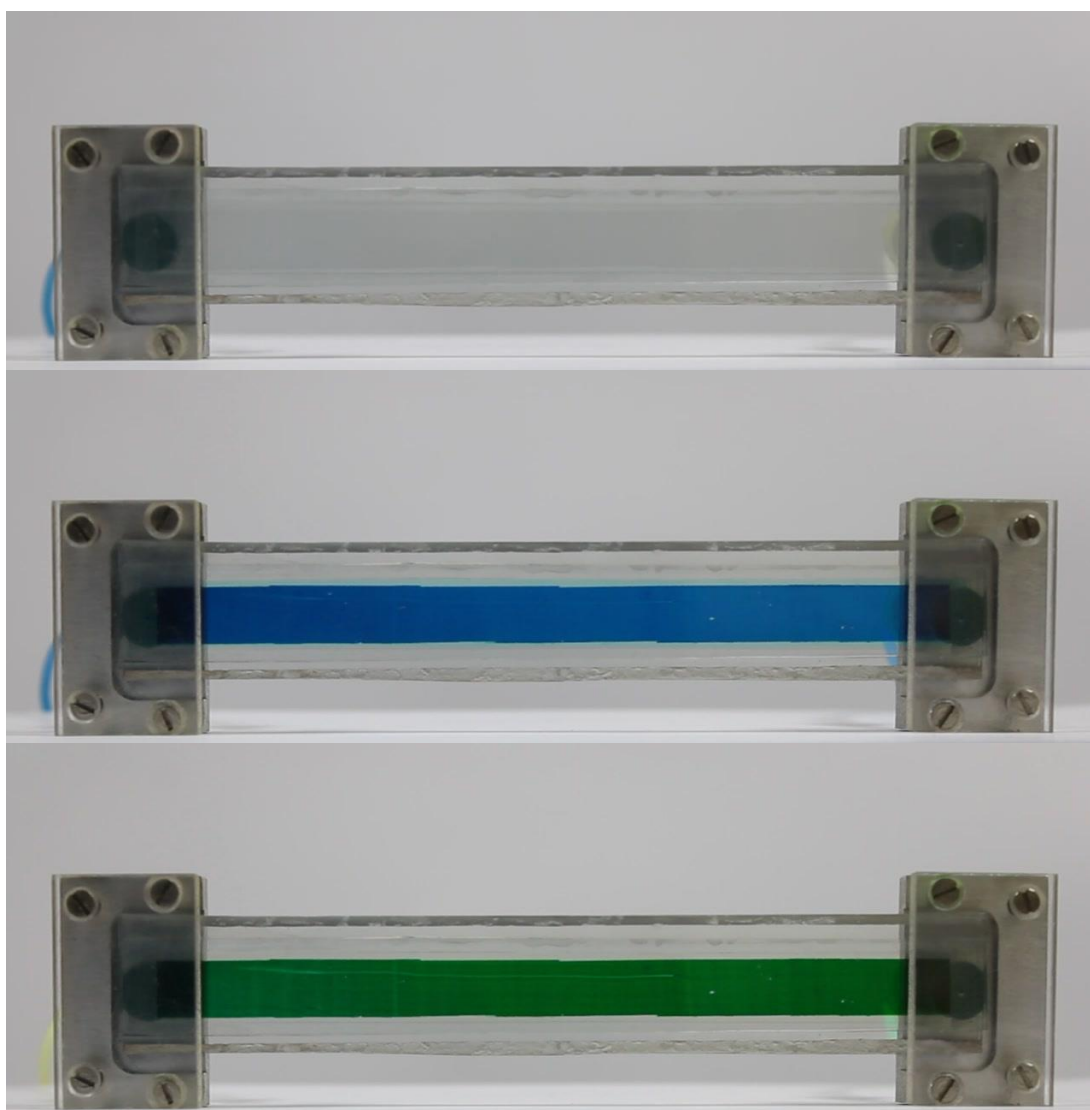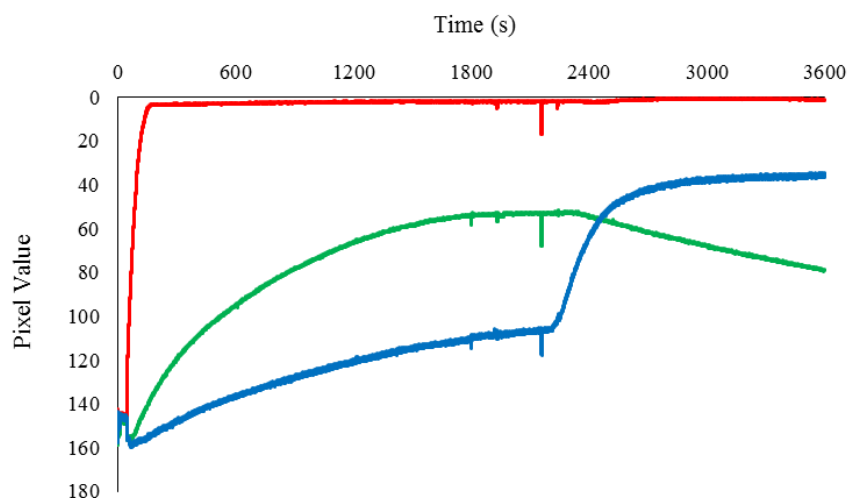**Figure 5.45** Left side RGB analysis of SQ1 then half squaraine with noise reduction.
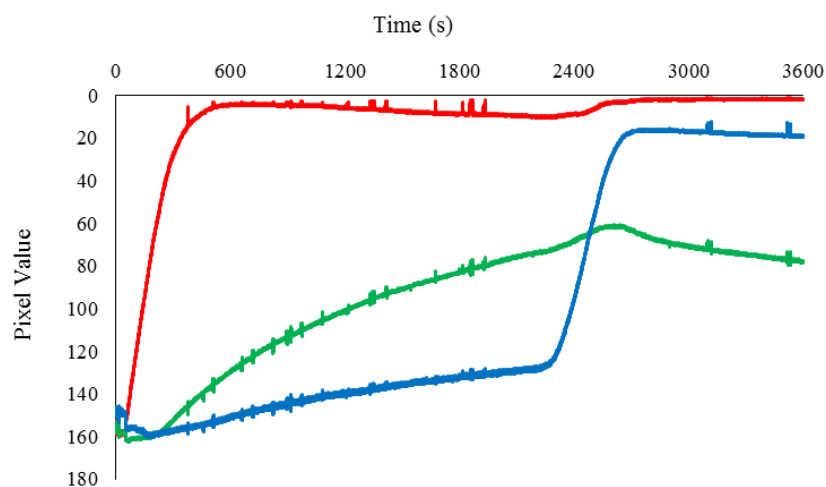
Figure 5.46 Right side RGB analysis of SQ1 then half squaraine with noise reduction.

The left side RGB data show the uptake of SQ1 is initially very quick but does not fully saturate the surface until *ca.* 2200 seconds. The half squaraine dye has a lower initial gradient but does not fully level out, indicating more time is needed for complete dye uptake. The right side RGB data show a lower initial gradient than the left side as expected. The decrease in the red RGB value after 600 seconds could possibly indicate some desorption of the dye has occurred. However it is most likely due the removal of excess platinum on the counter electrode which has been washed away by the solution.

5.10 Dye Analysis of SQ1 and Half Squaraine Dye Cocktail

The alternative method to co-sensitisation is to use a cocktail of multiple dyes to sensitise the device. In this experiment a 1:3 cocktail of SQ1 and half squaraine was prepared and deposited on Dyesol® 18NRT paste. This mix was used due to the high molar extinction coefficient of SQ1 relative to the lower coefficient for half squaraine. Images taken before and after the sensitisation process are shown in Figure 5.47.

Figure 5.47 Images of the device before sensitisation (Top) and after pump dyeing with a mix of 1:3 SQ1 to half squaraine (Bottom).

126

The same setup was used for the fast dye process and the imaging was conducted using the same method. Initial data is shown in Figure 5.48 and Figure 5.49.
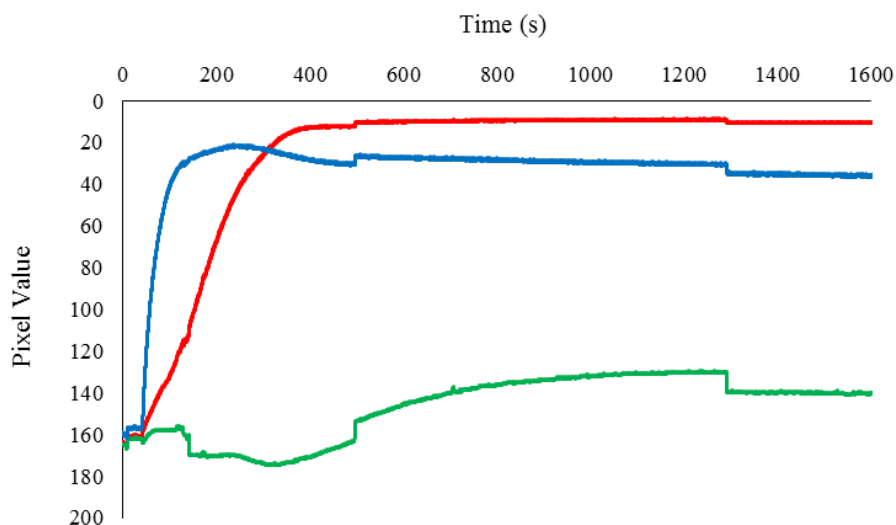
Figure 5.48 Left side RGB analysis of 1:3 mixture of SQ1 and half squaraine.
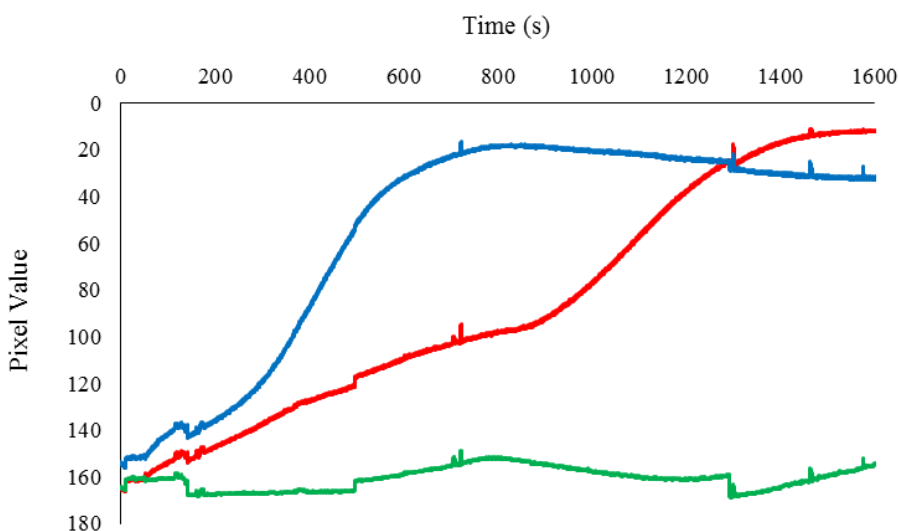
Figure 5.49 Right side RGB analysis of 1:3 mixture of SQ1 and half squaraine.

The left side RGB data show a high initial gradient which is likely due to the half squaraine dye as this is similar to the initial data of half squaraine then SQ1 in Figure 5.49. The drop in RGB values between 500 and 1300 seconds is most likely caused by a light level decrease. The right side RGB data show a lower initial gradient due to the decreased concentration of the dye. There are a small number of data spikes on the graph. This may have been caused by shadowing.

127

The control deviation was deducted from the original RGB values to give a reduction in noise levels. Corrected data is shown in Figure 5.50 and Figure 5.51.

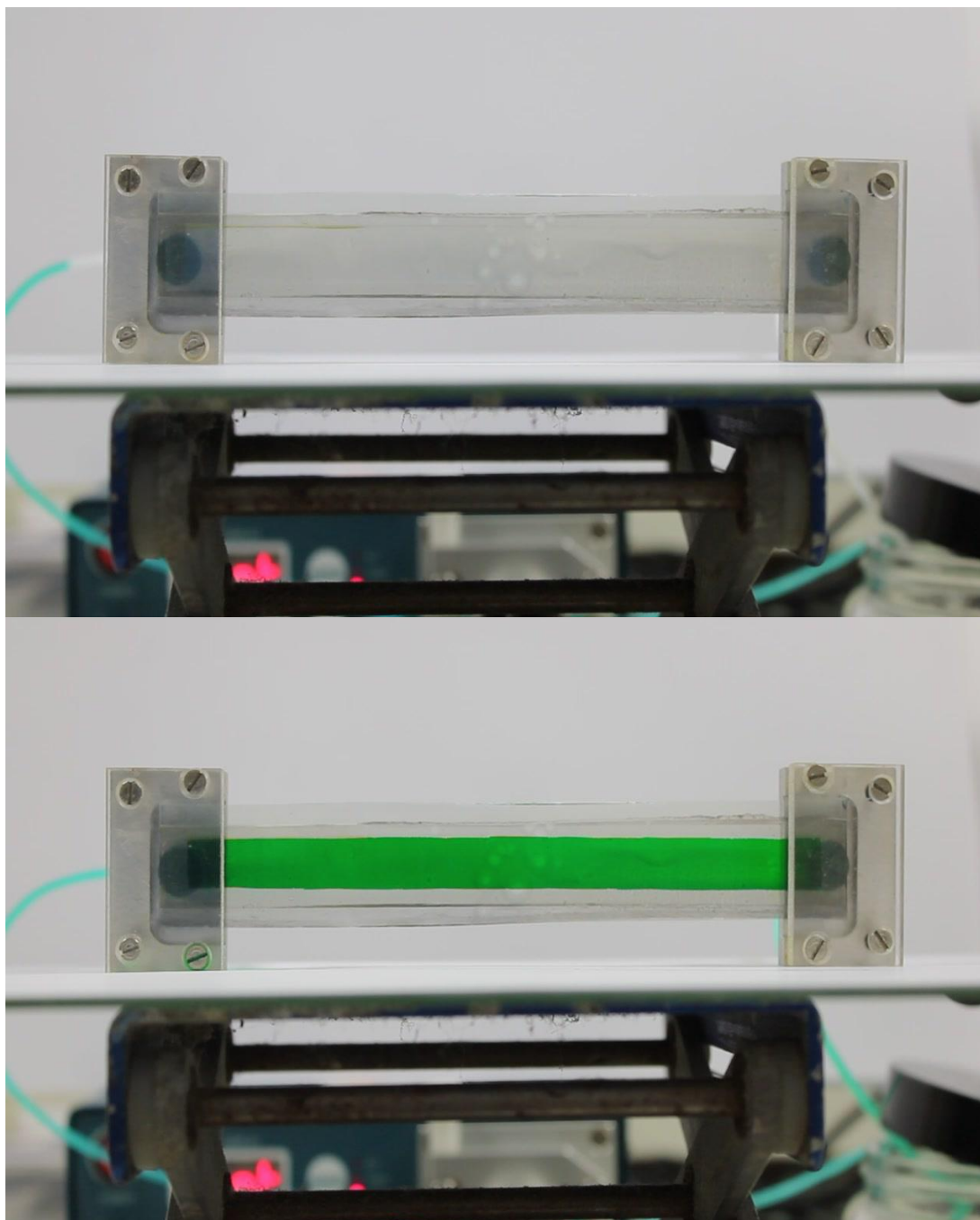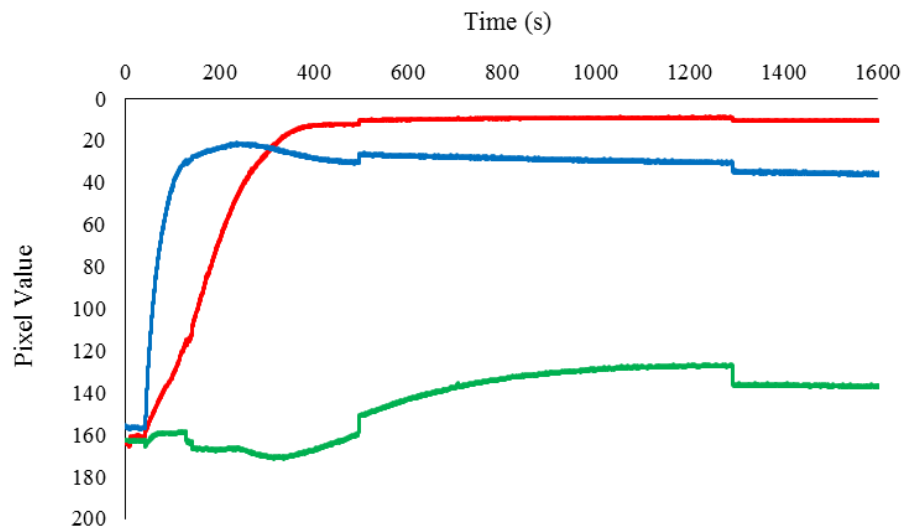**Figure 5.50** Left side RGB analysis of 1:3 mixture of SQ1 and half squaraine with noise reduction.
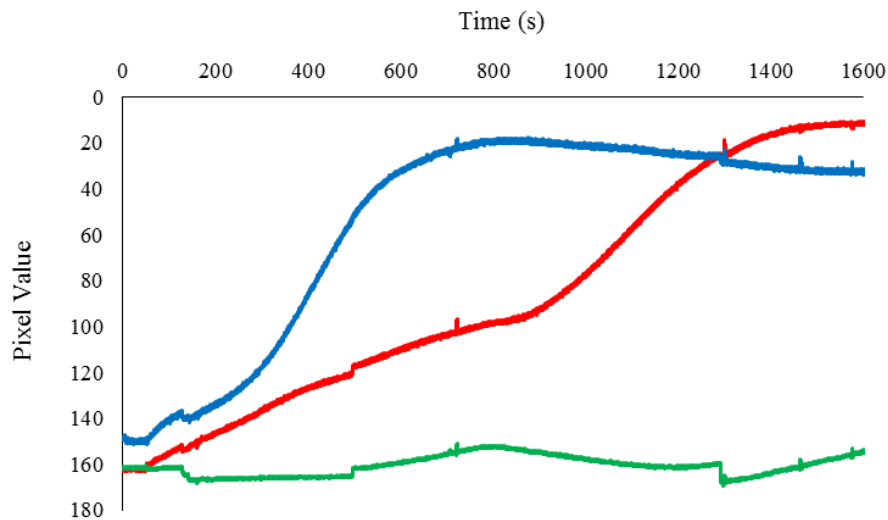
Figure 5.51 Right side RGB analysis of 1:3 mixture of SQ1 and half squaraine with noise reduction.

The left side RGB data show a smoother initial start, followed by a high gradient change in pixel value in the first 200 seconds. The pixel values then gradually level out. The drop in RGB values between 500 and 1300 seconds is most likely an artefact, caused by a light being switched off outside the room and then turned back on again. The right side RGB data show a more gradual rate of change and some spikes in light levels most likely due to people walking past the lab.

128

5.11 Conclusions from Ultrafast Dye Uptake

This chapter has proven that ultrafast dye uptake can be successfully monitored using RGB analysis. In addition it has shown that a wide range of dyes from ruthenium based dyes to organic dyes are well suited to ultrafast dyeing. The fast dye process has also been successfully upscaled to allow sensitisation of devices as long as 15 cm.

The setup for the ultrafast dye analysis has been developed and adapted for noise reduction. This has been shown by the substantial drop in control deviation from the initial experiments (Figure 5.52) to the final experiment (Figure 5.53).
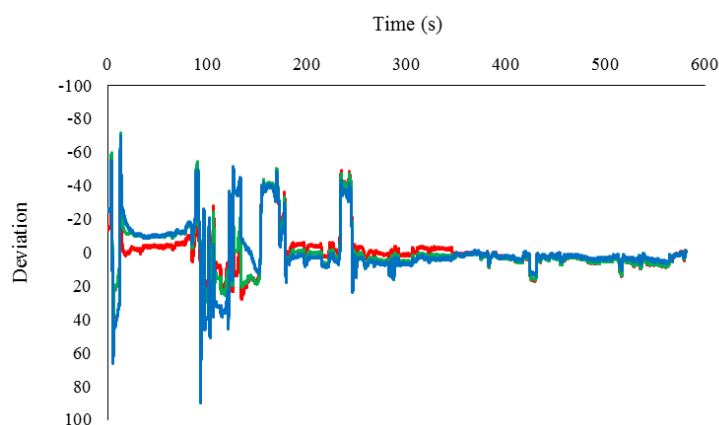
Figure 5.52 Left side control mean deviation for the first experiment.
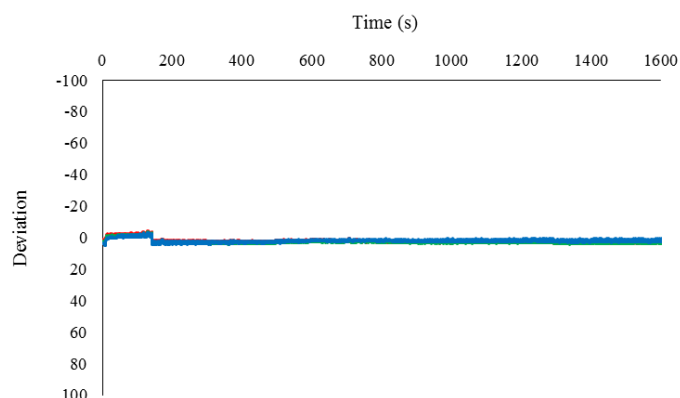
Figure 5.53 Control deviation for the final experiment.

The significant decrease in noise levels between Figure 5.52 and Figure 5.53 shows that the imaging process has be successfully optimised to monitor dye uptake on mesoporous TiO_2 films.

129

Chapter 6 Conclusions

6.1 General Conclusions

At the start of this thesis, the aim was to investigate two key challenges for DSSC technology: device lifetime and processing.

The device lifetime presented several challenges to be overcome. The first being the number of samples. DSSC is a multicomponent device each of which can be varied including the photoelectrode, substrate, particle size, dyes, electrolytes, counter electrode, additives and encapsulation. To compare different variables, a large number of devices would need to be constructed and monitored for degradation. Due to the process developed in this thesis it would now be possible to measure 100 samples simultaneously. It was also crucial that there was consistent initial IV data from devices to ensure reliable trends in data. Even small differences in the performance of devices could affect the results so consistency was achieved. Additionally running devices simultaneously was required to ensure consistency, especially when exposed to natural light which would vary significantly. Development of accelerated testing using dyed electrodes was vital as exposing devices to 10,000 h of real-time exposure would take far too long. Accurate timing of the length of the tests was also required to determine the total exposure time for devices. The automation of the experiments was another challenge presented by the lifetime work. The size of devices needed to be consistent, so that when the analysis was run using the macro the correct areas were analysed. The method for lifetime analysis also needed to be saleable so larger devices could be tested if necessary. A range of testing conditions also needed to be developed to allow artificial and natural light exposure. Another obstacle was the cost of analytical equipment, which needed to be kept to a minimum to have an advantage over using a solar simulator. Setup of the image analysis method described in this thesis would cost under £300 compared to much higher costs for a solar simulator of £8000[193].

The other key challenge was the device processing. The different steps and timings needed to be appropriate for upscaling devices. First the larger devices needed to be constructed and sealed sufficiently for the fast dye process to be successfully completed. Next the device holder needed to be adapted to hold large scale commercial

devices. Passive dyeing would originally take 18 hours and required a large dye bath, the fast dye process needed to be setup to sensitise the dye in the minimum possible time. In situ imaging of multiple dyes off the same pump was another challenge.

This thesis has studied the correlation between device colour changes in RGB values extracted from digital images and degradation of devices. RGB analysis has been conducted on large scale devices and on many smaller devices simultaneously. The alternative option is to measure DSSC device performance is to test each device individually on a solar simulator. After the initial test, devices be light soaked and re-tested to monitor degradation. The disadvantage of using a solar simulator for measurements is that it is expensive (£8,000 for a commercial solar simulator capable of measuring a 2 cm^2 area[193]) and only one device could be tested at a time unless a multiplexer was used.

The work conducted on dye uptake in this thesis has shown that the fast dye process can be successfully upscaled. Initial devices sensitised using the fast dye process consisted of 0.5 x 2 cm test cells, these were upscaled to 1 x 15 cm devices. This thesis has also shown the progress of the dye uptake can be monitored. The gradient of plotted RGB values shows the progress of dye uptake. When the gradient remains constant, the fast dye process is complete.

In the future the process of imaging cells will likely be used by manufacturers of DSSC devices for optimisation and quality control. This will hopefully provide a better quality end product at an affordable price, making the technology more widely available.

6.2 Future work

The fast dye setup could be used for sensitisation of large scale devices which would be suitable for use on buildings or solar farms. From this manufacturers of dye sensitised solar cells could accelerate and optimise their dyeing processes. The dyeing process could be monitored with RGB analysis and the time taken for complete and uniform sorption of the dye to the TiO$_2$ could be determined. This optimum time could then be used for dyeing all the devices of that specification. The flow rate of the pump could also be increased to speed up the fast dye process and the imaging could ensure

that the dye coverage on the TiO_2 was complete. Different optimums could be determined and implemented for a range of dyes and variations in the original specifications of cells. This would have the advantage of reducing the construction cost of the cell as the optimum amount of dye could be used. The manufacturers could also use the RGB analysis on their end products as a form of quality control. This could be used to check for defects in the TiO_2, leaked electrolyte or degradation of the dye or electrolyte. Devices which did not meet the required level of quality could then be excluded from sales. This process could then be setup on a production line with images taken at regular intervals so each device could be analysed without slowing production.

Further development of the degradation setup in the lightbox would be beneficial as it would allow a more detailed analysis of the link between the RGB values and device degradation. This could be automated with a solar simulator and a programmed switching system. The devices could then all be linked to the solar simulator with a multiplexer. Once activated the multiplexer could close one relay at a time, completing the circuit and linking cell. A delay between the activation of the next relay would allow the solar simulator to run an IV curve for the connected cell. When the first one had been completed the second relay could be activated and the process could be repeated. Once all the cells had been completed, none of the relays would be closed and the circuit would be in an off state where none of the devices were connected to the solar simulator. This would allow the cells to remain at open circuit between IV curves being run. This setup would allow cells to be tested on a more frequent basis since the minimum time between measurements would be the time taken for a complete set of IV curves to be taken. The measurement of each cell would take under 30 seconds so a set of 60 cells could be measured every half hour. This alone could yield some very interesting data on the degradation process showing whether there is a sudden drop in cell efficiency or a more gradual decline. This data could then be compared directly to the RGB data to measure the correlation between the two. This whole process could be automated which would allow continuous measurements of data throughout the day and night, allowing for a much more detailed analysis.

The other way the dye uptake could be monitored is by implementing a flow cell into the dye outtake which could be placed inside a UV-Vis spectrometer during processing. A flow cell is a cuvette with two tubes attached so liquids can flow into

and out of the cell. This would allow the dye from the outtake to pass into the flow cell where the absorbance could be measured. Measurements on the UV-Vis spectrometer could be automated to run every minute which would monitor the concentration of the dye. If the dye outtake concentration is lower than the stock solution then this means dye is sorbing to the TiO_2 surface on the device. This is shown in Figure 6.1.
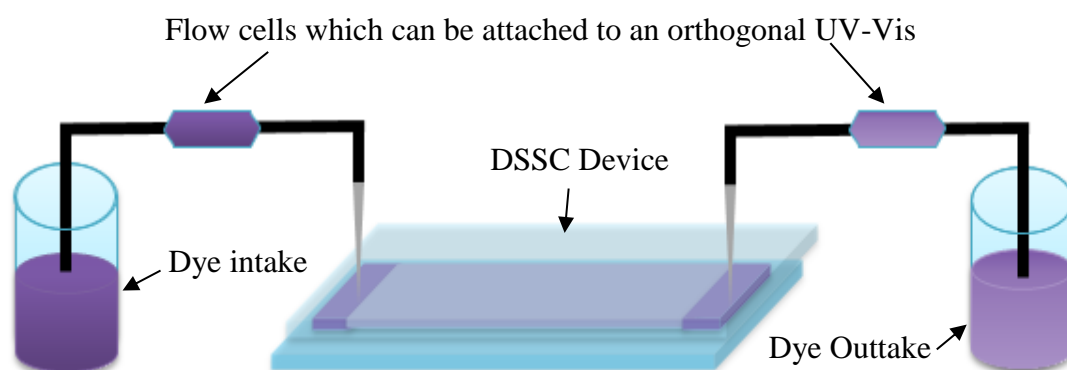
Figure 6.1 Setup for operando dye uptake. Dye is measured prior to entering the cell and at the outtake. When the absorbance of the flow cell at the dye outtake is the same as the one at the dye intake the device has become fully sensitised as no more dye is sorbing onto the device.

Differences would be especially noticeable at the start of the fast dyeing process as the dye concentration would be considerably lower after passing through the cell due to the high number of free sites available for dye on the TiO_2 surface. As more of these sites are occupied the sorption will slow down and there will be a gradual increase in the concentration of the dye passing though the flow cell. When all of the sites on the TiO_2 have been occupied the concentration of the dye in the flow cell will be the same as the stock solution. Therefore once the absorbance of the flow cell is the same as the stock the end point has been reached and the dyeing process is complete. To determine if the dye had formed an optimum monolayer and not aggregated, multiple cells could be tested by solar simulation and image analysis. The cells would be tested across a range of dyeing times and corresponding RGB values to determine the cell with the highest efficiency could. The optimum RGB value from the device with the highest efficiency could then be used to determine the end point.

Chapter 7 Appendices

7.1 Image Analysis Macro

```
Sub Main
Dim App As Object
Set App = CreateObject("SigmaScan.Application")
Dim Worksheet As Object
' Recorded macro begins...
Dim IMG_0001 As Object
Dim intN As Integer
Dim strPic As String
Set Worksheet = App.GetWorksheet
For INTN= 0 To 10000
If INTN <10 Then
strpic = "C:\Documents and Settings\user1\Desktop\Multi Grid\IMG_" & "000" &
intN & ".jpg"
ElseIf INTN<100 Then
strpic = "C:\Documents and Settings\user1\Desktop\Multi Grid\IMG_" & "00" & intN
& ".jpg"
Elseif INTN <1000 Then
strpic = "C:\Documents and Settings\user1\Desktop\Multi Grid\IMG_" & "0" & intN
& ".jpg"
Elseif INTN <10000 Then
strpic = "C:\Documents and Settings\user1\Desktop\Multi Grid\IMG_" & intN &
".jpg"
End If
If Dir(strpic) <>"" Then'we have aqn image
Set IMG_0001 = App.OpenImage(strpic)
Worksheet.Show
Worksheet.MakePermanent
ResultCode = IMG_0001.MeasurementLeftClick(2000, 700)
ResultCode = IMG_0001.MeasurementLeftClick(2120, 700)
ResultCode = IMG_0001.MeasurementLeftClick(2120, 580)
```

ResultCode = IMG_0001.MeasurementLeftClick(2000, 580)

ResultCode = IMG_0001.MeasurementRightClick(2000, 700)

ResultCode = IMG_0001.MeasurementLeftClick(2120, 700)

ResultCode = IMG_0001.MeasurementLeftClick(2240, 700)

ResultCode = IMG_0001.MeasurementLeftClick(2240, 580)

ResultCode = IMG_0001.MeasurementLeftClick(2120, 580)

ResultCode = IMG_0001.MeasurementRightClick(2120, 700)

ResultCode = IMG_0001.MeasurementLeftClick(2000, 580)

ResultCode = IMG_0001.MeasurementLeftClick(2120, 580)

ResultCode = IMG_0001.MeasurementLeftClick(2120, 460)

ResultCode = IMG_0001.MeasurementLeftClick(2000, 460)

ResultCode = IMG_0001.MeasurementRightClick(2000, 580)

ResultCode = IMG_0001.MeasurementLeftClick(2120, 580)

ResultCode = IMG_0001.MeasurementLeftClick(2240, 580)

ResultCode = IMG_0001.MeasurementLeftClick(2240, 460)

ResultCode = IMG_0001.MeasurementLeftClick(2120, 460)

ResultCode = IMG_0001.MeasurementRightClick(2120, 580)

ResultCode = IMG_0001.MeasurementLeftClick(1360, 1340)

ResultCode = IMG_0001.MeasurementLeftClick(1480, 1340)

ResultCode = IMG_0001.MeasurementLeftClick(1480, 1220)

ResultCode = IMG_0001.MeasurementLeftClick(1360, 1220)

ResultCode = IMG_0001.MeasurementRightClick(1360, 1340)

ResultCode = IMG_0001.MeasurementLeftClick(1480, 1340)

ResultCode = IMG_0001.MeasurementLeftClick(1600, 1340)

ResultCode = IMG_0001.MeasurementLeftClick(1600, 1220)

ResultCode = IMG_0001.MeasurementLeftClick(1480, 1220)

ResultCode = IMG_0001.MeasurementRightClick(1480, 1340)

ResultCode = IMG_0001.MeasurementLeftClick(1360, 1220)

ResultCode = IMG_0001.MeasurementLeftClick(1480, 1220)

ResultCode = IMG_0001.MeasurementLeftClick(1480, 1100)

ResultCode = IMG_0001.MeasurementLeftClick(1360, 1100)

ResultCode = IMG_0001.MeasurementRightClick(1360, 1220)

ResultCode = IMG_0001.MeasurementLeftClick(1480, 1220)

ResultCode = IMG_0001.MeasurementLeftClick(1600, 1220)

ResultCode = IMG_0001.MeasurementLeftClick(1600, 1100)

ResultCode = IMG_0001.MeasurementLeftClick(1480, 1100)

ResultCode = IMG_0001.MeasurementRightClick(1480, 1220)

ResultCode = IMG_0001.MeasurementLeftClick(2000, 1340)

ResultCode = IMG_0001.MeasurementLeftClick(2120, 1340)

ResultCode = IMG_0001.MeasurementLeftClick(2120, 1220)

ResultCode = IMG_0001.MeasurementLeftClick(2000, 1220)

ResultCode = IMG_0001.MeasurementRightClick(2000, 1340)

ResultCode = IMG_0001.MeasurementLeftClick(2120, 1340)

ResultCode = IMG_0001.MeasurementLeftClick(2240, 1340)

ResultCode = IMG_0001.MeasurementLeftClick(2240, 1220)

ResultCode = IMG_0001.MeasurementLeftClick(2120, 1220)

ResultCode = IMG_0001.MeasurementRightClick(2120, 1340)

ResultCode = IMG_0001.MeasurementLeftClick(2000, 1220)

ResultCode = IMG_0001.MeasurementLeftClick(2120, 1220)

ResultCode = IMG_0001.MeasurementLeftClick(2120, 1100)

ResultCode = IMG_0001.MeasurementLeftClick(2000, 1100)

ResultCode = IMG_0001.MeasurementRightClick(2000, 1220)

ResultCode = IMG_0001.MeasurementLeftClick(2120, 1220)

ResultCode = IMG_0001.MeasurementLeftClick(2240, 1220)

ResultCode = IMG_0001.MeasurementLeftClick(2240, 1100)

ResultCode = IMG_0001.MeasurementLeftClick(2120, 1100)

ResultCode = IMG_0001.MeasurementRightClick(2120, 1220)

ResultCode = IMG_0001.MeasurementLeftClick(2640, 1340)

ResultCode = IMG_0001.MeasurementLeftClick(2760, 1340)

ResultCode = IMG_0001.MeasurementLeftClick(2760, 1220)

ResultCode = IMG_0001.MeasurementLeftClick(2640, 1220)

ResultCode = IMG_0001.MeasurementRightClick(2640, 1340)

ResultCode = IMG_0001.MeasurementLeftClick(2760, 1340)

ResultCode = IMG_0001.MeasurementLeftClick(2880, 1340)

ResultCode = IMG_0001.MeasurementLeftClick(2880, 1220)

ResultCode = IMG_0001.MeasurementLeftClick(2760, 1220)

ResultCode = IMG_0001.MeasurementRightClick(2760, 1340)

ResultCode = IMG_0001.MeasurementLeftClick(2640, 1220)

ResultCode = IMG_0001.MeasurementLeftClick(2760, 1220)

ResultCode = IMG_0001.MeasurementLeftClick(2760, 1100)

ResultCode = IMG_0001.MeasurementLeftClick(2640, 1100)

ResultCode = IMG_0001.MeasurementRightClick(2640, 1220)

ResultCode = IMG_0001.MeasurementLeftClick(2760, 1220)

ResultCode = IMG_0001.MeasurementLeftClick(2880, 1220)

ResultCode = IMG_0001.MeasurementLeftClick(2880, 1100)

ResultCode = IMG_0001.MeasurementLeftClick(2760, 1100)

ResultCode = IMG_0001.MeasurementRightClick(2760, 1220)

ResultCode = IMG_0001.MeasurementLeftClick(1360, 1970)

ResultCode = IMG_0001.MeasurementLeftClick(1480, 1970)

ResultCode = IMG_0001.MeasurementLeftClick(1480, 1850)

ResultCode = IMG_0001.MeasurementLeftClick(1360, 1850)

ResultCode = IMG_0001.MeasurementRightClick(1360, 1970)

ResultCode = IMG_0001.MeasurementLeftClick(1480, 1970)

ResultCode = IMG_0001.MeasurementLeftClick(1600, 1970)

ResultCode = IMG_0001.MeasurementLeftClick(1600, 1850)

ResultCode = IMG_0001.MeasurementLeftClick(1480, 1850)

ResultCode = IMG_0001.MeasurementRightClick(1480, 1970)

ResultCode = IMG_0001.MeasurementLeftClick(1360, 1850)

ResultCode = IMG_0001.MeasurementLeftClick(1480, 1850)

ResultCode = IMG_0001.MeasurementLeftClick(1480, 1730)

ResultCode = IMG_0001.MeasurementLeftClick(1360, 1730)

ResultCode = IMG_0001.MeasurementRightClick(1360, 1850)

ResultCode = IMG_0001.MeasurementLeftClick(1480, 1850)

ResultCode = IMG_0001.MeasurementLeftClick(1600, 1850)

ResultCode = IMG_0001.MeasurementLeftClick(1600, 1730)

ResultCode = IMG_0001.MeasurementLeftClick(1480, 1730)

ResultCode = IMG_0001.MeasurementRightClick(1480, 1850)

ResultCode = IMG_0001.MeasurementLeftClick(2000, 1970)

ResultCode = IMG_0001.MeasurementLeftClick(2120, 1970)

ResultCode = IMG_0001.MeasurementLeftClick(2120, 1850)

ResultCode = IMG_0001.MeasurementLeftClick(2000, 1850)

ResultCode = IMG_0001.MeasurementRightClick(2000, 1970)

ResultCode = IMG_0001.MeasurementLeftClick(2120, 1970)

ResultCode = IMG_0001.MeasurementLeftClick(2240, 1970)

ResultCode = IMG_0001.MeasurementLeftClick(2240, 1850)

ResultCode = IMG_0001.MeasurementLeftClick(2120, 1850)

ResultCode = IMG_0001.MeasurementRightClick(2120, 1970)

ResultCode = IMG_0001.MeasurementLeftClick(2000, 1850)

ResultCode = IMG_0001.MeasurementLeftClick(2120, 1850)

ResultCode = IMG_0001.MeasurementLeftClick(2120, 1730)

ResultCode = IMG_0001.MeasurementLeftClick(2000, 1730)

ResultCode = IMG_0001.MeasurementRightClick(2000, 1850)

ResultCode = IMG_0001.MeasurementLeftClick(2120, 1850)

ResultCode = IMG_0001.MeasurementLeftClick(2240, 1850)

ResultCode = IMG_0001.MeasurementLeftClick(2240, 1730)

ResultCode = IMG_0001.MeasurementLeftClick(2120, 1730)

ResultCode = IMG_0001.MeasurementRightClick(2120, 1850)

ResultCode = IMG_0001.MeasurementLeftClick(2640, 1970)

ResultCode = IMG_0001.MeasurementLeftClick(2760, 1970)

ResultCode = IMG_0001.MeasurementLeftClick(2760, 1850)

ResultCode = IMG_0001.MeasurementLeftClick(2640, 1850)

ResultCode = IMG_0001.MeasurementRightClick(2640, 1970)

ResultCode = IMG_0001.MeasurementLeftClick(2760, 1970)

ResultCode = IMG_0001.MeasurementLeftClick(2880, 1970)

ResultCode = IMG_0001.MeasurementLeftClick(2880, 1850)

ResultCode = IMG_0001.MeasurementLeftClick(2760, 1850)

ResultCode = IMG_0001.MeasurementRightClick(2760, 1970)

ResultCode = IMG_0001.MeasurementLeftClick(2640, 1850)

ResultCode = IMG_0001.MeasurementLeftClick(2760, 1850)

ResultCode = IMG_0001.MeasurementLeftClick(2760, 1730)

ResultCode = IMG_0001.MeasurementLeftClick(2640, 1730)

ResultCode = IMG_0001.MeasurementRightClick(2640, 1850)

ResultCode = IMG_0001.MeasurementLeftClick(2760, 1850)

ResultCode = IMG_0001.MeasurementLeftClick(2880, 1850)

ResultCode = IMG_0001.MeasurementLeftClick(2880, 1730)

ResultCode = IMG_0001.MeasurementLeftClick(2760, 1730)

ResultCode = IMG_0001.MeasurementRightClick(2760, 1850)

ResultCode = IMG_0001.MeasurementLeftClick(1360, 2610)

ResultCode = IMG_0001.MeasurementLeftClick(1480, 2610)

ResultCode = IMG_0001.MeasurementLeftClick(1480, 2490)

ResultCode = IMG_0001.MeasurementLeftClick(1360, 2490)

ResultCode = IMG_0001.MeasurementRightClick(1360, 2610)

ResultCode = IMG_0001.MeasurementLeftClick(1480, 2610)

ResultCode = IMG_0001.MeasurementLeftClick(1600, 2610)

ResultCode = IMG_0001.MeasurementLeftClick(1600, 2490)

ResultCode = IMG_0001.MeasurementLeftClick(1480, 2490)

ResultCode = IMG_0001.MeasurementRightClick(1480, 2610)

ResultCode = IMG_0001.MeasurementLeftClick(1360, 2490)

ResultCode = IMG_0001.MeasurementLeftClick(1480, 2490)

ResultCode = IMG_0001.MeasurementLeftClick(1480, 2370)

ResultCode = IMG_0001.MeasurementLeftClick(1360, 2370)

ResultCode = IMG_0001.MeasurementRightClick(1360, 2490)

ResultCode = IMG_0001.MeasurementLeftClick(1480, 2490)

ResultCode = IMG_0001.MeasurementLeftClick(1600, 2490)

ResultCode = IMG_0001.MeasurementLeftClick(1600, 2370)

ResultCode = IMG_0001.MeasurementLeftClick(1480, 2370)

ResultCode = IMG_0001.MeasurementRightClick(1480, 2490)

ResultCode = IMG_0001.MeasurementLeftClick(2000, 2610)

ResultCode = IMG_0001.MeasurementLeftClick(2120, 2610)

ResultCode = IMG_0001.MeasurementLeftClick(2120, 2490)

ResultCode = IMG_0001.MeasurementLeftClick(2000, 2490)

ResultCode = IMG_0001.MeasurementRightClick(2000, 2610)

ResultCode = IMG_0001.MeasurementLeftClick(2120, 2610)

ResultCode = IMG_0001.MeasurementLeftClick(2240, 2610)

ResultCode = IMG_0001.MeasurementLeftClick(2240, 2490)

ResultCode = IMG_0001.MeasurementLeftClick(2120, 2490)

ResultCode = IMG_0001.MeasurementRightClick(2120, 2610)

ResultCode = IMG_0001.MeasurementLeftClick(2000, 2490)

ResultCode = IMG_0001.MeasurementLeftClick(2120, 2490)

ResultCode = IMG_0001.MeasurementLeftClick(2120, 2370)

ResultCode = IMG_0001.MeasurementLeftClick(2000, 2370)

ResultCode = IMG_0001.MeasurementRightClick(2000, 2490)

ResultCode = IMG_0001.MeasurementLeftClick(2120, 2490)

ResultCode = IMG_0001.MeasurementLeftClick(2240, 2490)

ResultCode = IMG_0001.MeasurementLeftClick(2240, 2370)

ResultCode = IMG_0001.MeasurementLeftClick(2120, 2370)

ResultCode = IMG_0001.MeasurementRightClick(2120, 2490)

ResultCode = IMG_0001.MeasurementLeftClick(2640, 2610)

ResultCode = IMG_0001.MeasurementLeftClick(2760, 2610)

ResultCode = IMG_0001.MeasurementLeftClick(2760, 2490)

ResultCode = IMG_0001.MeasurementLeftClick(2640, 2490)

ResultCode = IMG_0001.MeasurementRightClick(2640, 2610)

ResultCode = IMG_0001.MeasurementLeftClick(2760, 2610)

ResultCode = IMG_0001.MeasurementLeftClick(2880, 2610)

ResultCode = IMG_0001.MeasurementLeftClick(2880, 2490)

ResultCode = IMG_0001.MeasurementLeftClick(2760, 2490)

ResultCode = IMG_0001.MeasurementRightClick(2760, 2610)

ResultCode = IMG_0001.MeasurementLeftClick(2640, 2490)

ResultCode = IMG_0001.MeasurementLeftClick(2760, 2490)

ResultCode = IMG_0001.MeasurementLeftClick(2760, 2370)

ResultCode = IMG_0001.MeasurementLeftClick(2640, 2370)

ResultCode = IMG_0001.MeasurementRightClick(2640, 2490)

ResultCode = IMG_0001.MeasurementLeftClick(2760, 2490)

ResultCode = IMG_0001.MeasurementLeftClick(2880, 2490)

ResultCode = IMG_0001.MeasurementLeftClick(2880, 2370)

ResultCode = IMG_0001.MeasurementLeftClick(2760, 2370)

ResultCode = IMG_0001.MeasurementRightClick(2760, 2490)

```
            Set IMG_0001=Nothing
            End If
        Next INTN
    'Recorded Macro Ends
End Sub
```
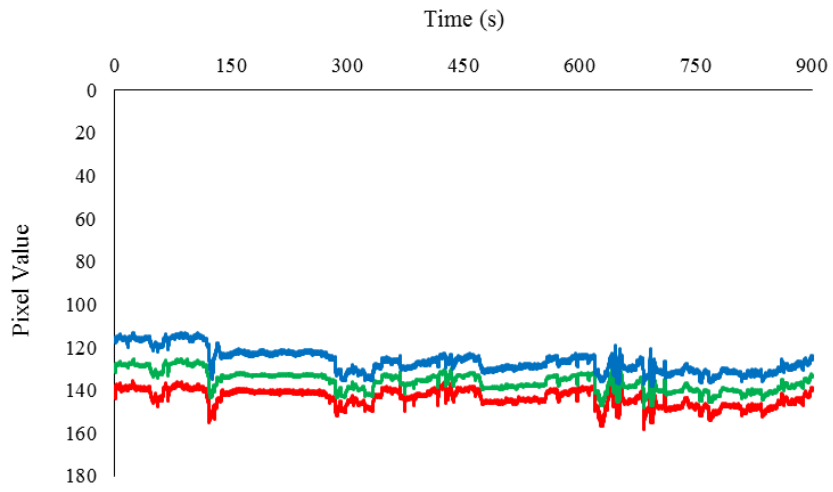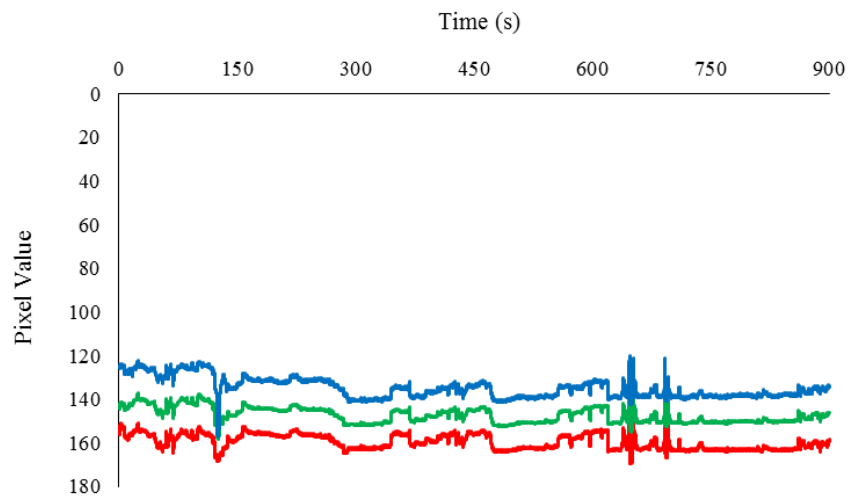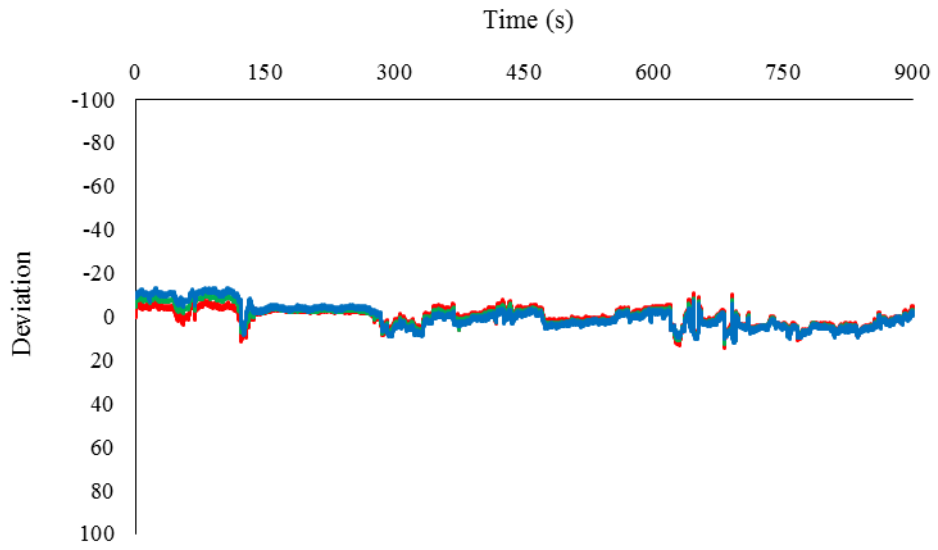
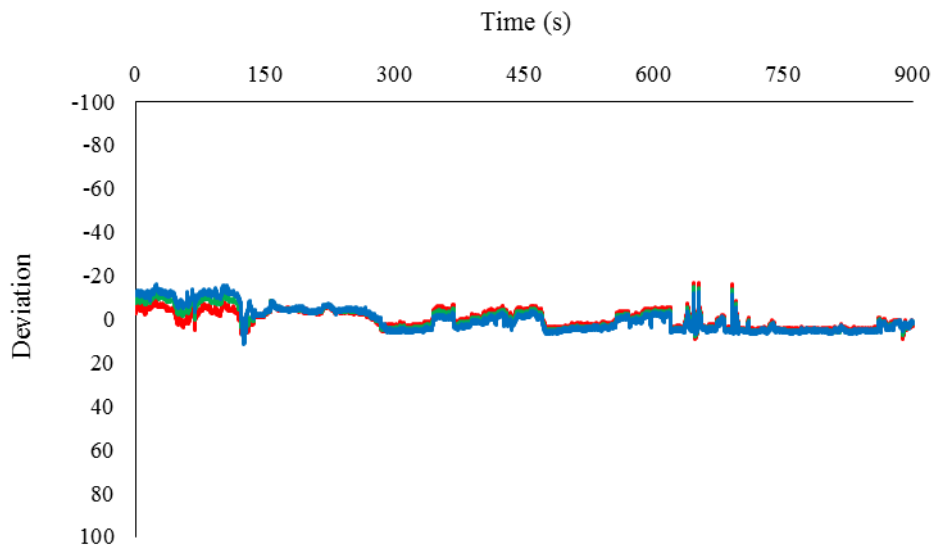## 7.2 Raw Data from Image Analysis

Figure 7.1 Control for left side of N719 RGB analysis on 18NRT Paste.
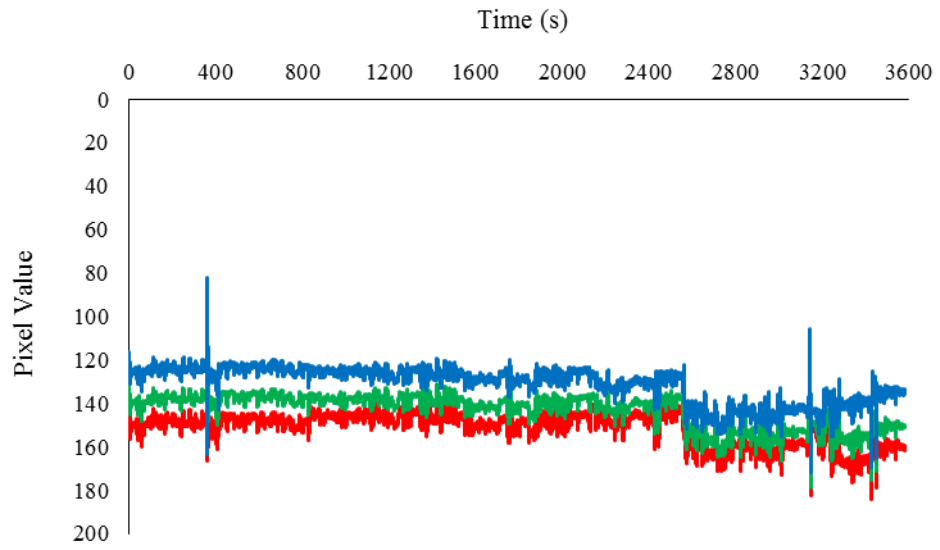

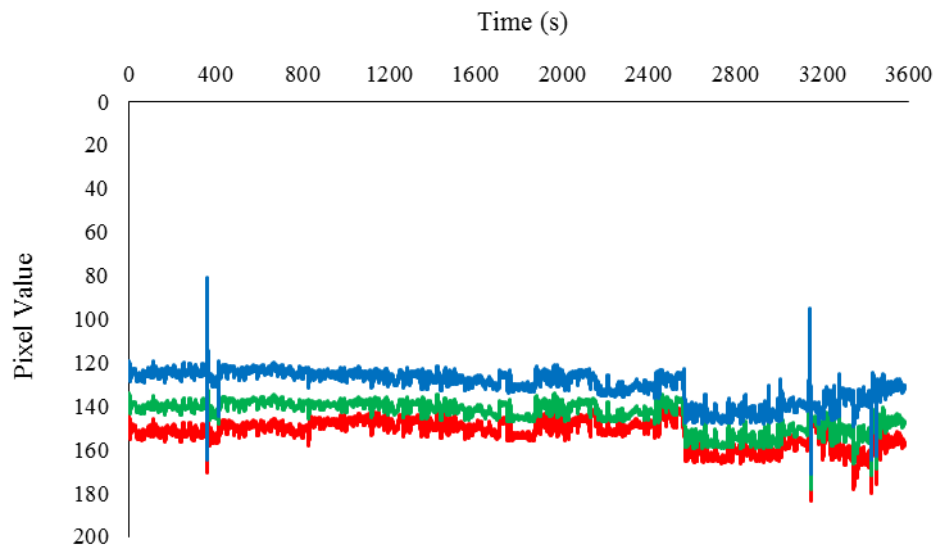**Figure 7.2** Control for right side of N719 RGB analysis on 18NRT Paste.

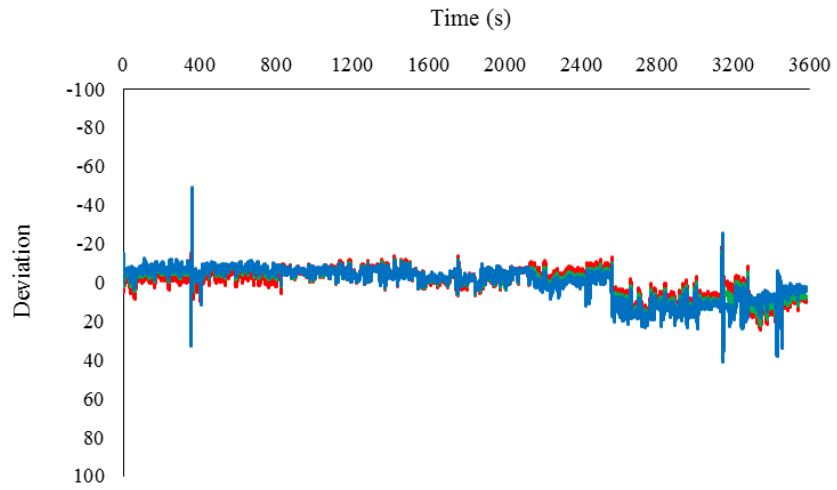**Figure 7.3** Control deviation for left side of N719 RGB analysis on 18NRT.

Figure 7.4 Control deviation for right side of N719 RGB analysis on 18NRT.
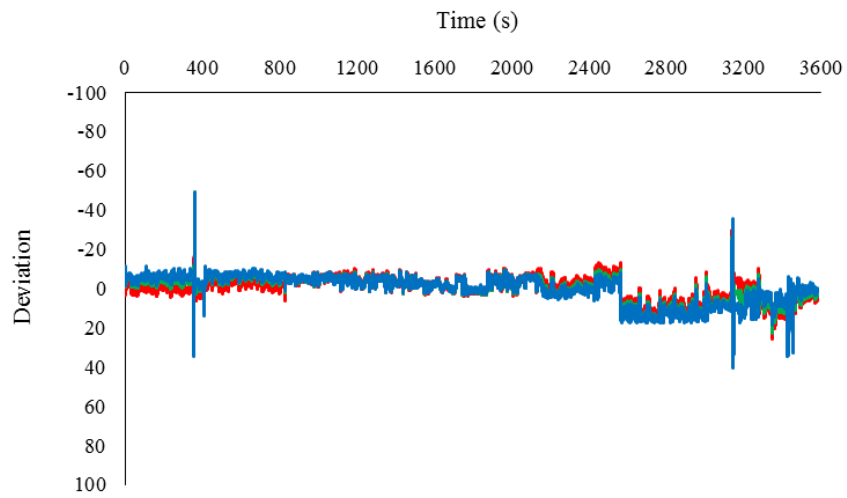
Figure 7.5 Control for left side of SQ2 RGB analysis.

Figure 7.6 Control for right side of SQ2 RGB analysis.

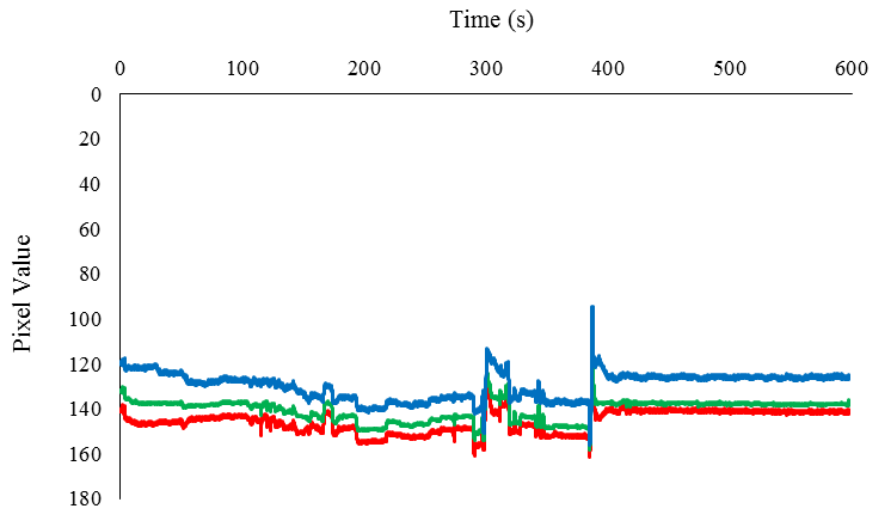**Figure 7.7** Control deviation for left side of SQ2 RGB analysis.

Figure 7.8 Control deviation for right side of SQ2 RGB analysis.

Figure 7.9 Control for left side of D131 RGB analysis.

Figure 7.10 Control for right side of D131 RGB analysis.

Figure 7.11 Control deviation for left side of D131 RGB analysis.
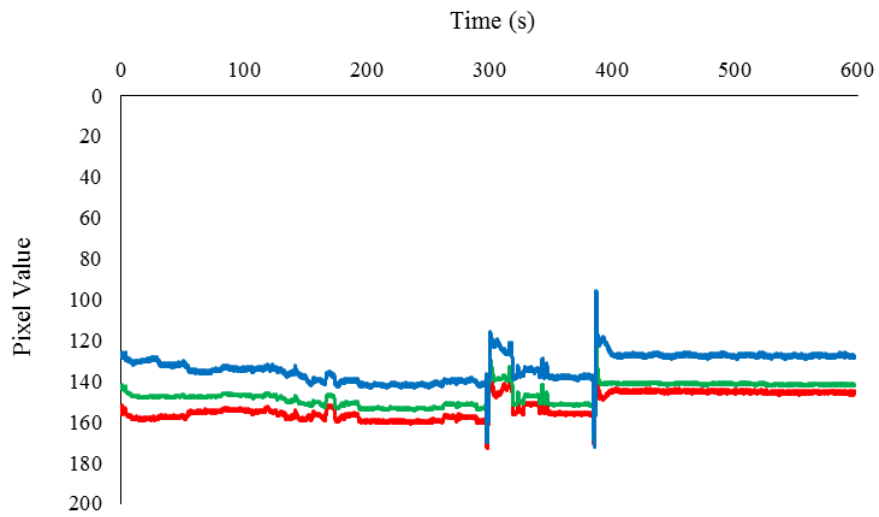

Figure 7.12 Control deviation for right side of D131 RGB analysis.

Figure 7.13 Control for left side of half squaraine RGB analysis.
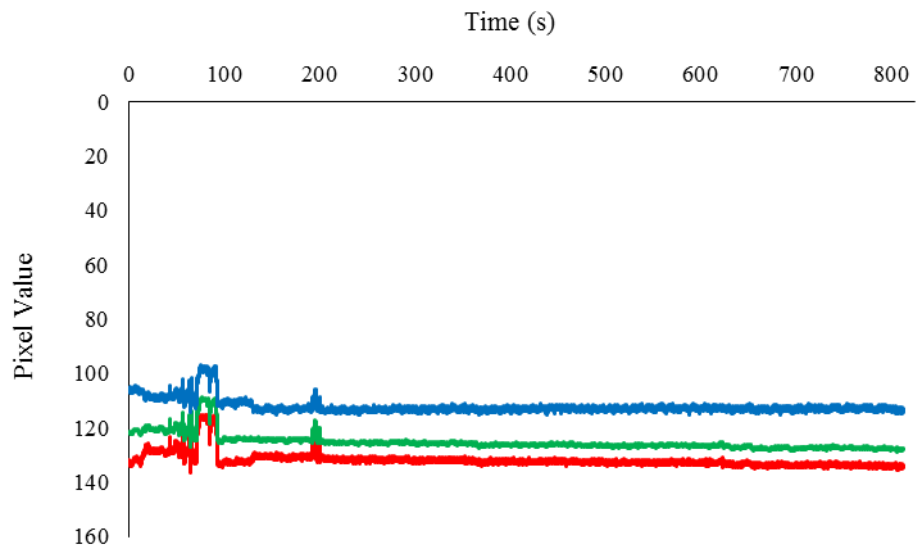
Figure 7.14 Control for right side of half squaraine RGB analysis.
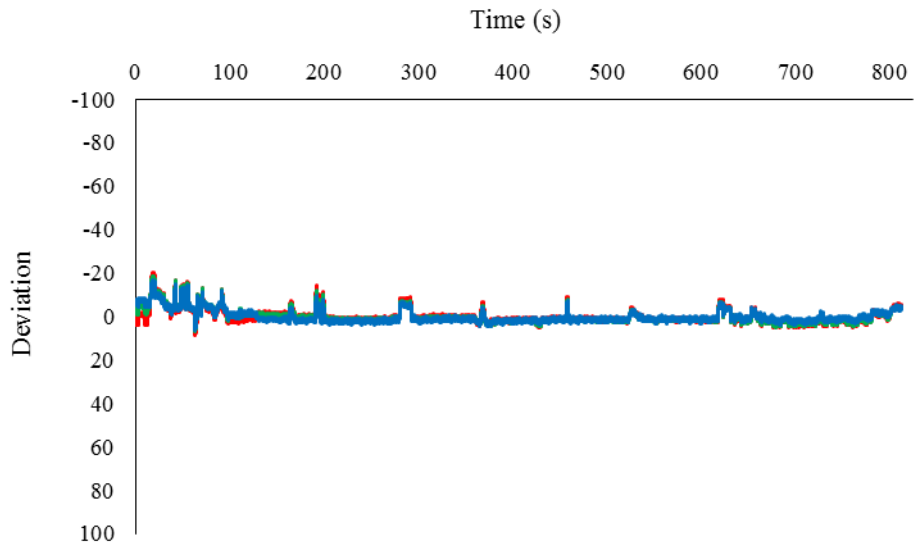
Figure 7.15 Control deviation for left side of half squaraine RGB analysis.
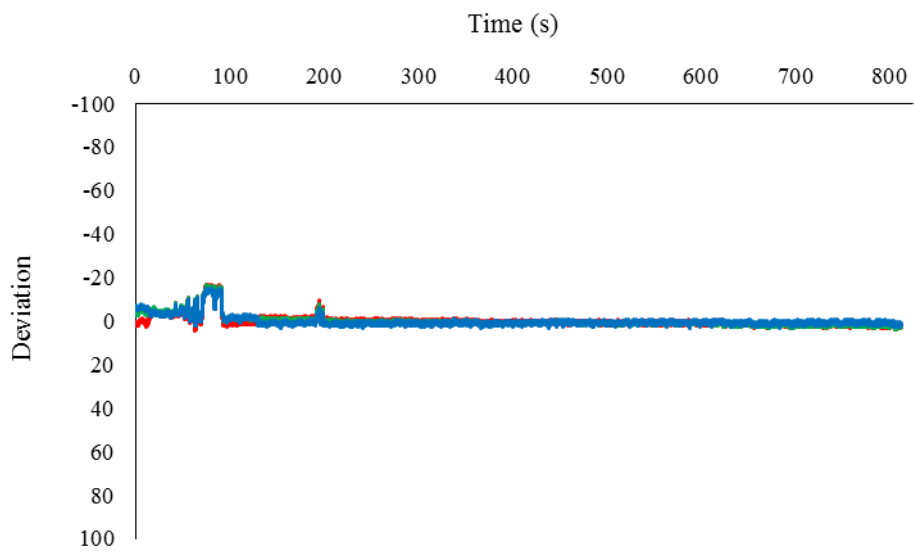
Figure 7.16 Control deviation for right side of half squaraine RGB analysis.
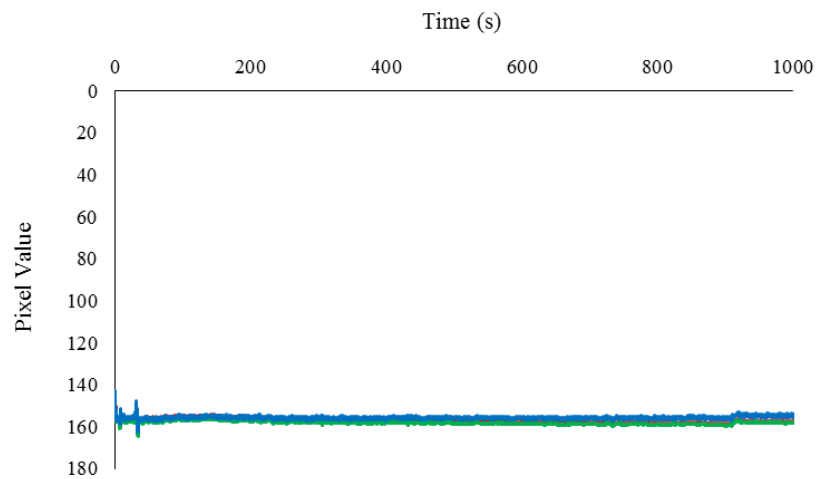
Figure 7.17 Control for left side of Rhodamine B RGB analysis.
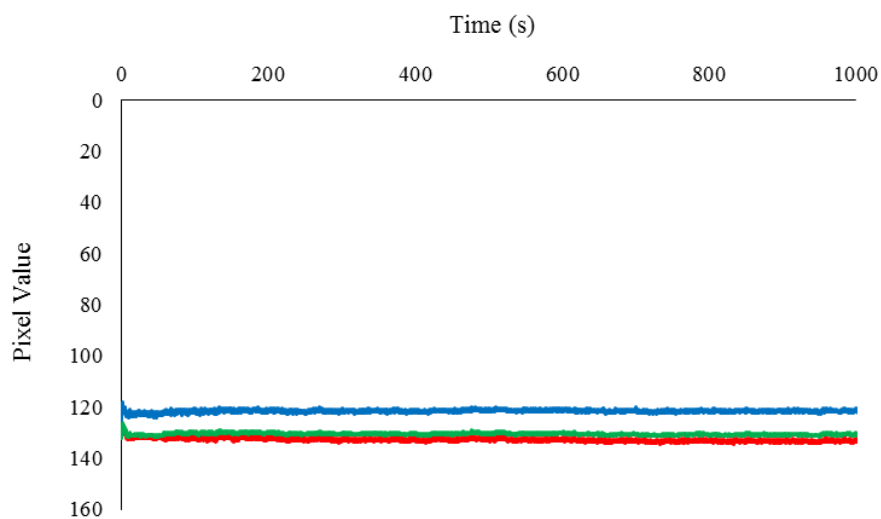
Figure 7.18 Control for right side of Rhodamine B RGB analysis.
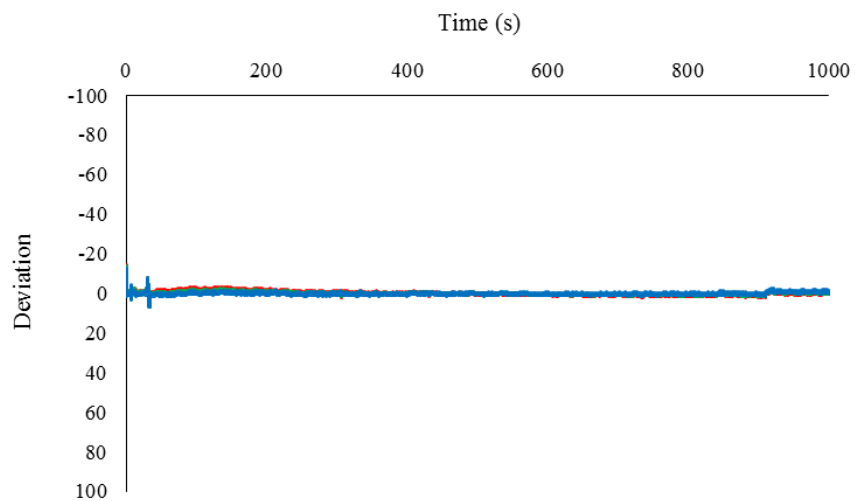
Figure 7.19 Control deviation for left side of Rhodamine B RGB analysis.
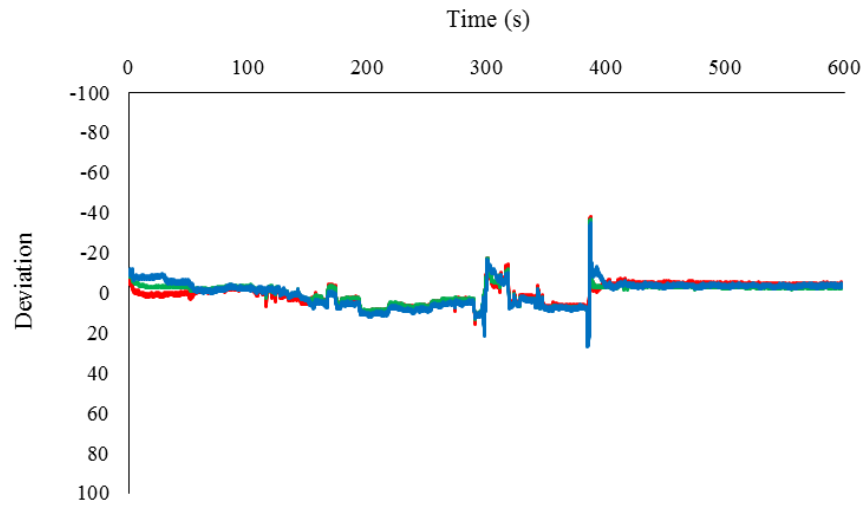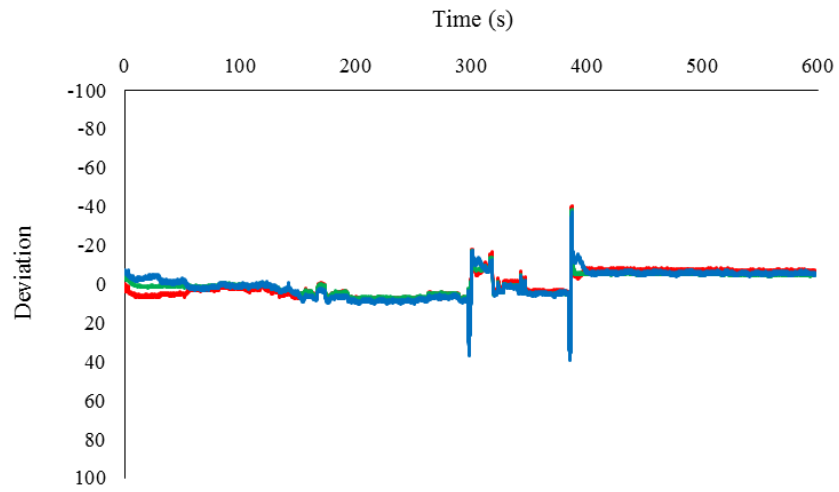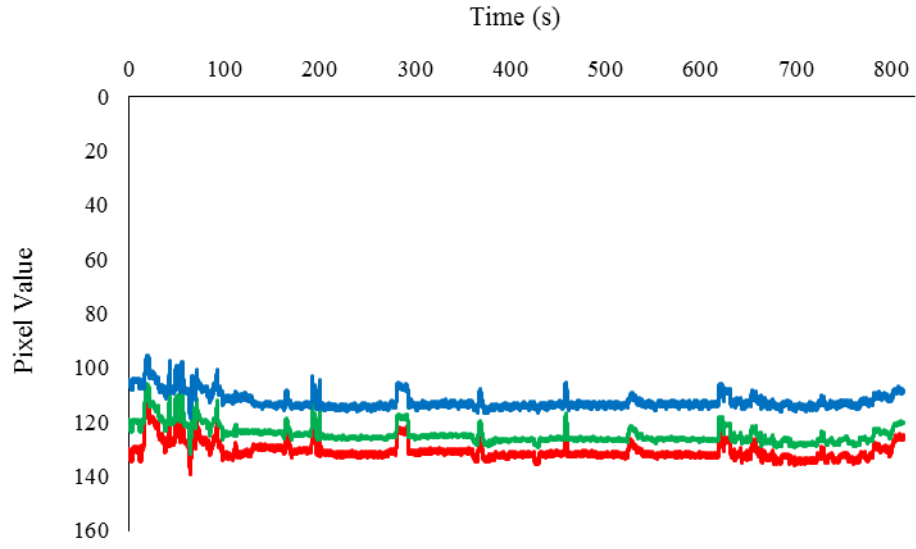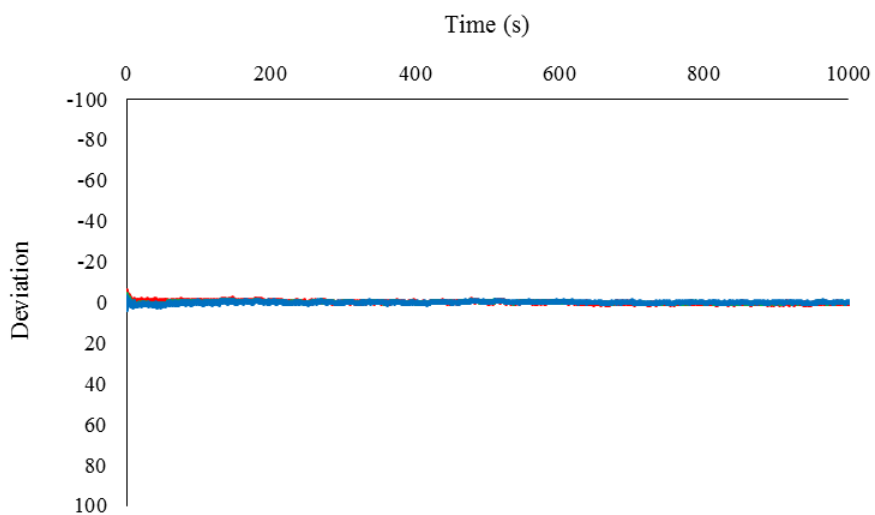

Figure 7.20 Control deviation for right side of Rhodamine B RGB analysis.
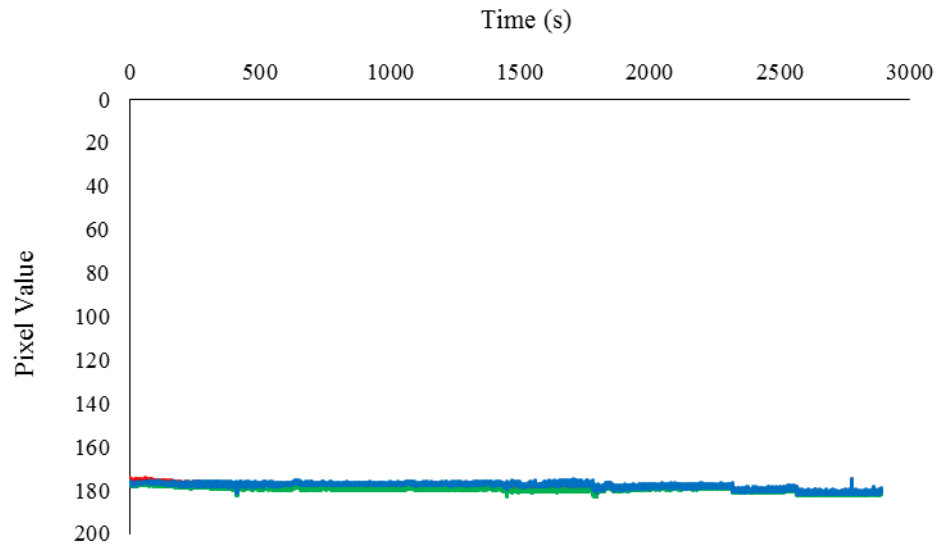
Figure 7.21 Control for left side of half squaraine then SQ1 RGB analysis.
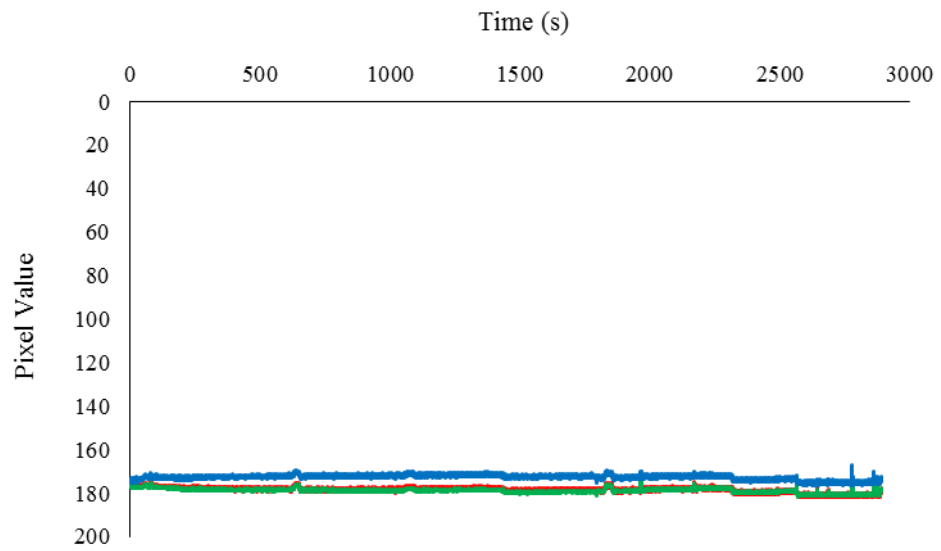
Figure 7.22 Control for right side of half squaraine then SQ1 RGB analysis.

151
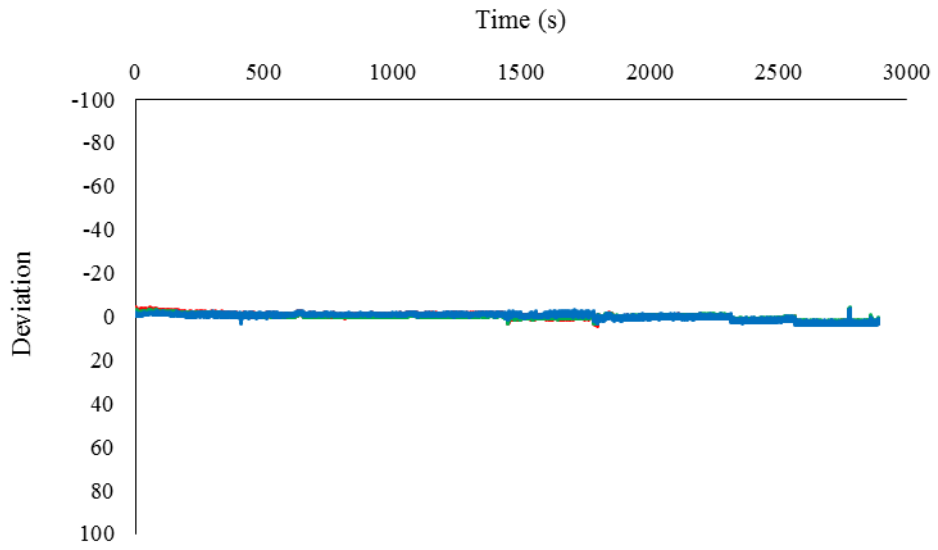
Figure 7.23 Control deviation for left side of half squaraine then SQ1 RGB analysis.
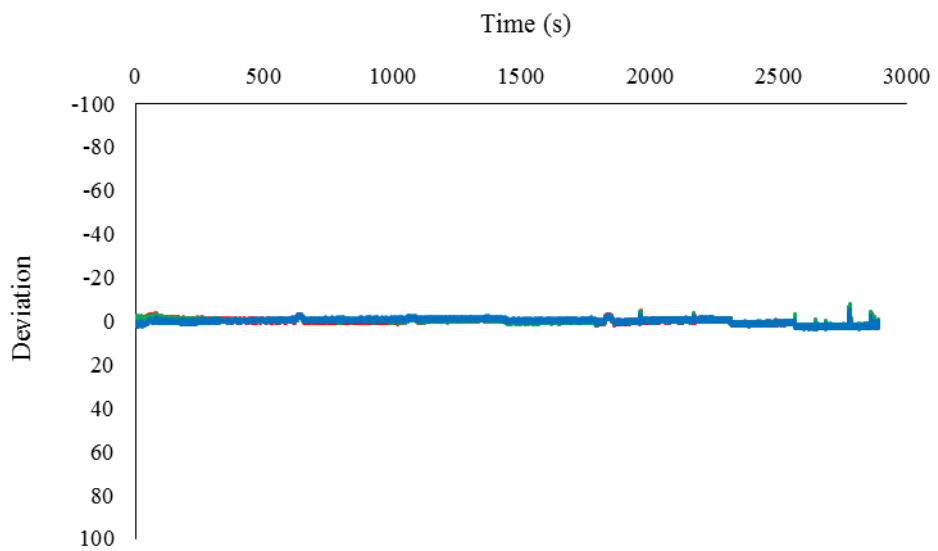
Figure 7.24 Control deviation for right side of half squaraine then SQ1 RGB analysis.
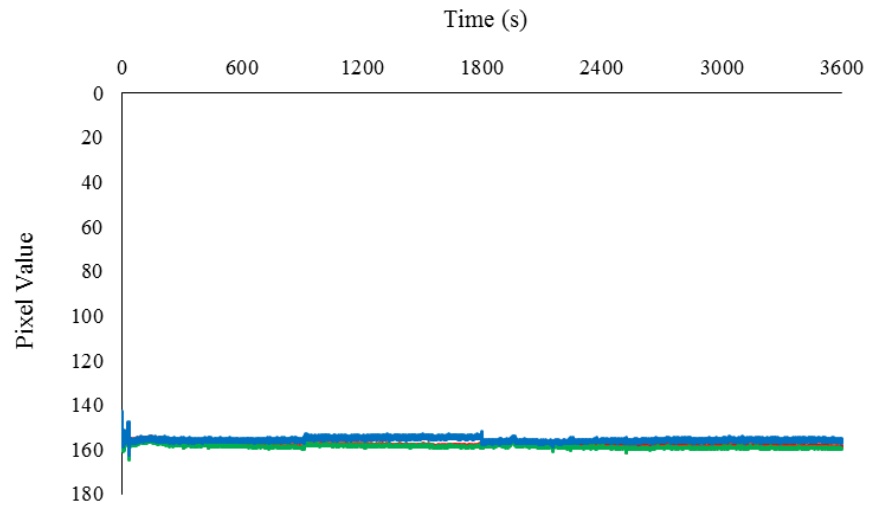
Figure 7.25 Control for left side of SQ1 then half squaraine RGB analysis.
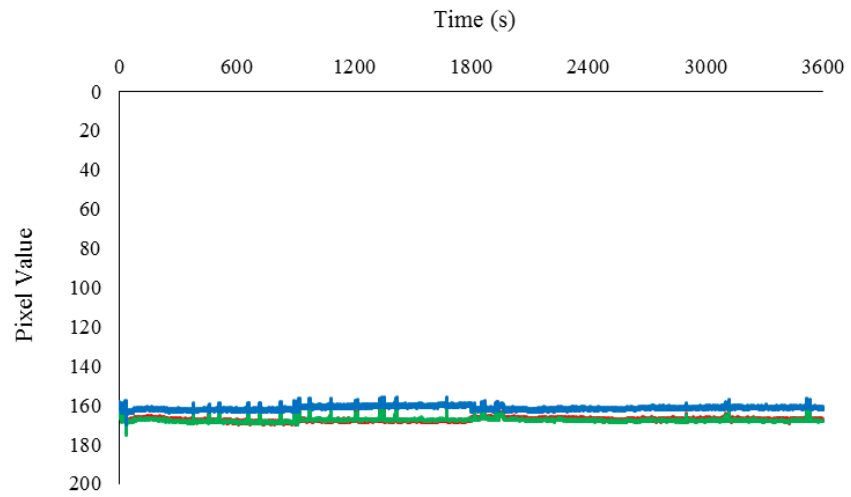
Figure 7.26 Control for right side of SQ1 then half squaraine RGB analysis.
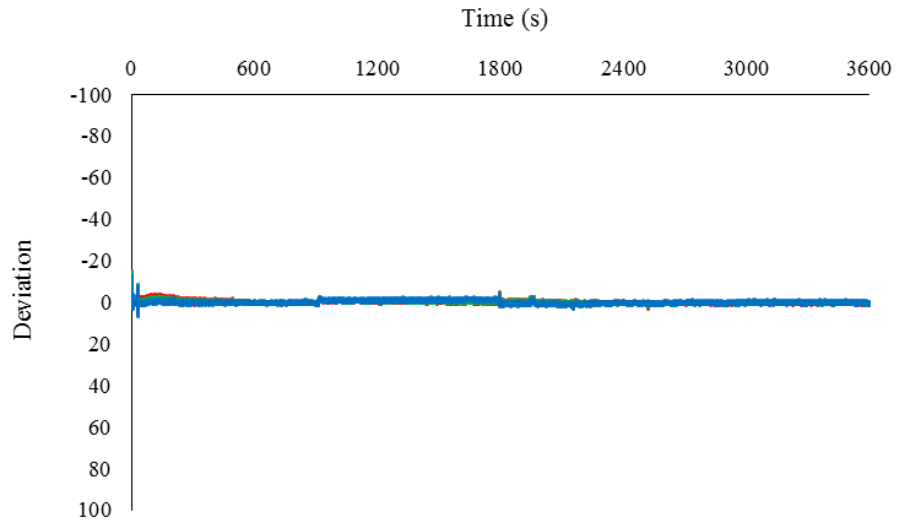
Figure 7.27 Control deviation for left side of SQ1 then half squaraine RGB analysis.
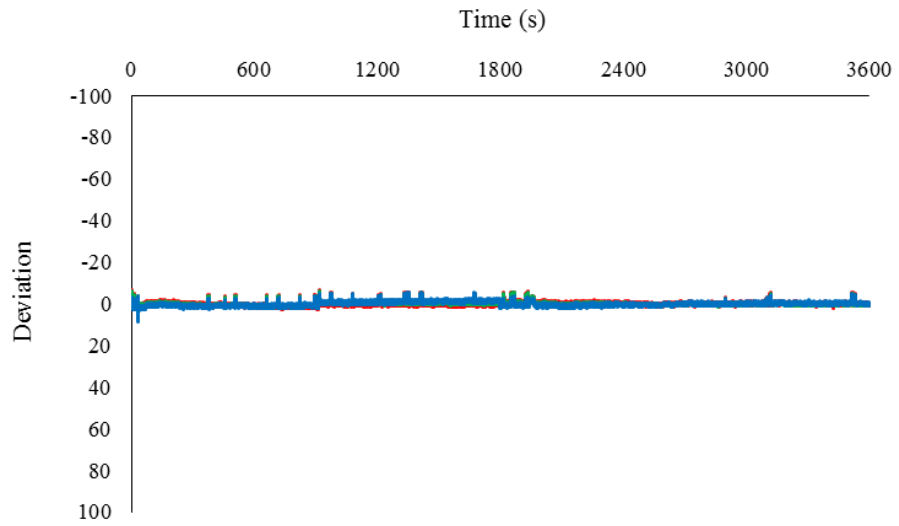
Figure 7.28 Control deviation for right side of SQ1 then half squaraine RGB analysis.
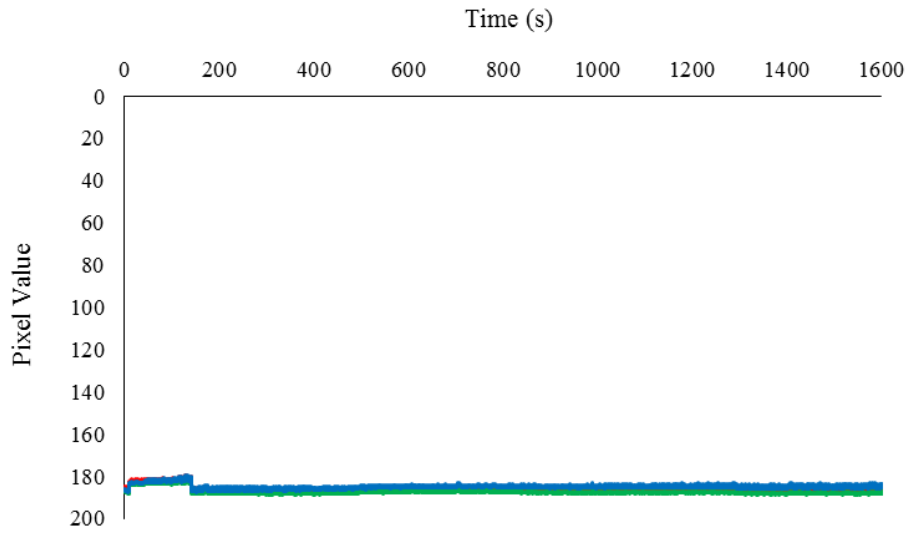
Figure 7.29 Control for left side of 1:3 mixture of SQ1 and half squaraine.
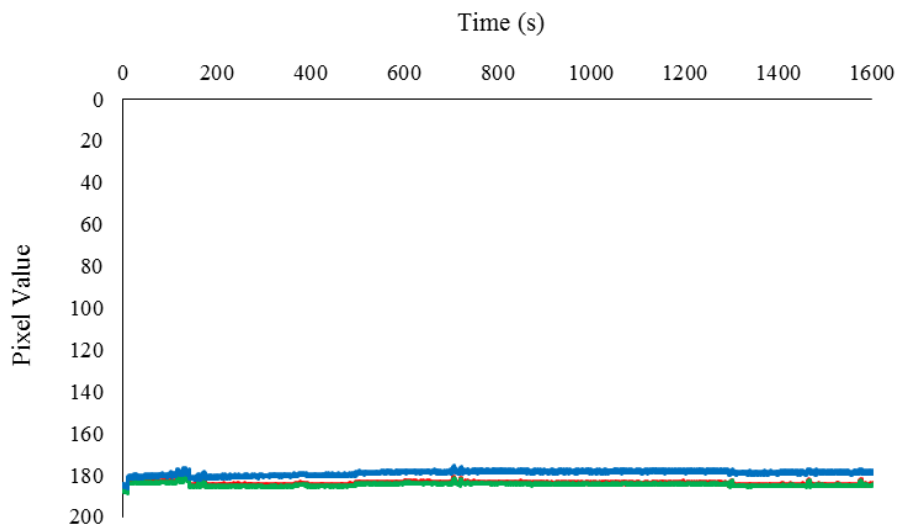
Figure 7.30 Control for right side of 1:3 mixture of SQ1 and half squaraine.
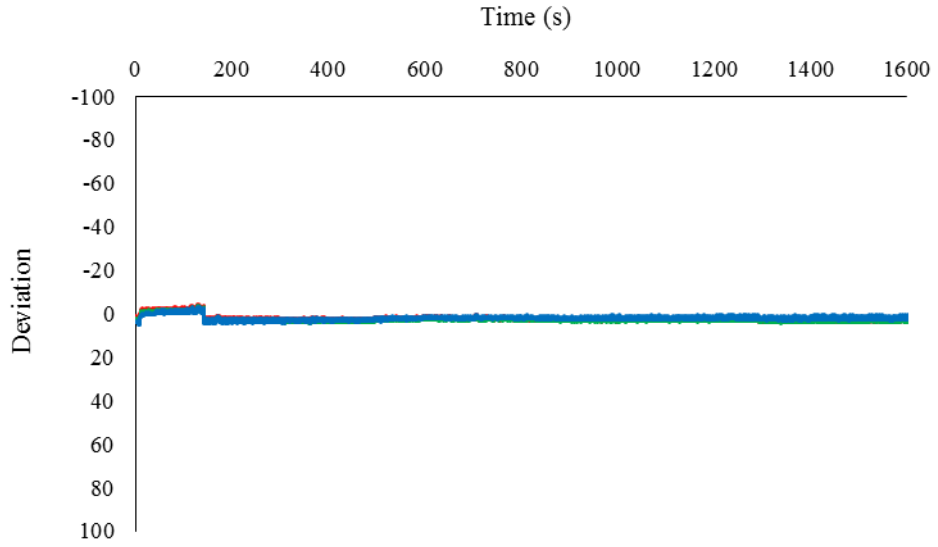
Figure 7.31 Control deviation for left side of 1:3 mixture of SQ1 and half squaraine.
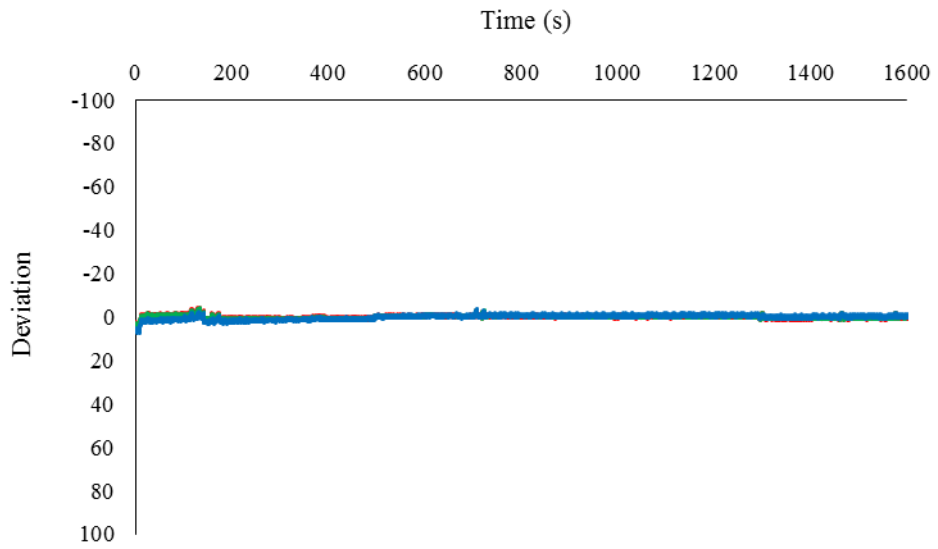
Figure 7.32 Control deviation for right side of 1:3 mixture of SQ1 and half squaraine.

156

Chapter 8 References

1. J. G. Canadell, C. Le Quéré, M. R. Raupach, C. B. Field, E. T. Buitenhuis, P. Ciais, T. J. Conway, N. P. Gillett, R. A. Houghton, G. Marland, *Proceedings of the National Academy of Sciences of the United States of America*, 2007, **104**, 18866–18870.
2. M. R. Allen, D. J. Frame, C. Huntingford, C. D. Jones, J. A. Lowe, M. Meinshausen, N. Meinshausen, *Nature*, 2009, **458**, 1163–1166.
3. P. Forster, V. Ramaswamy, *Changes in Atmospheric Constituents and in Radiative Forcing*, 2007, vol. 30.
4. R. J. Andres, G. Marland, I. Fung, E. Matthews, 1996, **10**, 419–429.
5. P. R. Ehrlich, J. P. Holdren, *Science*, 1971, **171**, 1212–1217.
6. W. S. Humphrey, J. Stanislaw, *Energy Policy*, 1979, **7**, 29–42.
7. R. E. H. Sims, H. H. Rogner, K. Gregory, *Energy Policy*, 2003, **31**, 1315–1326.
8. L. White, *Renewable Energy Focus*, 2015, **16**, 120–123.
9. E. A. Alsema, *Progress in Photovoltaics: Research and Applications*, 2000, **25**, 17–25.
10. M. R. Raupach, G. Marland, P. Ciais, C. Le Quéré, J. G. Canadell, G. Klepper, C. B. Field, *Proceedings of the National Academy of Sciences of the United States of America*, 2007, **104**, 10288–10293.
11. D. Turney, V. Fthenakis, *Renewable and Sustainable Energy Reviews*, 2011, **15**, 3261–3270.
12. J. Benemann, O. Chehab, E. Schaar-Gabriel, *Solar Energy Materials and Solar Cells*, 2001, **67**, 345–354.
13. B. P. Jelle, C. Breivik, H. Drolsum Røkenes, *Solar Energy Materials and Solar Cells*, 2012, **100**, 69–96.
14. M. Oliver, T. Jackson, *Energy*, 2001, **26**, 431–439.
15. M. Erol-Kantarci, H. T. Mouftah, *Computers and Communications (ISCC), 2010 IEEE Symposium on*, 2010, 456–458.
16. N. S. Lewis, *Science*, 2010, **798**, 798.
17. P. Río, *Energy Policy*, 2012, **41**, 139–151.
18. F. Baker, *Clean Energy Technologies*, 2015, **4**, 136–139.
19. *https://www.gov.uk/government/statistics/solar-photovoltaics-deployment*, (accessed September 2016).
20. J. Tinguely, R. Solarska, A. Braun, T. Graule, *Semiconductor Science and Technology*, 2011, **26**, 045007.
21. *www.nrel.gov/ncpv/images/efficiency_chart.jpg*, (accessed August 2016).
22. G. Marsh, *Renewable Energy Focus*, 2008, **9**, 58–62.
23. A. C. Veltkamp, *Presented at: 22nd European Photovoltaic Solar Energy Conference and Exhibition*, 2007, **3**, 3–7.
24. US Department of Energy, *The National Renewable Energy Laboratory*, 2004, 1–2.
25. B. O'Regan, M. Grätzel, *Nature*, 1991, **353**, 737–740.

26. M. K. Nazeeruddin, F. De Angelis, S. Fantacci, A. Selloni, G. Viscardi, P. Liska, S. Ito, B. Takeru, M. Grätzel, *Journal of the American Chemical Society*, 2005, **127**, 16835–47.

27. A. Hagfeldt, G. Boschloo, L. Sun, L. Kloo, H. Pettersson, *Chemical Reviews*, 2010, **110**, 6595–6663.

28. T. Horiuchi, H. Miura, K. Sumioka, S. Uchida, *J Am Chem Soc*, 2004, **126**, 12218–12219.

29. S. Ito, S. M. Zakeeruddin, R. Humphry-Baker, P. Liska, R. Charvet, P. Comte, M. K. Nazeeruddin, P. Péchy, M. Takata, H. Miura, S. Uchida, M. Grätzel, *Advanced Materials*, 2006, **18**, 1202–1205.

30. Q. Wang, S. Ito, M. Grätzel, F. Fabregat-Santiago, I. Mora-Seró, J. Bisquert, T. Bessho, H. Imai, *Journal of Physical Chemistry C*, 2006, **110**, 25210–25221.

31. J. Kawakita, *Science and Technology Trends*, 2010, **5**, 70–82.

32. J. M. Kroon, N. J. Bakker, H. J. P. Smit, P. Liska, K. R. Thampi, P. Wang, A. Hinsch, S. Hore, U. Wu, R. Sastrawan, J. R. Durrant, S. M. Zakeeruddin, M. Gra, E. Palomares, H. Pettersson, T. Gruszecki, J. Walter, K. Skupien, G. E. Tulloch, *Progress in Photovoltaics: Research and Applications*, 2007, **15**, 1–18.

33. W. U. Huynh, J. J. Dittmer, a P. Alivisatos, *Science*, 2002, **295**, 2425 LP – 2427.

34. W. Shockley, H. J. Queisser, *Journal of Applied Physics*, 1961, **32**, 510–519.

35. S. Rühle, *Solar Energy*, 2016, **130**, 139–147.

36. J. N. Munday, *Journal of Applied Physics*, 2012, **112**, 101063.

37. M. D. Archer, J. R. Bolton, *The Journal of Physical Chemistry*, 1990, **94**, 8028–8036.

38. M. Wanlass, P. Ahrenkiel, D. Albin, J. Carapella, A. Duda, K. Emery, D. Friedman, J. Geisz, K. Jones, A. Kibbler, J. Kiehl, S. Kurtz, W. McMahon, T. Moriarty, J. Olson, A. Ptak, M. Romero, S. Ward, *2006 IEEE 4th World Conference on Photovoltaic Energy Conference*, 2006, 729–732.

39. A. L. Rogach, L. Katsikas, A. Kornowski, S. Dangsheng, A. Eychmüller, H. Weller, *Ber. Bunsen Phys. Chem.*, 1996, **100**, 1772 – 1778.

40. M. Grätzel, *Journal of Photochemistry and Photobiology A: Chemistry*, 2004, **164**, 3–14.

41. N. Robertson, *Angewandte Chemistry*, 2008, **47**, 1012–1014.

42. N. Robertson, *Angewandte Communications*, 2006, **45**, 2338–45.

43. S. Holmberg, A. Perebikovsky, L. Kulinsky, M. Madou, *Micromachines*, 2014, **5**, 171–203.

44. J. Gong, J. Liang, K. Sumathy, *Renewable and Sustainable Energy Reviews*, 2012, **16**, 5848–5860.

45. H. J. Snaith, L. Schmidt-Mende, *Advanced Materials*, 2007, **19**, 3187–3200.

46. M. Grätzel, *Journal of Photochemistry and Photobiology C: Photochemistry Reviews*, 2003, **4**, 145–153.

47. *www.dupont.com//content/dam/dupont/products-and-services/packaging-materials-and-solutions/packaging-materials-and-solutions-*

landing/documents/Typical_Properties_of_Surlyn_.pdf, (accessed August 2016).

48. J. Kilner, S. Skinner, *Functional Materials for Sustainable Energy Applications*, 2012.

49. M. S. Silberberg, *Principles of General Chemistry*, McGraw-Hill Higher Education, 2006, vol. 1.

50. J. Dharma, A. Pisal, I. PerkinElmer, *Global Application Library*, 2012, 4–7.

51. N. Serpone, *Journal of Physical Chemistry B*, 2006, **110**, 24287–24293.

52. A. P. Popov, A. V. Priezzhev, J. Lademann, R. Myllyla, *Journal of Physics D: Applied Physics*, 2005, **38**, 2564–2570.

53. D. Wang, Y. Zou, S. Wen, D. Fan, *Applied Physics Letters*, 2009, **95**, 10–13.

54. Y.-Q. Wang, S.-G. Chen, X.-H. Tang, O. Palchik, a. Zaban, Y. Koltypin, a. Gedanken, *Journal of Materials Chemistry*, 2001, **11**, 521–526.

55. U. Diebold, *Surface Science Reports*, 2003, **48**, 53–229.

56. A. Fahmi, C. Minot, B. Silvi, M. Causá, *Physical Review B*, 1993, **47**, 11717–11724.

57. S. Di Mo, W. Y. Ching, *Physical Review B*, 1995, **51**, 13023–13032.

58. V. C. Fuertes, C. F. a Negre, M. B. Oviedo, F. P. Bonafé, F. Y. Oliva, C. G. Sánchez, *J. Phys.: Condens. Matter*, 2013, **25**, 5304–5307.

59. C. Dette, M. a. Pérez-Osorio, C. S. Kley, P. Punke, C. E. Patrick, P. Jacobson, F. Giustino, S. J. Jung, K. Kern, *Nano Letters*, 2014, **14**, 6533–6538.

60. D. Reyes-Coronado, G. Rodríguez-Gattorno, M. E. Espinosa-Pesqueira, C. Cab, R. de Coss, G. Oskam, *Nanotechnology*, 2008, **19**, 145605.

61. a. Amtout, R. Leonelli, *Physical Review B*, 1995, **51**, 6842–6851.

62. N. Wetchakun, B. Incessungvorn, K. Wetchakun, S. Phanichphant, *Materials Letters*, 2012, **82**, 195–198.

63. K. Kakiage, Y. Aoyama, T. Yano, K. Oya, J. Fujisawa, M. Hanaya, *Chemical communications*, 2015, **51**, 15894–15897.

64. O. Diwald, T. L. Thompson, T. Zubkov, S. D. Walck, J. T. Yates, *The Journal of Physical Chemistry B*, 2004, **108**, 6004–6008.

65. X. Hong, Z. Wang, W. Cai, F. Lu, J. Zhang, Y. Yang, N. Ma, Y. Liu, *Chemistry of Materials*, 2005, **17**, 1548–1552.

66. S. N. Frank, A. J. Bard, *Journal of the American Chemical Society*, 1975, **97**, 7427–7433.

67. a. M. Bakhshayesh, M. R. Mohammadi, *Ceramics International*, 2013, **39**, 7343–7353.

68. D. Dini, Y. Halpin, J. G. Vos, E. a. Gibson, *Coordination Chemistry Reviews*, 2015, **304**, 179–201.

69. H. Gerischer, *The Journal of Physical Chemistry*, 1991, **95**, 1356–1359.

70. J.-L. Lan, T.-C. Wei, S.-P. Feng, C.-C. Wan, G. Cao, *The Journal of Physical Chemistry C*, 2012, **116**, 25727–25733.

71. J. Teuscher, A. Marchioro, J. Andrès, L. M. Roch, M. Xu, S. M. Zakeeruddin, P. Wang, M. Grätzel, J. E. Moser, *Journal of Physical Chemistry C*, 2014, **118**, 17108–17115.

72. J. Jeon, I. William A. Goddard, H. Kim, *J. Am. Chem. Soc.*, 2013, **135**, 2431–2434.

73. S. a. Haque, E. Palomares, B. M. Cho, A. N. M. Green, N. Hirata, D. R. Klug, J. R. Durrant, *Journal of the American Chemical Society*, 2005, **127**, 3456–3462.

74. N. Tanabe, *Fujikura Technical Review*, 2013, **1**, 109–113.

75. N. Sridhar, D. Freeman, *Conference Proceedings of the 26th EU-PVSEC*, 2011, **3**, 232–236.

76. S. Yoon, S. Tak, J. Kim, Y. Jun, K. Kang, J. Park, *Building and Environment*, 2011, **46**, 1899–1904.

77. L. Thorington, *Annals of the New York Academy of Sciences*, 1985, **453**, 28–54.

78. S. V. Szokolay, *Solar Geometry*, Passive and Lowe Energy Architecture International, Brisbane, 2007, vol. 2.

79. P. Burgess, *Continuous Cover Forestry Group (CCFG) Scientific Meeting*, 2009, **29**, 1–10.

80. D. L. King, J. A. Kratochvil, W. E. Boyson, *Conference Record of the Twenty Sixth IEEE Photovoltaic Specialists Conference - 1997*, 1997, 1113–1116.

81. J. F. Petersen, D. Sack, R. E. Gabler, *Physical Geography*, Cengage Learning, Boston, USA, 11th edn., 2016.

82. S. R. Wenham, M. A. Green, M. E. Watt, R. Corkish, A. Sproul, *Applied Photovoltaics*, Earthscan, 3rd edn., 2007.

83. *www.rredc.nrel.gov/solar/spectra/am1.5/*, (accessed June 2015).

84. J. F. Randall, J. Jacot, *Renewable Energy*, 2003, **28**, 1851–1864.

85. C. A. Gueymard, *Solar Energy*, 2004, **76**, 423–453.

86. L. Schmidt-Mende, M. Grätzel, *Thin Solid Films*, 2006, **500**, 296–301.

87. M. Wang, J. Liu, N. Cevey-Ha, S. Moon, P. Liska, R. Humphry-Baker, J. Moser, C. Grätzel, P. Wang, S. M. Zakeeruddin, *Nano Today*, 2010, **5**, 169–174.

88. S. Mathew, A. Yella, P. Gao, R. Humphry-Baker, B. F. E. Curchod, N. Ashari-Astani, I. Tavernelli, U. Rothlisberger, M. K. Nazeeruddin, M. Grätzel, *Nature Chemistry*, 2014, **6**, 242–247.

89. T. Leijtens, I. Ding, T. Giovenzana, *ACS Nano*, 2012, **6**, 1455–1462.

90. C. Hsu, Y. Chen, R. Y. Lin, K. Ho, J. T. Lin, *Physical Chemistry Chemical Physics*, 2012, **14**, 14099–14109.

91. I. Ding, N. Tétreault, J. Brillet, B. E. Hardin, E. H. Smith, S. J. Rosenthal, F. Sauvage, M. Grätzel, M. D. McGehee, *Advanced Functional Materials*, 2009, **19**, 2431–2436.

92. I. Ding, J. Melas-Kyriazi, N. Cevey-Ha, K. G. Chittibabu, S. M. Zakeeruddin, M. Grätzel, M. D. McGehee, *Organic Electronics*, 2010, **11**, 1217–1222.

93. N. Cai, S.-J. Moon, L. Cevey-Ha, T. Moehl, R. Humphry-Baker, P. Wang, S. M. Zakeeruddin, M. Grätzel, *Nano Letters*, 2011, **11**, 1452–1456.

94. W. M. Campbell, A. K. Burrell, D. L. Officer, K. W. Jolley, *Coordination Chemistry Reviews*, 2004, **248**, 1363–1379.

95. S. M. Feldt, E. a Gibson, E. Gabrielsson, L. Sun, G. Boschloo, A. Hagfeldt, *Journal of the American Chemical Society*, 2010, **132**, 16714–24.

96. A. Mishra, M. K. R. Fischer, P. Bäuerle, *Angewandte Communications*, 2009, **48**, 2474–2499.

97. K. Hara, T. Sato, R. Katoh, a Furube, Y. Ohga, a Shinpo, S. Suga, K. Sayama, H. Sugihara, H. Arakawa, *J. Phys. Chem. B*, 2003, **107**, 597–606.

98. G. C. Vougioukalakis, A. I. Philippopoulos, T. Stergiopoulos, P. Falaras, *Coordination Chemistry Reviews*, 2011, **255**, 2602–2621.

99. *www.dyesol.com/products/dsc-materials/dyes*, (accessed September 2016).

100. P. J. Holliman, M. L. Davies, A. Connell, B. Vaca Velasco, T. M. Watson, *Chemical Communications*, 2010, **46**, 7256–7258.

101. R. Harikisun, H. Desilvestro, *Solar Energy*, 2011, **85**, 1179–1188.

102. J. H. Yum, S. J. Moon, R. Humphry-Baker, P. Walter, T. Geiger, F. Nüesch, M. Grätzel, M. D. K. Nazeeruddin, *Nanotechnology*, 2008, **19**, 4240–4245.

103. A. Islam, H. Sugihara, H. Arakawa, *Journal of Photochemistry and Photobiology A: Chemistry*, 2003, **158**, 131–138.

104. M. K. Nazeeruddin, A. Kay, E. Müller, P. Liska, N. Vlachopoulos, M. Grätzel, C. Lausanne, R. April, *Journal of the American Chemical Society*, 1993, **115**, 6382–6390.

105. M. K. Nazeeruddin, R. Splivallo, P. Liska, P. Comte, M. Grätzel, *Chemical Communications*, 2003, **12**, 1456–1457.

106. K. Kakiage, Y. Aoyama, T. Yano, T. Otsuka, T. Kyomen, M. Unno, M. Hanaya, *Chemical communications*, 2014, **50**, 6379–6381.

107. B. Xu, H. Tian, D. Bi, E. Gabrielsson, E. M. J. Johansson, G. Boschloo, A. Hagfeldt, L. Sun, *Journal of Materials Chemistry A*, 2013, **1**, 14467.

108. Y. Ren, Y.-Z. Zheng, J. Zhao, J.-F. Chen, W. Zhou, X. Tao, *Electrochemistry Communications*, 2012, **16**, 57–60.

109. M. M. K. Nazeeruddin, P. Pechy, M. Grätzel, P. Péchy, M. Grätzel, *Chemical Communications*, 1997, **1**, 1705–1706.

110. M. Nazeeruddin, P. Pechy, M. Grätzel, *Chemical Communications*, 1997, **1**, 1705–1706.

111. C. Sahin, C. Tozlu, K. Ocakoglu, C. Zafer, C. Varlikli, S. Icli, *Inorganica Chimica Acta*, 2008, **361**, 671–676.

112. H. Minoura, T. Yoshida, *Electrochemistry*, 2008, **76**, 109–117.

113. T. Maeda, H. Nakao, H. Kito, H. Ichinose, S. Yagi, H. Nakazumi, *Dyes and Pigments*, 2011, **90**, 275–283.

114. R. Lin, Y. Yen, Y. Cheng, C. Lee, Y. Hsu, H. Chou, C. Hsu, Y. Chen, J. T. Lin, K. Ho, C. Tsai, *Organic Letters*, 2012, **14**, 2010–2013.

115. A. Hinsch, J. M. Kroon, R. Kern, I. Uhlendorf, J. Holzbock, A. Meyer, J. Ferber, *Progress in Photovoltaics: Research and Applications*, 2001, **9**, 425–438.

116. T. Watson, P. Holliman, D. Worsley, *Journal of Materials Chemistry*, 2011, **21**, 4321–4325.

117. H. Tanaka, A. Takeichi, K. Higuchi, T. Motohiro, M. Takata, N. Hirota, J. Nakajima, T. Toyoda, *Solar Energy Materials and Solar Cells*, 2009, **93**, 1143–1148.

118. J. Wu, S. Hao, Z. Lan, J. Lin, M. Huang, Y. Huang, L. Fang, S. Yin, T. Sato, *Advanced Functional Materials*, 2007, **17**, 2645–2652.

119. K. Kakiage, Y. Aoyama, T. Yano, K. Oya, T. Kyomen, M. Hanaya, *Chemical Communications*, 2015, **51**, 6315–6317.

120. I. Chung, B. Lee, J. He, R. P. H. Chang, M. G. Kanatzidis, *Nature*, 2012, **485**, 486–489.

121. H. J. Snaith, A. J. Moule, C. Klein, K. Meerholz, R. H. Friend, M. Grätzel, *Nano Letters*, 2007, **7**, 3372–3376.

122. D. Kuang, C. Klein, H. J. Snaith, R. Humphry-Baker, S. M. Zakeeruddin, M. Grätzel, *Inorganica Chimica Acta*, 2008, **361**, 699–706.

123. Y. Cao, N. Cai, Y. Wang, R. Li, Y. Yuan, P. Wang, *Physical Chemistry Chemical Physics*, 2012, **14**, 8282–8286.

124. A. Kojima, K. Teshima, Y. Shirai, T. Miyasaka, *Journal of the American Chemical Society*, 2009, **131**, 6050–6051.

125. M. Green, K. Emery, *Progress in Photovoltaics: Research and Applications*, 2012, **20**, 606–614.

126. M. Saliba, T. Matsui, J.-Y. Seo, K. Domanski, J.-P. Correa-Baena, M. K. Nazeeruddin, S. M. Zakeeruddin, W. Tress, A. Abate, A. Hagfeldt, M. Grätzel, *Energy Environ. Sci.*, 2016, **9**, 1989–1997.

127. H. J. Snaith, *Physical Chemistry Letters*, 2013, **4**, 2623–3630.

128. G. Niu, X. Guo, L. Wang, *Journal of Materials Chemistry A*, 2015, **3**, 8970–8980.

129. N. K. Noel, S. D. Stranks, A. Abate, C. Wehrenfennig, S. Guarnera, A. Haghighirad, A. Sadhanala, G. E. Eperon, S. K. Pathak, M. B. Johnston, A. Petrozza, L. Herz, H. J. Snaith, *Energy & Environmental Science*, 2014, **7**, 3061–3068.

130. G. Pierre, F. Auzel, J.-C. Guillaume, K. Zahraman, *Journal of Applied Physics*, 1996, **35**, 4401–4402.

131. M. Konagai, M. Sugimoto, K. Takahashi, *Journal of Crystal Growth*, 1978, **45**, 277–280.

132. G. J. Bauhuis, P. Mulder, E. J. Haverkamp, J. C. C. M. Huijben, J. J. Schermer, *Solar Energy Materials and Solar Cells*, 2009, **93**, 1488–1491.

133. M. a. Stan, D. J. Aiken, P. R. Sharps, N. S. Fatemi, F. a. Spadafora, J. Hills, H. Yoo, B. Clevenger, *Conference Record of the Twenty-Ninth IEEE Photovoltaic Specialists Conference, 2002.*, 2002, **M**, 816–819.

134. P. Krogstrup, H. I. Jørgensen, M. Heiss, O. Demichel, J. V Holm, M. Aagesen, J. Nygard, A. Fontcuberta i Morral, *Nature Photonics*, 2013, **7**, 101038.

135. *www.altadevices.com/technology-overview/*, (accessed August 2016).

136. A. Hagfeldt, G. Boschloo, H. Lindström, E. Figgemeier, A. Holmberg, V. Aranyos, E. Magnusson, L. Malmqvist, *Coordination Chemistry Reviews*, 2004, **248**, 1501–1509.

137. L. Andrade, S. M. Zakeeruddin, M. K. Nazeeruddin, H. A. Ribeiro, A. Mendes, M. Grätzel, *ChemPhysChem*, 2009, **10**, 1117–1124.

138. P. Sommeling, M. Späth, H. Smit, N. Bakker, J. Kroon, *Journal of Photochemistry and Photobiology A: Chemistry*, 2004, **164**, 137–144.

139. G. Xue, Y. Guo, T. Yu, J. Guan, X. Yu, *International Journal of Electrochemical Science*, 2012, **7**, 1496–1511.

140. M. Giustini, D. Angelone, M. Parente, D. Dini, F. Decker, A. Lanuti, A. Reale, T. Brown, A. Carlo, *Journal of Applied Electrochemistry*, 2012, **43**, 209–215.

141. T. Bessho, E. Yoneda, J. Yum, M. Guglielmi, I. Tavernelli, H. Imai, U. Rothlisberger, M. H. Nazeeruddin, M. Grätzel, *Journal of the American Chemical Society*, 2009, **131**, 5930–5934.

142. S. Hwang, J. H. Lee, C. Park, H. Lee, C. Kim, C. Park, M.-H. Lee, W. Lee, J. Park, K. Kim, N.-G. Park, C. Kim, *Chemical Communications*, 2007, 4887.

143. A. Connell, P. J. Holliman, M. L. Davies, C. D. Gwenin, S. Weiss, M. B. Pitak, P. N. Horton, S. J. Coles, G. Cooke, *Journal of Materials Chemistry A*, 2014, **2**, 4055–4066.

144. A. Connell, P. J. Holliman, E. W. Jones, L. Furnell, C. Kershaw, M. L. Davies, C. D. Gwenin, M. B. Pitak, S. J. Coles, G. Cooke, *Journal of Materials Chemistry A*, 2015, **3**, 2883–2894.

145. T. Horiuchi, H. Miura, S. Uchida, *Chemical Communications*, 2003, 3036–3037.

146. P. J. Holliman, M. Mohsen, A. Connell, M. L. Davies, K. Al-Salihi, M. B. Pitak, G. J. Tizzard, S. J. Coles, R. W. Harrington, W. Clegg, C. Serpa, O. H. Fontes, C. Charbonneau, M. J. Carnie, *Journal of Materials Chemistry*, 2012, **22**, 13318.

147. D. Joly, L. Pellejà, S. Narbey, F. Oswald, J. Chiron, J. N. Clifford, E. Palomares, R. Demadrille, *Scientific reports*, 2014, **4**, 4033.

148. J. Gao, W. Yang, M. Pazoki, G. Boschloo, L. Kloo, *The Journal of Physical Chemistry C*, 2015, 24704–24713.

149. A. Burke, L. Schmidt-Mende, S. Ito, M. Grätzel, *Chemical Communications*, 2007, 234–236.

150. T. Geiger, S. Kuster, J.-H. Yum, S.-J. Moon, M. K. Nazeeruddin, M. Grätzel, F. Nüesch, *Advanced Functional Materials*, 2009, **19**, 2720–2727.

151. C.-M. Lan, H.-P. Wu, T.-Y. Pan, C.-W. Chang, W.-S. Chao, C.-T. Chen, C.-L. Wang, C.-Y. Lin, E. W.-G. Diau, *Energy & Environmental Science*, 2012, **5**, 6460–6464.

152. Z. Wu, Y. Wei, Z. An, X. Chen, P. Chen, *Bulletin of the Korean Chemical Society*, 2014, **35**, 1449–1454.

153. S. Paek, H. Choi, C. Kim, N. Cho, S. So, K. Song, M. K. Nazeeruddin, J. Ko, *Chemical communications*, 2011, **47**, 2874–2876.

154. C. Qin, Y. Numata, S. Zhang, X. Yang, A. Islam, K. Zhang, H. Chen, L. Han, *Advanced Functional Materials*, 2014, **24**, 3059–3066.

155. T. Wu, G. Liu, J. Zhao, *The Journal of Physical Chemistry B*, 1999, 4862–4867.

156. A. Fujishima, T. Rao, D. Tryk, *Journal of Photochemistry and Photobiology*, 2000, **1**, 1–21.

157. C. Karunakaran, R. Dhanalakshmi, *Solar Energy Materials and Solar Cells*, 2008, **92**, 1315–1321.

158. A. Barkschat, T. Moehl, B. Macht, H. Tributsch, *International Journal of Photoenergy*, 2008, 814951.

159. D. P. Hagberg, X. Jiang, E. Gabrielsson, M. Linder, T. Marinado, T. Brinck, A. Hagfeldt, L. Sun, *Journal of Materials Chemistry*, 2009, **19**, 7232–7238.

160. X. Jiang, K. M. Karlsson, E. Gabrielsson, E. M. J. Johansson, M. Quintana, M. Karlsson, L. Sun, G. Boschloo, A. Hagfeldt, *Advanced Functional Materials*, 2011, **21**, 2944–2952.

161. H. Tavallali, G. Deilamy-Rad, A. Parhami, N. Hasanli, *Journal of Hazardous Materials*, 2014, **266**, 189–197.

162. M. Mao, J. B. Wang, Z. F. Xiao, S. Y. Dai, Q. H. Song, *Dyes and Pigments*, 2012, **94**, 224–232.

163. K. Pydzińska, M. Ziółek, *Dyes and Pigments*, 2015, **122**, 272–279.

164. B. Fan, Y. Maniglio, M. Simeunovic, S. Kuster, T. Geiger, R. Hany, F. Nüesch, *International Journal of Photoenergy*, 2009, 10.1155/2009/581068.

165. *www.lumtec.com.tw*, (accessed June 2015).

166. H. Ozawa, R. Shimizu, H. Arakawa, *RSC Advances*, 2012, **2**, 3198–3200.

167. R. J. Tayade, T. S. Natarajan, H. C. Bajaj, *Industrial & Engineering Chemistry Research*, 2009, **48**, 10262–10267.

168. *www.metoffice.gov.uk/pub/data/weather/uk/climate/stationdata/valleydata.txt*, (accessed July 2015).

169. S. Muthu, F. J. P. Schuurmans, M. D. Pashley, *IEEE Journal of Selected Topics in Quantum Electronics*, 2002, **8**, 333–338.

170. R. W. G. Hunt, M. R. Pointer, *Measuring Colour*, John Wiley & Sons, 2011.

171. Y. He, W. Zhou, F. Wu, M. Li, E. Wang, *Journal of Photochemistry and Photobiology A: Chemistry*, 2004, **162**, 463–471.

172. P. Gijsman, J. Hennekens, D. Tummers, *Polymer Degradation and Stability*, 1993, **39**, 225–233.

173. P. Gijsman, *Polymer Degradation and Stability*, 1994, **43**, 171–176.

174. D. J. Carlsson, K. H. Chan, D. M. Wiles, *Journal of the American Chemical Society*, 1981, **5**, 61–83.

175. Alia, P. Mohanty, J. Matysik, *Amino Acids*, 2001, **21**, 195–200.

176. N. Kato, K. Higuchi, H. Tanaka, J. Nakajima, T. Sano, T. Toyoda, *Solar Energy Materials and Solar Cells*, 2011, **95**, 301–305.

177. V. Lebourgeois, A. Bégué, S. Labbé, B. Mallavan, L. Prévot, B. Roux, *Sensors*, 2008, **8**, 7300–7322.

178. R. F. Lyon, P. M. Hubel, *The Tenth Color Imaging Conference: Color Science and Engineering Systems, Technologies, Applications*, 2002, **10**, 349–355.

179. *http://micro.magnet.fsu.edu/primer/digitalimaging/concepts/images/quantum efficiencyfigure1.jpg*, (accessed September 2016).

180. N. Kato, Y. Takeda, K. Higuchi, A. Takeichi, E. Sudo, H. Tanaka, T. Motohiro, T. Sano, T. Toyoda, *Solar Energy Materials and Solar Cells*, 2009, **93**, 893–897.

181. E. Leonardi, S. Penna, T. M. Brown, A. Di Carlo, A. Reale, *Journal of Non-Crystalline Solids*, 2010, **356**, 2049–2052.

182. M. Carnie, D. Bryant, T. Watson, D. Worsley, *International Journal of Photoenergy*, 2012, 524590.

183. M. Pastore, F. De Angelis, *ACS Nano*, 2010, **4**, 556–562.

184. K. A. N. Nurain, Yaacob, *Sains Malaysiana*, 2016, **45**, 1227–1234.

185. C. Lee, W. Lee, C. Yang, *International Journal of Photoenergy*, 2013, **23**, 250397.

186. S. Gorard, *British Journal of Educational Studies*, 2005, **53**, 417–430.

187. K. Zhang, C. Qin, X. Yang, A. Islam, S. Zhang, H. Chen, L. Han, *Advanced Energy Materials*, 2014, **4**, 01966.

188. www.dyesol.com/products/dsc-materials/pastes/18nrt-transparent-titania-paste.html, (accessed August 2016).

189. www.dyesol.com/products/dsc-materials/pastes/18nrao-active-opaque-titania-paste.html, (accessed July 2016).

190. K. Nakata, A. Fujishima, *Journal of Photochemistry and Photobiology C: Photochemistry Reviews*, 2012, **13**, 169–189.

191. Y. Saito, S. Kambe, T. Kitamura, Y. Wada, S. Yanagida, *Solar Energy Materials and Solar Cells*, 2004, **83**, 02010.

192. H. Lan, F. Xue, Z. Liu, L. Chen, C. Huang, T. Yi, *Advanced Optical Materials*, 2016, **4**, 1367–1372.

193. D. Codd, A. Carlson, J. Rees, A. Slocum, *Solar Energy*, 2010, **84**, 1–19.